UNIVERSITY OF CALIFORNIA

Los Angeles

Pulsar-Based Navigation and Timing: Analysis and Estimation

A dissertation submitted in partial satisfaction

of the requirements for the degree

Doctor of Philosophy in Aerospace Engineering

by

Po-Ting Chen

2018

ABSTRACT OF THE DISSERTATION

Pulsar-Based Navigation and Timing: Analysis and Estimation

by

Po-Ting Chen
Doctor of Philosophy in Aerospace Engineering
University of California, Los Angeles, 2018
Professor Jason L. Speyer, Chair

Millisecond pulsars are extremely stable and rapidly rotating neutron stars that emit electromagnetic radiation along their magnetic axes. Due to the misalignment between the rotational and the magnetic axes, the observed pulsar signals are analogous to the light beams of distant lighthouses. The predictable pulsing behavior is the fundamental mechanism that allows researchers to use pulsars as tools for science and engineering. This research focused on the analysis, simulation, estimation, and verification associated with pulsar-based navigation and clock calibration.

The autonomous pulsar-based navigation problem is formulated in terms of a nonlinear filtering problem where a single filter is used to estimate the spacecraft position and velocity. The positioning accuracy of a spacecraft traveling at known constant velocity was analyzed to build insights into the general navigation problem. An analytical comparison between the measurement noises of X-ray based and radio based pulsar timing/navigation system is discussed. A variation of the Extended Kalman Filter was developed and implemented to track simulated X-ray pulsar measurements collected by an orbiting spacecraft. This filter uses a multirate structure to more efficiently process pulsar measurements. The ephemeris of the DAWN spacecraft was used to investigate the performance of pulsar-based navigation in a more realistic mission scenario.

In order to show the feasibility of pulsar-based navigation, several existing pulsar timing software packages and publicly available radio millisecond pulsar data were used to

experimentally verify the concept. An Unscented Kalman Filter was used to process the time-of-arrival measurements from 5 isolated millisecond pulsars in order to estimate the position of the radio telescope in Earth fixed coordinate system.

This research also investigated the theoretical frequency stability of pulsar-aided atomic clocks from power spectral densities. Hadamard variance was used to analyze the unfiltered and the filtered clock systems. The result of the analysis shows that pulsars have the potential of enhancing the long-term frequency stability of stand-alone compact atomic clocks.

The last chapter of this dissertation discusses relative positioning using differential phase measurement. The proposed method can be used to eliminate common mode errors embedded in the pulsar measurements when the two observed signal frequencies are known.

The dissertation of Po-Ting Chen is approved.

Lieven Vandenberghe

James S. Gibson

Tetsuya Iwasaki

Jason L. Speyer, Committee Chair

University of California, Los Angeles

2018

To my family,

Thank you for your unconditional love, encouragement, and support.

TABLE OF CONTENTS

LIST OF FIGURES

LIST OF TABLES

ACKNOWLEDGMENTS

First, I would like to thank my adviser, Professor Speyer, for giving me the opportunity to work with him in 2014. I am utmost grateful for his effort in educating and preparing me for a career in aerospace research and development. His extensive knowledge, countless success stories, and optimistic outlooks inspire me to continue to learn, be persistent and investigate new ideas. He will always be my role model for the rest of my professional career.

I would like to express my sincere appreciations to Dr. Walid Majid, Dr. David Bayard, and Dr. Lincoln Wood from the Jet Propulsion Laboratory. Dr. Majid gave me the chance to visit the lab and introduced me to the experimental aspect of pulsar timing. He pointed out several important research papers and software packages to help me complete my research. Dr. Bayard's technical guidance and thoughtful suggestions helped me understood the importance of covariance analysis in estimation and mission design. Furthermore, I am extremely grateful to his considerable effort for introducing me to the Guidance and Control Analysis Group. Dr. Wood's knowledge on various NASA missions and the state-of-the-art spacecraft navigation techniques enlightened me about the obstacles of real space exploration missions.

I would like to thank all my professors at UCLA for giving me support over the past 5 years, especially my committee members, Professor Iwasaki, Professor Gibson, and Professor Vandenberghe. Without them I will not be able to complete this research.

I thank Joanne and Keye for giving me the joy of life and for supporting me whenever I needed them. Lastly, I want to thank my friends, Dennis, Jinxin, Yu-Wei, and Jessica, for giving me sparks of excitement throughout my study.

VITA

2009	B.S. (Aerospace Engineering), University of California San Diego.
2010	M.S. (Aerospace Engineering), University of California San Diego.
2010-2013	Engineer, NextGen Aeronautics Inc.
2014–present	Graduate Student Researcher, Department of Mechanical and Aerospace Engineering, University of California Los Angeles.
2015–present	Research Affiliate, Jet Propulsion Laboratory, California Institute of Technology.

PUBLICATIONS

Po-Ting Chen, Walid A. Majid, and Jason L. Speyer. "Experimental Verification of Pulsar-Based Positioning System," AIAA Journal of Guidance, Control, and Dynamics. (Under review as a regular paper)

Po-Ting Chen, Jason L. Speyer, and Walid A. Majid. "Frequency Stability Analysis of Pulsar-Aided Atomic Clocks," IEEE Transactions on Signal Processing. (Under review as a regular paper)

Po-Ting Chen, Jason L. Speyer, David S. Bayard, and Walid A. Majid. "Autonomous Navigation Using X-Ray Pulsars and Multirate Processing", AIAA Journal of Guidance, Control, and Dynamics, Vol. 40, No. 9 (2017), pp. 2237-2249

Po-Ting Chen, Jason L. Speyer, and Walid A. Majid. Frequency Stability Analysis of Pulsar-Aided Atomic Clocks Precise Time and Timing Interval Meeting of the Institute of Navigation, Reston, VA, 2018

Po-Ting Chen, Walid A. Majid, and Jason L. Speyer. Pulsar-Based Positioning System, 2017 International Astronautical Congress, Adelaide, Australia, 2017

Po-Ting Chen, J. L. Speyer, D. S. Bayard and W. A. Majid. "Autonomous navigation using x-ray pulsars and multirate processing," 2017 American Control Conference (ACC), Seattle, WA, 2017, pp. 4563-4569

CHAPTER 1

Introduction

1.1 Significance of the Problem

As of April 2018, there are 28 active space exploration probes in the solar system[12]. Many of them are dependent on the navigation service provided by NASA's Deep Space Network (DSN) [13]. In addition to tracking space probes, the DSN also serves as a communication link between the probes and Earth. Commands from mission control are sent to the spacecraft using the radio uplink while scientific data collected by the probes are send back to Earth regularly via the downlink. Since the number of space probes is expected to increase in the future, the demand for accurate deep space tracking and communication remains high [14].

Current deep space navigation system relies on Earth based tracking stations. Radio signals are used to obtain range, range rate and angular position of the spacecraft to determine the position and velocity in inertial space. While this system is proven and has successfully directed multiple spacecraft to their missions in the Solar System, there are some fundamental limitations of Earth based navigation system. The first is the unavoidable communication delays, which is 8.33 min per AU[1]. At the edge of the solar system this delay is about 13 $hours$. Because of this delay, it is difficult to perform any real-time decision. For the current system, course corrections are made in a predictive manner. Furthermore, the tracking accuracy decreases as the distance from Earth increases. Therefore, it is difficult to fine-tune a spacecraft's trajectory using Earth based tracking station once it reaches the outer planets.

[1] $1\ AU = 149 \times 10^6\ km$

Pulsar based navigation is a potential solution to resolve the above limitations. It mitigates the impact of communication delay by introducing local autonomy into the spacecraft. Pulsar based onboard navigation system allows the spacecraft to make navigation decisions in real time. Therefore, the communication delay is removed in this sense. A pulsar based navigation system for our solar system is analogous to the GPS aided inertial navigation on Earth. This autonomous system observes naturally occurring signals. Thus, there is no need to construct and maintain expensive infrastructure such as the GPS constellations. Furthermore, unlike Earth based navigation system, the accuracy of a pulsar based navigation system is independent of the spacecraft's location in the solar system. This means that the accuracy of the navigation solution in low Earth orbit is the same as that in the outer edge of the solar system. This desirable quality is beyond the capability of Earth based navigation system.

1.2 Radiometric Tracking

The current deep space navigation capability is provided by NASA's Deep Space Network (DSN). This network consists of three radiometric communication facilities located roughly 120° apart on Earth to maintain continuous observability of the sky. Each complex consists of one $70\,m$ and several $34\,m$ steerable antennae. One of its primary missions is to determine the position and velocity of deep space spacecraft in the Solar System [15]. The distance information is obtained through the use of one-way, two-way or three-way ranging. A ranging signal from one of the stations is sent to the spacecraft using the communication uplink in one of three frequency bands (S, X, Ka). Once the signal is received and demodulated by the spacecraft, it is re-modulated and sent back to the ground station using the downlink. The transmitted and received signals are cross-correlated to obtain the time needed for the signal to leave and return to the station. The range information can be inferred from the estimated time. The turn around time associated with the onboard electronics is determined from pre-launch test [16]. The velocity information is obtained by determining the Doppler shift of the downlink signal. Combining the above two measurements, a precision fix of the

Figure 1.1: DSS-14 70 m reflector on an Alt/Az mount at Goldstone Complex [1]

spacecraft in three-dimensional space can be obtained. The 1σ error for ranging and Doppler are $\sim 1\,m$ and $\sim 0.05\,mm/s$ [17]. Doppler and two-way ranging are the most used methods for deep space navigation.

The most accurate navigation solution is obtained using a method called the Very Large Baseline Interferometry (VLBI). This technique utilizes two stations to measurement downlink wave front and calculates the angular direction of the spacecraft with respect to the baseline[2]. After measuring the downlink wave front, the two antennae would immediately slew directly to a near by quasar whose angular position in the sky is known to high precision. By comparing the measured quasar angular direction to the known angular value, common errors between the two stations can be identified and removed to obtain extremely accurate angular measurement of the spacecraft. This method is least used because it needs two stations simultaneously. The 1σ error for angular position using VLBI is $\sim 2.5\,nrad$ [17]. Converting it to position error gives

$$149597870.7\,km \times \tan(2.5 \times 10^{-9}) \approx 0.374\,km/AU, \tag{1.1}$$

where $1\ AU = 149597870.7\,km$. Using Eq. (1.1), the positioning accuracy of a spacecraft orbiting Mars, Jupiter, Saturn, and Pluto using VLBI are summarized in Table 1.1.

[2]Line connecting the two stations

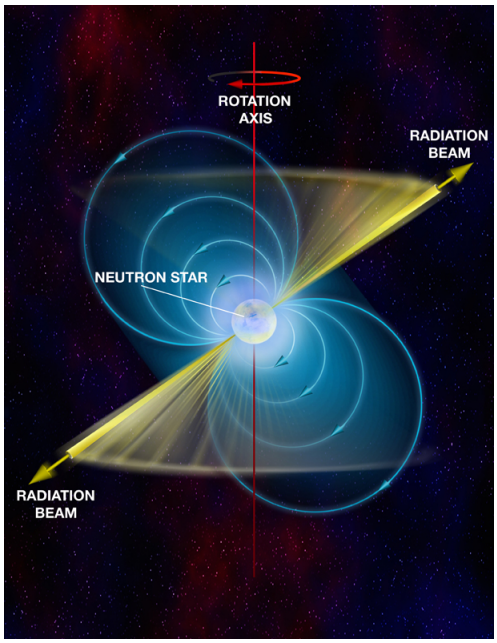

Figure 1.2: Lighthouse model [2].

Table 1.1: VLBI Position Accuracy

	Unit	Mars	Jupiter	Saturn	Pluto	Voyager 1
Average distance from Earth	AU	0.5	4.2	8.5	40	133
Position accuracy	km	0.19	1.57	3.18	14.96	49.74

1.3 Pulsar Timing Model

Pulsars are rapidly rotating and highly magnetized neutron stars [18]. When the pulsar rotates about its geological axis, charged particles along the magnetic field lines are accelerated and projected out in the direction of the magnetic axis as electromagnetic radiation. This beam of energy consists of components across the entire spectrum. Because of the misalignment between its rotational and magnetic axes, the energy beam sweeps across the sky as the pulsar rotates. The detection of the beam is only possible when the magnetic axis is aligned with the line-of-sight of an observer. From the perspective of the observer, a pulsar signal is analogous to the beacon of a distant lighthouse. See Fig. 1.2.

Pulsar timing has been an active research area since the discovery of the first pulsar in 1967. The discovery of millisecond pulsar in 1982 further enhanced the timing precision and allowed researchers to utilize pulsar timing in astrophysics, autonomous navigation, and universal timescale [19]. The idea of a pulsar-based timescale was first discussed in a *Science Magazine* article in 1987 [20]. The long-term stability of J1939+2134 at averaging time of $\tau = 10^7\ s$ rivaled that of the state-of-the-art atomic time standard at the time. As more millisecond pulsars were discovered, researchers began to consider the use of an ensemble of millisecond pulsars to establish a universal timescale that remains accessible indefinitely [21, 22, 23, 24, 25].

In order to discuss the pulsar model, it is important to first define the reference frame and timescale. The inertial reference frame for pulsar timing is the Barycentric Celestial Reference System (BCRS), whose origin is at the Solar System Barycenter. The timescale associated with BCRS is called the Barycentric Coordinate Time (TCB). The TCB timescale is a theoretical time that one would measure from a clock in the absence of the gravitational fields of the sun and the planets. The pulsar inertial frame is defined as the BCRS frame translated to the center of mass of the pulsar. Because the pulsar inertial frame is a simple translation, its timescale is also the TCB.

The pulsar rotational period of ranges from a few seconds to a few milliseconds. The definition of a millisecond pulsar is a pulsar whose rotation period is between $1\,ms$ to $10\,ms$. Millisecond pulsars are especially suitable for navigation purpose because of low timing noise. The long term stability of millisecond pulsars is comparable to terrestrial atomic clocks [23] [22] [21]. Thus, their signals can be modeled as a periodic function with very little fluctuations in the time evolution of the phase.

The following gives a brief summary of the pulsar timing model [26]. The functional form of the phase evolution in the pulsar inertial frame is

$$\phi(t^{psr}) = \phi_0 + \dot{\phi}\,[t^{psr} - t_0] + \frac{1}{2}\ddot{\phi}\,[t^{psr} - t_0]^2 + \dots . \tag{1.2}$$

The parameters $\dot{\phi}$, $\ddot{\phi}$,..., and t_0 are assumed to be known from prior timing surveys. In order to keep the timing model as accurate as possible, these parameters have to be updated from

time to time. As a result, regular monitoring of pulsars is needed to support pulsar-based positioning. The timing model of various pulsars can be found in current literature or in the Australia Telescope National Facilities (ATNF) Pulsar Database [6]. The initial phase offset, ϕ_0, is a value that is currently not recorded as a part of the timing model and has to be obtained through model calibration process.

The relationship between the emission time of the pulse, t_e^{psr}, and the arrival time of the pulse at an observer, t_a^{obs}, is

$$t_e^{psr} = t_a^{obs} - \Delta(t_a^{obs}, \boldsymbol{r}(t_a^{obs})). \tag{1.3}$$

The emission time t_e^{psr} is simply an instance on the TCB timescale, t^{psr}. On the other hand, the pulse arrival time t_a^{obs} is an instance of a local observer timescale, t^{obs}. For example, if the observer in on Earth, then t_a^{obs} is an instance of the Terrestrial Time (TT), which is algebraically related to Coordinated Universal Time (UTC).

The function, $\Delta_t(\cdot)$, accounts for spatial and temporal differences between the observer inertial frame and the pulsar inertial frame. It can be decomposed into Solar System, interstellar, and binary delays represented by $\Delta_\odot$, Δ_{IS}, and Δ_B respectively,

$$\Delta(t_a^{obs}, \boldsymbol{r}(t_a^{obs})) = \Delta_\odot(t_a^{obs}, \boldsymbol{r}(t_a^{obs})) + \Delta_{IS}(t_a^{obs}, \boldsymbol{r}(t_a^{obs})) + \Delta_B(t_a^{obs}). \tag{1.4}$$

The interstellar delay is due to dispersion effects of the interstellar medium and the binary delay accounts for the orbital motion of the pulsar if it is in a binary system. The Solar System delay can be further decomposed into

$$\begin{aligned}\Delta_\odot(t_a^{obs}, \boldsymbol{r}(t_a^{obs})) = \Delta_A(t_a^{obs}, \boldsymbol{r}(t_a^{obs})) + \Delta_{R\odot}(\boldsymbol{r}) + \Delta_p(\boldsymbol{r}(t_a^{obs})) \\ + \Delta_{E\odot}(t_a^{obs}, \boldsymbol{r}(t_a^{obs})) + \Delta_{S\odot}(\boldsymbol{r}(t_a^{obs})),\end{aligned} \tag{1.5}$$

where Δ_A is the atmospheric delay, $\Delta_{R\odot}$ is the Roemer delay; Δ_p is the parallax delay; $\Delta_{E\odot}$ is the Einstein delay; and $\Delta_{S\odot}$ is the Shapiro delay. Out of all these Solar System delays, the dominant term is the Roemer delay,

$$\Delta_{R\odot}(\boldsymbol{r}(t_a^{obs})) = -\frac{\boldsymbol{n}^T \boldsymbol{r}(t_a^{obs})}{c}, \tag{1.6}$$

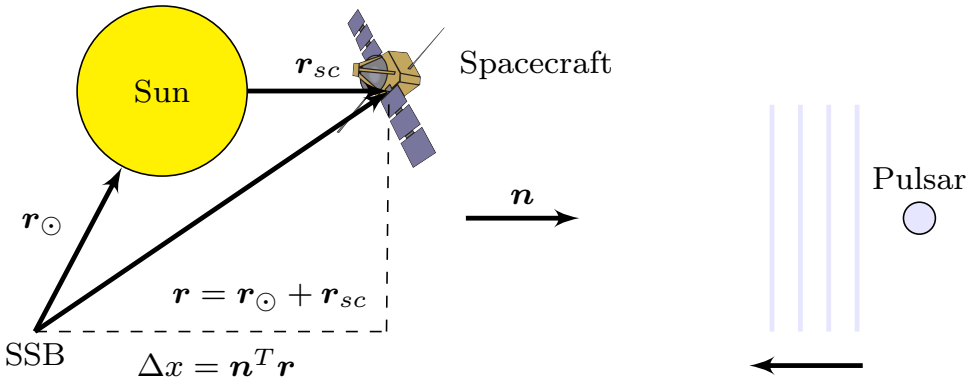

Figure 1.3: The spacecraft is in orbit around the sun.

where $\boldsymbol{n}$ is the pulsar direction relative to BCRS and c is the speed of light. Since the pulsar direction changes slowly with a timescale of a few years, in this research $\boldsymbol{n}$ is modeled as a constant vector. The Roemer delay is the time delay due to position offset from the SSB. Figure 1.3 shows the coordinate system and $\boldsymbol{r}_\oplus$ is the position of Earth relative to SSB. The atmospheric delay accounts of the effects of the troposphere on the pulsar signal. The Einstein delay accounts for relativistic time dilation, which is the conversion from the local timescale such as TT to TCB, i.e. $t^{tcb} = t^{obs(tt)} - \Delta_{E\odot}(t^{obs(tt)}, \boldsymbol{r}(t^{obs(tt)}))$. The Shapiro delay accounts for the curved spacetime due to gravitational field. The parallax delay accounts for non-planar wave front.

Assuming the local clock and the TCB clock are synchronized, then the phase equations of the observer should be equal to the phase evolution at the pulsar inertial frame, i.e. they detect the same signal,

$$\phi_{obs}(t^{obs}) = \phi(t^{psr}). \tag{1.7}$$

The functional form of $\phi_{obs}(t^{obs}(t))$ is unknown; however, $\phi(t)$ is known and is given by Eq. (1.2). This relationship is important because it relates the pulsar phase at an arbitrary location in the Solar System to the phase at the pulsar inertial frame. Substituting Eq. (1.3) into Eq. (1.7) and Eq. (1.2) gives

$$\phi_{obs}(t^{obs}) = \phi_0 + \dot{\phi}\left[t^{obs} - \Delta(t^{obs}, \boldsymbol{r}(t^{obs})) - t_0\right] + \frac{1}{2}\ddot{\phi}\left[t^{obs} - \Delta(t^{obs}, \boldsymbol{r}(t^{obs})) - t_0\right]^2 + \ldots \tag{1.8}$$

This equation gives the ideal phase evolution of the pulsar signal at the observer in terms

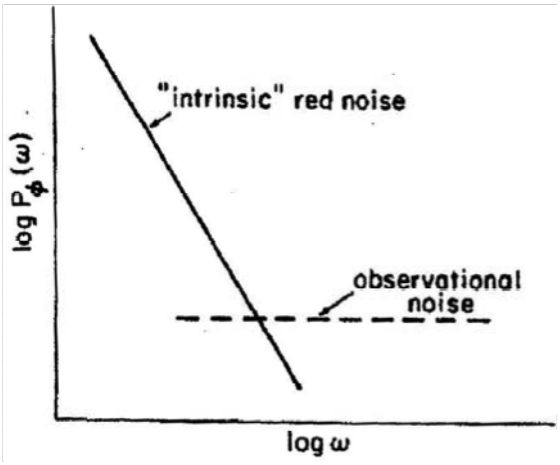

Figure 1.4: Power spectral densities of phase residual [3]

of the local observer time and its position relative to the SSB. The functional form of the observed phase evaluation is simply a phase shifted version of the phase evolution in the pulsar inertial frame.

While the periodicity of the pulsars is extremely predictable, there are still instabilities and noises. In order to develop accurate navigation system based on phase tracking, these noises have to be investigated and modeled. The timing noise of a pulsar signal is defined as an identifiable feature in the timing residual after the pulsar measurement has been corrected for all known orbital motions, glitches, braking and other effects [27]. The timing residual is the difference between the measured photon Time of Arrival (TOA) and the predicted TOA from a fitted timing model. If a timing model completely captures the characteristics of a pulsar signal, then the phase residual is statistically zero and white. Conversely, if the power spectral density of the residual is not white, then certain characteristics of the pulsar has been neglected in the model. In the frequency spectrum, these phase residuals show "intrinsic" red noise in addition to the white observation noise [3]. Most pulsar phase residuals have similar structures are shown in Figure 1.4 [3]. At low frequencies the power spectral density is dominated by red noise, whose relationship with frequency is proportional to $1/f^a$, where $a > 0$. The exponent of the timing noise can be even, odd, or fractional, e.g. 5.2 or 2.1. Approximation of this red noise effect can be obtained by feeding Gaussian white noise into a shaping filter.

1.4 Pulsar Signal Model

The model of the pulsar signal at the pulsar inertial frame is

$$\lambda(t^{psr}) = \lambda_b + \lambda_s s(\phi(t^{psr})), \tag{1.9}$$

where $\phi(t^{psr})$ is given by Eq. (1.2). λ_b is the background noise intensity and λ_s is the signal intensity. Eq. (1.9) is the underlying signal that enables pulsar navigation.

The waveform measurement at the observer is obtained by substituting Eq. (1.8) into Eq. (1.7) and Eq. (1.9).

$$y(t) = \lambda_b + \lambda_s s\left(\phi_{obs}(t)\right) + v(t), \tag{1.10}$$

where

$$\phi_{obs}(t) = \phi_0 + \dot{\phi}\left[t - \Delta(t, \boldsymbol{r}(t)) - t_0\right] + \frac{1}{2}\ddot{\phi}\left[t - \Delta(t, \boldsymbol{r}(t)) - t_0\right]^2 + \ldots \tag{1.11}$$

and the parameters λ_b and λ_s represents the background and source intensities. The superscript *obs* in Eq. (1.8) is dropped for simplicity. The term $v(t)$ is added to model measurement noise. The statistics of $v(t)$ depends on the measurement process, which is dependent on the observation spectrum. The periodic function $s(\cdot)$ is also known as the mean pulse profile, which describes the shape of the pulsar signal. This function can be modeled using either sum of Gaussian functions or Fourier series.

The mean profile is obtained experimentally by averaging raw pulsar signal measurements using the pulsar period [27, 28]. This averaging technique is known as epoch folding. The function $s(\cdot)$ is usually multi-modal, so this causes additional difficulties in tracking the phase of the signal. While pulsars emit signals across the entire spectrum, this research focuses on using radio and X-ray signals for spacecraft navigation. The signals observed by most radio telescopes on Earth are in the range of $1\ MHz - 10\ GHz$, while the X-ray signals measured in space have energy range of $0.1 - 12\,keV$. Equivalent frequency characterization is $30\ PHz - 3\ EHz$. Figure 1.5 shows the pulse profile of the Crab pulsar, which emits electromagnetic energy from radio frequencies to X-ray frequencies.

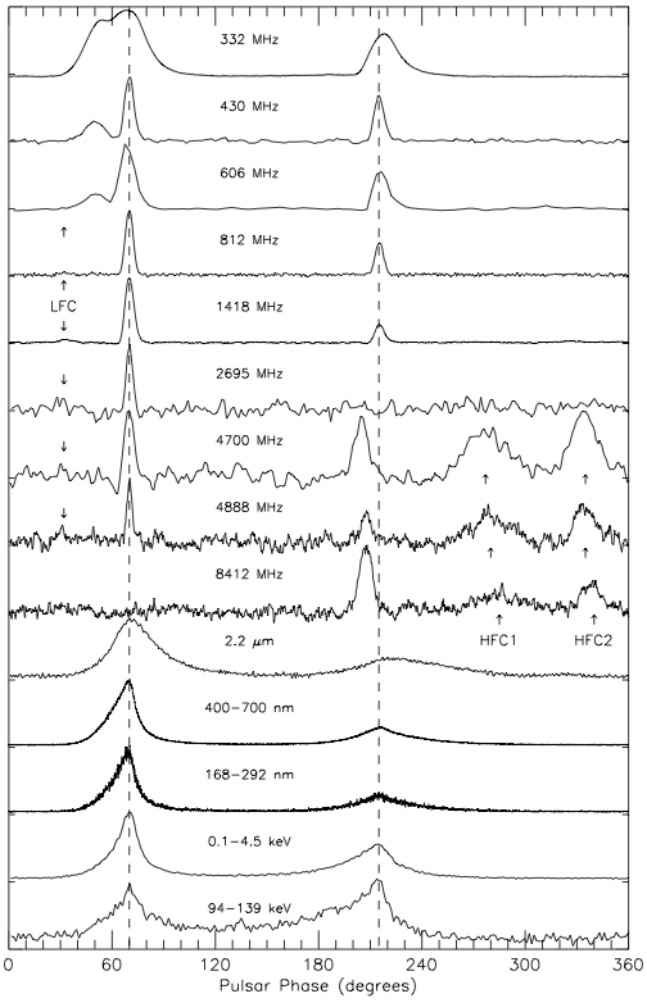

Figure 1.5: Pulse profile of Crab pulsar [4]

1.5 Pulsar-Based Navigation

Seven years after the discovery of the first pulsar, Downs an engineer from Jet Propulsion Laboratory published a paper on pulsar navigation in 1974, [29]. Since this first publication, there have been many research related to pulsar based navigation. The state-of-the-art pulsar navigation filter is based on the following concept and formulation. Consider two detectors, one is placed at the SSB and the other is placed on a spacecraft orbiting Earth. The measurement equation is formulated based on the idea that if the rate function of a pulsar signal is known at the SSB, then any deviation from this signal can be used to estimate the position and the velocity of the spacecraft. A single pulsar measurement provides information about the spacecraft position and velocity in the direction of the pulsar. The phase shift is related to the position while the Doppler frequency is related to the velocity.

The time shift, t_x, is due to position offset as shown in Figure 1.3.

$$t_x = \frac{\Delta x}{c} = \frac{\boldsymbol{n}^T \boldsymbol{r}}{c}. \tag{1.12}$$

Δx is the position offset between the spacecraft and the SSB in the direction of the pulsar. Since photons travel at the speed of light, c, dividing Δx by c gives the time offset t_x. Eq. (1.12) neglects time offset due to relativistic effects presented in [30]. Converting the time offset to phase space using the observed frequency gives

$$\psi = t_x f_o, \tag{1.13}$$

where the observed frequency, f_o, can be expressed as

$$f_o = f_s + f_d.$$

The instantaneous pulsar frequency at the SSB is f_s. The Doppler frequency, f_d, is approximated using the following first order formula, so relativistic effects are ignored as well.

$$f_d = \frac{\boldsymbol{n}^T \dot{\boldsymbol{r}}}{c} f_s, \tag{1.14}$$

where $\dot{\boldsymbol{r}}$ is the spacecraft velocity relative to the Earth. Since the inertial spacecraft velocity is much smaller than the speed of light, the Doppler frequency is a small but measurable

number. Figure 1.6 is the basic architecture of a pulsar based navigation system. It consists of a signal estimator and a navigation filter. The main purpose of the signal estimator is to obtain phase and Doppler frequency information from the raw measurements. These two pieces of information are fed into the navigation filter to determine the position and velocity of the observer. The measurement equations in the navigation filter are Eq. (1.13) and Eq. (1.14). Typically, the navigation filter is an Extended Kalman Filter that combines the phase and the frequency measurements with either an inertial measurement unit or a dynamical model to obtain *a posteriori* estimate of the position and the velocity. The current state-of-the-art signal estimation techniques are the binned method and the time-tagged method.

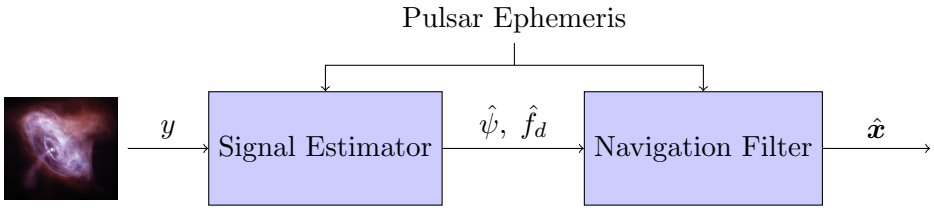

Figure 1.6: Filter block diagram. $\hat{\psi}$ and $\hat{f}_d$ are estimated phase and Doppler shifts.

The signal estimator may use a binned method known as epoch folding to construct a high Signal-to-Noise Ratio empirical profile from raw measurements. This empirical profile is then Cross-Correlated (CC) with another profile from a reference location to extract a phase offset, ψ, between the spacecraft and the reference location in the direction of the pulsar [31]. Alternatively, the pulse Time of Arrival (TOA) at the spacecraft can also be determined using this method and be processed by the navigation filter [30]. A disadvantage of this approach is that the ability to obtain an unbiased estimate is dependent on the signal intensity and the length of the observation time [31].

Another method known as time tagging relies on the use of a batch of time-tagged X-ray photons to find the phase shift and Doppler frequency, f_d, that maximize the log-likelihood function associated with the non-homogenous Poisson process. This method is asymptotically efficient, if the phase shift is the only estimated parameter [31, 32]. Others have applied the Maximum Likelihood Estimator (MLE) to moving spacecraft by augmenting

a digital phase locked loop to refine the estimates or by estimating both the phase and the signal frequency [32, 33]. The MLE has a similar observation time constraint as CC. The NASA Station Explorer X-ray Timing and Navigation Technology (SEXTANT) mission implements a refined version of the MLE that uses *a priori* mean of the spacecraft states to predict the signal phase in order to overcome the constraint on observation duration [8, 34].

CHAPTER 2

Autonomous Navigation Using X-Ray Pulsars and Multirate Processing

2.1 Overview

Building upon the previous pulsar based navigation research discussed in Section 1.5, this chapter presents a reformulation of the pulsar-based spacecraft navigation problem by explicitly connecting the pulsar waveform measurements to the underlying dynamical systems embedded in the pulsar signals namely orbital dynamics, clock dynamics, and timing noise dynamics. The advantages of this approach are the removal of the signal estimator and the coherent processing of time correlated noise embedded in the pulsar signal. The second point is often ignored in prior approaches. The disadvantage of this approach is the need to propagate the dynamical system using numerical integration. However, two solutions are offered in this chapter to reduce computation time. The main contributions of this chapter are the problem reformulation in Section 2.4, the observability analysis in Section 2.5, and the derivation of an Extended Kalman Filter (EKF) with multirate processing in Section 2.6. Simulation result is presented in Section 2.7.

2.2 Spacecraft Dynamics

The dynamics of the spacecraft is simplified to a restricted two-body problem [35]. The Sun is used as the primary body for the derivation. The Solar System Barycenter (SSB) frame is defined as an inertial frame located at the center of mass of the solar system. $\boldsymbol{r}_{\odot}$ and $\dot{\boldsymbol{r}}_{\odot}$ are the position and velocity vectors of the Sun relative to the SSB. Their values can

be obtained from the Solar System ephemeris [36]. The coordinate system of the navigation problem is shown in Fig. 2.1. The dynamical equation for the spacecraft's position relative to the Sun is

$$\begin{aligned} \ddot{\boldsymbol{r}}_{sc} &= -\frac{\boldsymbol{G}m_{\odot}}{\|\boldsymbol{r}_{sc}\|^3}\boldsymbol{r}_{sc} + \boldsymbol{f}_{J_2}(\boldsymbol{r}_{sc}) + \boldsymbol{w}_r \\ &= \boldsymbol{f}_{orbit}(\boldsymbol{r}_{sc}) + \boldsymbol{f}_{J_2}(\boldsymbol{r}_{sc}) + \boldsymbol{w}_r, \end{aligned} \tag{2.1}$$

where $m_{\odot}$ is the mass of the Sun and $\boldsymbol{G}$ is the gravitational constant. The J_2 acceleration perturbation is represented by $\boldsymbol{f}_{J_2}(\boldsymbol{r}_{sc})$. The white acceleration disturbance, $\boldsymbol{w}_r$, represents an unknown acceleration forcing function whose autocorrelation function is $E\left[\boldsymbol{w}_r(t)\boldsymbol{w}_r^T(\tau)\right] = W_r\delta(t-\tau)$. The Power Spectral Density (PSD) of the noise is W_r.

2.3 Pulsar Model

2.3.1 Signal and Timing Model

Let the X-ray photon detection process at the SSB be described by the non-homogenous Poisson process whose rate is

$$\lambda(t^{ssb}) = \lambda_b + \lambda_s s(\phi_{ssb}(t^{ssb})), \tag{2.2}$$

where λ_b and λ_s are the background and source intensities [31]. The unique waveform of the pulsar, $s(\cdot)$, is a normalized profile such that $\int_0^1 s(\varphi)\, d\varphi = 1$ and $s(\varphi) \geq 0$ for all $\varphi \in \mathbf{R}$. The pulsar signal phase evolution at the SSB is

$$\phi_{ssb}(t^{ssb}) = \phi_0 + \dot{\phi}[t^{ssb} - t_0] + \frac{1}{2}\ddot{\phi}[t^{ssb} - t_0]^2 + n_\eta(t^{ssb}), \tag{2.3}$$

where ϕ_0, $\dot{\phi}$ and $\ddot{\phi}$ are known parameters obtained from the pulsar ephemeris [7]. Equation (2.2) is the reference signal and any deviation from this signal can be used to identify the position of the spacecraft relative to the SSB. $\dot{\phi}$ is the pulsar frequency; $\ddot{\phi}$ is frequency rate; t_0 represents the starting time of an imaginary clock located at the SSB; $n_\eta(t^{ssb})$ represents the pulsar timing noise at the SSB at time t^{ssb}; and ϕ_0 is the phase at the SSB at time t_0 when $n_\eta(t_0) = 0$.

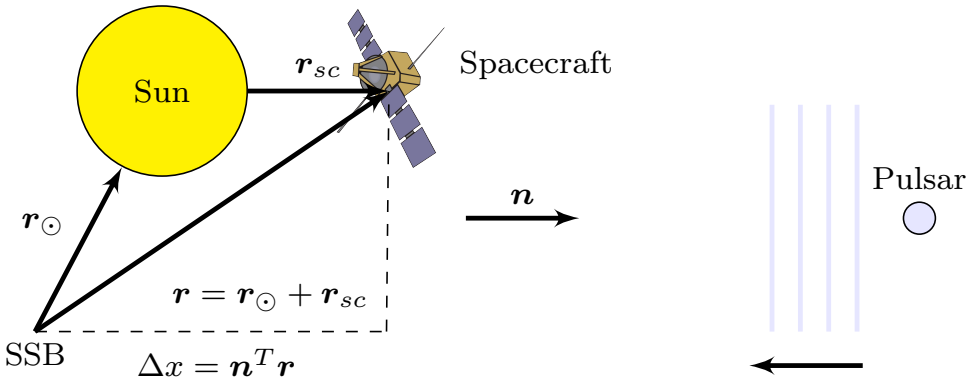

Figure 2.1: The spacecraft is in orbit around the Sun. $\boldsymbol{n}$ is the unit vector pointing towards the pulsar

Given the coordinate system in Fig. (2.1), let the spacecraft detect a pulse at time, t. At a later time, the same pulse is detected at the SSB, and this detection time is denoted as t^{ssb}. Assuming the spacecraft clock and the SSB clock are synchronized, then the phase equations for the two observers should be equal to each other, i.e. they detect the same signal.

$$\phi_{sc}(t^{sc}) = \phi_{ssb}(t^{ssb}) \tag{2.4}$$

The functional form of $\phi_{sc}(t^{sc})$ is unknown; however, $\phi_{ssb}(t^{ssb})$ is given by (2.3). Since t^{sc} is earlier than t^{ssb}, their difference has to be negative, i.e. $t^{sc} - t^{ssb} < 0$. This difference represents the time of flight for light to travel from the spacecraft to the SSB along the negative direction of $\boldsymbol{n}$. Therefore, the time difference is

$$t^{sc} - t^{ssb} = -\frac{\boldsymbol{n}^T \boldsymbol{r}}{c}, \tag{2.5}$$

where $\boldsymbol{r} = \boldsymbol{r}_\odot + \boldsymbol{r}_s$. The negative sign ensures the right hand side is a negative value since $\boldsymbol{n}^T \boldsymbol{r}$ is a positive value as defined in Fig. (2.1). Equation (2.5) is known as the time transfer equation. The more general form of the time transfer equation is the following which can be found in [26] and [37].

$$t^{ssb} = t^{sc} + t_c - (\underbrace{\Delta_{R\odot} + \Delta_p + \Delta_{dis} + \Delta_{S\odot} + \Delta_{E\odot}}_{\Delta_\odot}), \tag{2.6}$$

where Δ is defined as the sum of all time shifts. The time shift due to position offset shown in (2.5) is the Roemer delay, $\Delta_{R\odot}$. The true time is $t_{true} = t^{sc} + t_c$, where the clock deviation

is t_c. The parallax delay is Δ_p; dispersion delay is Δ_{dis}; the Shapiro delay is $\Delta_{S\odot}$; and the Einstein delay is $\Delta_{E\odot}$.

Equation (2.4) is important because it relates the pulsar phase at an arbitrary location to the phase at the SSB. Substituting Eq. (2.6) into Eq. (2.4) and Eq. (2.3) gives the measurement equation at the spacecraft,

$$\begin{aligned} y(t^{sc}) &= \lambda_b + \lambda_s s(\phi_{sc}(t^{sc})) + \nu(t^{sc}) \\ &= \lambda_b + \lambda_s s(\phi_{ssb}(t^{sc} + t_c - \Delta_\odot - t_0)) + \nu(t^{sc}), \end{aligned} \tag{2.7}$$

where $\nu(t^{sc})$ is Poisson measurement noise. The proposed pulsar-based navigation system uses Eq. (2.7) as the measurement for the navigation filter.

2.3.2 Measurement Noise

The superscript *sc* used to denote the photon TOA at the spacecraft in the previous section is dropped from this point onward to simplify notation. If the spacecraft carries an X-ray photon detector, then the measurements are described by the non-homogenous Poisson detection process [31]. Given a time interval, $\Delta\tau$, and the time at the beginning of the interval, t, the number of detected X-ray photons, $C(\tau,\ \Delta\tau)$, is modeled as a Poisson random variable. The non-homogenous Poisson probability mass function over $\Delta\tau$ is

$$f\Big(N(t+\Delta\tau) - N(t) = C(\tau,\ \Delta\tau) \ \Big|\ t,\ \Delta\tau\Big) = \frac{\Lambda(\tau,\ \Delta\tau)^{C(\tau,\ \Delta\tau)}}{C(\tau,\ \Delta\tau)!} e^{-\Lambda(\tau,\ \Delta\tau)}, \tag{2.8}$$

where

$$\Lambda\left(\tau,\ \Delta\tau\right) = \int_t^{t+\Delta\tau} \lambda(\sigma)\ d\sigma, \quad \tau = t + \frac{\Delta\tau}{2} \tag{2.9}$$

and $N(t)$ represents the number of detected photons from an initial time, t_0, to t. The rate function associated with the random process is $\lambda(\tau)$. A special property of the Poisson process is that the expected number of photons over an interval is equal to its variance, i.e.

$$\begin{aligned} E[C(\tau,\ \Delta\tau)] &= \mathrm{var}[C(\tau,\ \Delta\tau)] \\ &= \Lambda\left(\tau,\ \Delta\tau\right). \end{aligned} \tag{2.10}$$

The probability of detection is described by the intensity of the rate function.

A typical X-ray photon detection system provides the actual detection time of a photon rather than the photon rate (intensity). Thus, the photon rate of the pulsar signal is approximated using bins,

$$y(\tau) = \frac{C(\tau,\ \Delta\tau)}{\Delta\tau}. \tag{2.11}$$

The following derivation gives a formula for the measurement noise variance. Since the detection process is Poisson, the expected number of detected photons for each bin is $\Lambda(\tau)$. When $\Delta\tau$ is small, Eq. (2.9) can be approximated as

$$\Lambda(\tau,\ \Delta\tau) \approx \left[\lambda_b + \lambda_s s(\phi_{sc}(\tau))\right] \Delta\tau. \tag{2.12}$$

Taking the expectation of Eq. (2.11) gives

$$\begin{aligned} E[y(\tau)] &= \frac{E[C(\tau,\ \Delta\tau)]}{\Delta\tau} \\ &= \lambda_b + \lambda_s s\left(\phi_{sc}(\tau)\right). \end{aligned} \tag{2.13}$$

The measurement variance is

$$\begin{aligned} \mathrm{var}[y(\tau)] &= \frac{\mathrm{var}[C(\tau,\ \Delta\tau)]}{\Delta\tau^2} \\ &= \frac{\lambda_b + \lambda_s s\left(\phi_{sc}(\tau)\right)}{\Delta\tau}. \end{aligned} \tag{2.14}$$

Since the expected value of the measurement in Eq. (2.13) is the underlying rate function, $\lambda(\tau)$, the mean and variance of the measurement noise are

$$E[v(\tau)] = 0, \text{ and } \mathrm{var}[v(\tau)] = \frac{\lambda_b + \lambda_s s\left(\phi_{sc}(\tau)\right)}{\Delta\tau}. \tag{2.15}$$

Equation (2.14) shows that the measurement noise variance is dependent on both the background radiation, λ_b, and the source rate, λ_s.

2.3.3 Timing Noise

Even though millisecond pulsars are stable oscillators, they still exhibit a small amount of rotational fluctuation. This fluctuation is known as the pulsar timing noise, n_η, also known as red noise. While the origin of this noise is unknown, researchers have been using Brownian motion to approximate this timing noise [38]. Pulsar timing noise was found to be

more correlated to $\ddot{\phi}$ rather than $\dot{\phi}$. Therefore, a second order model was proposed [39]. The Power Spectral Density (PSD) of the input noise was determined empirically from pulsar data. The fitted function found in [40, 39] was

$$W_\eta \approx 10^{-28.8} P^{-2.8} (\dot{P} \times 10^{15})^{1.8}, \tag{2.16}$$

where $P = \dot{\phi}^{-1}$ is the period and has the unit of (s). $\dot{P} = -\ddot{\phi}\dot{\phi}^{-2}$ is the rate of change of period and has the unit of (s/s) and W_η has the unit of (cyc^2/s^3). The typical value of W_η for a millisecond pulsar is $< 10^{-28.5}\ cyc^2/s^3$. The dynamical system for the pulsar timing noise is

$$\begin{bmatrix} \dot{\eta}_1 \\ \dot{\eta}_2 \end{bmatrix} = \begin{bmatrix} 0 & 1 \\ 0 & 0 \end{bmatrix} \begin{bmatrix} \eta_1 \\ \eta_2 \end{bmatrix} + \begin{bmatrix} 0 \\ 1 \end{bmatrix} w_\eta \tag{2.17}$$

$$n_\eta = \eta_1,$$

where the noise autocorrelation function is $E[w_\eta(t) w_\eta(\tau)] = W_\eta \delta(t - \tau)$. η_1 and η_2 can be interpreted as the rotation angle and rate deviations. The timing model in Eq. (2.17) is a simplification of the actual red noise process, which should be modeled using fractional differential equation [41, 42]. However, the state space realization of a fractional system has infinite number of states [43].

2.4 Navigation System

The pulsar phase equation given in Eq. (2.3) and the general time transfer formula given in Eq. (2.4) make up the fundamental pulsar timing model. While these nonlinear equations are relevant to the design of an operational pulsar navigation system, many of them are outside the scope of this study. In order to simplify the study and analysis, all relativistic effects are not modeled and only three time shifts are considered: position offset, $\boldsymbol{n}^T \boldsymbol{r}/c$; clock deviation, t_c; and pulsar timing noise, n_η. Since $\ddot{\phi}$ is extremely small on the order of 10^{-14} to 10^{-16}, this parameter is assumed to be zero. However, the method presented in this chapter does not require $\ddot{\phi}$ to be 0. In fact making $\ddot{\phi}$ non-zero allows the filter to distinguish between t_c and n_η. Lastly, n_η has a timescale on the order of months to years, which is much larger than the time shift due to position offset, so $n_\eta \left(\tau + \boldsymbol{n}^T \boldsymbol{r}(\tau)/c\right) \approx n_\eta(\tau)$ [39]. τ is the

independent time parameter. The simplified pulsar phase equation at the spacecraft is

$$\phi_{sc}(\tau) = \phi_0 + \dot{\phi}\left[\tau + \frac{\boldsymbol{n}^T\boldsymbol{r}}{c} + t_c - t_0\right] + n_\eta. \tag{2.18}$$

If the spacecraft carries a standalone cesium atomic clock with specifications comparable to those used on a GPS satellite, then the clock deviation model is

$$\begin{bmatrix}\dot{t}_c \\ \dot{b}_c\end{bmatrix} = \begin{bmatrix}0 & 1 \\ 0 & 0\end{bmatrix}\begin{bmatrix}t_c \\ b_c\end{bmatrix} + \begin{bmatrix}1 & 0 \\ 0 & 1\end{bmatrix}\boldsymbol{w}_c. \tag{2.19}$$

The true time is defined as $\tau_{true} = \tau + t_c$, where τ is the clock readout. b_c is referred to as the frequency offset. The autocorrelation function of the white noise vector is $E[\boldsymbol{w}_c(t)\boldsymbol{w}_c^T(\tau)] = W_c\delta(t-\tau)$. Detailed information about this clock model can be found in [9].

Because t_c and η_1 are additive in Eq. (2.18) and are both the output of a second order integrator, the navigation filter is not able to distinguish the two using pulsar measurements. As a result, an auxiliary vector, $\boldsymbol{\zeta}$, has to be defined to reduce the order of the system.

$$\boldsymbol{\zeta} = \begin{bmatrix}\zeta_1 \\ \zeta_2\end{bmatrix} = \begin{bmatrix}\dot{\phi}t_c + \eta_1 \\ \dot{\phi}b_c + \eta_2\end{bmatrix} \tag{2.20}$$

Taking the time derivative of Eq. (2.20) and substituting Eq. (2.17) and Eq. (2.19) into the resulting expression gives

$$\begin{aligned}\underbrace{\begin{bmatrix}\dot{\zeta}_1 \\ \dot{\zeta}_2\end{bmatrix}}_{\dot{\boldsymbol{\zeta}}} &= \underbrace{\begin{bmatrix}0 & 1 \\ 0 & 0\end{bmatrix}}_{F_\zeta}\underbrace{\begin{bmatrix}\zeta_1 \\ \zeta_2\end{bmatrix}}_{\boldsymbol{\zeta}} + \underbrace{\begin{bmatrix}\begin{bmatrix}\dot{\phi} & 0 \\ 0 & \dot{\phi}\end{bmatrix} & \begin{bmatrix}0 \\ 1\end{bmatrix}\end{bmatrix}}_{G_\zeta}\underbrace{\begin{bmatrix}\boldsymbol{w}_c \\ w_\eta\end{bmatrix}}_{\boldsymbol{w}_\zeta} \\ \zeta_1 &= \underbrace{\begin{bmatrix}1 & 0\end{bmatrix}}_{H_\zeta}\begin{bmatrix}\zeta_1 \\ \zeta_2\end{bmatrix},\end{aligned} \tag{2.21}$$

where the noise PSD is $W_\zeta = \text{diag}[W_c,\ W_\eta]$. Since both the pulsar and the clock are imperfect oscillators, they cannot be used to calibrate each other. Despite this fact, the system remains observable because the time evolution of $\boldsymbol{\zeta}$ is not consistent with either the orbital dynamics nor the deterministic pulsing. This observability issue is a result of the use of a simplified pulsar-timing model; it is not a fundamental limitation of the pulsar-based

timing and navigation concept. Alternatively, one can use a stationary correlated process to approximate the pulsar timing noise.

Combining Eq. (2.1) with Eq. (2.21) gives the pulsar-based navigation system,

$$\begin{aligned}
\begin{bmatrix} \dot{\boldsymbol{r}}_{sc} \\ \ddot{\boldsymbol{r}}_{sc} \\ \dot{\boldsymbol{\zeta}}_p \end{bmatrix} &= \begin{bmatrix} \dot{\boldsymbol{r}}_{sc} \\ \boldsymbol{f}_{orbit}\left(\boldsymbol{r}_{sc}\right) \\ F_{\zeta,p}\boldsymbol{\zeta}_p \end{bmatrix} + \begin{bmatrix} 0 & 0 \\ I & 0 \\ 0 & G_{\zeta,p} \end{bmatrix} \begin{bmatrix} \boldsymbol{w}_r \\ \boldsymbol{w}_{\zeta,p} \end{bmatrix} \\
y_p(\tau_j) &= \lambda_{b,p} + \lambda_{s,p} s_p(\phi_{sc,p}(\tau_j)) + v_p(\tau_j) \\
\phi_{sc,p}(\tau_j) &= \phi_{0,p} + \dot{\phi}_p \left[\tau_j - t_0 + \frac{\boldsymbol{n}_p^T \left(\boldsymbol{r}_{\odot}(\tau_j) + \boldsymbol{r}_{sc}(\tau_j) \right)}{c} \right] + H_{\zeta,p}\boldsymbol{\zeta}_p(\tau_j),
\end{aligned} \tag{2.22}$$

where $p = 1...N_p$ and N_p is the number of pulsars. The sample interval is $\Delta\tau = \tau_j - \tau_{j-1}$. The above system is denoted as

$$\begin{aligned}
\dot{\boldsymbol{x}}(\tau) &= \boldsymbol{f}(\boldsymbol{x}(\tau), \tau) + G\boldsymbol{w}(\tau) \\
\boldsymbol{y}(\tau_j) &= \boldsymbol{h}(\boldsymbol{x}(\tau_j), \tau_j) + \boldsymbol{v}(\tau_j),
\end{aligned} \tag{2.23}$$

where the state vector and measurement vector are

$$\begin{aligned}
\boldsymbol{x}(\tau) &= \begin{bmatrix} \boldsymbol{r}_{sc}(\tau) & \dot{\boldsymbol{r}}_{sc}(\tau) & \boldsymbol{\zeta}_1(\tau) & \dots & \boldsymbol{\zeta}_{N_p}(\tau) \end{bmatrix}^T \\
\boldsymbol{y}(\tau_j) &= \begin{bmatrix} y_1(\tau_j) & \dots & y_{N_p}(\tau_j) \end{bmatrix}^T.
\end{aligned} \tag{2.24}$$

2.5 Observability and Covariance Analysis

2.5.1 Linearized Observability

Before discussing the estimation algorithm for Eq. (2.22), it is important to develop some intuitions about pulsar-based navigation system through the observability analysis of a simplified model. The simplifications are

- constant and known velocity, $\boldsymbol{v}_{sc}$, relative to the SSB frame,
- constant pulsar frequency, direction,
- no timing noise,

- sequential observation of four pulsars, i.e. $p = 1 \ldots 4$,
- continuous time Gaussian measurement noise with constant PSD, V_p,
- simple geometric delay (Roemer delay), and
- constant clock bias.
- Furthermore, the observation duration, $t_p^{obs} = t_p^{end} - t_p^{start}$, is a integer multiple of the signal period, $T_p = 1/f_{s,p}$, where $f_{s,p} = \dot{\phi}_p(1 + \boldsymbol{n}_p^T \boldsymbol{v}_{sc}/c)$.

Therefore, the observation duration for a single pulsar is $t_p^{obs} = M_p T_p$, where M_p is an integer. The distribution of the observations is shown in Figure 2.2. Even though these simplifications make this problem ideal, it captures the essence of pulsar-based navigation.

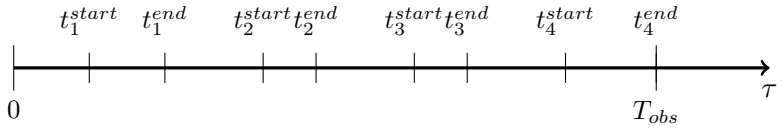

Figure 2.2: Three pulsars are observed in the time interval from 0 to T_{obs}

Under these assumptions, the system being considered is

$$\begin{bmatrix} \dot{\boldsymbol{r}}_{sc,0} \\ \dot{t}_c \end{bmatrix} = 0 \qquad \boldsymbol{y}(\tau) = \boldsymbol{h}(\tau, \boldsymbol{x}) + \boldsymbol{v}(\tau) \tag{2.25}$$

The state vector is defined as $\boldsymbol{x} = \begin{bmatrix} \boldsymbol{r}_{sc,0} & t_c \end{bmatrix}^T$, where $\boldsymbol{r}_{sc,0}$ is the initial spacecraft position vector relative to the SSB and t_c is the constant clock bias. Each pulsar measurement can be written as

$$y_p(\tau) = \Pi(\tau; t_p^{start}, t_p^{end}) \left[h_p(\phi_{sc,p}(\tau)) + v_p(\tau) \right] \tag{2.26}$$

where

$$\begin{aligned} \phi_{sc,p}(\tau) &= \phi_{p,0} + \dot{\phi}_p \left[\left[1 + \frac{\boldsymbol{n}_p^T \boldsymbol{v}_{sc}}{c} \right] [\tau - t_0] + \frac{\boldsymbol{n}_p^T \boldsymbol{r}_{sc,0}}{c} + t_c \right] \\ h_p(\phi_{sc,p}(\tau)) &= \lambda_{b,p} + \lambda_{s,p} \left[\frac{a_{p,0}}{2} + \sum_{j=1}^{N_{f,p}} a_{p,j} \cos(2\pi j \phi_{sc,p}(\tau)) + b_{p,j} \sin(2\pi j \phi_{sc,p}(\tau)) \right] \end{aligned} \tag{2.27}$$

Sequential observation is modeled using the boxcar function, $\Pi(\tau; t_i^{start}, t_i^{end}) = \mathbf{H}(\tau - t_i^{start}) - \mathbf{H}(\tau - t_i^{end})$, where t_i^{start} and t_i^{end} denotes the start and the terminal time of the observation as shown in Figure 2.2. The Heaviside step function is denoted as $\mathbf{H}(\tau)$. The pulsar measurement is expressed in terms of Fourier series. The linearized measurement matrix is

$$\begin{aligned} H(\tau) &= \left.\frac{d\boldsymbol{h}(\tau, \boldsymbol{x})}{d\boldsymbol{x}}\right|_{\boldsymbol{x}=\bar{\boldsymbol{x}}} \\ &= \underbrace{\begin{bmatrix} \gamma_1(\tau) & 0 & 0 & 0 \\ 0 & \gamma_2(\tau) & 0 & 0 \\ 0 & 0 & \gamma_3(\tau) & 0 \\ 0 & 0 & 0 & \gamma_4(\tau) \end{bmatrix}}_{\Gamma(\tau)} \underbrace{\begin{bmatrix} \dot{\phi}_1 \begin{bmatrix} \frac{\boldsymbol{n}_1^T}{c} & 1 \end{bmatrix} \\ \dot{\phi}_2 \begin{bmatrix} \frac{\boldsymbol{n}_2^T}{c} & 1 \end{bmatrix} \\ \dot{\phi}_3 \begin{bmatrix} \frac{\boldsymbol{n}_3^T}{c} & 1 \end{bmatrix} \\ \dot{\phi}_4 \begin{bmatrix} \frac{\boldsymbol{n}_4^T}{c} & 1 \end{bmatrix} \end{bmatrix}}_{\tilde{H}}, \end{aligned} \tag{2.28}$$

where the diagonal elements of $\Gamma(\tau)$ are

$$\begin{aligned} \gamma_p(\tau) &= \Pi(\tau; t_p^{start}, t_p^{end}) h_p'(\bar{\phi}_{sc,p}(\tau)) \\ h_p'(\bar{\phi}_{sc,p}(\tau)) &= 2\pi\lambda_{s,p} \sum_{j=1}^{N_{f,p}} j \left(b_{p,j} \cos(2\pi j \bar{\phi}_{sc,p}(\tau)) - a_{p,j} \sin(2\pi j \bar{\phi}_{sc,p}(\tau)) \right). \end{aligned} \tag{2.29}$$

The linearized observability gramian from 0 to T_{obs} for the system in Eq. (2.25) is

$$W_o(T_{obs}) = \int_0^{T_{obs}} H^T(\tau) H(\tau)\, d\tau = \tilde{H}^T \int_0^{T_{obs}} \Gamma^2(\tau)\, d\tau \tilde{H}. \tag{2.30}$$

Defining $\bar{S}_j = \sin(2\pi j \bar{\phi}_{sc,p}(\tau))$, $\bar{C}_j = \cos(2\pi j \bar{\phi}_{sc,p}(\tau))$, and evaluating the integral in Eq. (2.30)

give

$$
\begin{aligned}
\zeta_p &= \int_0^{T_{obs}} \gamma_p^2(\tau)\, d\tau = \int_0^{T_{obs}} \left(\Pi(\tau; t_p^{start}, t_p^{end}) h_p'(\bar{\phi}_{sc,p}(\tau))\right)^2 \, d\tau \\
&= 4\pi^2 \lambda_{s,p}^2 \int_0^{T_{obs}} \left[\mathbf{H}(\tau - t_p^{start}) - \mathbf{H}(\tau - t_p^{end})\right] \left(\sum_{j=1}^{N_{f,p}} j b_{p,j} \bar{C}_j - j a_{p,j} \bar{S}_j\right)^2 \, d\tau \\
&= 4\pi^2 \lambda_{s,p}^2 \sum_{j=1}^{N_{f,p}} \sum_{i=1}^{N_{f,p}} ij \left[\int_{t_p^{start}}^{t_p^{end}} \left(b_{p,j}\bar{C}_j - a_{p,j}\bar{S}_j\right)\left(b_{p,i}\bar{C}_i - a_{p,i} S_i\right) \, d\tau\right] \\
&= 4\pi^2 \lambda_{s,p}^2 \sum_{j=1}^{N_{f,p}} \sum_{i=1}^{N_{f,p}} ij \left[b_{p,j} b_{p,i} \int_{t_p^{start}}^{t_p^{end}} \bar{C}_j \bar{C}_i \, d\tau - 2 a_{p,i} b_{p,j} \int_{t_p^{start}}^{t_p^{end}} \bar{S}_j \bar{C}_i \, d\tau + a_{p,j} a_{p,i} \int_{t_p^{start}}^{t_p^{end}} \bar{S}_j \bar{S}_i \, d\tau\right] \\
&= 4\pi^2 \lambda_{s,p}^2 \sum_{j=1}^{N_{f,p}} j^2 \left(a_{p,j}^2 \frac{M_p}{2 f_{s,p}} + b_{p,j}^2 \frac{M_p}{2 f_{s,p}}\right) \\
&= \frac{2\pi^2 c \lambda_{s,p}^2 M_p}{\dot{\phi}_p \left(c + \boldsymbol{n}_p^T \boldsymbol{v}_{sc}\right)} \sum_{j=1}^{N_{f,p}} j^2 \left(a_{p,j}^2 + b_{p,j}^2\right) \\
&= \begin{cases} > 0, \text{ when } \boldsymbol{n}_p^T \boldsymbol{v}_{sc} < c \\ < 0, \text{ when } \boldsymbol{n}_p^T \boldsymbol{v}_{sc} > c \end{cases},
\end{aligned}
\tag{2.31}
$$

where the orthogonality of $\sin(\cdot)$ and $\cos(\cdot)$ was used. Since physical spacecraft cannot travel faster than speed of light, Eq. (2.31) is positive. Finally, the observability gramian is

$$
\begin{aligned}
W_o(T_{obs}) &= \sum_{p=1}^{4} \zeta_p \dot{\phi}_p^2 \begin{bmatrix} \frac{\boldsymbol{n}_p \boldsymbol{n}_p^T}{c^2} & \frac{\boldsymbol{n}_p}{c} \\ \frac{\boldsymbol{n}_p^T}{c} & 1 \end{bmatrix} \\
&= \tilde{H}^T \operatorname{diag}\left(\begin{bmatrix} \zeta_1 & \zeta_2 & \zeta_3 & \zeta_4 \end{bmatrix}\right) \tilde{H},
\end{aligned}
\tag{2.32}
$$

From the form of $\tilde{H}$, one can see that each pulsar direction adds one rank to the observability gramian. If $\det(\tilde{H}) \neq 0$, then W_o is positive definite, which implies $\boldsymbol{r}_{sc,0}$ and t_c are observable. While this analysis provides the necessary and sufficient conditions for observability, it does not indicate the accuracy or performance of the pulsar-based navigation system.

2.5.2 Positioning Accuracy

This section derives the theoretical estimation accuracy of the pulsar-based navigation using an EKF for Eq. (2.25). The estimation error covariance, $P(\tau) = E[(\boldsymbol{x} - \hat{\boldsymbol{x}})\,(\boldsymbol{x} - \hat{\boldsymbol{x}})^T]$, of an EKF is given by the differential Riccati equation [44],

$$\dot{P} = FP + PF^T - PH^TV^{-1}HP + GWG^T. \tag{2.33}$$

Given that the two estimated quantities are constant and that there is no process noise, $F = 0$ and $W = 0$. As a result, Eq. (2.33) reduces to

$$\dot{P} = -PH^TV^{-1}HP. \tag{2.34}$$

The measurement noise PSD matrix, V, for the pulsar measurements is

$$V = \text{diag}\begin{bmatrix} V_1 & V_2 & V_3 & V_4 \end{bmatrix}. \tag{2.35}$$

Defining the information matrix as $\mathcal{I} := P^{-1}$. Taking the time derivative of the identity $PP^{-1} = P\mathcal{I} = I$ and substituting Eq. (2.34) into the result give

$$\dot{\mathcal{I}} = H^TV^{-1}H. \tag{2.36}$$

The solution of $\mathcal{I}$ is

$$\begin{aligned} \mathcal{I}(T_{obs}) &= \mathcal{I}(0) + \int_0^{T_{obs}} H^T(\tau)V^{-1}H(\tau)\,d\tau \\ &= \mathcal{I}(0) + \tilde{H}^T \int_0^{T_{obs}} \Gamma(\tau)^TV^{-1}\Gamma(\tau)\,d\tau\tilde{H}. \end{aligned} \tag{2.37}$$

Substituting Eq. (2.31) into Eq. (2.37) gives

$$\mathcal{I}(T_{obs}) = \mathcal{I}(0) + 2\pi^2 \sum_{p=1}^{4} \frac{c\lambda_{s,p}^2 M_p \dot{\phi}_p}{V_p(c + \boldsymbol{n}_p^T\boldsymbol{v}_{sc})} \left(\sum_{j=1}^{N_{f,p}} j^2 \left(a_{p,j}^2 + b_{p,j}^2\right) \right) \begin{bmatrix} \frac{\boldsymbol{n}_p\boldsymbol{n}_p^T}{c^2} & \frac{\boldsymbol{n}_p}{c} \\ \frac{\boldsymbol{n}_p^T}{c} & 1 \end{bmatrix} \tag{2.38}$$

From the form of Eq. (2.38), it suggests that one should observe a pulsar whose direction is opposite of the spacecraft velocity vector because it increases the size of the information

matrix when the rest of the parameters are fixed. This result can be explained from the definition of the observation time, which is

$$t_p^{obs} = \frac{c}{c + \boldsymbol{n}_p^T \boldsymbol{v}_{sc}} \frac{M_p}{\dot{\phi}_p}. \tag{2.39}$$

For a fixed number of cycles, M, choosing $\boldsymbol{n}_p^T \boldsymbol{v}_{sc} < 0$ effectively makes t_p^{obs} longer than that of a spacecraft moving towards the pulsar. As a result, more measurements are processed and the error covariance reduces. Rewriting Eq. (2.38) using Eq. (2.39) gives

$$\begin{aligned} \mathcal{I}(T_{obs}) &= \mathcal{I}(0) + 2\pi^2 \sum_{p=1}^{4} \frac{\lambda_{s,p}^2 \dot{\phi}_p^2 t_p^{obs}}{V_p} \left(\sum_{j=1}^{N_{f,p}} j^2 \left(a_{p,j}^2 + b_{p,j}^2 \right) \right) \begin{bmatrix} \frac{\boldsymbol{n}_p \boldsymbol{n}_p^T}{c^2} & \frac{\boldsymbol{n}_p}{c} \\ \frac{\boldsymbol{n}_p^T}{c} & 1 \end{bmatrix} \\ &= \mathcal{I}(0) + \breve{H}^T \breve{V}^{-1} \breve{H} \end{aligned} \tag{2.40}$$

where

$$\begin{aligned} \breve{H} &= \begin{bmatrix} \frac{\boldsymbol{n}_1^T}{c} & 1 \\ \frac{\boldsymbol{n}_2^T}{c} & 1 \\ \frac{\boldsymbol{n}_3^T}{c} & 1 \\ \frac{\boldsymbol{n}_4^T}{c} & 1 \end{bmatrix} \\ \breve{V} &= \text{diag} \begin{bmatrix} \breve{V}_1 & \breve{V}_2 & \breve{V}_3 & \breve{V}_4 \end{bmatrix} \\ \breve{V}_p &= \frac{V_p}{2\pi^2 \lambda_{s,p}^2 \dot{\phi}_p^2 t_p^{obs}} \left[\sum_{j=1}^{N_{f,p}} j^2 \left(a_{p,j}^2 + b_{p,j}^2 \right) \right]^{-1} \end{aligned} \tag{2.41}$$

Finally the error covariance, $P(T_{obs})$, is obtained by inverting $\mathcal{I}(T_{obs})$ using the matrix inversion lemma,

$$P(T_{obs}) = P(0) - P(0)\breve{H}^T \left(\breve{H} P(0) \breve{H}^T + \breve{V} \right)^{-1} \breve{H} P(0). \tag{2.42}$$

$[P(T_{obs})]_{1:3,1:3}$ is the positioning accuracy and $[P(T_{obs})]_{4,4}$ is the timing accuracy. For any set of navigation pulsars, Eq. (2.40) provides the accuracy of pulsar-based navigation system based on the pulsar profiles, intensities, directions, frequencies, and the observation time. This EKF covariance matrix is known *a priori* because it is independent of the linearization points. It is worth pointing out that one can interpret Eq. (2.42) as the *a posteriori* error covariance of an equivalent one-step discrete time Kalman filter from $\tau = 0$ to $\tau = T_{obs}$,

whose gain is $K = P(0)\breve{H}^T \left(\breve{H}P(0)\breve{H}^T + \breve{V}\right)^{-1}$. The measurement noise variance of this equivalent filter is $\tilde{V}$. This result implies that for this scenario using an EKF to estimate spacecraft position from the pulsar waveform is equivalent to using an Kalman filter to estimate spacecraft position from pulsar phase. In order to minimize the error covariance, the navigation pulsars should have

1. high pulsating frequency, $\dot{\phi}_p$,
2. high peak intensity, $\lambda_{s,p}$,
3. low measurement noise, V_p, and
4. large Fourier coefficients, $a_{p,j}$, and $b_{p,j}$, for the higher order harmonics.

The sum of Fourier coefficients in Eq. (2.40) is larger when the pulsar profile is narrower. If the pulsar profile, $s(\cdot)$, is modeled by a single Gaussian function, then a narrower profile is one that has smaller variance. The effect of pulsar direction on the error covariance is not as explicit, but it can be analyzed using the GPS dilution of precision technique discussed in [45].

2.5.3 Relationship with the Cramér-Rao Lower Bound

The guidelines presented above can also be obtained using the Cramér-Rao Lower Bound (CRLB), although the dependence of the positioning accuracy on pulsar profile and direction is not as explicit [31, 32]. The following shows the relationship between the $P(T_{obs})$ of the EKF and the CRLB obtained from parameter estimation approach. Rewriting $\Gamma(\tau)$ in Eq. (2.28) without explicitly taking the derivative gives

$$\Gamma(\tau) = \text{diag}\left[\lambda_{s,1}s_1'(\bar{\phi}_{sc,1}(\tau)),\ \lambda_{s,2}s_2'(\bar{\phi}_{sc,2}(\tau)),\ \lambda_{s,3}s_3'(\bar{\phi}_{sc,3}(\tau)),\ \lambda_{s,4}s_4'(\bar{\phi}_{sc,4}(\tau))\right]. \quad (2.43)$$

The PSD, V_p, is converted to photon measurement noise variance using the typical PSD to variance approximation [44]. Substituting in Eq. (2.15) gives $V_p = \lambda_{b,p} + \lambda_{s,p}s_{sc,p}(\bar{\phi}_{sc,p}(\tau))$.

Using the above notation in Eq. (2.37) gives

$$\begin{aligned}\mathcal{I}(T_{obs}) &= \mathcal{I}(0) + \sum_{p=1}^{4} \dot{\phi}_p^2 \int_{t_p^{start}}^{t_p^{end}} \frac{[\lambda_{s,p} s_p'(\bar{\phi}_{sc,p}(\tau))]^2}{\lambda_{b,p} + \lambda_{s,p} s_p(\bar{\phi}_{sc,p}(\tau))}\, d\tau \begin{bmatrix} \frac{\boldsymbol{n}_p \boldsymbol{n}_p^T}{c^2} & \frac{\boldsymbol{n}_p}{c} \\ \frac{\boldsymbol{n}_p^T}{c} & 1 \end{bmatrix} \\ &= \mathcal{I}(0) + \sum_{p=1}^{4} \dot{\phi}_p^2 t_p^{obs} \int_{0}^{1} \frac{[\lambda_{s,p} s_p'(\varphi)]^2}{\lambda_{b,p} + \lambda_{s,p} s_p(\varphi)}\, d\varphi \begin{bmatrix} \frac{\boldsymbol{n}_p \boldsymbol{n}_p^T}{c^2} & \frac{\boldsymbol{n}_p}{c} \\ \frac{\boldsymbol{n}_p^T}{c} & 1 \end{bmatrix}.\end{aligned} \tag{2.44}$$

The CRLB derived in [31, 32] applies to the time delay, t_c, estimation using a single pulsar and is given here as

$$CRLB(t_c) = \left[t^{obs} f_s^2 \int_0^1 \frac{[\lambda_s s'(\varphi)]^2}{\lambda_b + \lambda_s s(\varphi)} d\varphi \right]^{-1}, \tag{2.45}$$

where f_s is the observed signal frequency. For time delay estimation, one only needs to consider $[\mathcal{I}(T_{obs})]_{4,4}$ in Eq. (2.44). Inverting it gives

$$\text{var}[t_c(t^{end})] = \frac{\text{var}[t_c(0)]}{1 + [\text{var}[t_c(0)] t^{obs} \dot{\phi}^2 \int_0^1 \frac{(\lambda_s s'(\varphi))^2}{\lambda_b + \lambda_s s(\varphi)}\, d\varphi}. \tag{2.46}$$

Since the CC and MLE methods have no *a priori* information, one has to take the limit of $\text{var}[t_c(t^{end})]$ as $\text{var}[t_c(0)] \to \infty$ to obtain comparable error variance. The result is

$$\text{var}[t_c(t^{end})] = \left[t^{obs} \dot{\phi}^2 \int_0^1 \frac{(\lambda_s s'(\varphi)^2}{\lambda_b + \lambda_s s(\varphi)}\, d\varphi \right]^{-1}. \tag{2.47}$$

This expression is equal to the CRLB given in Eq. (2.45). The CRLB derivation in [31, 32] does not distinguish between the observed signal frequency, f_s, and the intrinsic pulsar frequency, $\dot{\phi}$. Equation (2.47) can only be achieved if the true value of t_c were available. In practice, a well-tuned EKF would improve the estimate used for linearization as more measurements are processed. As a result, the actual error variance would slowly converge towards the ideal value given by Eq. (2.46). Equation (2.46) also highlights the advantage of incorporating *a priori* information, $\text{var}[t_c(0)]$. If *a priori* variance is available and is less than infinity, then the error variance would be less than the CRLB defined in Eq. (2.45).

2.6 Estimation Algorithm

2.6.1 Epoch Folding of Aperiodic Signal

Epoch Folding (EF) is a well-known technique in the astronomy community for observing weak astronomical sources buried beneath the receiver noise floor and it has been applied to X-ray pulsar-based navigation by [31] for a purely periodic signal. In essence, epoch folding sorts photon measurements into bins according to their fractional phases, $[0, 1)$; the measurements in each bin are arithmetically averaged to obtain a folded signal. Given that the mean and variance of a Poisson distribution are well defined and finite, epoch folding condenses the number of measurements according to Central Limit Theorem when the signal frequency is known. This section extends the epoch folding procedure to an aperiodic signal. The aperiodicity is a result of non-zero frequency rate or time varying time shifts. Let the spacecraft observe the p^{th} pulsar over an observation period of $\Delta t = t_i - t_{i-1}$. Assembling all the measurements in a vector gives

$$\boldsymbol{y}_p(t_i) = \begin{bmatrix} y_p(\tau_1) \\ \vdots \\ y_p(\tau_M) \end{bmatrix}, \tag{2.48}$$

where M is the number of measurements. For a periodic signal one can simply use the measurement time τ_j and the pulsar frequency, $\dot{\phi}$, to estimate the phase of the measurements for sorting. However, for an aperiodic signal, the full nonlinear dynamical system has to be incorporated into the epoch folding procedure.

Assume that the state vector, $\boldsymbol{x}(t_{i-1})$, at the start of the pulsar observation and the continuous white noise from t_{i-1} to τ_j are known. The signal phase associated with $y_p(\tau_j)$, can be found by propagating Eq. (2.22) from t_{i-1} to τ_j. The signal phase, $\phi_{sc,p}(\tau_j)$, can then be calculated using $\boldsymbol{x}(\tau_j)$ and the phase equation in Eq. (2.23). Taking the modulo of $\phi_{sc,p}(\tau_j)$ gives

$$\varphi_p(\tau_j) = modulo\left(\phi_{sc,p}(\tau_j), 1\right). \tag{2.49}$$

Each $\varphi_p(\tau_j)$ is sorted into a bin of size, $\Delta\theta = 1/N_b$, where N_b is the number of bins used in

the sorting. Let $c_{p,l}$ be the number of measurements in the l^{th} bin centered at θ_l.

$$\theta_1 = \frac{\Delta\theta}{2}, \quad \theta_l = \theta_{l-1} + \Delta\theta, \quad l = 2, \ldots, N_b. \tag{2.50}$$

The sorting process places each $y_p(\tau_j)$ into a bin based on its corresponding fractional phase, $\varphi_p(\tau_j)$. During the sorting process, $y_p(\tau_j)$ and τ_j are relabeled as $z_{p,l,k}$ and $\xi_{l,k}$, namely

- $z_{p,l,k}$ is the label assigned to the k^{th} measurement of the l^{th} bin, and
- $\xi_{l,k}$ is the label assigned to the k^{th} measurement time of the l^{th} bin.

Once the sorting is completed, sum all $z_{p,l,k}$ in the l^{th} bin and divide by c_l to obtain the epoch folded measurements,

$$\boldsymbol{y}_p^{ave} = \begin{bmatrix} y_{p,1}^{ave} \\ \vdots \\ y_{p,N_b}^{ave} \end{bmatrix} = \begin{bmatrix} \frac{1}{c_{p,1}} \sum_{k=1}^{c_{p,1}} z_{p,1,k} \\ \vdots \\ \frac{1}{c_{p,N_b}} \sum_{k=1}^{c_{p,N_b}} z_{p,N_b,k} \end{bmatrix}, \tag{2.51}$$

where $M = \sum_{l=1}^{N_b} c_l$. Epoch folding condenses M number of measurements into N_b number of measurements. The expected value of y_l^{ave} is obtained by considering Eq. (2.15) and realizing that each measurement in the l^{th} bin is an independent and identically distributed Poisson random variable with rate, $\lambda_{b,p} + \lambda_{s,p} s(\theta_l)$. Taking the expectation of Eq. (2.51) gives

$$\begin{aligned} E[y_{p,l}^{ave}] &= E\left[\frac{1}{c_{p,l}} \sum_{k=1}^{c_{p,l}} \lambda_{b,p} + \lambda_{s,p} s_p(\theta_l) + v_p(\xi_{l,k})\right] \\ &= \lambda_{b,p} + \lambda_{s,p} s_p(\theta_l) \end{aligned} \tag{2.52}$$

The variance is obtained by using the variance operator and substituting in Eq. (2.15).

$$\begin{aligned} \text{var}[y_{p,l}^{ave}] &= \text{var}\left[\frac{1}{c_{p,l}} \sum_{k=1}^{c_{p,l}} \lambda_{b,p} + \lambda_{s,p} s_p(\theta_l) + v_p(\xi_{l,k})\right] \\ &= \frac{1}{c_{p,l}^2} \sum_{k=1}^{c_{p,l}} \text{var}\left[v_p(\xi_{l,k})\right] \\ &= \frac{\lambda_{b,p} + \lambda_{s,p} s_p(\theta_l)}{c_{p,l} \Delta\tau}. \end{aligned} \tag{2.53}$$

Since the expected measurement in Eq. (2.52) is unbiased, the mean and variance of the folded measurement noise are

$$E[v_{p,l}^{ave}] = 0, \text{ and } \text{var}[v_{p,l}^{ave}] = \frac{\lambda_{b,p} + \lambda_{s,p} s_p(\theta_l)}{c_{p,l}\Delta\tau}, \tag{2.54}$$

where $l = 1, \ldots, N_b$. The variance of $v_{p,l}^{ave}$ decreases inversely with $c_{p,l}$ which is the number of measurements in the l^{th} bin.

2.6.2 Extended Kalman Filter with Multirate Processing

2.6.2.1 Epoch Folding

Unlike the previous use of epoch folding in [31], this method fuses Eq. (2.51) into an EKF to perform state estimation. Applying epoch folding to the pulsar signal means the filter needs to wait for a period of time, Δt, to collect measurements before computing an update. As a result, the filter update time, t_i, is not the same as the measurement sample time, τ_j. In order to account for this mismatch, batch processing is used [46]. The *a priori* estimate, $\hat{\boldsymbol{x}}_{i|i-1}$, is the estimate given measurement history up to t_{i-1}, and the *a posteriori* estimate, $\hat{\boldsymbol{x}}_{i|i}$, is the estimate given measurement history up to t_i.

Define the nominal trajectory for linearization from t_{i-1} to t_i as

$$\dot{\bar{\boldsymbol{x}}}(t) = \boldsymbol{f}\left(\bar{\boldsymbol{x}}(t), t\right), \quad \bar{\boldsymbol{x}}(t_{i-1}) = \hat{\boldsymbol{x}}_{i-1|i-1}. \tag{2.55}$$

Linearizing the state and measurement equations about $\bar{\boldsymbol{x}}(t)$ and $\bar{\boldsymbol{x}}(\tau_j)$ gives

$$\begin{aligned} \delta\dot{\boldsymbol{x}}(t) &= F(t)\delta\boldsymbol{x}(t) + G\boldsymbol{w}(t) \\ \delta\boldsymbol{y}(\tau_j) &= H(\tau_j)\delta\boldsymbol{x}(\tau_j) + \boldsymbol{v}(\tau_j) \end{aligned} \tag{2.56}$$

where the state perturbation is defined as $\delta\boldsymbol{x}(t) = \boldsymbol{x}(t) - \bar{\boldsymbol{x}}(t)$. The linearized system matrices are

$$F(t) = \left.\frac{\partial \boldsymbol{f}\left(\boldsymbol{x}(t), t\right)}{\partial \boldsymbol{x}}\right|_{\boldsymbol{x}(t)=\bar{\boldsymbol{x}}(t)} \text{ and } H(\tau) = \left.\frac{\partial \boldsymbol{h}\left(\boldsymbol{x}(\tau), \tau\right)}{\partial \boldsymbol{x}}\right|_{\boldsymbol{x}(\tau)=\bar{\boldsymbol{x}}(\tau)}. \tag{2.57}$$

The state transition matrix for Eq. (2.56) is

$$\dot{\Phi}\left(t, t_{i-1}\right) = F(t)\Phi\left(t, t_{i-1}\right), \quad \Phi\left(t_{i-1}, t_{i-1}\right) = I. \tag{2.58}$$

Relating the individual state perturbation, $\delta\boldsymbol{x}(\tau_j)$, to the state perturbation at time t_i gives $\delta\boldsymbol{x}(\tau_j) = \Phi\left(\tau_j, t_i\right)\delta\boldsymbol{x}(t_i)$. The measurement times, τ_j in Eq. (2.48) are all smaller than the update time t_i. Equation (2.55) and Eq. (2.58) are propagated forward from t_{i-1} to t_i, and $\Phi(\tau_j, t_i)$ is obtained by using the transition matrices,

$$\Phi(\tau_j, t_i) = \Phi(\tau_j, t_{i-1})\Phi^{-1}(t_i, t_{i-1}). \tag{2.59}$$

Collecting a batch of measurement perturbations for the p^{th} pulsar from t_{i-1} to t_i gives

$$\begin{bmatrix} \delta y_p(\tau_1) \\ \vdots \\ \delta y_p(\tau_M) \end{bmatrix} = \begin{bmatrix} H_p(\tau_1)\Phi\left(\tau_1, t_i\right) \\ \vdots \\ H_p(\tau_M)\Phi\left(\tau_M, t_i\right) \end{bmatrix} \delta\boldsymbol{x}\left(t_i\right) + \begin{bmatrix} \nu_p(\tau_1) \\ \vdots \\ \nu_p(\tau_M) \end{bmatrix}, \tag{2.60}$$

The measurement deviations in Eq. (2.60) is sorted according to their estimated phase, $\bar{\phi}_{sc,p}(\tau_j)$. which can be obtained by substituting $\bar{\boldsymbol{x}}(\tau_j)$ into the pulsar phase equation in Eq. (2.22). Once $\bar{\phi}_{sc,p}(\tau_j)$ is known, $\bar{\varphi}_p(\tau_j)$ can be calculated using Eq. (2.49). The fractional phases, $\bar{\varphi}_p(\tau_j)$, are used to sort measurement perturbations into bins. During the sorting process, each $\delta y_p(\tau_j)$ is reordered and relabeled using δz. $\delta z_{p,l,k}$ is the label assigned to the k^{th} measurement perturbation of the l^{th} bin. The definition of $\xi_{l,k}$ remains the same as the previous section. Sum all $\delta z_{p,l,k}$ in the l^{th} bin and divide by $c_{p,l}$ to obtain the folded measurement perturbations,

$$\underbrace{\begin{bmatrix} \frac{1}{c_{p,1}} \sum_{k=1}^{c_{p,1}} \delta z_{p,1,k} \\ \vdots \\ \frac{1}{c_{p,N_b}} \sum_{k=1}^{c_{p,N_b}} \delta z_{p,N_b,k} \end{bmatrix}}_{\delta\boldsymbol{y}_p^{ave}(t_i)} = \underbrace{\begin{bmatrix} \frac{1}{c_{p,1}} \sum_{k=1}^{c_{p,1}} H(\xi_{1,k})\Phi\left(\xi_{1,k}, t_i\right) \\ \vdots \\ \frac{1}{c_{p,N_b}} \sum_{k=1}^{c_{p,N_b}} H(\xi_{N_b,k})\Phi\left(\xi_{N_b,k}, t_i\right) \end{bmatrix}}_{H_p^{ave}(t_i)} \delta\boldsymbol{x}(t_i) + \underbrace{\begin{bmatrix} v_{p,1}^{ave} \\ \vdots \\ v_{p,N_b}^{ave} \end{bmatrix}}_{\boldsymbol{v}_p^{ave}(t_i)}, \tag{2.61}$$

Stacking the averaged perturbations of all the pulsars into a vector gives

$$\begin{aligned} \delta\boldsymbol{y}^{ave}(t_i) &:= H^{ave}(t_i)\delta\boldsymbol{x}(t_i) + \boldsymbol{v}^{ave}(t_i) \\ &\approx \boldsymbol{y}^{ave}(t_i) - \bar{\boldsymbol{y}}^{ave}(t_i), \end{aligned} \tag{2.62}$$

where $\bar{\boldsymbol{y}}^{ave}(t_i)$ is Eq. (2.52) evaluated at every bin and pulsar. Replacing the measurement equation in Eq. (2.56) with Eq. (2.62) forms the dynamical system for state estimation. This

system can be estimated with a Kalman filter whose *a priori* estimate of $\delta\boldsymbol{x}(t_i)$ is $\delta\hat{\boldsymbol{x}}_{i|i-1} = 0$. Therefore, the *a posteriori* state estimate is

$$\begin{aligned} \delta\hat{\boldsymbol{x}}_{i|i} &= \delta\hat{\boldsymbol{x}}_{i|i-1} + K_i\delta\boldsymbol{y}_i^{ave} \\ \hat{\boldsymbol{x}}_{i|i} &= \hat{\boldsymbol{x}}_{i|i-1} + \delta\hat{\boldsymbol{x}}_{i|i}, \end{aligned} \tag{2.63}$$

where $\hat{\boldsymbol{x}}_{i|i-1} = \bar{\boldsymbol{x}}(t_i)$ and $\delta\boldsymbol{y}_i^{ave} := \delta\boldsymbol{y}^{ave}(t_i)$. The filter gain and the *a posteriori* error covariance are

$$\begin{aligned} K_i &= M_i(H_i^{ave})^T\left(H_i^{ave}M_i(H_i^{ave})^T + V_i^{ave}\right)^{-1} \\ P_i &= \left(I - K_iH_i^{ave}\right)M_i\left(I - K_iH_i^{ave}\right)^T + K_iV_i^{ave}K_i^T. \end{aligned} \tag{2.64}$$

The *a priori* covariance associated with $\hat{\boldsymbol{x}}_{i|i-1}$ is $M_i = M(t_i)$, and the time propagation equation is

$$\dot{M} = F(t)M(t) + M(t)F^T(t) + GWG^T \quad M(t_{i-1}) = P_{i-1}, \tag{2.65}$$

where $W = diag[W_r, W_\zeta]$ and P_{i-1} is the *a posteriori* covariance at time t_{i-1}. The covariance of $\boldsymbol{v}^{ave}(t_i)$ is $V_i^{ave} = diag[V_{i,1}^{ave}, \ldots, V_{i,N_p}^{ave}]$, where $V_{i,p}^{ave}$ is obtained by substituting (2.50) into (2.54).

Unlike the epoch folding procedure introduced in the previous section, the epoch folding process of the navigation filter only has access to the estimated phase, $\bar{\varphi}(\tau_j)$ rather than $\varphi(\tau_j)$. Since epoch folding is a type of time averaging, the time evolution of $\bar{\varphi}(\tau_j)$, which is related to the spacecraft velocity and pulsar timing model, is important. Therefore, the velocity estimation error, $\hat{\boldsymbol{e}}_{\dot{\boldsymbol{r}}_{sc}} = \dot{\boldsymbol{r}}_{sc} - \dot{\hat{\boldsymbol{r}}}_{sc}$ has an adverse effect on epoch folding, which is the fundamental limitation of epoch folding in pulsar-based navigation system. As a result, one should experiment with various epoch folding duration, Δt, in simulation to trade between the computation time and measurement corruption. Alternatively, one can use Eq. (2.66) and the filter error covariance, P_i, to derive a formula for variable epoch folding duration.

The necessary and sufficient condition for epoch folded measurements to converge to Eq. (2.52) under the assumption of constant velocity and stepwise pulsar signal intensity is the following [31].

$$\boldsymbol{n}_p^T\hat{\boldsymbol{e}}_{\dot{\boldsymbol{r}}_{sc}}(t) < \frac{c\dot{\phi}_{sc,p}(t)}{N_b\Delta t\dot{\phi}_{sc,p}^2(t) + \dot{\phi}_{ssb,p}(t^{ssb})} \tag{2.66}$$

where $\dot{\phi}_{sc,p}(t)$ is the instantaneous observed pulsar frequency on the spacecraft at time t, and $\dot{\phi}_{ssb,p}(t^{ssb})$ is the instantaneous pulsar frequency at the detection time t^{ssb} at the SSB frame origin. Since the actual spacecraft velocity and the pulsar intensities are neither constant nor stepwise, any velocity estimation errors would increase the measurement noise variance. When the velocity error is on the order of Eq. (2.66), empirical results show the following compensation technique is effective.

$$V_{tuned,i}^{ave} = V_i^{ave}(V_b + V_a e^{-t_i/V_\tau}), \tag{2.67}$$

where V_b, V_a, and V_τ are tuning parameters. Equation (2.66) serves as a guideline on the required accuracy of the velocity estimate used to initialize the navigation filter. If a sufficiently accurate initial velocity estimate is not available, then one possible solution is to first observe pulsars with low frequency and then switch to high frequency pulsars once the filter has sufficiently converged on the spacecraft velocity. Two other possible solutions are adding a velocity measurement to help the filter determine the time evolution of φ and/or initialized with a batch maximum likelihood estimator to obtain a more accurate estimate of the initial spacecraft states.

2.6.2.2 Approximation of the Phase Equation

In addition to the observation interval, Δt, and sampling interval, $\Delta\tau$, there is another time interval in the navigation filter. That is the integration time step, $\Delta\sigma = \sigma_k - \sigma_{k-1}$ of Eq. (2.55) and Eq. (2.58). The typical choice of $\Delta\sigma$ is simply $\Delta\tau$, but this is undesirable given that $\Delta\tau$ is a small number ($\Delta\tau \ll \dot{\phi}_p^{-1}$). Looking at the phase, $\phi_{sc,p}(\tau_j)$, in the measurement equation more closely reveals that it consists of several timescales. The time constant associated with the fast timescale is the period of the pulsar. The slow component is composed of $\boldsymbol{r}_\odot$, $\boldsymbol{r}_{sc}$, and $\boldsymbol{\zeta}$ and the fastest of them is the spacecraft orbital dynamics. Because of the large timescale difference between the spacecraft orbital and the pulsar rotation periods, one can choose $\Delta\sigma$ to be larger than $\Delta\tau$ in order to reduce the computation time needed for state propagation. In other words, the slow component is approximately constant over $\Delta\sigma$. The first thought is to linearize the measurement function, $h_p\left(\boldsymbol{x}(\tau), \tau\right)$,

about time σ_k and state $\bar{\boldsymbol{x}}(\sigma_k)$ and then extend the result to cover the entire or a fraction of the observation interval. Unfortunately, the highly nonlinear pulse shape renders this approximation inadequate for $\Delta\sigma > \dot{\phi}_p^{-1}$.

An alternative solution is the following. In a typical EKF, the linearized measurement matrix is

$$\begin{aligned} H_p(\tau_j) &= \left.\frac{\partial h_p\left(\boldsymbol{x}(\tau),\tau\right)}{\partial \boldsymbol{x}}\right|_{\boldsymbol{x}(\tau)=\bar{\boldsymbol{x}}(\tau_j)} \\ &= \lambda_{s,p} s_p'(\bar{\phi}_{sc,p}(\tau_j)) \left[\tfrac{\dot{\phi}_p}{c}\boldsymbol{n}_p^T \quad 0 \quad H_{\zeta,p}\right], \end{aligned} \tag{2.68}$$

where the prime symbol denotes the derivative with respect to the argument of the function. The only term that is a function of $\bar{\boldsymbol{x}}(\tau_j)$ in (2.68) is $\bar{\phi}_{sc,p}(\tau_j)$, which means that an accurate approximation of the phase equation in terms of time allows one to circumvent the need to propagate the slow dynamics with small time steps. One simple approximation is to linearize the phase equation instead, which gives

$$\begin{aligned} \bar{\phi}_{sc,p}^{app}(\tau_j,\sigma_k) &= \psi_p(\sigma_k) + L_p(\sigma_k)\left(\tau_j - \sigma_k\right) \\ &\approx \bar{\phi}_{sc,p}(\tau_j) \end{aligned} \tag{2.69}$$

where

$$\begin{aligned} \psi_p(\sigma_k) &= \phi_{p,0} + \dot{\phi}_p\left[\sigma_k - t_0 + \frac{\boldsymbol{n}_p^T\bar{\boldsymbol{r}}_{sc}(\sigma_k)}{c}\right] + H_{\zeta,p}\bar{\boldsymbol{\zeta}}_p(\sigma_k) \\ L_p(\sigma_k) &= \left.\frac{d\phi_{sc,p}}{d\tau}\right|_{\boldsymbol{x}(\tau)=\bar{\boldsymbol{x}}(\sigma_k)} \\ &= \dot{\phi}_p\left[1 + \frac{\boldsymbol{n}_p^T\dot{\bar{\boldsymbol{r}}}_{sc}(\sigma_k)}{c}\right] + H_{\zeta,p}\dot{\bar{\boldsymbol{\zeta}}}_p(\sigma_k). \end{aligned} \tag{2.70}$$

The reasoning for this choice is that the phase equation is approximately linear in time over $\Delta\sigma$ due to the large timescale difference. Using this approximation the filter linearization occurs at time σ_k instead of τ_j. The fastest filter time interval is $\Delta\tau$ and its size is related to the approximation in Eq. (2.12). The relative size between the three time parameters is $\Delta t > \Delta\sigma \gg \Delta\tau$. Using this approximation, empirical results show that $\Delta\sigma$ can be increased from 50 μs to ~ 10 s with negligible impact on the estimation errors.

2.6.3 Quadrature Formulation

Since the pulsar measurement in Eq. (2.22) can be approximated by Fourier series, one can design an alternative filter to estimate the spacecraft position and velocity. The measurement equation expressed in Fourier series is

$$y_p = \lambda_{b,p} + \lambda_{s,p}\left[\frac{a_{p,0}}{2} + \sum_{j=1}^{N_{f,p}} a_{p,j}\cos\left(j2\pi\phi_{sc,p}\right) + b_{p,j}\sin(j2\pi\phi_{sc,p})\right] + \nu_p. \tag{2.71}$$

Manipulating the above gives

$$y_p = A_{p,0} + \sum_{j=1}^{N_{f,p}} C_{p,j}A_{p,j} + S_{p,j}B_{p,j} + \nu_p, \tag{2.72}$$

where

$$\begin{aligned}
A_{p,0} &= \lambda_{b,p} + \lambda_{s,p}\frac{a_{p,0}}{2} \\
A_{p,j} &= \lambda_{s,p}\left(a_{p,j}\cos(j2\pi\dot{\phi}_p\tau_j) + b_{p,j}\sin(j2\pi\dot{\phi}_p\tau_j)\right) \\
B_{p,j} &= \lambda_{s,p}\left(b_{p,j}\cos(j2\pi\dot{\phi}_p\tau_j) - a_{p,j}\sin(j2\pi\dot{\phi}_p\tau_j)\right) \\
S_{p,j} &= \sin\left(j2\pi\left[\phi_{0,p} + \dot{\phi}_p\left[-t_0 + \frac{\boldsymbol{n}_p^T\left(\boldsymbol{r}_\odot + \boldsymbol{r}_{sc}\right)}{c}\right] + H_{\zeta,p}\boldsymbol{\zeta}_p\right]\right) \\
C_{p,j} &= \cos\left(j2\pi\left[\phi_{0,p} + \dot{\phi}_p\left[-t_0 + \frac{\boldsymbol{n}_p^T\left(\boldsymbol{r}_\odot + \boldsymbol{r}_{sc}\right)}{c}\right] + H_{\zeta,p}\boldsymbol{\zeta}_p\right]\right)
\end{aligned} \tag{2.73}$$

The non-zero terms of the Ito differentials for S_j and C_j are

$$\begin{bmatrix} dS_{p,j} \\ dC_{p,j} \end{bmatrix} = \begin{bmatrix} \frac{\partial C_{p,j}}{\partial\tau} & \frac{\partial C_{p,j}}{\partial\boldsymbol{r}_\odot} & \frac{\partial C_{p,j}}{\partial\boldsymbol{r}_{sc}} & \frac{\partial C_{p,j}}{\partial\boldsymbol{\zeta}_p} \\ \frac{\partial S_{p,j}}{\partial\tau} & \frac{\partial S_{p,j}}{\partial\boldsymbol{r}_\odot} & \frac{\partial S_{p,j}}{\partial\boldsymbol{r}_{sc}} & \frac{\partial S_{p,j}}{\partial\boldsymbol{\zeta}_p} \end{bmatrix} \begin{bmatrix} d\tau \\ d\boldsymbol{r}_\odot \\ d\boldsymbol{r}_{sc} \\ d\boldsymbol{\zeta}_p \end{bmatrix} + \frac{1}{2}\begin{bmatrix} tr\left(G_{\zeta,p}W_{\zeta,p}G_{\zeta,p}^T\frac{\partial^2 S_{p,j}}{\partial\boldsymbol{\zeta}_p^2}\right) \\ tr\left(G_{\zeta,p}W_{\zeta,p}G_{\zeta,p}^T\frac{\partial^2 C_{p,j}}{\partial\boldsymbol{\zeta}_p^2}\right) \end{bmatrix} d\tau. \tag{2.74}$$

Converting Eq. (2.74) from stochastic differential equation form to state space form gives

$$\dot{\boldsymbol{q}}_{p,j} = F_{p,j}(\dot{\boldsymbol{r}}_{sc}, [\boldsymbol{\zeta}_p]_2)\boldsymbol{q}_{p,j} + G_{p,j}(\boldsymbol{q}_{p,j})\boldsymbol{w}_{\zeta,p}, \tag{2.75}$$

where $\boldsymbol{q}_{p,j} = \left[S_{p,j}, C_{p,j}\right]^T$ are the quadratures and

$$
\begin{aligned}
\left[F_{p,j}(\dot{\boldsymbol{r}}_s, [\boldsymbol{\zeta}_p]_2)\right]_{1,1} &= -2(j\pi\dot{\phi}_p)^2[W_{\zeta,p}]_{11} \\
\left[F_{p,j}(\dot{\boldsymbol{r}}_s, [\boldsymbol{\zeta}_p]_2)\right]_{1,2} &= j2\pi\left[\left(\frac{\boldsymbol{n}_p^T\left(\dot{\boldsymbol{r}}_\odot + \dot{\boldsymbol{r}}_{sc}\right)}{c}\right)\dot{\phi}_p + [\boldsymbol{\zeta}_p]_2\right] \\
\left[F_{p,j}(\dot{\boldsymbol{r}}_s, [\boldsymbol{\zeta}_p]_2)\right]_{2,1} &= -j2\pi\left[\left(\frac{\boldsymbol{n}_p^T\left(\dot{\boldsymbol{r}}_\odot + \dot{\boldsymbol{r}}_{sc}\right)}{c}\right)\dot{\phi}_p + [\boldsymbol{\zeta}_p]_2\right] \\
\left[F_{p,j}(\dot{\boldsymbol{r}}_s, [\boldsymbol{\zeta}_p]_2)\right]_{2,2} &= -2(j\pi\dot{\phi}_p)^2[W_{\zeta,p}]_{11} \\
G_{p,j}(\boldsymbol{q}_{p,j}) &= j2\pi\dot{\phi}_p\begin{bmatrix} C_{p,j} & 0 & 0 \\ -S_{p,j} & 0 & 0 \end{bmatrix}.
\end{aligned}
\tag{2.76}
$$

The symbol, $[A]_{ij}$, indicates the i^{th} row and the j^{th} column of A. If only one subscript is given, then A is a vector. The transformed plant and the measurement equations are

$$
\begin{aligned}
\begin{bmatrix} \dot{\boldsymbol{r}}_{sc} \\ \ddot{\boldsymbol{r}}_{sc} \\ \dot{\boldsymbol{q}}_{p,j} \\ \left[\dot{\boldsymbol{\zeta}}_p\right]_2 \end{bmatrix} &= \begin{bmatrix} \dot{\boldsymbol{r}}_{sc} \\ \boldsymbol{f}_{orbit}\left(\boldsymbol{r}_{sc}\right) \\ F_{p,j}(\dot{\boldsymbol{r}}_{sc}, [\boldsymbol{\zeta}_p]_2)\boldsymbol{q}_{p,j} \\ 0 \end{bmatrix} + \begin{bmatrix} 0 & 0 \\ I & 0 \\ 0 & G_{p,j}(\boldsymbol{q}_{p,j}) \\ 0 & [G_{\zeta,p}]_{2,:} \end{bmatrix}\begin{bmatrix} \boldsymbol{w}_r \\ \boldsymbol{w}_{\zeta,p} \end{bmatrix} \\
y_p(\tau_j) &= A_{p,0} + \sum_{j=1}^{N_{f,p}} A_{p,j}(\tau_j)C_{p,j}(\tau_j) + B_{p,j}(\tau_j)S_{p,j}(\tau_j) + v_p(\tau_j),
\end{aligned}
\tag{2.77}
$$

The extended version of the state dependent noise filter in [47] is used to estimate the states of Eq. (2.77). As an option to reduce the dimension of the state vector, $S_{p,j}$ and $C_{p,j}$ can be computed recursively as

$$
S_{p,j} = \sum_{k=1}^{\text{odd}}(-1)^{\frac{k-1}{2}}\binom{j}{k}C_{p,1}^{j-k}S_{p,1}^k, \quad C_{p,j} = \sum_{k=2}^{\text{even}}(-1)^{\frac{k}{2}}\binom{j}{k}C_{p,1}^{j-k}S_{p,1}^k. \tag{2.78}
$$

This means the pulse profile can be approximated using multiple Fourier series terms without increasing the number of states. However, this reduction comes at the cost of the measurement no longer being linear. The following simulation results leverage the trigonometric identities to reduce state vector dimension.

2.7 Numerical Simulation

2.7.1 Orbiter Mission

The orbit of the International Space Station was chosen for the orbiter simulation. The position and velocity of Earth were set to $\boldsymbol{r}_{\odot} = \dot{\boldsymbol{r}}_{\odot} = 0$ for simplicity. The simulation assumed that all pulsars can be observed simultaneously with unobstructed line-of-sight throughout the orbit for 20 hr. The Root Sum Square (RSS) and time averaged RSS performance metrics used in this chapter are

$$\begin{aligned}
\hat{e}_{\boldsymbol{r}_{sc},rss}(t_i) &= \sqrt{[\hat{\boldsymbol{e}}(t_i)]_1^2 + [\hat{\boldsymbol{e}}(t_i)]_2^2 + [\hat{\boldsymbol{e}}(t_i)]_3^2} \\
\sigma_{\boldsymbol{r}_{sc},rss}(t_i) &= \sqrt{[P(t_i)]_{11} + [P(t_i)]_{22} + [P(t_i)]_{33}} \\
\hat{e}_{\boldsymbol{r}_{sc},rms} &= \sqrt{\frac{1}{N_m}\sum_{i}^{N_m} \hat{e}^2_{\boldsymbol{r}_{sc},rss}(t_i)} \\
\sigma_{\boldsymbol{r}_{sc},mrss} &= \frac{1}{N_m}\sum_{i}^{N_m} \sigma_{\boldsymbol{r}_{sc},rss}(t_i),
\end{aligned} \tag{2.79}$$

where $\hat{\boldsymbol{e}} = \boldsymbol{x} - \hat{\boldsymbol{x}}$ and N_m is the number of terms used in the average. The symbol, $[A]_{ij}$, indicates the i^{th} row and the j^{th} column of A. The performance metrics associated with the velocity estimation errors were calculated similarly. They are denoted as $\hat{e}_{\dot{\boldsymbol{r}}_{sc},rss}$, $\sigma_{\dot{\boldsymbol{r}}_{sc},rss}$, $\hat{e}_{\dot{\boldsymbol{r}}_{sc},rms}$, and $\sigma_{\dot{\boldsymbol{r}}_{sc},mrss}$.

For the orbiter mission, the PSD of the white acceleration disturbance in the i^{th} axis was chosen such that the standard deviation of $[\boldsymbol{w}_r(\tau_j)]_i$ is equal to the average magnitude of the J_2 perturbation in order to capture the remaining disturbances such as drag, solar pressure, and other high order gravitational effects. The value of the PSD was $[W_r]_{ii} = 10^{-14}\ km^2/s^3$. The PSD of the input noises driving the error model of the cesium clock were $W_c = diag\left(\left[1.6 \times 10^{-21}\ s^2/s,\ \ 10^{-32}\ s^{-1}\right]\right)$ [48, 49]. The PSD of the input noises associated with the pulsar timing noise were calculated using Eq. (2.16). The initial position and velocity were assumed to be Gaussian distributed, whose means in the perifocal frame were $\boldsymbol{r}^{pf}(t_0) = \left[6.768 \times 10^3, 0, 0\right]^T\ km$ and $\dot{\boldsymbol{r}}^{pf}(t_0) = \left[0, 7.676, 0\right]^T\ km/s$. This condition corresponds to the periapsis of the orbit, so the x-component can be interpreted as the radial direction and y and z-components are the along-track and cross-

Table 2.1: Pulsar Parameters [7, 8]

Pulsar	$\lambda_b\ (ph/s)$	$\lambda_s\ (ph/s)$	$\dot{\phi}\ (Hz)$	RA (°)	DEC (°)
J0030+4501	0.2	0.193	205.5	7.61	4.86
J0437-4715	0.62	0.283	173.7	69.32	−47.25
B1821-24	0.22	0.093	327.9	−89.59	−24.87
J0218+4232	0.2	0.082	430.5	34.53	42.54

track directions. Their covariance matrices were $P^{pf}_{\boldsymbol{r}}(t_0) = diag\left(\left[5^2, 50^2, 50^2\right]\right)\ km^2$ and $P^{pf}_{\dot{\boldsymbol{r}}}(t_0) = diag\left(\left[0.01^2, 0.05^2, 0.05^2\right]\right)\ (km/s)^2$. Since Eq. (2.22) is defined in terms of a planet centered inertial frame, the simulation initial conditions had to be transformed using orbital elements [35]. The initial state vector associated with the clock model was zero mean, and the covariance matrix was $diag\left(\left[P_{t_c}(t_0), P_{b_c}(t_0)\right]\right) = diag\left(\left[10^{-10}\ s^2, 10^{-20}\ (s/s)^2\right]\right)$. The initial states for the pulsar timing noises were zero mean and the covariance matrices were $P_{\boldsymbol{\eta}_1}(t_0) = P_{\boldsymbol{\eta}_2}(t_0) = P_{\boldsymbol{\eta}_3}(t_0) = P_{\boldsymbol{\eta}_4}(t_0) = \text{diag}\left(\left[10^{-6}\ cyc^2, 10^{-24}\ (cyc/s)^2\right]\right)$. The pulsar signals were realized using non-homogenous Poisson process and the true model was propagated using an Euler integration scheme with a time-step of 50 μs [31]. The relevant pulsar characteristics are listed in Table 2.1. The pulsar profiles used in the simulation can be found in [8]. Modeling error was not considered in this study. All model parameters and functional forms were assumed to be known.

Three phase filters were simulated. The first is without Epoch Folding (EF), and it is simply denoted as EKF. The second and the third trials use EF, and they are denoted as EKF EF. The fourth filtering result uses quadrature formulation with EF, and it is denoted as EKF EF Quad. The time interval settings and the measurement noise covariance boost are summarized in Table 2.2. The time intervals were determined empirically. The simulation initial errors are shown in Table 2.3. The RSS position and velocity estimation errors for one realization of the orbiter mission are plotted in Fig. 2.3 and Fig. 2.4. Table 2.4 shows the time averaged Root Mean Square error, $\hat{e}_{\boldsymbol{r}_{sc},rms}$, over the last 2 hr.

Table 2.2: Simulation Trials

	Trial Number and Filter Type			
Parameters	1 EKF	2 EKF EF	3 EKF EF	4 EKF EF Quad
$\Delta\tau$	50 μs	50 μs	50 μs	50 μs
$\Delta\sigma$	5 ms	1 s	1 s	1 s
Δt	–	50 s	500 s	50 s
V_b	2	2	2	2
V_a	19	19	19	0
V_τ	2000 s	2000 s	2000 s	0 s

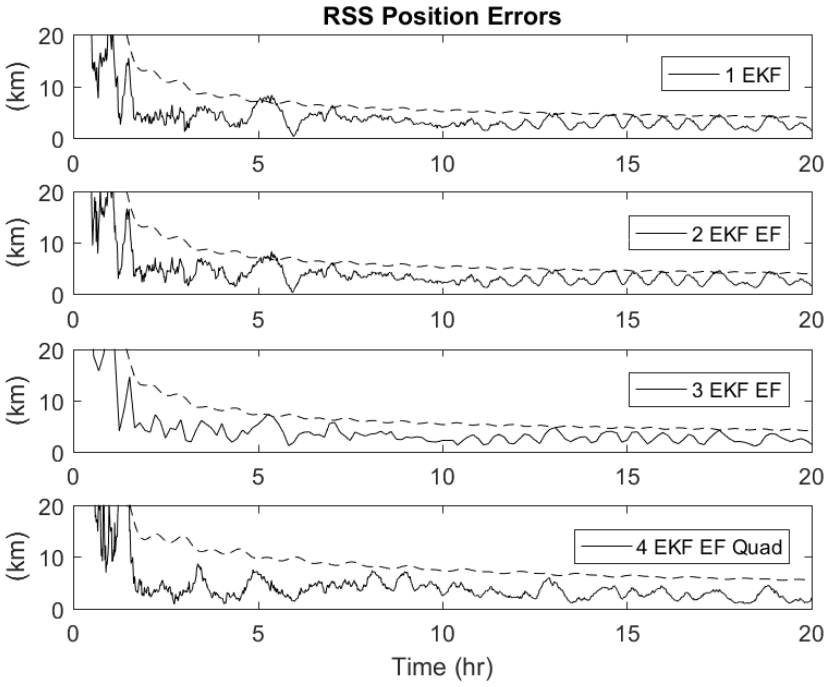

Figure 2.3: The dashed and the solid lines are $\sigma_{\boldsymbol{r}_{sc},rss}$ and $\hat{e}_{\boldsymbol{r}_{sc},rss}$ of the orbiter mission.

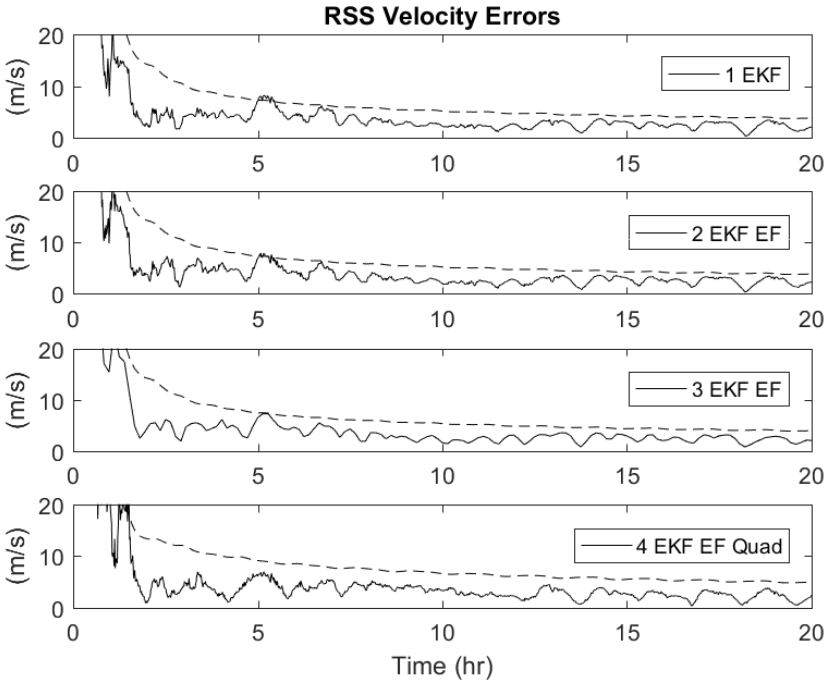

Figure 2.4: The dashed and the solid lines are $\sigma_{\dot{\boldsymbol{r}}_{sc},rss}$ and $\hat{e}_{\dot{\boldsymbol{r}}_{sc},rss}$ of the orbiter mission.

2.7.2 Deep Space Mission

The orbital parameters for the deep space mission were chosen to be a Hohmann transfer from Earth to Jupiter, so $\boldsymbol{f}_{J_2}(\boldsymbol{r}_{sc}) = 0$. The initial condition of the simulation corresponds to the case where the spacecraft is one year away from Earth. The simulation time was 20 hr. The PSD of the input noises associated with the acceleration disturbance, clock noise and pulsar timing noise were the same as the orbiter mission. The initial conditions were assumed to be Gaussian distributed, whose mean in perifocal frame were $\boldsymbol{r}_{sc}^{pf}(t_0) = \left[-4.235 \times 10^8, 3.317 \times 10^8, 0\right]^T$ km and $\dot{\boldsymbol{r}}_{sc}^{pf}(t_0) = \left[-14.181, -2.522, 0\right]^T$ km/s. The covariance matrix for position was $P_{\boldsymbol{r}_{sc}}^{pf}(t_0) = \text{diag}\left(\left[50^2, 50^2, 50^2\right]\right)$ km^2, and the covariance matrix for velocity was $P_{\dot{\boldsymbol{r}}_{sc}}^{pf}(t_0) = \text{diag}\left(\left[0.05^2, 0.05^2, 0.05^2\right]\right)$ $(km/s)^2$. The simulation initial errors are shown in Table 2.3. The RSS position and velocity estimation errors for one realization of the deep space mission are plotted in Fig. 2.5 and Fig. 2.6.

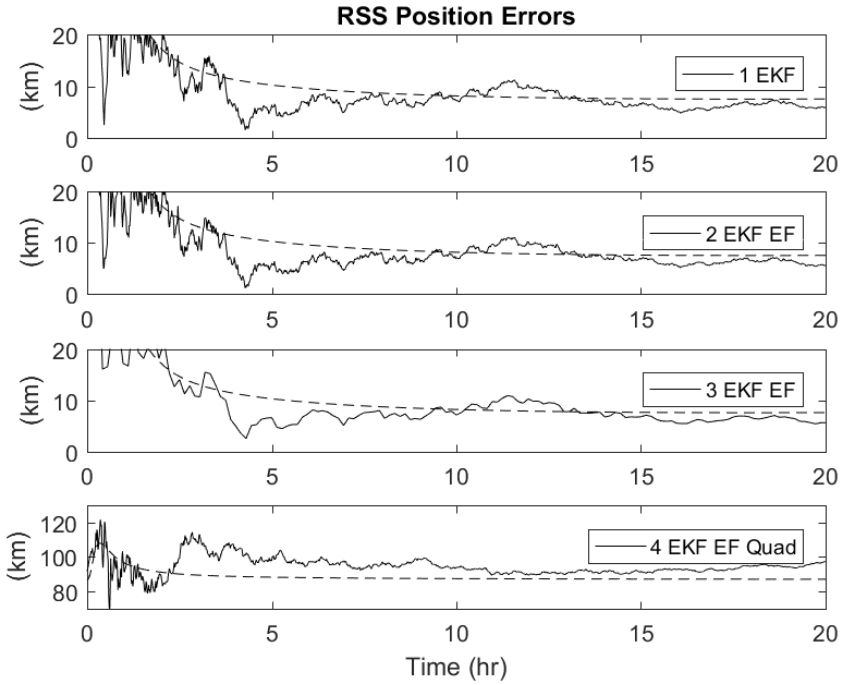

Figure 2.5: The dashed and the solid lines are $\sigma_{\boldsymbol{r}_{sc},rss}$ and $\hat{e}_{\boldsymbol{r}_{sc},rss}$ of the deep space mission.

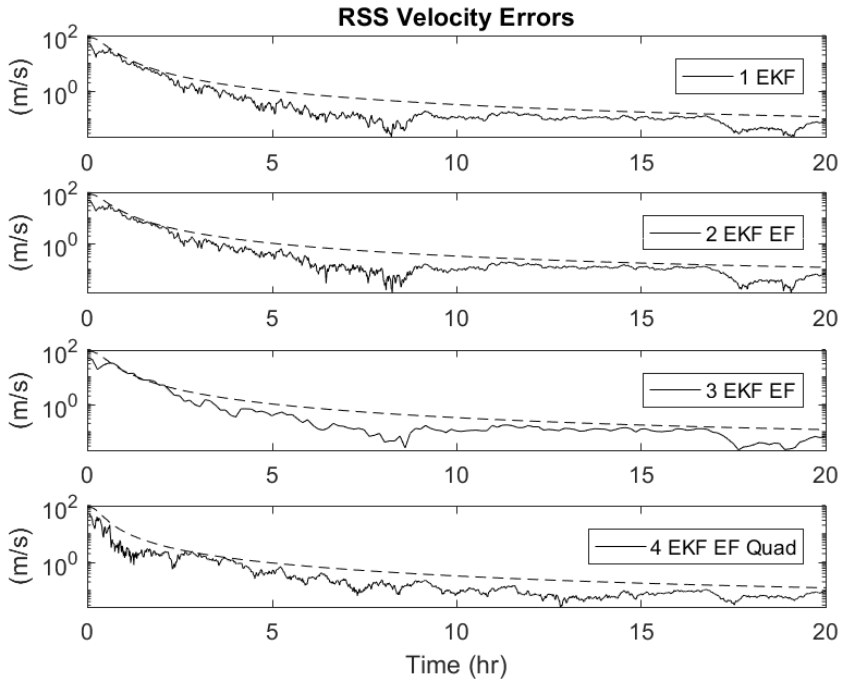

Figure 2.6: The dashed and the solid lines are $\sigma_{\dot{\boldsymbol{r}}_{sc},rss}$ and $\hat{e}_{\dot{\boldsymbol{r}}_{sc},rss}$ of the deep space mission. The y-axis is in log scale

Table 2.3: Initial Errors and Bounds

	Units	Orbiter	Deep Space
$\hat{e}_{\boldsymbol{r}_{sc},x}$	(km)	5.9	11.5
$\hat{e}_{\boldsymbol{r}_{sc},y}$	(km)	56.8	63.5
$\hat{e}_{\boldsymbol{r}_{sc},z}$	(km)	-52.3	-64.8
$\hat{e}_{\dot{\boldsymbol{r}}_{sc},x}$	(m/s)	11.6	25.2
$\hat{e}_{\dot{\boldsymbol{r}}_{sc},y}$	(m/s)	60.3	42.5
$\hat{e}_{\dot{\boldsymbol{r}}_{sc},z}$	(m/s)	-66.5	4.1
$\hat{e}_{\boldsymbol{r}_{sc},rms}$	(km)	77.4	91.4
$\hat{e}_{\dot{\boldsymbol{r}},rms}$	(m/s)	90.5	49.6
$\sigma_{\boldsymbol{r}_{sc},rss}$	(km)	70.9	86.6
$\sigma_{\dot{\boldsymbol{r}},rss}$	(m/s)	71.4	86.6

Table 2.4: Filter Performance (averaged over the last 2 hr)

	Orbiter				Deep Space			
Trial #	1	2	3	4	1	2	3	4
$\hat{e}_{\boldsymbol{r}_{sc},rms}$ (km)	2.71	2.75	2.29	2.34	6.49	6.30	6.24	95.07
$\hat{e}_{\dot{\boldsymbol{r}},rms}$ (m/s)	2.22	2.28	2.02	2.21	0.052	0.042	0.045	0.067
$\sigma_{\boldsymbol{r}_{sc},mrss}$ (km)	4.13	4.16	4.24	5.67	7.55	7.57	7.57	87.04
$\sigma_{\dot{\boldsymbol{r}},mrss}$ (m/s)	3.89	3.92	3.98	5.01	0.126	0.128	0.127	0.132
Computation Time (hr)	55.0	4.7	8.7	6.7	54.7	4.7	8.6	6.7
Normalized Time	1	0.09	0.16	0.12	1	0.09	0.16	0.12

2.8 Discussion

For both scenarios, the errors stay within or near the RSS bounds, which is an indication that the filter is working properly. The time averaged RSS bounds were obtained from the linearized error covariance; therefore, it is only an approximation and should be verified using Monte Carlo simulation. The time averaged RSS bounds for the orbiter mission are $\sigma_{\boldsymbol{r}_{sc},mrss} \approx 4\ km$ and $\sigma_{\dot{\boldsymbol{r}}_{sc},mrss} \approx 2\ m/s$. For the deep space mission, they are $\sigma_{\boldsymbol{r}_{sc},mrss} \approx 7.5\ km$ and $\approx 50\ cm/s$ except for the quadrature filter. This result seems to suggest that a more dynamic trajectory enhances the position estimate whereas a steadier trajectory enhances the velocity estimate.

Since X-ray millisecond pulsars are weaker when comparing to other X-ray pulsars, a folding time of 50 s in trial #2 and #4 would only accumulate around $10-50$ photons from the background and the source, so the CLT argument is not valid. However, empirical results show that the EKF can still process the folded signal without causing filter divergence. In trial #3, the folding time was increased to 500 s. In this case, the folded measurements are more Gaussian than trial #2, consequently the RSS errors of trial #3 are slightly lowered. However, this slight performance increase is achieved at the cost of higher computation time.

Since the quadrature filter RSS position bound for the deep space mission stays relatively flat as shown in Fig. 2.5, it is not suitable for deep space mission. From Table 2.3 and Table 2.4, one can see that $\sigma_{\dot{r}_{sc},mrss} > \sigma_{\boldsymbol{r}_{sc},rss}(t_0)$. This is caused by the increasing trend of $\sigma_{\boldsymbol{r}_{sc},rss}$ before $t = 0.38\ hr$. After the initial increase, $\sigma_{\boldsymbol{r}_{sc},rss}$ decreases monotonically, which indicates the quadrature filter is observable. In addition, the orbiter mission result also shows the quadrature filter is observable, so the fact that the position bound stays relatively flat for the deep space mission has to be related to the orbital trajectory. In a deep space mission, the system parameters vary slowly due to the low gravitational acceleration; therefore, time invariant observability analysis can be used to analyze the linearized system. The linearized

phase system is

$$F_{phase}(t) = \begin{bmatrix} 0 & I & 0 & 0 \\ * & 0 & 0 & 0 \\ 0 & 0 & 0 & 1 \\ 0 & 0 & 0 & 0 \end{bmatrix} \quad \boldsymbol{x} = \begin{bmatrix} \boldsymbol{r}_{sc} \\ \dot{\boldsymbol{r}}_{sc} \\ [\boldsymbol{\zeta}]_1 \\ [\boldsymbol{\zeta}]_2 \end{bmatrix} \tag{2.80}$$
$$H_{phase}(t) = \begin{bmatrix} * & 0 & * & 0 \end{bmatrix}.$$

Based on the form of $F_{phase}(t)$ and $H_{phase}(t)$, one can see that each pulsar measurement directly provides information about spacecraft position and pulsar timing noise. The velocity is estimated through internal coupling indicated by non-zero $[F_{phase}(t)]_{2,1}$. In short, the pulsar measurement behaves like a position measurement in the phase formulation.

Linearizing the quadrature system in Eq. (2.77) gives

$$F_{quad}(t) = \begin{bmatrix} 0 & I & 0 & 0 \\ * & 0 & 0 & 0 \\ 0 & * & F_1 & * \\ 0 & 0 & 0 & 0 \end{bmatrix} \quad \boldsymbol{x} = \begin{bmatrix} \boldsymbol{r}_{sc} \\ \dot{\boldsymbol{r}}_{sc} \\ \boldsymbol{q} \\ [\boldsymbol{\zeta}]_2 \end{bmatrix} \tag{2.81}$$
$$H_{quad}(t) = \begin{bmatrix} 0 & 0 & * & 0 \end{bmatrix}.$$

One can see that each pulsar measurement directly provides information about the quadrature components. The velocity is estimated through $[F_{quad}(t)]_{3,2}$. The position is estimated through the internal dynamics of the gravitational model indicated by the non-zero $[F_{quad}(t)]_{2,1}$. If $[F_{quad}(t)]_{2,1}$ were zero, then position is unobservable. In this formulation, the pulsar measurement behaves like a velocity measurement, which explains why velocity estimation error is smaller using this formulation. Based on this analysis, we argue that the quadrature filter is not suitable for deep space mission. The reason is that the spacecraft velocity is mostly unchanged due to small gravitational acceleration, i.e. small $[F_{quad}(t)]_{2,1}$, which means the spacecraft velocity is not sensitive to its position. As a result, it requires a significant amount of time for the filter to infer position from velocity.

The last two rows of Table 2.4 show the actual computation time and the normalized time with respect to the phase filter without epoch folding. The simulations were programmed

in Matlab and computed by a workstation with a 3.5GHz Intel Xeon E5-1650v3 CPU and 32GB of RAM. The time needed for the phase filters with epoch folding to complete signal processing is roughly 9% to 16% of that of the phase filter without epoch folding depending on the choice of Δt. Since the estimation results between the phase filters are comparable, epoch folding is a reasonable approach for reducing computation time for the above scenarios.

CHAPTER 3

Pulsar-Based Spacecraft Navigation: A Case Study

3.1 Overview

This chapter investigates the performance of pulsar-based spacecraft navigation using a Design Reference Mission (DRM). The trajectory of DAWN spacecraft was chosen for this study. The purpose of using a DRM is to consider a more realistic deep space mission scenario that requires sequential pulsar observation and subjects to significant process noises such as maneuver execution errors and clock errors. Section 3.2 and Section 3.3 discuss the DRM, spacecraft dynamics and pulsar model. Section 3.4 shows the state space model for the numerical simulation. A covariance analysis is included in Section 3.5, and simulation results are shown in Section 3.6.

3.2 Design Reference Mission

NASA launched DAWN in September 2007. Its mission is to travel to the asteroid belt using ion propulsion and to survey two large asteroids named Vesta and Ceres. Figure 3.1 shows the mission timeline from launch to completion. This spacecraft is equipped with three ion thrusters developed using proven technologies from Deep Space 1. These thrusters enable DAWN to enter and leave the orbits around Vesta and Ceres. After deploying its solar panels, DAWN has a wingspan of 19.7 m. The total mass of the spacecraft at the start of the mission is 1217 kg, which consists of a 747 kg spacecraft mass, 425 kg of xenon propellant and 46 kg of hydrazine propellant [50]. As indicated by Fig. 3.1, the spacecraft went through multiple coasting and thrusting segments.

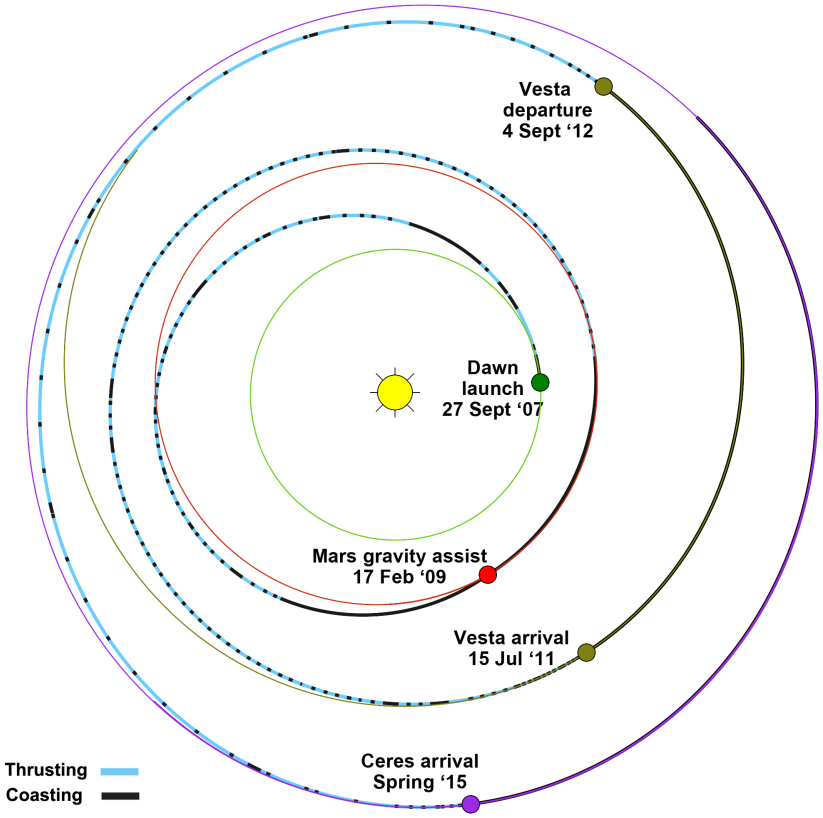

Figure 3.1: Complete Mission Trajectory [5]

The DAWN ephemeris file consists of 11 columns of data: XYZ position, XYZ velocity, XYZ thrust, time, and spacecraft mass. The starting date is 2454385 JED and the terminal date is 2455759 JED, where JED is Julian Ephemeris Day. These two dates correspond to the time of departure from Earth and time of arrival at Vesta respectively. The 3-dimensional trajectory from the ephemeris is plotted in Fig. 3.2, where the red star is the Sun. The red triangle is the start of the ephemeris file. The kink in the trajectory following by a large change in orbital inclination corresponds to the gravity assist at Mars on Feb. 17, 2009 (2454879.5 JED).

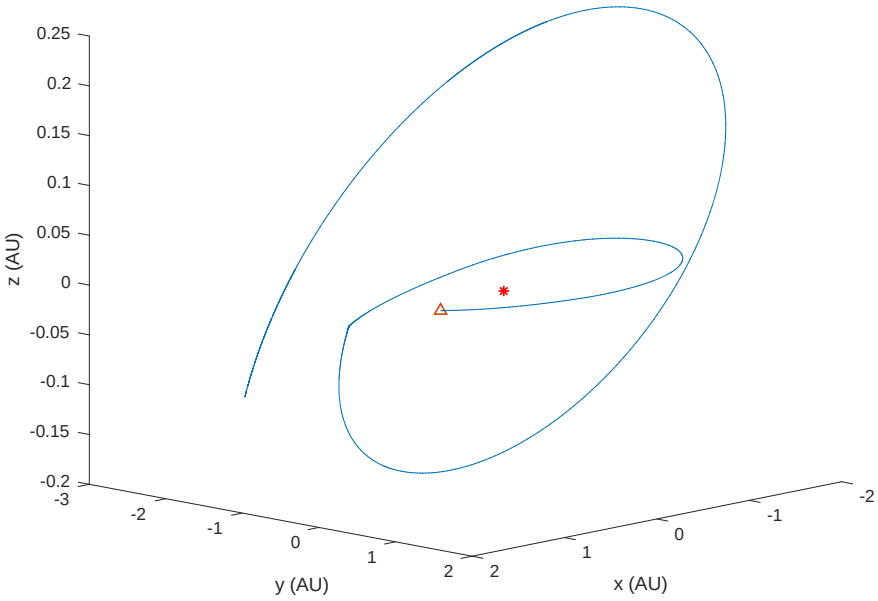

Figure 3.2: 3D heliocentric trajectory of DAWN from Earth to Vesta.

3.2.1 Spacecraft Dynamics

In order to use the ephemeris for the study while simplifying the dynamical model of the spacecraft, the following approximation was used. It was assumed that the spacecraft acceleration could be approximately modeled as

$$\ddot{\boldsymbol{r}}_{sc}(t) = -\frac{\mathcal{G}m_{\odot}}{\|\boldsymbol{r}_{sc}(t)\|^3}\boldsymbol{r}_{sc}(t) + \boldsymbol{d}(t) + \boldsymbol{u}(t), \tag{3.1}$$

where $\mathcal{G}$ is the gravitational constant; $m_{\odot}$ is the mass of the Sun; $\boldsymbol{r}_{sc}(t)$ is the spacecraft position relative to the Sun; $\boldsymbol{d}(t)$ is unknown residual acceleration; and $\boldsymbol{u}(t)$ is the commanded acceleration from the ion thrusters. Since the velocity of the spacecraft, $\dot{\boldsymbol{r}}_{sc}(t)$, is provided in the ephemeris file, numerical finite difference method was used to determine the approximate value for the left hand side of Eq. (3.1) denoted as $\ddot{\boldsymbol{r}}^{fd}_{sc}(t)$. Therefore, the unknown acceleration can be determined by solving Eq. (3.1) for $\boldsymbol{d}(t)$ and substituting in the finite differenced accelerations,

$$\boldsymbol{d}(t) = \ddot{\boldsymbol{r}}^{fd}_{sc}(t) + \frac{\mathcal{G}m_{\odot}}{\|\boldsymbol{r}_{sc}(t)\|^3}\boldsymbol{r}_{sc}(t) - \boldsymbol{u}(t). \tag{3.2}$$

This residual acceleration is treated as a deterministic term in numerical simulation and filter design. Figure 3.3 shows the duration of the thrusting and coasting segments of the

ephemeris in the top plot. The magnitude of $\boldsymbol{u}(t)$ is plotted in the middle plot and the last plot shows the magnitude of $\boldsymbol{d}(t)$. The large spike at around day 500 in the last plot is the Mars gravity assist. From the top plot, one can see that the typical coasting segment is between 7 to 8 hours and the thrusting segment is between 6 to 7 days. If the pulsar-based navigation system is only allowed to observe pulsars during coasting segments, then the spacecraft spends roughly 5% of the time for pulsar observation during its cruise to Vesta.

In addition to the above deterministic model, two stochastic acceleration disturbances are added. The first is $\boldsymbol{w}_r(t)$, which is a white disturbance with a constant Power Spectral Density (PSD) of W_r. The second disturbance, $\boldsymbol{w}_g(t)$, is also white and is a result of using the ion thrusters. In other words, if $\|\boldsymbol{u}(t)\| = 0$, then $\boldsymbol{w}_g(t) = 0$. The first component of $\boldsymbol{w}_g(t)$ is the disturbance in the thrusting direction and the two other components correspond to disturbances normal to the thrusting direction. The three components are modeled as uncorrelated with each other. The PSD of this disturbance is denoted as $W_g(t)$ and it is determined following the Gates method [51],

$$[W_g(t)]_{ii} = \frac{(\sigma_{fixed,i}\Delta t)^2 + (\sigma_{prop,i}\Delta V(t))^2}{\Delta t}, \tag{3.3}$$

where $i = 1, 2, 3$; $\Delta V(t) = \|\boldsymbol{u}(t)\|\Delta t$; and Δt is the integration time step. The symbol $[A]_{ij}$, means the i^{th} row and j^{th} component of the A matrix. If the argument is a vector, then only one index is provided. The Gates method separates the acceleration disturbance into a fixed part, $\sigma_{fixed,i}$, and a proportional part, $\sigma_{prop,i}$. The coefficient $\sigma_{fixed,i}$ models disturbances from the ion thrusters that are independent of the magnitude of the commanded acceleration in the i^{th} direction. The coefficient $\sigma_{prop,i}$ models disturbances that are proportional to the magnitude of the commanded acceleration. Adding $\boldsymbol{w}_r(t)$ and $\boldsymbol{w}_g(t)$ to Eq. (3.1) gives

$$\begin{aligned}\ddot{\boldsymbol{r}}_{sc}(t) = -\frac{\mathcal{G}m_{\odot}}{\|\boldsymbol{r}_{sc}(t)\|^3}\boldsymbol{r}_{sc}(t) + \boldsymbol{d}(t) + \boldsymbol{u}(t) \\ + \boldsymbol{w}_r(t) + G_g(t)\boldsymbol{w}_g(t),\end{aligned} \tag{3.4}$$

where $G_g(t)$ is a transformation matrix from the thruster frame to the inertial frame,

$$
\begin{aligned}
G_g(t) &= \begin{bmatrix} C_\alpha & -S_\alpha & 0 \\ S_\alpha & C_\alpha & 0 \\ 0 & 0 & 1 \end{bmatrix} \begin{bmatrix} C_\beta & 0 & S_\beta \\ 0 & 1 & 0 \\ -S_\beta & 0 & C_\beta \end{bmatrix} \\
\alpha(t) &= \operatorname{atan2}\left([\hat{\boldsymbol{u}}(t)]_2, [\hat{\boldsymbol{u}}(t)]_1\right) \\
\beta(t) &= -\operatorname{atan2}\left([\hat{\boldsymbol{u}}(t)]_3, \sqrt{[\hat{\boldsymbol{u}}(t)]_1^2 + [\hat{\boldsymbol{u}}(t)]_2^2}\right) \\
\hat{\boldsymbol{u}}(t) &= \frac{\boldsymbol{u}(t)}{\|\boldsymbol{u}(t)\|},
\end{aligned}
\tag{3.5}
$$

where $S_\alpha = \sin(\alpha(t))$ and $C_\alpha = \cos(\alpha(t))$. The thruster frame is defined such that the x-axis ($i = 1$) corresponds to the thrusting direction.

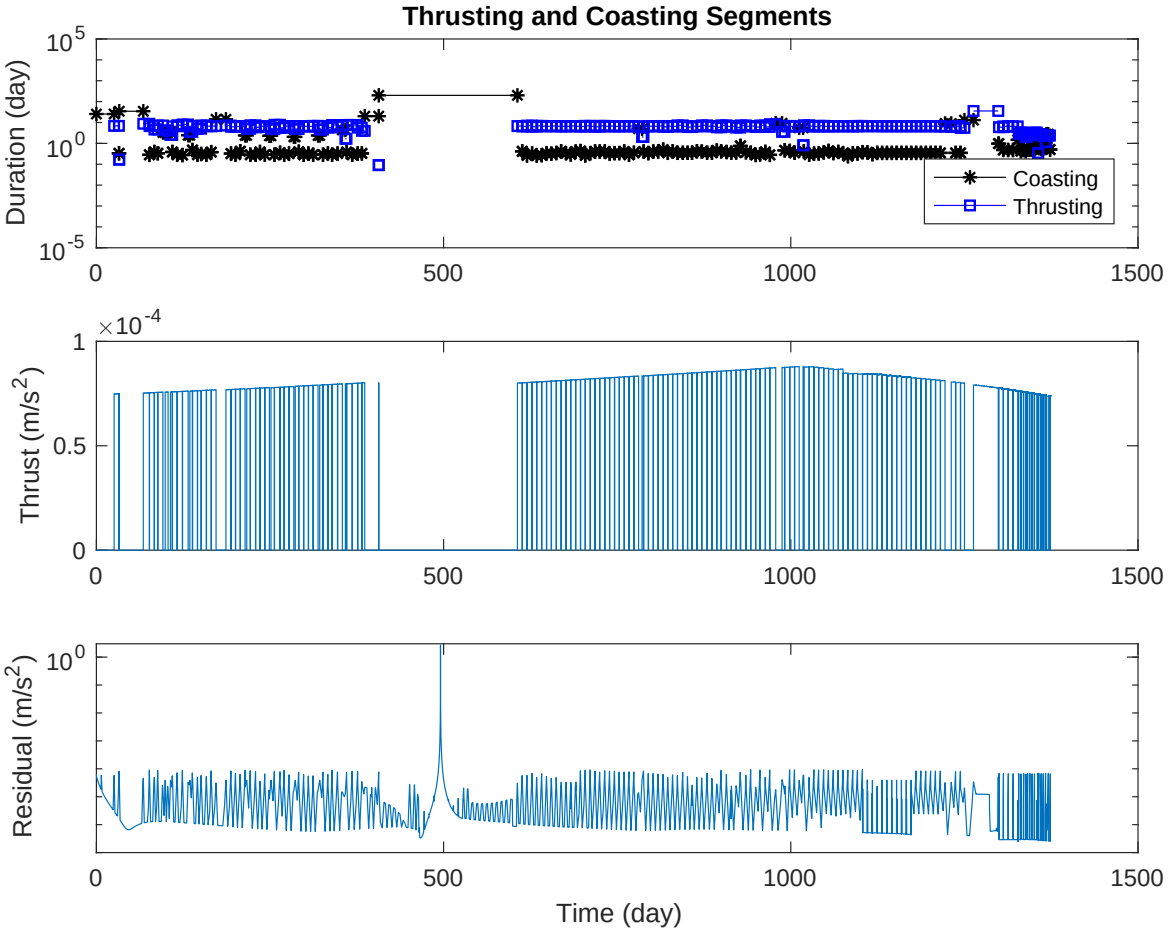

Figure 3.3: Thrust and coasting schedule.

3.3 Pulsar Model

Let the signal waveform of the pulsar at the Solar System Barycenter (SSB) be modeled as

$$\lambda(t) = \lambda_b + \lambda_s s(\phi(t)), \tag{3.6}$$

where λ_b is the background rate and λ_s is the source rate. The function $s(\cdot)$ is periodic and describes the pulsar signal profile. The phase equation is

$$\phi(t) = \phi_0 + \dot{\phi}(t - t_0), \tag{3.7}$$

where ϕ_0, $\dot{\phi}$ and t_0 are all known values. The measurement equation at the spacecraft is

$$y(t) = \lambda_b + \lambda_s s(\phi_{sc}(t)) + v(t). \tag{3.8}$$

In order to limit the scope of the study, only the geometric delay, $\boldsymbol{r}_{sc}(t)$, clock error, $t_c(t)$, and pulsar timing noise, $n_\eta(t)$, are modeled. Therefore, the phase equation at the spacecraft is

$$\phi_{sc}(t) = \phi_0 + \dot{\phi}\left[t + \frac{\boldsymbol{n}^T \boldsymbol{r}_{sc}(t)}{c} + t_c(t) - t_0\right] + n_\eta(t), \tag{3.9}$$

where $\boldsymbol{n}$ is the direction of the pulsar. The phase equation at the spacecraft is basically a phase shifted version of Eq. (3.7). The general time transfer is significantly more complex and requires Solar System and time ephemerides [26, 36, 52].

The statistical properties of the measurement noise, $v(t)$, depend on the pulsar observation frequency. If radio pulsars are used, then Gaussian process is used to model the measurement of the signal waveform. The measurement noise PSD, V, is given by the following radiometer equation [18].

$$V = \frac{T_{sys}^2}{G^2 n_p \Delta f}, \quad G = \frac{A a_\eta}{2k_B}, \quad \text{and} \quad A = \frac{\pi d^2}{4}, \tag{3.10}$$

where G is the antenna gain; T_{sys} is the system temperature; Δf is the system bandwidth; n_p is the number of polarization; d is the antenna diameter; a_η is antenna efficiency; A is the projected area; and k_B is Boltzmann constant. The corresponding measurement noise variance for the simulation is $\text{var}[v(t)] = V/\Delta\tau$, where $\Delta\tau$ is the sampling interval [44].

If X-ray pulsars are used as navigation beacons, then non-homogenous Poisson process is used to model the detection of the individual X-ray photon by an X-ray telescope [31]. Given a time interval, $\Delta\tau$, and the time at the beginning of the interval, t, the number of detected X-ray photons, $C(\tau)$, is modeled as a non-homogenous Poisson random variable The Poisson probability density function is

$$f\Big(N(t+\Delta\tau)-N(t)=C(\tau)|t,\Delta\tau\Big)=\frac{\Lambda(\tau)^{C(\tau)}}{C(\tau)!}e^{-\Lambda(\tau)}, \tag{3.11}$$

where

$$\Lambda\left(\tau\right)=\int_{t}^{t+\Delta\tau}\lambda(\sigma)\,d\sigma,\quad \tau=t+\frac{\Delta\tau}{2} \tag{3.12}$$

$N(t)$ represents the number of detected photon from an initial time, t_0, to t, and $\lambda(t)$ is the rate function associated with the random process. A special property of the Poisson process is that the expected number of photon over an interval is equal to its variance, i.e.

$$\begin{aligned} E[C(\tau)] &= \mathrm{var}[C(\tau)] \\ &= E[C(\tau)^2]-E[C(\tau)]^2 \\ &= \Lambda\left(\tau\right). \end{aligned} \tag{3.13}$$

The probability of detection is described by the strength of the rate function, $\lambda(t)$.

A typical X-ray photon detection system provides the actual detection time of a photon rather than photon rate measurement (intensity). Thus, the photon rate of the pulsar signal has to be approximated using bins. Thus, the measurement is $Y(\tau)=C(\tau)/\Delta\tau$, where $\Delta\tau$ is the size of the bin and it has to be sufficiently small in order to approximate the underlying rate function. Since the detection process is Poisson, the expected number of detected photons for each bin is $\Lambda(\tau)$. When $\Delta\tau$ is small, Eq. (3.12) can be approximated as $\Lambda(\tau)\approx\Big(\lambda_b+\lambda_s s(\phi_{sc}(\tau))\Big)\Delta\tau$. Taking the expectation of $Y(\tau)$ gives

$$\begin{aligned} E[Y(\tau)] &= \frac{E[C(\tau)]}{\Delta\tau} \\ &= \lambda_b+\lambda_s s(\phi_{sc}(\tau)). \end{aligned} \tag{3.14}$$

The measurement variance is

$$\begin{aligned} \mathrm{var}[Y(\tau)] &= \frac{E[C(\tau)^2]-E[C(\tau)]^2}{\Delta\tau^2} \\ &\approx \frac{\lambda_b+\lambda_s s(\phi_{sc}(t))}{\Delta\tau}. \end{aligned} \tag{3.15}$$

Since the expected measurement in Eq. (3.14) is the underlying rate function, Eq. (3.15) can also be interpreted as the measurement noise variance,

$$E[v(\tau)] = 0, \text{ and } \text{var}[v(\tau)] = \frac{\lambda_b + \lambda_s s(\phi_{sc}(\tau))}{\Delta\tau}. \tag{3.16}$$

Because of the form of Eq. (3.16), one can interpret the non-homogenous process as having a periodic PSD of $V(t) = \lambda_b + \lambda_s s(\phi_{sc}(t))$.

While millisecond pulsars have stable rotation dynamics, they are still corrupted by a small amount of fractional stationary noise whose PSD is

$$S_n(\omega) = \frac{W_\eta}{\left(1 + \left(\frac{\omega}{\omega_c}\right)^2\right)^\alpha}, \tag{3.17}$$

where W_r, α, and ω_c are positive fitting parameters [42]. They represent the strength of the white noise, the integration order, and the corner frequency of the fractional Linear Time Invariant (LTI) system. The parameters of Eq. (3.17) for various pulsars can be found in current literature [53]. The reason $S_n(\omega)$ is considered as a fractional PSD is because α is a real number. If $\alpha = 1.21$, then the slope of the high frequency roll-off in log-log plot is -2.42. This is different from the typical LTI system whose roll-off is an integer multiple of 2. The fractional PSD in Eq. (3.17) can be approximated by finite dimensional LTI system [54]. The approximated system is essentially a high order stable LTI system. Therefore, the pulsar timing noise in this study is modeled using a shaping filter with large correlation time,

$$\begin{aligned} \dot{\boldsymbol{\eta}}(t) &= F_\eta \boldsymbol{\eta}(t) + G_\eta w_\eta(t) \\ n_\eta(t) &= H_\eta \boldsymbol{\eta}(t) \end{aligned} \tag{3.18}$$

where F_η is a stable matrix.

3.4 Navigation System

It is assumed that the spacecraft carries a clock whose error model is

$$\begin{aligned}\begin{bmatrix}\dot{t}_c(t)\\ \dot{b}_c(t)\end{bmatrix} &= \underbrace{\begin{bmatrix}0 & 1\\ 0 & 0\end{bmatrix}}_{F_c}\underbrace{\begin{bmatrix}t_c(t)\\ b_c(t)\end{bmatrix}}_{\boldsymbol{t}_c} + \underbrace{\begin{bmatrix}1 & 0\\ 0 & 1\end{bmatrix}}_{G_c}\boldsymbol{w}_c(t)\\ t_c(t) &= \underbrace{\begin{bmatrix}1 & 0\end{bmatrix}}_{H_c}\begin{bmatrix}t_c(t)\\ b_c(t)\end{bmatrix},\end{aligned} \tag{3.19}$$

where $t_c(t)$ is the clock bias and $b_c(t)$ is the clock drift [9]. Combining Eq. (3.4) with Eq. (3.8), Eq. (3.18), and Eq. (3.19) gives the state space model for this study,

$$\begin{bmatrix}\dot{\boldsymbol{r}}_{sc}(t)\\ \ddot{\boldsymbol{r}}_{sc}(t)\\ \dot{\boldsymbol{t}}_c(t)\\ \dot{\boldsymbol{\eta}}_p(t)\end{bmatrix} = \begin{bmatrix}\dot{\boldsymbol{r}}_{sc}(t)\\ -\frac{\mathcal{G}m_\odot}{\|\boldsymbol{r}_{sc}(t)\|^3}\boldsymbol{r}_{sc}(t) + \boldsymbol{d}(t) + \boldsymbol{u}(t)\\ F_c\boldsymbol{t}_c(t)\\ F_{\eta,p}\boldsymbol{\eta}_p(t)\end{bmatrix} + \begin{bmatrix}0 & 0 & 0 & 0\\ I & G_g(t) & 0 & 0\\ 0 & 0 & G_{t_c} & 0\\ 0 & 0 & 0 & G_{\zeta,p}\end{bmatrix}\begin{bmatrix}\boldsymbol{w}_r(t)\\ \boldsymbol{w}_g(t)\\ \boldsymbol{w}_c(t)\\ \boldsymbol{w}_{\eta,p}(t)\end{bmatrix} \tag{3.20}$$

$$y_p(\tau_j) = \lambda_{b,p} + \lambda_{s,p}s_p(\phi_{sc,p}(\tau_j)) + v_p(\tau_j).$$

The phase equation at the spacecraft is

$$\phi_{sc,p}(\tau_j) = \phi_{0,p} + \dot{\phi}_p\left[\tau_j - t_0 + \frac{\boldsymbol{n}_p^T\boldsymbol{r}_{sc}(\tau_j)}{c} + H_c\boldsymbol{t}_c(\tau_j)\right] + H_{\eta,p}\boldsymbol{\eta}_p(\tau_j), \tag{3.21}$$

where $p = 1...N_p$ and N_p is the number of observed pulsars. The measurement noise variance is given by Eq. (3.16). The navigation system is formulated using continuous time dynamics and discrete time measurement. The measurement is $y_p(\tau_j)$ and the state vector is

$$\boldsymbol{x} = \begin{bmatrix}\boldsymbol{r}_{sc}(t) & \dot{\boldsymbol{r}}_{sc}(t) & \boldsymbol{t}_c(t) & \boldsymbol{\eta}_p(t)\end{bmatrix}^T. \tag{3.22}$$

The time correlations of the process noises are

$$\begin{aligned}E[\boldsymbol{w}_r(t)\boldsymbol{w}_r^T(\tau)] &= W_r\delta(t-\tau)\\ E[\boldsymbol{w}_g(t)\boldsymbol{w}_g^T(\tau)] &= W_g(t)\delta(t-\tau)\\ E[\boldsymbol{w}_c(t)\boldsymbol{w}_c^T(\tau)] &= W_c\delta(t-\tau)\\ E[\boldsymbol{w}_{\eta,p}(t)\boldsymbol{w}_{\eta,p}^T(\tau)] &= W_{\eta,p}\delta(t-\tau).\end{aligned} \tag{3.23}$$

3.5 Covariance Analysis

As shown by Eq. (3.20), the general navigation problem has nonlinear dynamics and measurements. The measurement function is given in terms of pulsar parameters such as frequency, direction, intensity and waveform profile. The measurement noise covariance is also related to the pulsar parameters as shown in Section 3.3. Due to the measurement nonlinearity, the impact of individual pulsar parameter on the overall navigation accuracy is not obvious. Therefore, this section uses linearized covariance analysis to develop a few intuitions.

3.5.1 X-ray Based vs. Radio Based Pulsar Timing System

Let the timing accuracy of the X-ray based system due to photon noise (non-homogenous Poisson process) and the timing accuracy of the radio based system due to radiometer noise (Gaussian process) be defined as σ_{xr}^2 and σ_{rf}^2 respectively. In this analysis, the system parameters of the Neutron star Interior Composition ExploreR Mission (NICER) is used [55]. For the X-ray based system, the uncertainty is quantified using the Cramér-Rao Lower Bound [31],

$$\sigma_{xr}^2 = \frac{1}{\tilde{\lambda}_{s,xr}^2 T_{obs} \dot{\phi}^2} \left[\int_0^1 \frac{s'(\varphi)^2}{\tilde{\lambda}_{b,xr} + \tilde{\lambda}_{s,xr} s(\varphi)} d\varphi \right]^{-1}, \tag{3.24}$$

where

$$\tilde{\lambda}_{b,xr} = \frac{\lambda_{b,xr} N_e}{56}, \quad \text{and} \quad \tilde{\lambda}_{s,xr} = \frac{\lambda_{s,xr} N_e}{56}. \tag{3.25}$$

The parameter T_{obs} is the observation time; $\dot{\phi}$ is the pulsar frequency; N_e is the number of NICER telescope element; $\lambda_{s,xr}$ is the X-ray signal intensity; and $\lambda_{b,xr}$ is the background intensity for the 56 element NICER telescope. Note the number of NICER element is proportional to the detector area, so $N_e \propto A$.

On the other hand, the timing uncertainty of the radio based system is obtained using Eq. (3.10) and the covariance analysis result in [56],

$$\sigma_{rf}^2 = \frac{V}{2\pi^2 \lambda_{s,rf}^2 T_{obs} \dot{\phi}^2} \left[\sum_{j=1}^{N_f} j^2 \left(a_j^2 + b_j^2 \right) \right]^{-1}, \tag{3.26}$$

Table 3.1: Parameters for the Comparison

	J0347-4715	J1939+2134	J2124-3358
$\lambda_{s,rf}$ (mJy)	149	13.2	3.6
$\lambda_{b,xr}$ (ph/s)	0.62	0.24	0.20
$\lambda_{s,xr}$ (ph/s)	0.283	0.029	0.074
$\dot{\phi}$ (Hz)	174	641	203
a_η		0.6	
n_p		1	
Δf (MHz)		500	
T_{sys} (K)		30	

where V is the PSD of the radiometer noise; $\lambda_{s,rf}$ is the signal intensity; a_j and b_j are the Fourier coefficients describing the signal profile; and N_f is the number of Fourier series terms. The pulsar and system parameters used in the comparison are listed in Table 3.1. The pulsar profiles can be obtained from current literature and online database [8, 57]. From Eq. (3.10), $V \propto 1/A^2$. As a result, if the antenna size is not a factor of consideration, then radio based system is more effective at achieving high timing accuracy because $\sigma_{rf}^2 \propto 1/A^2$ whereas $\sigma_{xf}^2 \propto 1/A$.

Solving Eq. (3.24) for T_{obs} gives an expression for the required observation time in terms of antenna size, pulsar parameters and timing accuracy for the X-ray based system. Performing the same operation to Eq. (3.26) gives an analogous expression for the radio based system. Figure 4.9, Fig. 3.5 and Fig. 3.6 plot the two resulting expressions for three different millisecond pulsars. These plots are comparing the impact of the measurement noise on timing accuracy. The black solid line in all three plots indicates the required observation time for the 56 element NICER system to achieve a timing accuracy of 1 μs. Therefore, the intersection of the black curve and the 1 μs blue curve indicates the required radio antenna size to achieve the same timing accuracy. From the plots, the required radio antenna diameters to achieve the same performance as the 56 element NICER system are 4 m, 17 m and 19 m for $J0437-4715$, $J1939+2134$ and $J2124-3358$ respectively. The required radio

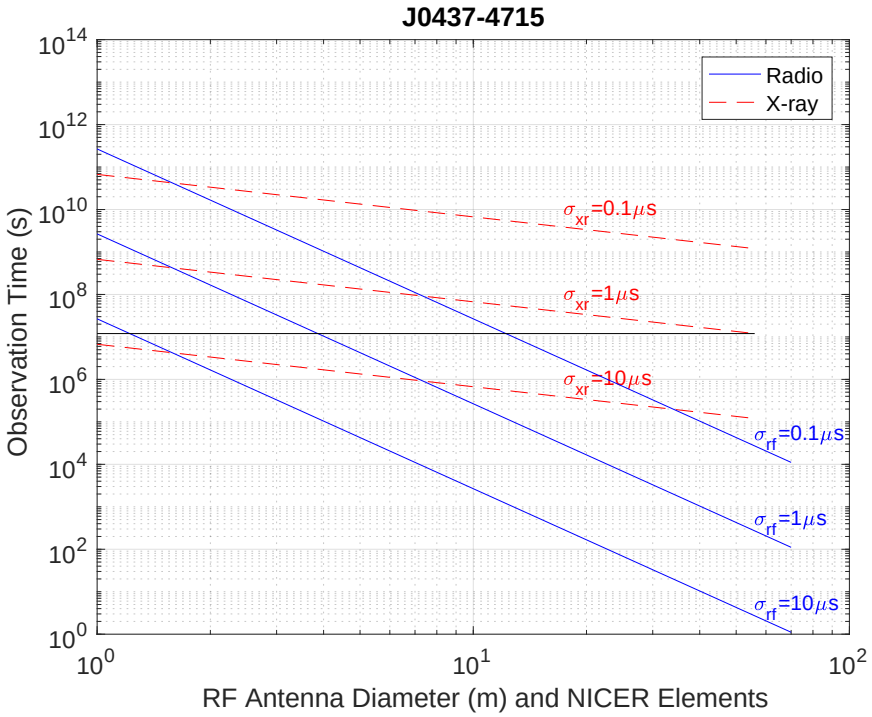

Figure 3.4: Required observation time for a given timing accuracy and detector size for J0437-4715.

antenna diameter for $J0437-4715$ is much smaller than the other two pulsars because its intensity in the radio frequency is much higher. Unfortunately, out of all known millisecond pulsars only $J0437-4715$ emits radio signal on the order of 100 mJy at 1.4 GHz. Since the minimum number of pulsars needed for navigation in the absence of clock error is 3, a relatively large radio antenna is needed to achieve comparable accuracy as the X-ray based system.

3.5.2 Navigation Accuracy for Pseudo-Periodic Thrusting Schedule

Continuing the development from the previous section, this section considers the covariance analysis for the 3-dimensional navigation problem. From the ephemeris of DAWN, it is clear that the use of ion thrusters results in a pseudo-periodic thrusting schedule. The typical thrusting segment lasts several days and is followed by a few hours of coasting. Similar to the DAWN simulation in the previous section, it is assumed that the spacecraft is only

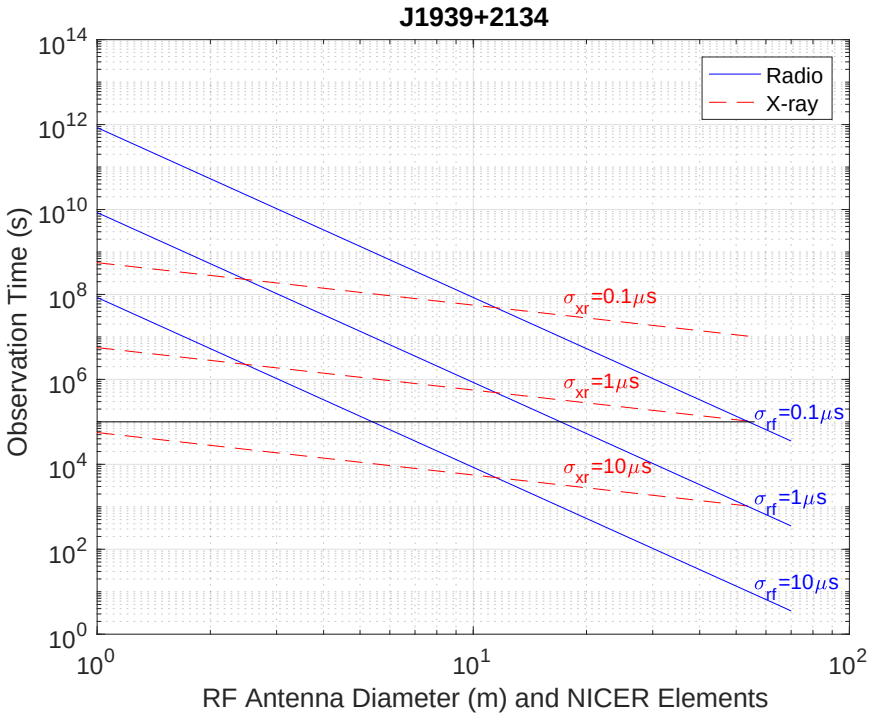

Figure 3.5: Required observation time for a given timing accuracy and detector size for J1939+2134.

allowed to observe pulsars sequentially during coasting segment. However, instead of using Eq. (3.4) as the system model, a double integrator system is used to simplify the analysis. Let the state space system be

$$\begin{aligned} \dot{\boldsymbol{r}}_{sc}(t) &= F\boldsymbol{r}_{sc}(t) + G\boldsymbol{w}(t) + G\boldsymbol{u}(t) \\ y_p(t) &= h_p(t, \boldsymbol{r}_{sc}) + v_p(t), \end{aligned} \tag{3.27}$$

where $\boldsymbol{r}_{sc}(t)$ is the spacecraft position vector; $\boldsymbol{u}(t)$ is the ion thruster input; $\boldsymbol{w}(t)$ is the ion thruster process noise; and $v_p(t)$ is measurement nosie. The system matrices and measurement functions are

$$\begin{aligned} F &= \begin{bmatrix} 0 & I_{3x3} \\ 0 & 0 \end{bmatrix}, \quad G = \begin{bmatrix} 0 \\ I_{3x3} \end{bmatrix} \\ h_p(t, \boldsymbol{r}_{sc}) &= \lambda_{b,p} + \lambda_{s,p} s_p(\phi_{sc,p}(t)) \\ \phi_{sc,p}(t) &= \phi_{0,p} + \dot{\phi}_p \left[t + \frac{\boldsymbol{n}_p^T \boldsymbol{r}_{sc}(t)}{c} - t_{0,p} \right], \end{aligned} \tag{3.28}$$

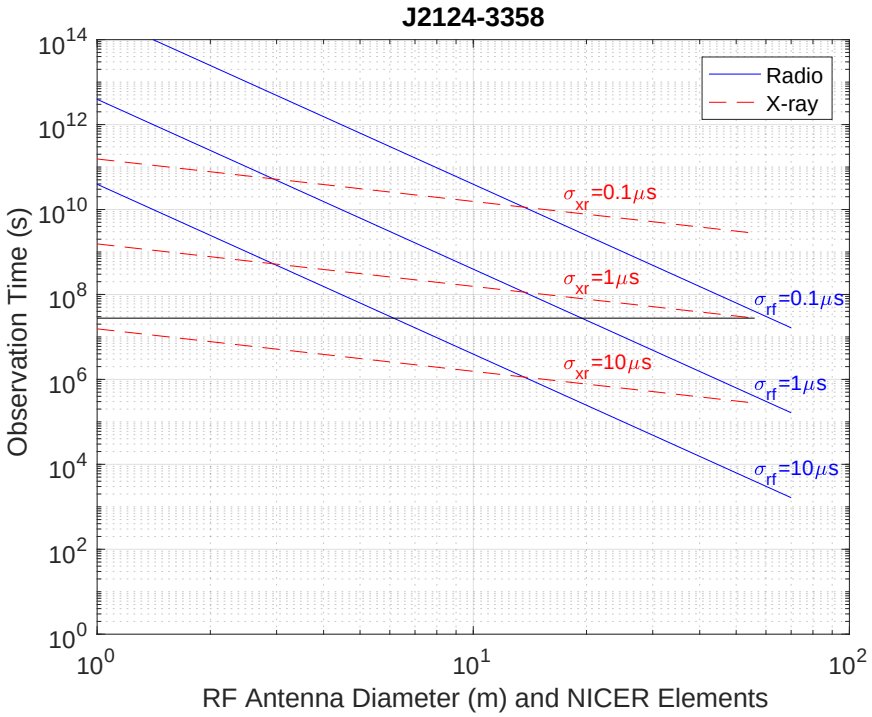

Figure 3.6: Required observation time for a given timing accuracy and detector size for J2124-3358.

where $\lambda_{b,p}$ is background signal intensity; $\lambda_{s,p}$ is pulsar signal intensity; $s_p(\cdot)$ is a periodic function; $\boldsymbol{n}_p$ is the pulsar direction; $\dot{\phi}_p$ is the pulsar frequency; and p is the pulsar index. This system has linear dynamics and nonlinear measurement $y_p(t)$.

The process noise PSD, $W(t)$, and the thrust $\boldsymbol{u}(t)$ are assumed to be constant during the thrusting segment. During the coasting segment, $\boldsymbol{u}(t) = 0$ and $W(t) = 0$. Assuming an EKF is used to process pulsar waveform measurements, then the error covariance is governed by the Ricatti equation,

$$\begin{aligned} \dot{P}(t) &= FP(t) + P(t)F^T + GW(t)G^T - PH^T(t)V^{-1}(t)H(t)P(t) \\ P(t_0) &= P_0, \end{aligned} \tag{3.29}$$

where

$$H(t) = \begin{bmatrix} h_1'(\phi_{sc,p}(t)) & 0 & 0 \\ 0 & \ddots & 0 \\ 0 & 0 & h_p'(\phi_{sc,p}(t)) \end{bmatrix} \begin{bmatrix} \dot{\phi}_1 \frac{\boldsymbol{n}_1^T}{c} & 0 \\ \vdots & \vdots \\ \dot{\phi}_p \frac{\boldsymbol{n}_p^T}{c} & 0 \end{bmatrix} \tag{3.30}$$

$$V(t) = \text{diag}([V_1(t), \ldots, V_p(t)]),\ p = 1, \ldots, N_p.$$

The phase, $\phi_{sc,p}(t)$, is evaluated along the true trajectory. Since there is no pulsar observation during thrusting segment and no thrusting during pulsar observation, the differential Ricatti equation in Eq. (3.29) reduces to two Lyapunov differential equations. Let the time axis be partitioned as follows:

1. If t is between t_i and t_{i+1}, where i is 0 or even, then this segment is defined as the thrusting segment.

2. If t is between t_i and t_{i+1}, where i is odd, then this segment is defined as the coasting segment.

Using the above partition, the Lyapunov differential equation for the thrusting segment is

$$\dot{M}(t) = FM(t) + M(t)F^T + GW(t_i)G^T, \tag{3.31}$$

where the initial condition is $M(t_i) = P(t_i)$. The solution for Eq. (3.31) is

$$M(t_{i+1}) = \Phi_{thr}(t_i)M(t_i)\Phi_{thr}^T(t_i) + \begin{bmatrix} \frac{W(t_i)}{3} t_i^{thr\,3} & \frac{W(t_i)}{2} t_i^{thr\,2} \\ \frac{W(t_i)}{2} t_i^{thr\,2} & W(t_i) t_i^{thr} \end{bmatrix}, \tag{3.32}$$

where

$$\Phi_{thr}(t_i) = \begin{bmatrix} I_{3x3} & I_{3x3} t_i^{thr} \\ 0 & I_{3x3} \end{bmatrix} \tag{3.33}$$

and $W(t_i)$ is the noise PSD for the i^{th} segment. The error covariance at the end of the thrusting segment is $P(t_{i+1}) = M(t_{i+1})$. The thrusting duration is $t_i^{thr} = t_{i+1} - t_i$, where i is 0 or even. Because of the process noise, the increase in position error bound is proportional to $\sqrt{t^3}$ while the velocity error bound is proportional to $\sqrt{t}$.

The Lyapunov differential equation for the coasting segment is

$$\dot{X}(t) = -F^T X(t) - X(t)F(t) + H^T(t)V^{-1}(t)H(t), \tag{3.34}$$

where the initial condition is $X(t_i) = P^{-1}(t_i)$. Since there is no process noise, $\boldsymbol{w}(t)$, or thruster input, $\boldsymbol{u}(t)$, during the coasting segment, the spacecraft trajectory during this segment has constant velocity, i.e., $\boldsymbol{r}_{sc}(t) = \boldsymbol{r}_{sc}(t_i) + \dot{\boldsymbol{r}}_{sc}(t_i)(t - t_i)$. Therefore, the phase equation is

$$\phi_{sc,p}(t) = f_{s,p}(t_i)t + \psi_p(t_i), \tag{3.35}$$

where the frequency and the constant phase offset are

$$\begin{aligned} f_{s,p}(t_i) &= \dot{\phi}_p \left[1 + \frac{\boldsymbol{n}_p^T \dot{\boldsymbol{r}}_{sc}(t_i)}{c}\right] \\ \psi_p(t_i) &= \phi_{0,p} + \dot{\phi}_p \left[\frac{\boldsymbol{n}_p^T \left[\boldsymbol{r}_{sc}(t_i) - \dot{\boldsymbol{r}}_{sc}(t_i)t_i\right]}{c} - t_{0,p}\right]. \end{aligned} \tag{3.36}$$

The form of Eq. (3.35) implies that the pulsar signals have constant frequencies and constant phase offsets during coasting segments. The coasting duration can be partitioned into multiple pulsar observations,

$$t_i^{coast} = t_{i+1} - t_i = \sum_{p=1}^{N_p} t_{i,p}^{obs}, \tag{3.37}$$

where i is an odd integer. The pulsar observation duration is $t_{i,p}^{obs} = t_{i,p}^e - t_{i,p}^s$, where $t_{i,p}^s$ and $t_{i,p}^e$ are the observation starting and ending times for the p^{th} pulsar in the i^{th} time segment. Let $t_i = t_{i,1}^s$, and $t_{i+1} = t_{i,N_p}^e = t_{i,N_p+1}^s$, then the solution for Eq. (3.34) can be written as

$$X(t_{i,p+1}^s) = \Phi_{obs}(t_{i,p}^s) X(t_{i,p}^s) \Phi_{obs}^T(t_{i,p}^s) + Q(t_{i,p}^s) \tag{3.38}$$

for $p = 1, \ldots, N_p$, where

$$\begin{aligned} Q(t_{i,p}^s) &= \dot{\phi}_p^2 \int_{t_{i,p}^s}^{t_{i,p+1}^s} \frac{{h_p'}^2(\phi_{sc,p}(t))}{V_p(t)} \begin{bmatrix} \frac{\boldsymbol{n}_p \boldsymbol{n}_p^T}{c^2} & -\frac{\boldsymbol{n}_p \boldsymbol{n}_p^T}{c^2}(t_{i,p+1}^s - t) \\ -\frac{\boldsymbol{n}_p \boldsymbol{n}_p^T}{c^2}(t_{i,p+1}^s - t) & \frac{\boldsymbol{n}_p \boldsymbol{n}_p^T}{c^2}(t_{i,p+1}^s - t)^2 \end{bmatrix} dt \\ &= \dot{\phi}_p^2 \int_0^{t_{i,p}^{obs}} \frac{{h_p'}^2(\phi_{sc,p}(t_{i,p+1}^s - \tau))}{V_p(t_{i,p+1}^s - \tau)} \begin{bmatrix} \frac{\boldsymbol{n}_p \boldsymbol{n}_p^T}{c^2} & -\frac{\boldsymbol{n}_p \boldsymbol{n}_p^T}{c^2}\tau \\ -\frac{\boldsymbol{n}_p \boldsymbol{n}_p^T}{c^2}\tau & \frac{\boldsymbol{n}_p \boldsymbol{n}_p^T}{c^2}\tau^2 \end{bmatrix} d\tau, \end{aligned} \tag{3.39}$$

and

$$\Phi_{obs}(t^s_{i,p}) = \begin{bmatrix} I_{3x3} & 0 \\ -I_{3x3}t^{obs}_{i,p} & I_{3x3} \end{bmatrix}. \tag{3.40}$$

Note the change in integration variable, $\tau = t^e_{i,p} - t$, in Eq. (3.39).

If radio pulsars are used, then $V_p(t)$ is a constant representing the Gaussian radiometer noise PSD. If X-ray pulsars are used, then $V_p(t) = \lambda_{b,p} + \lambda_{s,p}s_p(\phi_{sc,p}(t))$ for non-homogenous Poisson process. If the observation time is much larger than the signal period ($t^{obs}_{i,p} \gg 1/f_{s,i,p}$), then the integrals in Eq. (3.39) can be approximated using the following expressions [31],

$$\begin{aligned} \int_0^{t^{obs}_{i,p}} \frac{{h'_p}^2(\phi_{sc,p}(T-\tau))}{V_p(T-\tau)} d\tau &\approx t^{obs}_{i,p} I_p \\ \int_0^{t^{obs}_{i,p}} \frac{\tau {h'_p}^2(\phi_{sc,p}(T-\tau))}{V_p(T-\tau)} d\tau &\approx \frac{{t^{obs}_{i,p}}^2}{2} I_p \\ \int_0^{t^{obs}_{i,p}} \frac{\tau^2 {h'_p}^2(\phi_{sc,p}(T-\tau))}{V_p(T-\tau)} d\tau &\approx \frac{{t^{obs}_{i,p}}^3}{3} I_p, \end{aligned} \tag{3.41}$$

where

$$I_p = \int_0^1 \frac{\lambda^2_{s,p}{s'_p}^2(\theta)}{V_p(\theta)} d\theta, \tag{3.42}$$

and T is a constant time offset. The above approximation is only valid for signals with constant frequencies. Substituting Eq. (3.41) into Eq. (3.38) gives

$$X(t^s_{i,p+1}) \approx \Phi_{obs}(t^s_{i,p}) X(t^s_{i,p}) \Phi^T_{obs}(t^s_{i,p}) + \dot{\phi}^2_p I_p \begin{bmatrix} \frac{\boldsymbol{n}_p \boldsymbol{n}_p^T}{c^2} t^{obs}_{i,p} & -\frac{\boldsymbol{n}_p \boldsymbol{n}_p^T}{c^2} \frac{{t^{obs}_{i,p}}^2}{2} \\ -\frac{\boldsymbol{n}_p \boldsymbol{n}_p^T}{c^2} \frac{{t^{obs}_{i,p}}^2}{2} & \frac{\boldsymbol{n}_p \boldsymbol{n}_p^T}{c^2} \frac{{t^{obs}_{i,p}}^3}{3} \end{bmatrix}. \tag{3.43}$$

The error covariance at the end of each coasting segment is $P(t_{i+1}) = X^{-1}(t^s_{i,N_p+1})$. Since $X(t)$ is the information matrix, intuitively one would like to choose pulsars and observation schedule to maximize $X(t)$. Therefore, the navigation pulsars should have high signal frequency and large I_p. From Eq. (3.42), I_p is large when the signal-to-noise ratio is high. The impact of the pulsar waveform profile is also accounted by the integral. Longer observation duration also improves the navigation accuracy. The impact of the pulsar geometry on the

Table 3.2: Radio Pulsar Parameters [7]

Order	Pulsar	$\lambda_b\ (Jy)$	$\lambda_s\ (Jy)$	$\dot{\phi}\ (Hz)$	RA (°)	DEC (°)
1	J0437-4715	686	0.1490	173.7	69.32	−47.25
2	J0711-6830	686	0.0032	182.1	107.98	−68.51
3	J1045-4509	686	0.0027	133.8	161.46	−45.17
4	J1713+0747	686	0.0102	218.8	258.46	7.79
5	J1939+2134	686	0.0132	641.9	294.91	21.58
RA is right ascension and DEC is declination of the celestial coordinate system						

information matrix is more difficult to recognize, so it is necessary to evaluate Eq (3.43) numerically.

Equation (3.31) and Eq. (3.43) can be evaluated in an alternating manner to compute the error covariance of the EKF for the system in Eq. (3.27). The thrusting and observation schedule used in the following analysis consists of 5 thrusting segments and 4 coasting segments. Each thrusting segment is 7 days and each coasting segment is 8 hours. In other words, thrusting duty cycle is 95%. Gates parameters for the process noise are $\sigma_{fixed,i} = 0$ and $\sigma_{prop,i} = 0.87\%$ for $i = 1, 2, 3$. The acceleration magnitude over each thrusting segment is constant at $8 \times 10^{-5}\ m/s^2$. Each system observes 5 different pulsars sequentially following the order in Table 3.2 and Table 3.3. The observation duration for each pulsar is 1 hour. The pulsar parameters are listed in Table 3.2 and Table 3.3. The radiometer noise PSD is calculated using the system parameters in Table 3.1 and Eq. (3.10), where the antenna diameter is 16 m. The initial XYZ position and XYZ velocity bounds are 50 km and 0.01 m/s respectively.

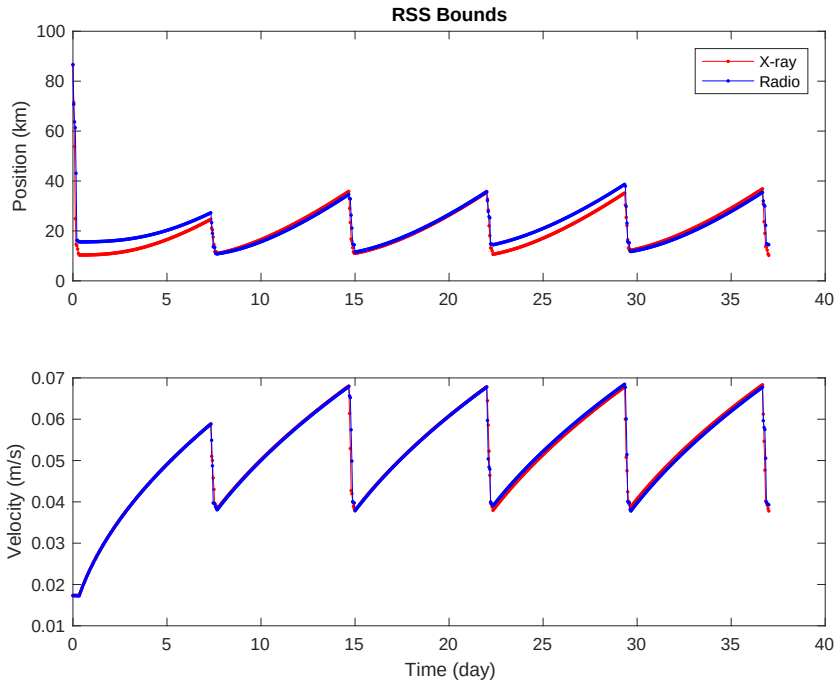

Figure 3.7: Covariance analysis for pseudo-periodic thrusting schedule.

The analysis result is plotted in Fig. 3.7. Because the thrusting and observation segments tend to increase and decrease the error bounds respectively, the position error variance exhibits a pseudo-periodic pattern. Therefore, it is necessary to have sufficient observation time to keep the error bounds to within ± 0.5 *cyc* of the wavelength of the fastest pulsar. In this analysis, the radio antenna is sized such that the radio based system has a similar performance as the X-ray based system. Once the system is in a periodic steady state, the Root-Sum-Square (RSS) position bounds for both systems at the start of the coasting segment are approximately 34 km. At the end of the coasting segment they reduced to approximately 12 km. This pattern repeats for every thrusting and coasting pair.

3.6 Numerical Simulation

3.6.1 Estimation Algorithm

The estimation algorithm used in this study is a modified version of the Extended Kalman Filter (EKF) with epoch folding and multirate processing [56]. The filter operation can be

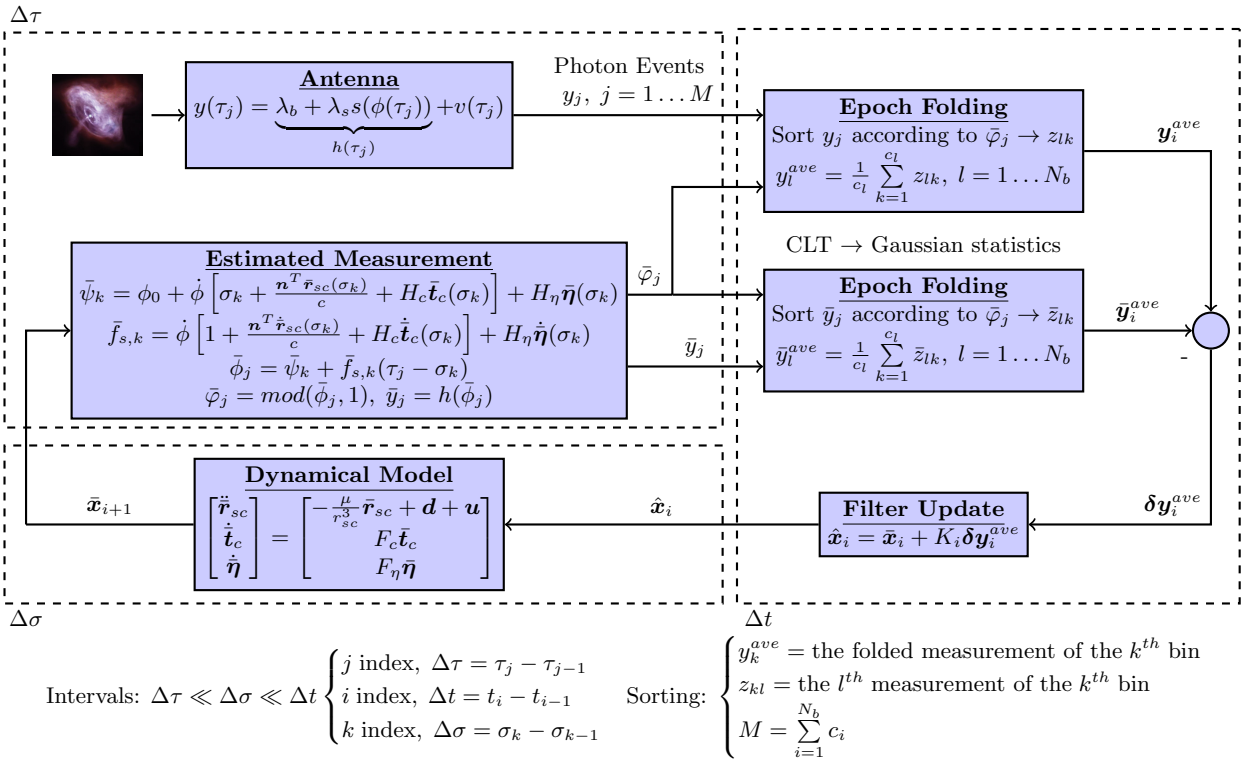

Figure 3.8: Algorithm block diagram

separated into three time intervals: epoch folding interval, Δt, integration interval, $\Delta\sigma$, and measurement sample interval, $\Delta\tau$. These parameters are essentially tuning parameters and they are chosen according to the trajectory of the spacecraft. The estimator architecture is shown in Fig. 3.8. Even though this algorithm was developed for X-ray pulsar, it is also applicable to radio pulsars as long as the first and second moments of the noise process are available.

3.6.2 Simulation Parameters

It is assumed that the spacecraft carries a X-ray detector similar to the 56 element NICER X-ray telescope; the pulsar parameters for Eq. (3.20) are listed in Table 3.3. The dynamics of the pulsar timing noise is a first order lag with a time constant of 17 years to simulate the slow varying behavior. The PSD of the input noise is $W_{\eta,p} = 9.4 \times 10^{-5}\ s^2/s$. The PSD of the clock process noise is $W_c = \text{diag}[1.6 \times 10^{-21}\ s^2/s,\ 1.0 \times 10^{-32}\ s^2/s^3]$ [49, 48]. The persistent white acceleration disturbance has a PSD of $W_r = \text{diag}[10^{-24},\ 10^{-24},\ 10^{-24}]\ km^2/s^3$. The

Table 3.3: X-ray Pulsar Parameters [7, 8]

Order	Pulsar	λ_b (ph/s)	λ_s (ph/s)	$\dot{\phi}$ (Hz)	RA (°)	DEC (°)
1	J0437-4715	0.62	0.283	173.7	69.32	−47.25
2	J0030+0451	0.20	0.193	205.5	7.61	4.86
3	J2124-3358	0.20	0.074	202.8	321.18	−33.98
4	J0218+4232	0.20	0.082	430.5	34.53	42.54
5	B1821-24	0.22	0.093	327.9	270.4	−24.87
RA is right ascension and DEC is declination of the celestial coordinate system						

strength of the ion thruster disturbance, $W_g(t)$, is set according to Eq. (3.3), where

$$\begin{aligned} \sigma_{fixed,i} &= 0 \text{ for } i = 1,2,3 \\ \sigma_{prop,i} &= \begin{cases} 0.5\% & \text{for } i = 1 \\ 8.7\ mrad & \text{for } i = 2,3 \end{cases}. \end{aligned} \tag{3.44}$$

3.6.3 Simulation Result

The initial conditions for the true spacecraft position and velocity are randomly generated according to a Gaussian distribution around the values, $\bar{\boldsymbol{r}}_{sc}(t_0)$ and $\dot{\bar{\boldsymbol{r}}}_{sc}(t_0)$, from the DAWN ephemeris. The EKF is initialized using the mean value. The initial error covariance matrix is

$$P(t_0) = \text{diag}\left[P_{\boldsymbol{r}_{sc}}(t_0) \quad P_{\dot{\boldsymbol{r}}_{sc}}(t_0) \quad P_{\boldsymbol{t}_c}(t_0) \quad P_{\boldsymbol{\eta}}(t_0)\right], \tag{3.45}$$

where

$$\begin{aligned} P_{\boldsymbol{r}_{sc}}(t_0) &= 2500 I_{3x3}\ (km^2) \\ P_{\dot{\boldsymbol{r}}_{sc}}(t_0) &= 1.22 \times 10^{-10} I_{3x3}\ (km^2/s^2) \\ P_{\boldsymbol{t}_c}(t_0) &= \text{diag}[2.5 \times 10^{-9}\ (s^2),\ 10^{-20}\ (s^2/s^2)] \\ P_{\boldsymbol{\eta}}(t_0) &= 2.5 \times 10^{-12} I_{5x5}\ (s^2). \end{aligned} \tag{3.46}$$

The initial velocity covariance is scaled according to the initial position covariance, the mean position vector, and the mean velocity vector,

$$[P_{\dot{\boldsymbol{r}}}(t_0)]_{ii} = [P_{\boldsymbol{r}}(t_0)]_{ii} \left(\frac{\|\dot{\bar{\boldsymbol{r}}}(t_0)\|}{\|\bar{\boldsymbol{r}}(t_0)\|} \right)^2 . \tag{3.47}$$

The initial time, t_0, in this scenario is 2454981.66 JED which is a few days after the Mars gravity assist (2454879.5 JED). Figure 3.9 shows the simulation segments. The scenario starts with roughly 9.6 days of coasting before the first thrusting segment. A total of 6 thrusting segments and 7 coasting segments are included in the simulation.

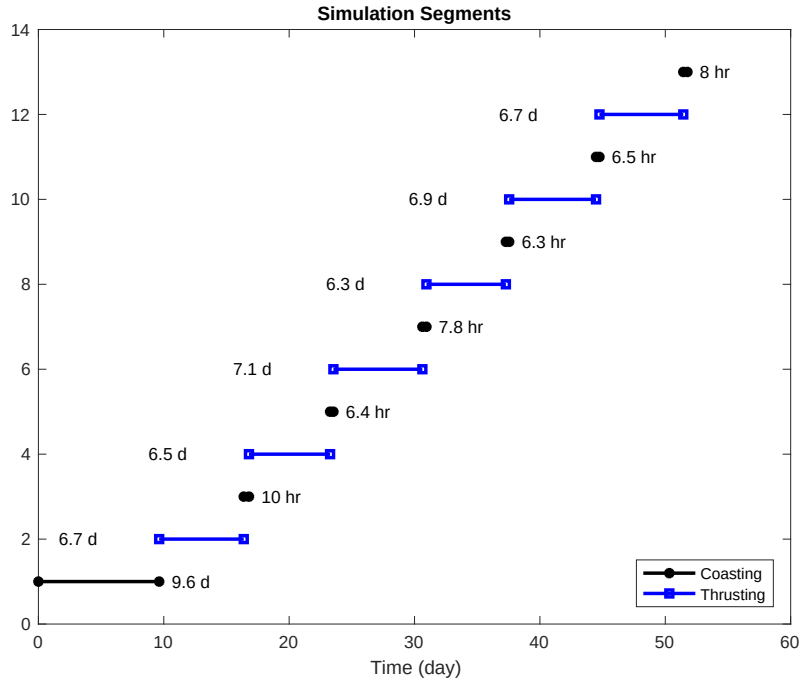

Figure 3.9: Thrusting and coasting schedule

It is assumed that the spacecraft is only allowed to observe pulsars during the coasting segments using a single body mounted detector. Therefore, the spacecraft can only observe one pulsar at a time and the order of observation is listed in Table 3.3. After observing the fifth pulsar in the table, the spacecraft returns to observe the first pulsar. The observation time allowed for each pulsar is $T_{obs} = 50\ min$. The time interval between the ends of two pulsar observations within one coasting segment is $\Delta t = 1\ hr$. The number of pulsar observations within each coasting segment depends on the duration of the coasting segment.

Figure 3.10 shows the RSS position and velocity estimation errors. The black stars indicate updated estimates; therefore, they only occur during the coasting segment. The red circles indicate filter predictions. The red lines indicate the RSS bounds for the filter predictions. After processing pulsar data for 4 days, the RSS position and velocity bounds decrease from 87 km to 7 km and from 0.019 m/s to 0.01 m/s respectively. Because of the high process noise and no measurement during the thrusting segments, the RSS bounds and estimation error tend to increase. On average the RSS bounds at the end of each thrusting segment are 35 km and 0.06 m/s. After approximately 8 hours of observation, the RSS bounds decrease to 16 km and 0.035 m/s at the end of the coasting segment. The values are consistent with that of Fig. 3.7. The clock estimation errors are plotted in Fig. 3.11. Similar behavior occurs in the estimate of the clock bias, $t_c(t)$. This correlation is because both position, $\boldsymbol{r}_{sc}(t)$, and the clock bias are explicit in the pulsar phase equation, $\phi_{sc}(t)$.

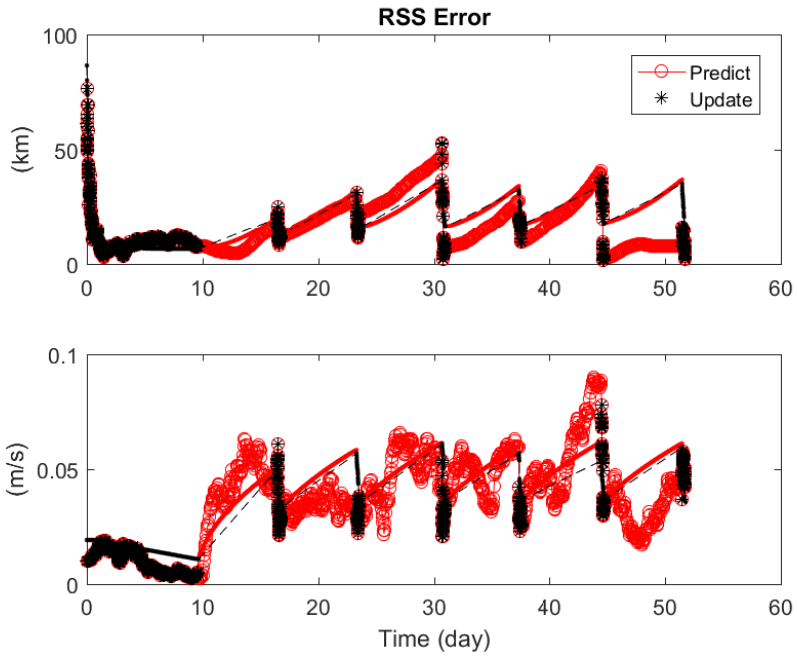

Figure 3.10: RSS position and velocity estimation errors and RSS 1σ bounds

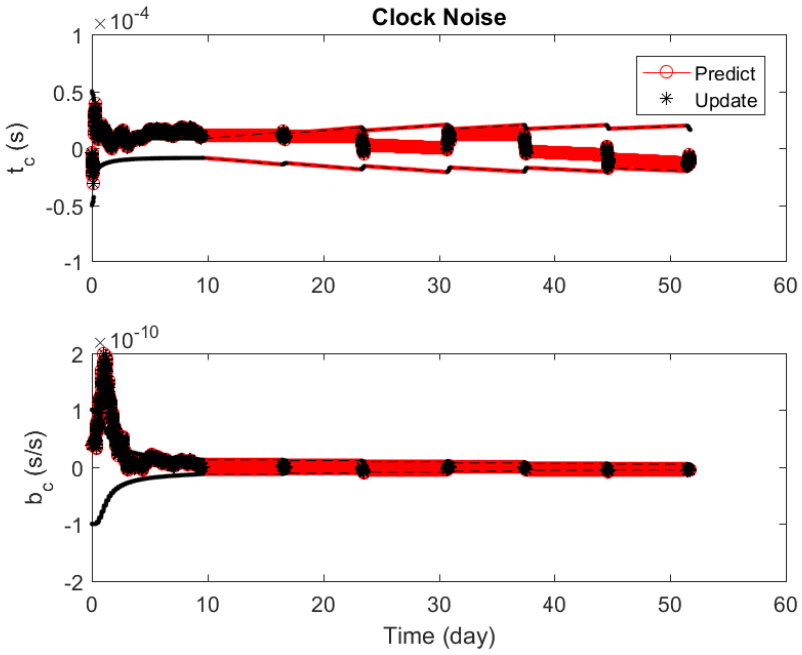

Figure 3.11: Clock deviation estimation error and 1σ bounds

3.7 Discussion

The set of X-ray and radio pulsars used in the covariance analysis is not optimized. However, it is reasonable to infer from Fig. 3.7 that a radio based system with comparable performance as the NICER system would require an antenna diameter greater than 16 m given the stochastic nature of the interstellar dispersion. Nevertheless, a radio based system does have a few advantages over X-ray based system. Namely, a radio antenna can be designed using lightweight materials and be stored in compact containers. In addition, the antenna size can be reduced slightly by improving antenna efficiency, increasing system bandwidth, reducing system temperature or using double-polarization. Combining these points with the inherent stochastic advantage over the X-ray based system makes the radio based system more attractive for missions that allow the deployment of a large radio antenna.

Equation (3.31) and Eq. (3.43) are derived using a double integrator system with acceleration input. This simplified system represents a spacecraft on a trajectory composed of segments of constant acceleration and constant velocity. Since the gravitational acceleration

due to the Sun in deep space is relatively small when comparing to a spacecraft in orbit around a planet, the double integer system can be used to approximate a small segment of a nominal spacecraft trajectory from Earth to deep space. Therefore, within each segment Eq. (3.31) and Eq. (3.43) can be used as a first step in determining a set of navigation pulsars that minimize the position and velocity error covariance.

Because of the high strength of the ion thruster process noise, $\boldsymbol{w}_g(t)$, and the limited observation time between two thrusting segments, the navigation filter is not able to obtain enough measurements to reach an RSS bound of 7 km as indicated by Fig. 3.10. This simulation illustrates the importance of the observation duration when there is significant process noise. If one wants to use pulsars as navigation beacons, it is necessary to schedule the thrusting to allow sufficient time for observation. An alternative solution is to mount the detector on a gimbal to allow the spacecraft to observe pulsars while thrusting.

CHAPTER 4

Experimental Verification of Pulsar Positioning System

4.1 Overview

Pulsar-based navigation can use either radio or X-ray pulsars. While the detection and measurement models are different for these two types of pulsars, the fundamental navigation concept and the pulsar timing models are applicable to both. X-ray pulsar signals can be detected using a relatively small detector; as a result, they are favored in space-borne applications [30, 31, 34, 56]. On the other hand, radio pulsars have relatively high signal-to-noise ratio, and they can be measured from Earth's surface. Moreover, there are more known radio pulsars than X-ray pulsars, which improves observability and accessibility. These advantages allow us to utilize existing hardware, software, and data to show the feasibility of pulsar-based navigation for the first time.

The aim of this chapter is to develop a robust Pulsar Positioning System (PPS) for the pulsar timing hardware attached to the 70 m Deep Space Network (DSN) antennas [58]. In order to achieve this objective, simulation tools and estimation algorithms have to be developed and verified in preparation for actual experiments using the DSN. This chapter focuses on using surveyed radio millisecond pulsars to determine the location of an observatory (radio telescope) on Earth. This estimation problem is essentially an inverse of the standard pulsar timing process, which solves for the pulsar timing model given an observatory position. The organization of the chapter is as follows. The timing model, the observability analysis, and the estimation algorithm are given in Section 4.4 and Section 4.5. The numerical and experimental verifications of the implementation are shown in Sections 4.6 and 4.7. Following these sections is discussion in Sections 4.8.

4.2 Pulsar Timing Model

The pulsar signal waveform is modeled as

$$z(t^{psr}) = \underbrace{\lambda_b + \lambda_s s(\phi(t^{psr}))}_{g(t^{psr})}, \tag{4.1}$$

where λ_b, and λ_s are the background and source intensities respectively. The periodic function, $s(\cdot)$, describes the pulse profile and is typically approximated by a sum of Gaussian functions. The phase evolution, $\phi(t^{psr})$, describes the pulsar rotation, where the independent variable t^{psr} is defined with respect to the inertial frame of the pulsar. The functional form of the phase evolution is

$$\phi(t^{psr}) = \phi_0 + \dot{\phi}\,[t^{psr} - t_0] + \frac{1}{2}\ddot{\phi}\,[t^{psr} - t_0]^2 + \eta(t^{psr}), \tag{4.2}$$

where $\eta(t^{psr})$ is pulsar timing noise [26]. The parameters $\dot{\phi}$, $\ddot{\phi}$, and t_0 are assumed to be known from prior timing surveys. In order to keep the timing model as accurate as possible, these parameters have to be updated from time to time. As a result, regular monitoring of pulsars is needed to support pulsar-based positioning. The timing model of various pulsars can be found in current literature or in the Australia Telescope National Facilities (ATNF) Pulsar Database [6]. The initial phase offset, ϕ_0, is a value that is currently not recorded as a part of the timing model and has to be obtained through model calibration process.

The relationship between the emission time at the pulsar inertial frame, t^{psr}, and the arrival time at an observatory, t^{obs}, is modeled by a system of equations,

$$\begin{aligned} t^{ssb} &= t^{obs} - \Delta_{\odot}(t^{obs}, t^{bb}, \boldsymbol{x}) \\ t^{bb} &= t^{ssb} - \Delta_{IS}(t^{ssb}, t^{bb}, \boldsymbol{x}) \\ t^{psr} &= t^{bb} - \Delta_{B}(t^{bb}, t^{psr}, \boldsymbol{x}), \end{aligned} \tag{4.3}$$

where t^{ssb}, and t^{bb} are the arrival times at the SSB and the pulsar binary barycenter respectively. The position of the observatory in the International Terrestrial Reference System (ITRS) is denoted by $\boldsymbol{x}$. The Solar System, interstellar, and binary delays are represented by $\Delta_{\odot}$, Δ_{IS}, and Δ_B respectively. The dominant component related to the observatory position

is embedded in the Solar System delay, which can be further decomposed into

$$\begin{aligned}\Delta_{\odot}(t^{obs}, t^{bb}, \boldsymbol{x}) = \Delta_{A}(t^{obs}, \boldsymbol{x}) + \Delta_{R\odot}(t^{obs}, t^{bb}, \boldsymbol{x}) \\ + \Delta_{p}(t^{obs}, \boldsymbol{x}) + \Delta_{E\odot}(t^{obs}, \boldsymbol{x}) + \Delta_{S\odot}(t^{obs}, \boldsymbol{x}),\end{aligned} \tag{4.4}$$

where Δ_A is the atmospheric delay, $\Delta_{R\odot}$ is the Roemer delay; Δ_p is the parallax delay; $\Delta_{E\odot}$ is the Einstein delay; and $\Delta_{S\odot}$ is the Shapiro delay. While every term in Eq. (4.4) depends on the position of the observatory, $\boldsymbol{x}$, the main contribution comes from $\Delta_{R\odot}$.

$$\Delta_{R\odot} = -\frac{\boldsymbol{n}^T \overbrace{(\boldsymbol{r}_{\oplus} + L\boldsymbol{x})}^{\boldsymbol{r}}}{c}, \tag{4.5}$$

where c is the speed of light; $\boldsymbol{r}$ is the observatory position in the Barycentric Celestial Reference System (BCRS); $\boldsymbol{n}$ is the pulsar direction; and $\boldsymbol{r}_{\oplus}$ is the position of Earth relative to the SSB. The transformation matrix, L, converts ITRS coordinates (Earth-fixed) to Geocentric Celestial Reference System (GCRS) inertial coordinates. For pulsar timing, GCRS is equivalent to BCRS, which is an inertial reference frame whose origin is at the SSB.

4.3 Pulsar Positioning System

The previous estimation problem focuses on estimating the observatory position from the position deviation in the Roemer delay, $\Delta_{R\odot}$, and assumes the position deviation in the rest of the terms in Eq. (4.4) are negligible [59]. Under this assumption, the position deviation, $\delta\boldsymbol{r}$, is parameterized using Taylor series,

$$\begin{aligned}\delta\boldsymbol{r} &:= \boldsymbol{r} - \bar{\boldsymbol{r}} \\ &= \boldsymbol{\delta r}_0 + \boldsymbol{\delta r}_1(t - t_0),\end{aligned} \tag{4.6}$$

where the *a priori* estimate of the observatory position in BCRS is $\bar{\boldsymbol{r}}$. The Taylor coefficients, $[\boldsymbol{\delta r}_0, \boldsymbol{\delta r}_1]$, are estimated with a weighted nonlinear least squares method.

Instead of using the above approach, this research focuses on estimating the observatory position, $\boldsymbol{x}$, in the ITRS using an Unscented Kalman Filter (UKF). This approach has several advantages: (i) the accounting of position errors in all the delays of Eq. (4.3); (ii) the incorporation of a Gaussian prior on $\boldsymbol{x}$; (iii) the straightforward augmentation of pulsar

timing noise, and other time varying states for future enhancements; and (iv) consistent formulation for direct application of other nonlinear estimators such as Gaussian mixture filters, and particle filters.

Given a pulse TOA at the observatory, t^{obs}, the observatory coordinates, $\boldsymbol{x}$, and the parameters of the pulsar timing model, the TEMPO2 software package is used to solve for the emission time, t^{psr}, of the pulse [60]. The solution process is iterative since Eq. (4.3) is implicit. For notation simplicity, Eq. (4.3) is represented by

$$t^{psr} = m(t^{obs}, \boldsymbol{x}). \tag{4.7}$$

Combining Eq. (4.1), (4.2) and (4.7) forms the state space model for the pulsar positioning problem,

$$\begin{aligned} \dot{\boldsymbol{x}} &= 0 \\ z_p(t^{obs}) &= g_p\left(m_p(t^{obs}, \boldsymbol{x})\right) + \nu_{rad,p}(t^{obs}), \end{aligned} \tag{4.8}$$

where $p = 1 \ldots N_{psr}$ and N_{psr} is the number of observed pulsars. The measurement noise of the waveform is represented by $\nu_{rad,p}(\cdot)$, whose noise Power Spectral Density (PSD) is $V_{rad,p}$.

The pulsar timing noise is not included as part of the state vector because it is approximately constant over the period of a few weeks, i.e. $\eta_p(t) \approx \eta_p$. As a result, a new variable can be defined by adding the initial phase offset and the timing noise together, i.e.,

$$\psi_p := \phi_{0,p} + \eta_p. \tag{4.9}$$

By formulating the model this way, ψ_p can be determined during the model calibration step. The following simulation and experimental verification results were obtained with this simplification, which implies that this first implementation of pulsar-based positioning is only valid for relatively short-term operations. Section 4.4 discusses the reason behind this limitation and Section 4.8 presents a possible enhancement to achieve long-term operations.

Eq. (4.8) is useful for covariance analysis, and navigation filter design. However, the form of Eq. (4.8) is not convenient given the conventions established by the pulsar astronomy community. Since this positioning algorithm leverages TEMPO2 timing model, the measurement equation has to be reformulated to match the conventions. Rather than processing the waveform, $z_p(t^{obs})$, the conventions focus on processing the pulse Time of Arrivals

(TOA) measured at the observatory. The i^{th} TOA of the p^{th} pulsar is simply an instant on the t^{obs} timescale and is denoted as $t^{obs}_{p,i}$. As a result, $t^{obs}_{p,i}$ has to be transformed to $t^{psr}_{p,i}$ using Eq. (4.7). The uncertainty of the TOA estimate, $\bar{t}^{obs}_{p,i}$, using cross-correlation technique is

$$\begin{aligned} \sigma^2_{p,i} &:= var[\bar{e}^{obs}_{p,i}] \\ \bar{e}^{obs}_{p,i} &= t^{obs}_{p,i} - \bar{t}^{obs}_{p,i}, \end{aligned} \tag{4.10}$$

whose Root-Mean-Square (RMS) value is $\sigma_{p,i}$. The theoretical development of cross-correlation technique in pulsar astronomy and the analytical expression of $\sigma^2_{p,i}$ is

$$\sigma^2_{p,i} = \frac{V_{rad,p}}{2\pi^2 \lambda^2_{s,p} \dot{\phi}^2_p T_{obs,p}} \left[\sum_{j=1}^{N_{four}} j^2 \left(a^2_{p,j} + b^2_{p,j} \right) \right]^{-1}, \tag{4.11}$$

where $T_{obs,p}$ is the observation duration; $a_{p,j}$ and $b_{p,j}$ are Fourier coefficients used to represent the p^{th} pulse profile [31, 61]. Eq. (4.11) can be re-derived from the positioning accuracy point of view [56]. In short, the pulsar positioning accuracy is enhanced when the selected pulsars exhibit the following conditions: (i) broad distribution in the sky, (ii) high signal-to-noise ratio, (iii) high rotational frequency, (iv) long observation duration, (v) narrow pulse shape, and (vi) multiple peaks in the pulse profile.

Assuming the accumulation of TOA uncertainty and the time transfer error is smaller than $\pm$ 0.5 *cyc*, then the pulse number associated with $t^{obs}_{p,i}$ relative to the timing model is

$$y_{p,i} := [\phi(\bar{t}^{psr}_{p,i})]_{int}, \tag{4.12}$$

where $[\cdot]_{int}$ represents rounding to the nearest integer. Eq. (4.12) is the left-hand-side of the measurement equation. On the right-hand-side, the measurement function is

$$\begin{aligned} h_{p,i}(\boldsymbol{x}) = \psi_p &+ \dot{\phi}_p \left[m_p(\bar{t}^{obs}_{p,i}, \boldsymbol{x}) - t_{0,p} \right] \\ &+ \frac{1}{2} \ddot{\phi}_p \left[m_p(\bar{t}^{obs}_{p,i}, \boldsymbol{x}) - t_{0,p} \right]^2. \end{aligned} \tag{4.13}$$

The measurement equation is formulated in this way because inversion of Eq. (4.2) is numerically infeasible due to the small magnitude of $\ddot{\phi}$, which is between 10^{-14} to 10^{-16}. TEMPO2 uses the same measurement equation to solve for the pulsar timing model given a known observatory position [60]. The TOA, $t^{obs}_{p,i}$, can also be interpreted as the measurement time of the discrete-time measurement in Eq. (4.12).

Combining Eq. (4.12) and (4.13) gives

$$\begin{aligned} \dot{\boldsymbol{x}} &= \boldsymbol{w} \\ y_{p,i} &= h_{p,i}(\boldsymbol{x}_i) + v_{p,i}, \end{aligned} \tag{4.14}$$

where $v_{p,i} = \dot{\phi}_p \bar{e}_{p,i}^{obs}$ represents zero mean white Gaussian phase noise whose variance is

$$\text{var}[v_{p,i}] = \dot{\phi}_p^2 \sigma_{p,i}^2. \tag{4.15}$$

The measurement noise can be modeled as additive because the quadratic term is small. The process noise, $\boldsymbol{w}$, is added to account for un-modeled dynamics. The covariance matrix of $\boldsymbol{w}$ serves as a tuning parameter. Since Eq. (4.14) is written in the standard nonlinear state space form, $\boldsymbol{x}$ can be estimated using an UKF.

4.4 Observability Analysis

Before discussing the UKF, this section analyzes the observability of pulsar-based positioning and shows analytically why it is impractical to estimate $\boldsymbol{\psi}$ and $\boldsymbol{x}$ simultaneously. The elements of $\boldsymbol{\psi}$ are the unknown phase bias of each pulsar, ψ_p. In order to facilitate the analysis, a simplified but representative system is used. The first step in formulating the simplified model is to augment the state space of Eq. (4.14) with $\boldsymbol{\psi}$. Second, the measurement equation is converted to continuous-time. Third, the small frequency rate, $\ddot{\phi}$ is dropped to keep the measurement linear. Since the Solar System Roemer delay, $\Delta_{R\odot}$, is the dominant time delay associated with the pulsar positioning problem, only this delay is considered in the analysis.

After simplification, the system being analyzed is

$$\begin{aligned} \begin{bmatrix} \dot{\boldsymbol{x}}(t) \\ \dot{\boldsymbol{\psi}}(t) \end{bmatrix} &= 0 \\ \boldsymbol{y}(t) &= \underbrace{\begin{bmatrix} N^T L(t) & I \end{bmatrix}}_{H(t)} \begin{bmatrix} \boldsymbol{x}(t) \\ \boldsymbol{\psi}(t) \end{bmatrix} + \boldsymbol{v}(t), \end{aligned} \tag{4.16}$$

where the PSD of the white measurement noise, $\boldsymbol{v}(t)$, is a constant matrix V. The rotational matrix $L(t)$ defined in the Conventions of the International Earth Rotation and Reference Systems Service represents the orientation of Earth with respect to the GCRS [62]. It can be decomposed into

$$L(t) = QR(t)W. \tag{4.17}$$

The precession-nutation matrix Q represents Celestial Intermediate Reference System (CIRS) with respect to the GCRS, and the matrix W models the changes of the ITRS relative to the Terrestrial Intermediate Reference System (TIRS) due to polar motion. Since both motions are extremely slow, they are represented by products of constant rotational matrices in this analysis. The matrix $R(t)$ represents the orientation of TIRS relative to CIRS. It accounts for the primary rotation of Earth and has the form

$$\begin{aligned} R(t) &= \begin{bmatrix} \cos(\theta(t)) & -\sin(\theta(t)) & 0 \\ \sin(\theta(t)) & \cos(\theta(t)) & 0 \\ 0 & 0 & 1 \end{bmatrix} := \begin{bmatrix} \tilde{R}(t) & 0 \\ 0 & 1 \end{bmatrix} \\ \theta(t) &= \omega_{\oplus} t, \end{aligned} \tag{4.18}$$

where $\omega_{\oplus} = 2\pi \; rad/day$ is the angular rotation rate of Earth. The matrix N is

$$N = \begin{bmatrix} \frac{\dot{\phi}_1 \boldsymbol{n}_1}{c} & \frac{\dot{\phi}_2 \boldsymbol{n}_2}{c} & \cdots & \frac{\dot{\phi}_p \boldsymbol{n}_p}{c} \end{bmatrix}, \tag{4.19}$$

where $\dot{\phi}_p$ and $\boldsymbol{n}_p$ are the rotational frequency and the unit direction vector of the p^{th} pulsar. It is assumed that a minimum of three pulsars with linearly independent directions are observed; therefore, N has full row rank. The dimensions of N is $3 \times N_{psr}$.

From state space system theory, the weighted observability gramian for Eq. (4.16) is

$$\mathcal{O} = \int_0^{T_{obs}} H^T(t) V^{-1} H(t) dt, \tag{4.20}$$

where the observation duration, T_{obs}, is defined as a multiple of the rotational period of Earth, $P_{\oplus} = 2\pi/\omega_{\oplus}$. The weighted observability gramian is the inverse of the error covariance matrix, i.e., $\mathcal{O} = P^{-1}$ [44]. Substituting $H(t)$ from Eq. (4.16) into Eq. (4.20) gives

$$\mathcal{O} = \int_0^{T_{obs}} \begin{bmatrix} L^T(t) N V^{-1} N^T L(t) & L^T(t) N V^{-1} \\ V^{-1} N^T L(t) & V^{-1} \end{bmatrix} dt. \tag{4.21}$$

According to the observability criteria, Eq. (4.16) is observable if and only if $\mathcal{O}$ is positive definite.

The following derivation uses Schur complement to show that $\mathcal{O}$ is not positive definite. The Schur complement of $\mathcal{O}$ is

$$\tilde{\mathcal{O}} = \int_0^{T_{obs}} L^T(t) N V^{-1} N^T L(t) dt - \int_0^{T_{obs}} L^T(t) N V^{-1} dt \frac{V}{T_{obs}} \int_0^{T_{obs}} V^{-1} N^T L(t) dt. \tag{4.22}$$

Substituting Eq. (4.17) into Eq. (4.22) gives

$$\tilde{\mathcal{O}} = W^T \left[\int_0^{T_{obs}} R^T(t) Q^T N V^{-1} N^T Q R(t) dt - \int_0^{T_{obs}} R^T(t) dt \frac{Q^T N V^{-1} N^T Q}{T_{obs}} \int_0^{T_{obs}} R(t) dt \right] W. \tag{4.23}$$

Let

$$U := Q^T N V^{-1} N^T Q. \tag{4.24}$$

Since $Q^T N$ has full row rank and V^{-1} is positive definite, U is also positive definite and can be decomposed as

$$U = \begin{bmatrix} U_1 & \boldsymbol{u}_2 \\ \boldsymbol{u}_2^T & u_3 \end{bmatrix} \quad \Rightarrow U_1 > 0, \text{ and } u_3 > 0, \tag{4.25}$$

where

$$U_1 = \begin{bmatrix} u_{11} & u_{12} \\ u_{12} & u_{13} \end{bmatrix} \quad \Rightarrow u_{11} > 0, \text{ and } u_{13} > 0. \tag{4.26}$$

As a result of the decomposition and the definition of $R(t)$, Eq. (4.23) becomes

$$\begin{aligned}
\tilde{\mathcal{O}} &= W^T \Bigg\{ \int_0^{T_{obs}} \begin{bmatrix} \tilde{R}^T(t) & 0 \\ 0 & 1 \end{bmatrix} \begin{bmatrix} U_1 & \boldsymbol{u}_2 \\ \boldsymbol{u}_2^T & u_3 \end{bmatrix} \begin{bmatrix} \tilde{R}(t) & 0 \\ 0 & 1 \end{bmatrix} dt \\
&\qquad - \begin{bmatrix} \int_0^{T_{obs}} \tilde{R}^T(t)dt & 0 \\ 0 & T_{obs} \end{bmatrix} \frac{1}{T_{obs}} \begin{bmatrix} U_1 & \boldsymbol{u}_2 \\ \boldsymbol{u}_2^T & u_3 \end{bmatrix} \begin{bmatrix} \int_0^{T_{obs}} \tilde{R}(t)dt & 0 \\ 0 & T_{obs} \end{bmatrix} \Bigg\} W \\
&= W^T \Bigg\{ \int_0^{T_{obs}} \begin{bmatrix} \tilde{R}^T(t)U_1\tilde{R}(t) & \tilde{R}^T(t)\boldsymbol{u}_2 \\ \boldsymbol{u}_2^T\tilde{R}(t) & u_3 \end{bmatrix} dt \\
&\qquad - \begin{bmatrix} \int_0^{T_{obs}} \tilde{R}^T(t)dt \frac{U_1}{T_{obs}} \int_0^{T_{obs}} \tilde{R}(t)dt & \int_0^{T_{obs}} \tilde{R}^T(t)\boldsymbol{u}_2 dt \\ \int_0^{T_{obs}} \boldsymbol{u}_2^T\tilde{R}(t)dt & T_{obs}u_3 \end{bmatrix} \Bigg\} W \\
&= W^T \underbrace{\begin{bmatrix} \int_0^{T_{obs}} \tilde{R}^T(t)U_1\tilde{R}(t)dt - \int_0^{T_{obs}} \tilde{R}^T(t)dt \frac{U_1}{T_{obs}} \int_0^{T_{obs}} \tilde{R}(t)dt & 0 \\ 0 & 0 \end{bmatrix}}_{E \not> 0} W.
\end{aligned} \tag{4.27}$$

Since the $(2,2)$ element of E is 0, $\tilde{\mathcal{O}}$ is not positive definite. This implies Eq. (4.16) is unobservable.

A physical interpretation of this analysis result is that since the dominant rotation of Earth is only about one axis, the motion of the observatory with respect to the GCRS is not sufficient to allow an estimator to determine the embedded signatures of $\boldsymbol{x}$ from $\boldsymbol{\psi}$ using $\boldsymbol{y}(t)$. This issue cannot be resolved by observing more pulsars because each additional pulsar measurement introduces one additional unknown phase. In other words, the rank of $\mathcal{O}$ is always one less than the dimension of the state vector. Even though the complete pulsar timing model in Eq. (4.2) and Eq. (4.3) have several nonlinearities, such as frequency rate and dispersion delay, that can enhance the observability of the state, they are either slowly varying or are much smaller compare to Roemer delay. As a result, they cannot be used to effectively reduce the estimation error covariance. These reasons are why a calibration step is necessary when using pulsars to determine the position of the observatory for short-term operations.

If $\boldsymbol{\psi}$ is removed from the state space, then Eq. (4.20) becomes

$$\mathcal{O} = W^T \left\{ \int_0^{T_{obs}} \begin{bmatrix} \tilde{R}^T(t) U_1 \tilde{R}(t) & \tilde{R}^T(t) \boldsymbol{u}_2 \\ \boldsymbol{u}_2^T \tilde{R}(t) & u_3 \end{bmatrix} dt \right\} W. \tag{4.28}$$

Evaluating the integral gives

$$\mathcal{O} = T_{obs} W^T \begin{bmatrix} \frac{u_{11}+u_{13}}{2} & 0 & 0 \\ 0 & \frac{u_{11}+u_{13}}{2} & 0 \\ 0 & 0 & u_3 \end{bmatrix} W > 0, \tag{4.29}$$

which implies Eq. (4.14) is observable.

Eq. (4.20) can also be integrated numerically to verify observability. Table 4.1 gives a summary of the numerical results for five different estimation scenarios. It is important to note that these results were obtained assuming the state vector is composed of unknown constants. The observability or the degree of observability for each scenario can be satisfied or enhanced if there is a dynamical system describing the time evolution of the states. Examples are observer dynamics, pulsar timing noise dynamics, and dispersion measure dynamics. This is the distinguishing feature between a Kalman-type estimator and the weighted nonlinear least squares estimator.

4.5 Estimation Algorithm

4.5.1 Unscented Transformation

Given a nonlinear transform, $\boldsymbol{y} = \boldsymbol{h}(\boldsymbol{x})$, the unscented transformation is a deterministic sampling method that approximates the mean and covariance of $\boldsymbol{y}$ from the mean and covariance of $\boldsymbol{x}$. This technique was applied to state estimation and filtering [63, 64]. Let the mean and covariance of $\boldsymbol{x}$ be $\bar{\boldsymbol{x}}$ and P_x respectively, where the dimension of $\boldsymbol{x}$ is n_x. This method generates $n_{\mathcal{X}} = 2n_x + 1$ number of sample points, denoted by $\mathcal{X}_k$, from $\bar{\boldsymbol{x}}$ and P_x, and then they are propagated through the nonlinearity, $\boldsymbol{h}(\cdot)$ to obtain the output sample point, $\mathcal{Y}_k$. The mean and the covariance matrix of $\boldsymbol{y}$ are constructed using the weighted sum

Table 4.1: Observability Analysis Using Eq. (4.20) for Several Estimation Scenarios

Scenario Descriptions	**Estimated States**	**Observable**
Simultaneous/sequential observation of 1 or more pulsars	Observatory position	Yes
Simultaneous/sequential observation of 3 or more pulsars	Observatory position, and clock bias	Yes
Simultaneous/sequential observation of 3 or more pulsars	Observatory position, and ephemeris bias	Yes
Simultaneous/sequential observation of 3 or more pulsars	Observatory position, ephemeris, and clock biases	No
Simultaneous/sequential observation of 3 or more pulsars	Observatory position, and 3 or more phase bias	No
The above scenarios assume repetitive observations.		

of $\mathcal{Y}_k$. The set of sample points are calculated using the following formulas.

$$\begin{aligned}
\mathcal{X}_0 &= \bar{\boldsymbol{x}} \\
\mathcal{X}_k &= \bar{\boldsymbol{x}} + \left\{\sqrt{(n_x+\lambda)P_x}\right\}_k, \quad k = 1,\ldots,n_x \\
\mathcal{X}_k &= \bar{\boldsymbol{x}} - \left\{\sqrt{(n_x+\lambda)P_x}\right\}_{k-n_x}, \quad k = n_x+1,\ldots,2n_x
\end{aligned} \tag{4.30}$$

where $\{\sqrt{A}\}_k$ denotes the k^{th} row of the Cholesky factorization S where $A = S^T S$. The weights are

$$\begin{aligned}
W_0^m &= \lambda/\left(n_x+\lambda\right) \\
W_0^c &= \lambda/\left(n_x+\lambda\right) + \left(1-\alpha^2+\beta\right) \\
W_k^c &= W_k^m = 1/\left(2(n_x+\lambda)\right), \quad k = 1,\ldots,2n_x,
\end{aligned} \tag{4.31}$$

where $\lambda = \alpha^2\left(n_x+\kappa\right) - n_x$. The tuning parameters α, β and κ control the distribution and the relative weights of $\mathcal{X}_k$. Propagating $\mathcal{X}_k$ through the nonlinearity gives $\mathcal{Y}_k = \boldsymbol{h}(\mathcal{X}_k)$. The

mean and covariance of $\boldsymbol{y}$ are

$$\begin{aligned} \bar{\boldsymbol{y}} &= \sum_{k=0}^{2n_x} W_k^m \mathcal{Y}_k \\ P_{yy} &= \sum_{k=0}^{2n_x} W_k^c \left[\mathcal{Y}_k - \bar{\boldsymbol{y}}\right] \left[\mathcal{Y}_k - \bar{\boldsymbol{y}}\right]^T . \end{aligned} \tag{4.32}$$

4.5.2 Unscented Kalman Filter

The UKF combines the unscented transformation with the architecture of a Kalman filter to form an estimator for a nonlinear system. The following is a brief review of the UKF applied to a nonlinear system with additive process and measurement noises,

$$\begin{aligned} \boldsymbol{x}_{i+1} &= \boldsymbol{f}_i(\boldsymbol{x}_i) + G_i \boldsymbol{w}_i \\ \boldsymbol{y}_i &= \boldsymbol{h}_i(\boldsymbol{x}_i) + D_i \boldsymbol{v}_i. \end{aligned} \tag{4.33}$$

The variances of the two zero-mean white noises are W_i and V_i. Let the *a posteriori* mean and covariance at time t_{i-1} be denoted as $\hat{\boldsymbol{x}}_{i-1}$ and P_{i-1} respectively. The *a priori* mean and covariance at time t_i are

$$\begin{aligned} \bar{\boldsymbol{x}}_i &= \sum_{k=0}^{2n_x} W_k^m \bar{\mathcal{X}}_{k,i} \\ M_i &= \sum_{k=0}^{2n_x} W_k^c \left[\bar{\mathcal{X}}_{k,i} - \bar{\boldsymbol{x}}_i\right] \left[\bar{\mathcal{X}}_{k,i} - \bar{\boldsymbol{x}}_i\right]^T + G_i W_i G_i^T, \end{aligned} \tag{4.34}$$

where $\bar{\mathcal{X}}_{k,i} = \boldsymbol{f}_i(\hat{\mathcal{X}}_{k,i-1})$, and $\hat{\mathcal{X}}_{k,i-1}$ is generated using $\hat{\boldsymbol{x}}_{i-1}$, P_{i-1}, and Eq. (4.30). The *a posteriori* estimate and covariance are

$$\begin{aligned} \hat{\boldsymbol{x}}_i &= \bar{\boldsymbol{x}}_i + K_i(\boldsymbol{y}_i - \bar{\boldsymbol{y}}_i) \\ K_i &= P_{xy,i} P_{yy,i}^{-1} \\ P_i &= M_i - K_i P_{yy,i} K_i^T. \end{aligned} \tag{4.35}$$

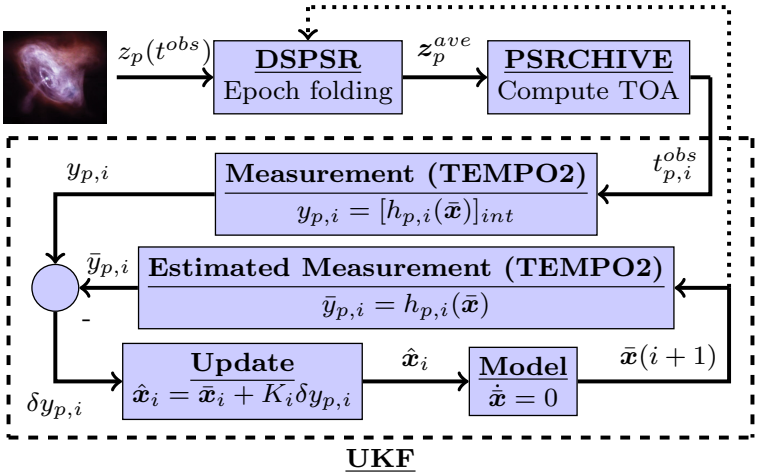

Figure 4.1: The PPS relies on DSPSR for epoch folding of raw waveform signals, $z_p(t^{obs})$; PSRCHIVE for determining pulse TOA, $t_{p,i}^{obs}$; and TEMPO2 for generating the estimated measurement, $\bar{y}_{p,i}$.

The measurement mean, covariance, and cross-covariance are

$$\begin{aligned}
\bar{\boldsymbol{y}}_i &= \sum_{k=0}^{2n_x} W_k^m \bar{\mathcal{Y}}_{k,i} \\
P_{xy,i} &= \sum_{k=0}^{2n_x} W_k^c \left[\bar{\mathcal{X}}_{k,i} - \bar{\boldsymbol{x}}_i\right] \left[\bar{\mathcal{Y}}_{k,i} - \bar{\boldsymbol{y}}_i\right]^T \\
P_{yy,i} &= \sum_{k=0}^{2n_x} W_k^c \left[\bar{\mathcal{Y}}_{k,i} - \bar{\boldsymbol{y}}_i\right] \left[\bar{\mathcal{Y}}_{k,i} - \bar{\boldsymbol{y}}_i\right]^T + D_i V_i D_i^T,
\end{aligned} \tag{4.36}$$

where $\bar{\mathcal{Y}}_{k,i} = \boldsymbol{h}_i(\bar{\mathcal{X}}_{k,i})$.

Comparing it with the Extended Kalman Filter (EKF), the practical advantage of UKF in this particular problem is that the Jacobian matrix of the measurement equation is not needed. The computation of Eq. (4.2) and Eq. (4.7) require multiple software libraries; therefore, it is more practical to implement an UKF. The overall architecture of the PPS is illustrated in Fig. 4.1.

Table 4.2: Employed Pulsars in Numerical Simulation

Pulsar	$\dot{\phi}\ (Hz)$	$\lambda\ (km)$	**# of TOA**	**RMS** (μs)
J0711-6830	182.1	1647.3	4	1
J1730-2304	123.1	2436.8	4	1
J1744-1134	245.4	1222.4	4	1
J1939+2134	641.9	467.3	4	1
J2124-3358	202.7	1479.3	4	1
$\dot{\phi}$ represents pulsar frequency				
λ represents the signal wavelength				

4.6 Numerical Simulation

In order to verify the implementation of the algorithm described in Section 4.5, 800-trial Monte Carlo analyses were used to determine the ensemble mean and the ensemble covariance of the estimation error, $\hat{\boldsymbol{e}}_i = \boldsymbol{x} - \hat{\boldsymbol{x}}_i$, where $\hat{\boldsymbol{x}}_i$ is the *a posteriori* position estimate. The ITRS coordinates of the DSN Goldstone 70 m antenna were used in the simulation. They are $\boldsymbol{x} = \begin{bmatrix} -2353.62122 & -4641.34152 & 3677.052352 \end{bmatrix}^T$ (km). The position estimate, $\hat{\boldsymbol{x}}_0$, used to initialize the UKF was a Gaussian random vector distributed around $\boldsymbol{x}$ with a covariance matrix of $P_0 = \text{diag}([100, 100, 100])$ (km^2). The process noise $\boldsymbol{w}$ was set to zero. Five isolated radio millisecond pulsars were used for the analysis, and they are listed in Table 4.2 and plotted in Fig. 4.2. The observation center frequency was 1440 MHz.

The observation scenario assumes that each pulsar is observed once a day for four consecutive days. Two alternating day-to-day schedules were used in the simulation in order to leverage the motion of Earth to improve accuracy. The observation schedules for the first and the third day are the same. Similarly, the schedules for the second and the fourth day are the same. The TOA RMS values for all pulsars were set to 1 μs for simplicity. In other words, telescope data collection system observes each pulsar and epoch folds the measured waveform signals until a TOA RMS of 1 μs is achieved. Therefore, the observation duration for one pulsar is different from another pulsar. This accuracy can be achieved with mod-

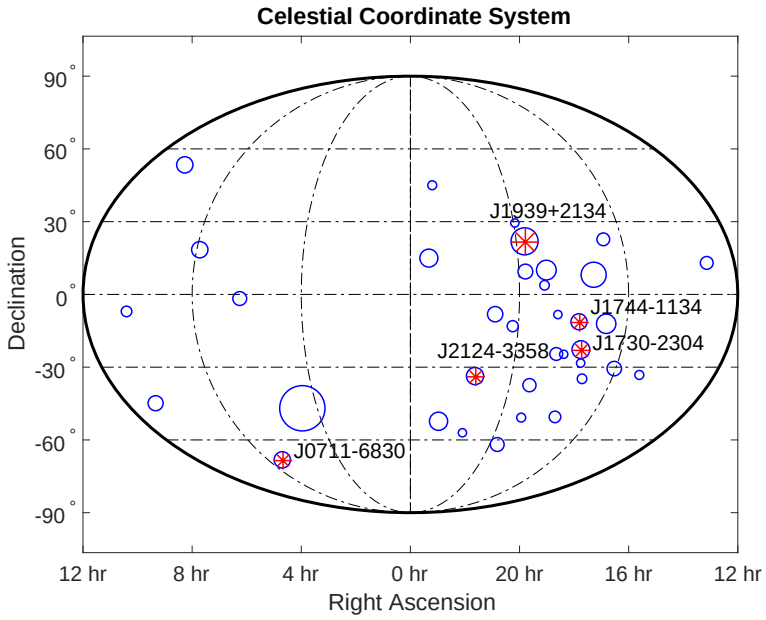

Figure 4.2: This figure shows 36 millisecond pulsars with period less than 10 ms, period derivative less than 5×10^{-18} s/s and strength greater than 1 mJy at 1400 MHz [6].

ern pulsar timing hardware [58]. The 1σ bound for the X, Y, and Z directions in ITRS or equivalently $k = 1,\ 2,\ 3$ are defined as

$$[\boldsymbol{\sigma}_i]_k = \sqrt{\text{diag}(P_i)}, \tag{4.37}$$

where P_i is the filter error covariance at time t_i. The symbol, $[\cdot]_{kl}$, indicates the k^{th} row and the l^{th} column of a matrix. If the argument is a vector, then only one index is given.

The ensemble error and the ensemble error covariance are

$$\begin{aligned} \hat{\boldsymbol{e}}_{en,i} &= \frac{1}{N_{real}} \sum_{j=1}^{N_{real}} \hat{\boldsymbol{e}}_{i,j} \\ P_{en,i} &= \frac{1}{N_{real}-1} \sum_{j=1}^{N_{real}} \left[\hat{\boldsymbol{e}}_{i,j} - \hat{\boldsymbol{e}}_{en,i}\right] \left[\hat{\boldsymbol{e}}_{i,j} - \hat{\boldsymbol{e}}_{en,i}\right]^T, \end{aligned} \tag{4.38}$$

where $\hat{\boldsymbol{e}}_{i,j}$ is the estimation error of the j^{th} realization at time t_i, and N_{real} is the number of realizations.

The Root-Sum-Square (RSS) filter estimation error and 1σ bound are defined as

$$\begin{aligned} \hat{e}_{rss,i} &= \sqrt{[\hat{\boldsymbol{e}}_i]_1^2 + [\hat{\boldsymbol{e}}_i]_2^2 + [\hat{\boldsymbol{e}}_i]_3^2} \\ \sigma_{rss,i} &= \sqrt{[P_i]_{11} + [P_i]_{22} + [P_i]_{33}}. \end{aligned} \tag{4.39}$$

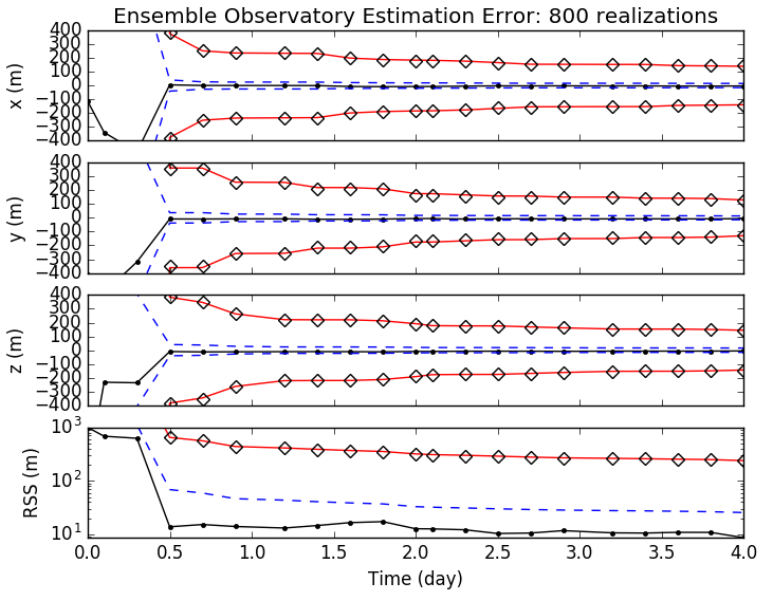

Figure 4.3: Black dots are ensemble errors; black diamonds are ensemble 1σ; red lines are the filter 1σ; blue dash lines in the top three plots are $3\boldsymbol{\sigma}_{clt,i}$; and the blue dash line in the last plot is $3\sigma_{rss,clt,i}$.

The RSS ensemble estimation error and 1σ bound are defined as

$$\begin{aligned} \hat{e}_{rss,en,i} &= \sqrt{[\hat{\boldsymbol{e}}_{en,i}]_1^2 + [\hat{\boldsymbol{e}}_{en,i}]_2^2 + [\hat{\boldsymbol{e}}_{en,i}]_3^2} \\ \sigma_{rss,en,i} &= \sqrt{[P_{en,i}]_{11} + [P_{en,i}]_{22} + [P_{en,i}]_{33}}. \end{aligned} \tag{4.40}$$

According to the Central Limit Theorem (CLT), the 1σ bound and the RSS bound associated with averaging independent-identically-distributed random variables are

$$\begin{aligned} \boldsymbol{\sigma}_{clt,i} &= \sqrt{\frac{\text{diag}(P_{en,i})}{N_{real}}} \\ \sigma_{rss,clt,i} &= \sqrt{\frac{[P_{en,i}]_{11} + [P_{en,i}]_{22} + [P_{en,i}]_{33}}{N_{real}}}. \end{aligned} \tag{4.41}$$

The Monte Carlo simulation result is shown in Fig. 4.3. The first three plots in the figure show the errors in the X, Y, and Z directions in ITRS. The fourth plot shows the RSS ensemble estimation errors. In the figure, the ensemble RSS estimation error is $\hat{e}_{rss,en,i} \approx 20\ m$, which is well within the $3\sigma_{rss,clt,i}$ bound (blue dash lines). The filter bounds (red lines) are on top of the ensemble bounds (black diamonds), i.e. $P_i \approx P_{en,i}$. Both of these results

indicate that the filter was programmed correctly. The process noise and measurement noise covariance matrices of the UKF were not adjusted, which means that for this problem the covariance of the UKF is representative of the actual covariance of the conditional density function. The last plot in Fig. 4.3 shows that after processing 20 measurements collected with the above observation schedule, $\sigma_{rss,i}$ can be reduced from 10 km to 240 m. The ensemble RSS, $\sigma_{rss,en,i}$, at the last TOA measurement is 241 m.

4.7 Experimental Verification

4.7.1 Dataset

The pulsar data used to verify the positioning algorithm described in Section 4.5 was obtained from the online data access portal of the Commonwealth Scientific and Industrial Research Organization [65]. Information about the dataset is listed in Table 4.3. These measurements were collected at the 64 m Parkes Radio Observatory in Australia with CPSR2 recorder [66]. The dataset is roughly 7 hr long and consists of $N = 384$ number of TOA measurements. The uncertainties of the TOA are computed via the PSRCHIVE software package [67, 68]. Observation center frequencies are 1341 MHz and 1405 MHz. The dataset spans from 54101.1 MJD to 54102.4 MJD. The observation sequence is $J1939 + 2134$ on 54101.1 MJD followed by $J1744 - 1134$ on 54101.9 MJD, $J1730 - 2304$ on 54102.0 MJD, $J2124 - 3358$ on 54102.2 MJD, and lastly $J0711 - 6830$ on 54102.3 MJD. The datasets are stored in PSRFIT file format; therefore, the pulse TOA at the observatory have to be calculated using PSRCHIVE. The observatory ITRS coordinates are $\boldsymbol{x} = \begin{bmatrix} -4554.2315 & 2816.7591 & -3454.0363 \end{bmatrix}^T$ (km). The standard templates required to perform cross-correlation were obtained from the European Pulsar Network Data Archive, which organizes data from various publications [57, 69]. The pulsar timing parameters were obtained via the ATNF pulsar database, which organizes data from various publications [6, 60, 53, 70]. The observatory clock correction files required for this verification are included in the TEMPO2 software distribution.

Table 4.3: A List of Datasets from CSIRO

Pulsar	**File Name**	**Time (min)**	**Center Freq. (Hz)**	**# of TOA**	**Ave. RMS** (μs)
J0711-6830	n2007-01-02-08:51:20.rf	64	1341	58	8.2
	m2007-01-02-08:51:20.rf	64	1405	58	7.5
J1730-2304	n2007-01-02-00:3:33.rf	20	1341	18	10.0
	m2007-01-02-00:3:33.rf	20	1405	18	7.6
J1744-1134	n2007-01-01-23:22:23.rf	64	1341	58	3.1
	m2007-01-01-23:22:23.rf	64	1405	58	2.6
J1939+2134	n2007-01-01-02:28:26.rf	32	1341	29	0.1
	m2007-01-01-02:28:26.rf	32	1405	29	0.2
J2124-3358	n2007-01-02-06:51:15.rf	32	1341	29	3.4
	m2007-01-02-06:51:15.rf	32	1405	29	3.3

4.7.2 Model Calibration

As explained in Section 4.4 it is impractical to estimate ψ_p and $\boldsymbol{x}$ simultaneously. Therefore, ψ_p was obtained using TEMPO2 in the model calibration step, which processed the 1341 MHz dataset and required the actual observatory position to compute a phase estimate $\hat{\psi}_p$. Since the dataset is limited, none of the pulsar timing parameters from ATNF catalogue were changed. In the estimation step, the UKF uses the calibrated model and the 1405 MHz dataset to estimate the observatory position.

4.7.3 Expected Accuracy

Before processing the actual experimental data, a 200-trial Monte Carlo simulation was performed to determine the expected accuracy from processing the 1405 MHz datasets. In this Monte Carlo simulation, the position estimate, $\hat{\boldsymbol{x}}_0$, used to initialize the UKF was a Gaussian random vector distributed around the true observatory position, $\boldsymbol{x}$, with a covariance matrix of $P_0 = \text{diag}([100, 100, 100])$ (km^2). The TOA uncertainties used in the

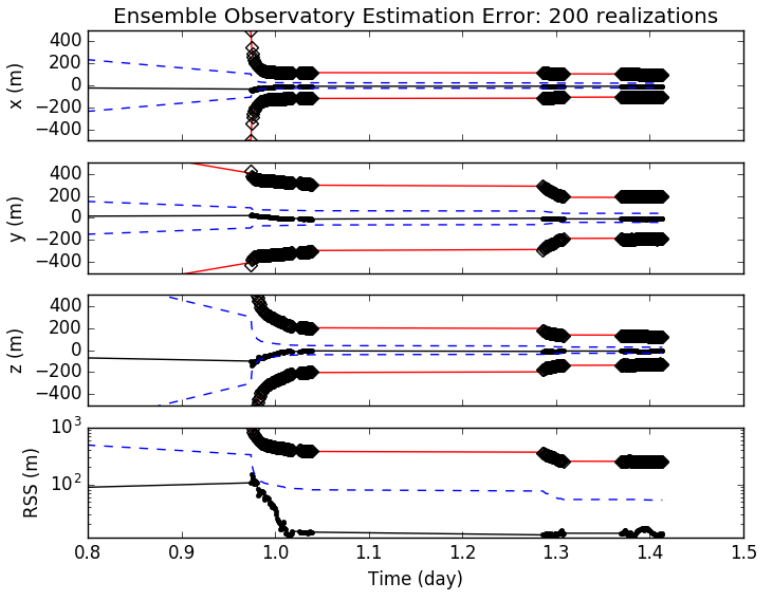

Figure 4.4: Black dots are ensemble errors; black diamonds are ensemble 1σ; red lines are the filter 1σ; blue dash lines in the top three plots are $3\boldsymbol{\sigma}_{clt,i}$; and the blue dash line in the last plot is $3\sigma_{rss,clt,i}$.

simulation are listed in Table 4.3. The filter measurement noise covariance matrix was not boosted, and the process noise covariance matrix was set to zero. The expected accuracy for scenario #1 is plotted in Fig. 4.4. The figure shows the last 4 pulsar observations. The origin of the x-axis corresponds to 54101.0 MJD. The data points are marked with black dots. As expected the filter 1σ bounds (red lines) match with the ensemble 1σ bounds (black diamonds). The ensemble RSS bound, $\sigma_{rss,en,N}$, and filter RSS bound, $\sigma_{rss,N}$, at the last TOA are 250 m and 243 m respectively. The ensemble RSS estimation error, $\hat{e}_{rss,en,i}$, is below the $3\sigma_{rss,clt,i}$ (blue dash lines) as indicated by the fourth plot. Based on this simulation, the expected accuracy for processing the 1405 MHz datasets is 243 m. Because there are a lot more TOA in this simulation than that of Section 4.6, the PPS was able to achieve similar accuracy much more quickly.

Table 4.4: Experimental Trials

Initial Errors and Bounds					
Trial #	*1*	*2*	*3*	*4*	*5*
$\hat{e}_{rss,0}$ (km)	4.8	20.4	10.8	16.8	12.1
$\sigma_{rss,0}$ (km)	17.3	17.3	17.3	17.3	17.3
Final Errors and Bounds					
Trial #	*1*	*2*	*3*	*4*	*5*
$\hat{e}_{rss,N}$ (m)	865	954	810	986	845
$\sigma_{rss,N}$ (m)	1100	1100	1100	1100	1100

4.7.4 Actual Accuracy

The position estimate, $\hat{\boldsymbol{x}}_0$, used to initialize the filter has the same statistics as that of Section 4.7.3. The positioning accuracy achieved from processing the actual data is summarized in Table 4.4. Since there is only one dataset, Monte Carlo analysis is not possible. However, five randomly generated initial guesses of the observatory position were used to show the feasibility of the system. The estimation errors for trial #1 and #2 are shown in Fig. 4.5 and Fig. 4.6 respectively. The zoomed-in plots are shown in Fig. 4.7 and Fig. 4.8. These figures show more details and include the last four pulsar observations. These results were obtained after the UKF measurement noise covariance was increased by a factor of 25 to keep the estimation errors within the 1σ bound defined by Eq. (4.37). The UKF process noise covariance was 0. In Fig. 4.7 and Fig. 4.8, the RSS estimation errors, $\hat{e}_{rss,i}$, lie within the 1σ RSS bounds, $\sigma_{rss,i}$, most of the time. This is an indication that the filter is properly tuned and that the overall estimation scheme is consistent with the actual pulsar and observer dynamics. The 1σ bounds in all five trials decrease with every TOA measurement, which verify Eq. (4.14) is observable. It also proves pulsar based position is a feasible concept. Based on the results in Table 4.4, we conclude the accuracy of the experimental verification is $\sigma_{rss,N} \sim 1\ km$. This value is 5 times higher than the expected $\sigma_{rss,N}$ from Monte Carlo simulation. An explanation of this gap is given in the discussion section.

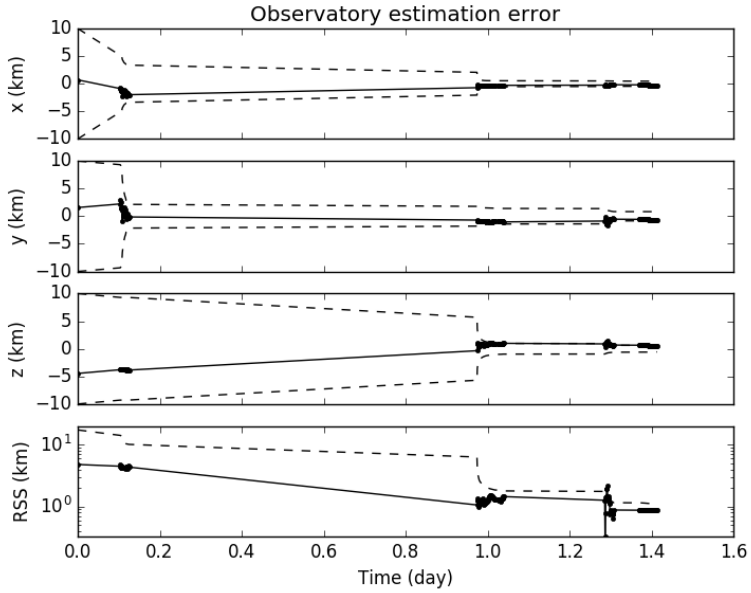

Figure 4.5: Trial #1: The dash lines are the filter 1σ bounds and the dots are the estimation errors.

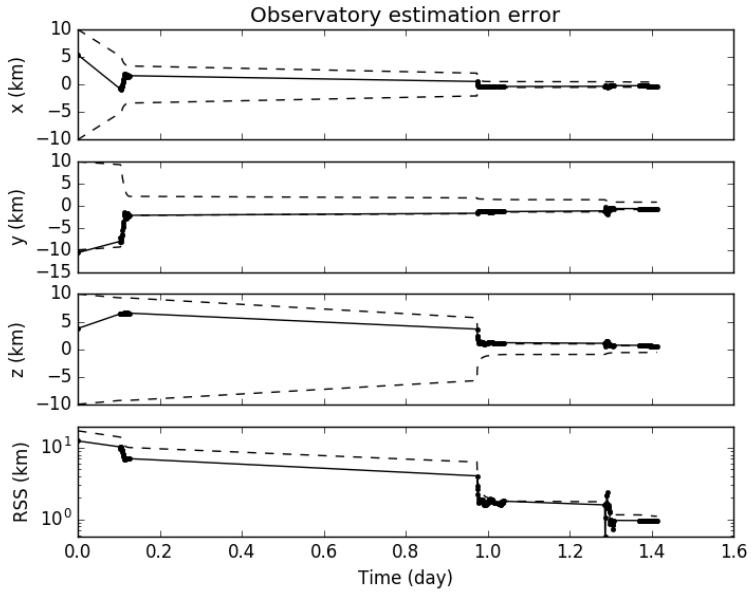

Figure 4.6: Trial #2: The dash lines are the filter 1σ bounds and the dots are the estimation errors.

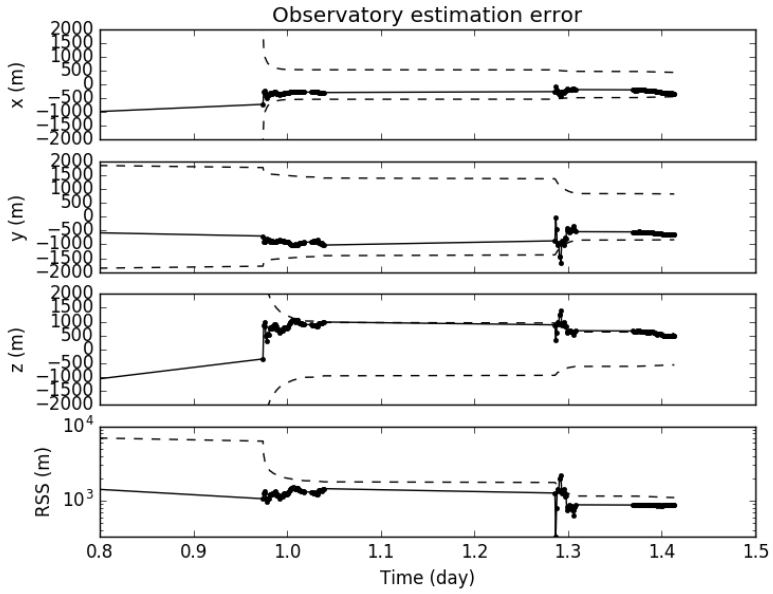

Figure 4.7: Trial #1: Zoomed-in plot

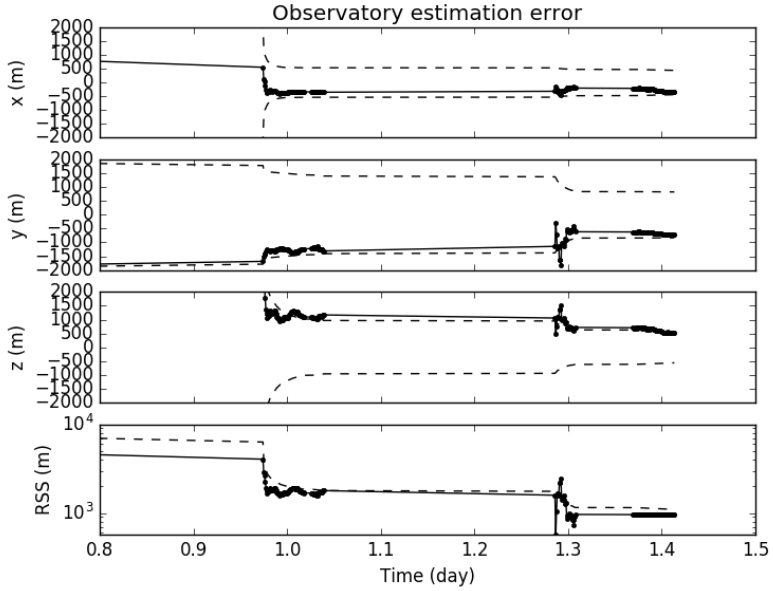

Figure 4.8: Trial #2: Zoomed-in plot

4.8 Discussion

Given that this chapter has shown pulsar-based positioning is feasible, there are several ways to improve the accuracy beyond $\sim 1\ km$ from data processing point of view. The first one is increase the number of TOA measurements because it allows the UKF to average out the undesired effects of white measurement noise. In addition, extending the observation duration also enables the UKF to leverage Earth's motion to improve observability. This feature is not fully utilized in the experimental verification because of the short observation duration. In addition to processing more data, observing bright and stable binary pulsars such as $J0437-4715$ and $J1713+0747$ can also be used to improve the accuracy of the PPS.

Another important reason for wanting to process more data is that it helps us understand the advantages and the deficiencies of the above approach and guide us in the development of a robust PPS. Comparing the actual accuracy in Section 4.7.4 with the expected accuracy in Section 4.7.3 shows that there is a mismatch between the two $\boldsymbol{\sigma}_{rss,N}$ values. The former is 1100 m and the latter is 243 m. This difference in the filter bound is a direct result of boosting the measurement noise covariance by a factor of 25 when processing actual pulsar measurements. There are a few possibilities that would explain the need for the boost: (i) inaccurate estimate of the phase offset, ψ_p; (ii) optimistic RMS values from PSRCHIVE, $\sigma_{p,i}^2$, in Eq. (4.10) (lower than the actual RMS values); (iii) undesired effects from un-modeled error sources; or (iv) small errors in the parameters of the pulsar timing model. Out of these four possibilities, a combination of case (i) and case (ii) is the most likely reason. Since ψ_p was determined using a much smaller dataset, the uncertainty of $\hat{\psi}_p$ is large compare to the rest of the timing model parameters. Furthermore, the trends of the RSS estimation errors in Fig. 4.7 and Fig. 4.8 resemble a bias error, which can be induced by errors in $\hat{\psi}_p$. Case (ii) is also possible because it is difficult to determine the exact variance of the TOA estimates when the actual TOA values are not known. Further investigation and data processing are necessary to determine the actual cause. Resolving this issue would bridge the gap between the actual and the expected RSS bounds.

The waveform measurements, $z_p(\cdot)$, from the radiometer are epoch folded using the DSPSR software, which relies on either a polynomial phase model, a constant period, or real-time parameter search [71]. If the polynomial phase model is used, then the position estimate of the UKF has to be fed back to DSPSR. This feedback is illustrated by the dotted line in Fig. 4.1. Since the raw measurements are discarded after folding, this portion of the algorithm can not be tested using archival data. However, this bypass is unlikely to severely affect the positioning accuracy of the DSN experiment. As more measurements are processed the observatory estimate used in epoch folding would improve, which in turn reduces the TOA uncertainty to the same level as that of the archival data. In other words, longer observation duration is needed to achieve comparable positioning accuracy.

As described in Section 4.3, the pulsar timing noise, $\eta_p(t)$, is added with $\phi_{0,p}$ to form ψ_p, and this simplification assumes the pulsar timing noise is constant over the observation duration. Such assumption is not valid for long-term operations, where pulsar timing noise, $\eta_p(t)$, would deviate slowly due to the correlated noise dynamics. Therefore, it is essential to design an estimator to track $\eta_p(t)$ over larger timescale. While $\psi_p(t)$ can be estimated with the help of the correlated noise model of $\eta_p(t)$, the convergence of the estimate, $\hat{\psi}_p(t)$, is extremely slow because of two reasons. First, the initial uncertainty of $\phi_{0,p}$ is large since it can be anywhere between ± 0.5 *cyc*. Second, pulsar timing noise has large correlation time on the order of months to years [42]. Therefore, it is beneficial to perform model calibration to obtain a phase estimate $\hat{\phi}_{0,p}$ prior to estimating observatory position and set the initial estimate of $\eta_p(t)$ to be zero mean with a variance equal to that of $\hat{\phi}_{0,p}$. Since Eq. (4.14) is expressed in state space form, it is straightforward to augment the state space to include a correlated noise model for $\eta_p(t)$. The fractional timing noise PSD for several well known pulsars are available from publications [53], and they can be approximated with a state space model using the frequency domain method [54].

The dataset used in this verification was collected by a 64 m diameter radio telescope. At first thought, this seems to be a limiting factor for using radio pulsars for navigation as opposed to the X-ray pulsars. However, one should recognize that the convergence rate and the accuracy in Fig. 4.5 and Fig. 4.6 are relatively faster and higher than that of a X-ray

pulsar navigation system [34]. These differences imply that one can trade the performance for a smaller antenna size. The following comparison investigates the TOA uncertainty of the X-ray based system, σ_{xr}^2, due to photon noise (non-homogenous Poisson process) and that of the radio system, σ_{rf}^2, due to radiometer noise (Gaussian process). For the X-ray based system, the uncertainty is quantified using the Cramér-Rao Lower Bound [31],

$$\sigma_{xr}^2 = \frac{1}{\tilde{\lambda}_{s,xr}^2 T_{obs} \dot{\phi}^2} \left[\int_0^1 \frac{s'(\varphi)^2}{\tilde{\lambda}_{b,xr} + \tilde{\lambda}_{s,xr} s(\varphi)} d\varphi \right]^{-1}, \tag{4.42}$$

where

$$\tilde{\lambda}_{b,xr} = \frac{\lambda_{b,xr} N_e}{56}, \quad \text{and} \quad \tilde{\lambda}_{s,xr} = \frac{\lambda_{s,xr} N_e}{56}. \tag{4.43}$$

The parameter T_{obs} is the observation time; N_e is the number of NICER telescope element; $\lambda_{s,xr}$ is the X-ray signal intensity; and $\lambda_{b,xr}$ is the background intensity. On the other hand, the TOA uncertainty of the radio system is obtained using the result of the covariance analysis and the radiometer equation in [56, 18],

$$\sigma_{rf}^2 = \frac{V}{2\pi^2 \lambda_{s,rf}^2 T_{obs} \dot{\phi}^2} \left[\sum_{j=1}^{N_f} j^2 \left(a_j^2 + b_j^2 \right) \right]^{-1}, \tag{4.44}$$

where

$$V = \frac{T_{sys}^2}{G^2 n_p \Delta f}, \quad G = \frac{A\eta}{2k_B}, \quad \text{and} \quad A = \frac{\pi d^2}{4}. \tag{4.45}$$

The parameter V is the PSD of the radiometer noise; G is the antenna gain; d is the antenna diameter; A is the projected area; a_j and b_j are the Fourier coefficients describing the signal profile; N_f is the number of Fourier series terms; and k_B is Boltzmann constant. The rest of the parameters are listed in Table 4.5.

Given a required TOA estimation uncertainty, Fig. 4.9 shows the relationship between the observation time, T_{obs}, and the telescope size, d, and N_e for radio and X-ray pulsar signals respectively. This plot is constructed using the signal properties of J0437-4715, the parameters of the 70 m DSN system and the system parameters of the NICER X-ray telescope [8]. At the intersection of the $\sigma_{xr} = 1\ \mu s$ curve and $\sigma_{rf} = 1\ \mu s$ curve, one can see the observation time of a X-ray telescope consisting of 2 NICER elements is roughly equal to that of a 2 m radio antenna for this particular pulsar. Because of the different slopes

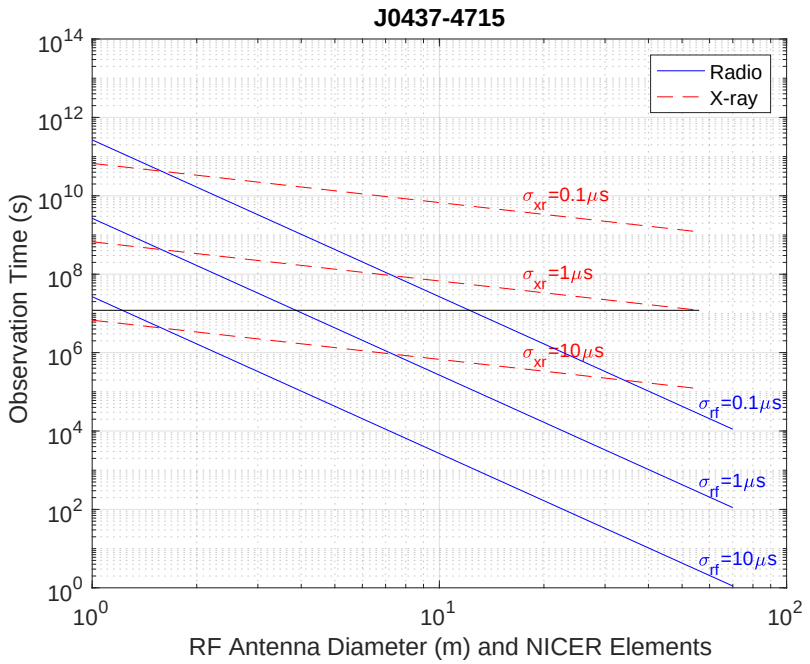

Figure 4.9: Observation time vs. antenna size for a given TOA uncertainty. The slope of the X-ray based system is -1 while the slope of the radio based system is -4.

in the log-log plot, the observation time needed to achieve the same level of uncertainty using the full 56 element NICER telescope is roughly equal to that of a 4 m radio antenna as indicated by the black solid line and the blue 1 μs curve. As a result, utilizing radio millisecond pulsars for navigation remains competitive given that radio antenna is lightweight and can be deployed from a compact container. However, it should be mentioned that the uncertainty due to the stochastic nature of the interstellar dispersion delay is not included in the comparison; therefore, Fig. 4.9 is slightly biased towards the radio system. Nevertheless, this result warrants a more detail trade study between the two approaches.

This work on pulsar-based positioning is complementary to the NICER/SEXTANT mission at Goddard Space Flight Center [55, 34]. Since the fundamental navigation concept is the same for both radio and X-ray pulsars, the ability to use the DSN for pulsar-based positioning can serve as a risk reduction tool for future missions. It allows researchers to test and verify their algorithms on the ground before deploying them in space.

Table 4.5: System Parameters Used in the Comparison

Radio System			
Signal intensity	$\lambda_{s,rf}$	0.149	Jy
System temperature	T_{sys}	30	K
Pulsar frequency	$\dot{\phi}$	173.6	Hz
Receiver bandwidth	Δf	500	MHz
Antenna efficiency	η	0.6	
Number of polarization	n_p	1	
X-ray System			
Signal intensity	$\lambda_{s,xr}$	0.283	cnt/s
Background intensity	$\lambda_{b,xr}$	0.62	cnt/s
Pulsar frequency	$\dot{\phi}$	173.6	Hz
$1\ Jy = 10^{-26}\ W/(m^2\ Hz)$			

CHAPTER 5

Frequency Stability Analysis of Pulsar-Aided Atomic Clocks

5.1 Overview

Pulsar timing has been an active research area since the discovery of the first pulsar in 1967. The discovery of millisecond pulsar in 1982 further enhanced the timing precision and allowed researchers to utilize pulsar timing in astrophysics, autonomous navigation, and universal timescale [19]. The idea of a pulsar-based timescale was first discussed in a *Science Magazine* article in 1987 [20]. The long-term stability of J1939+2134 at averaging time of $\tau = 10^7\ s$ rivaled that of the state-of-the-art atomic time standard at the time. As more millisecond pulsars were discovered, researchers began to consider the use of an ensemble of millisecond pulsars to establish a universal timescale that remains accessible indefinitely [21, 22, 24]. However, the precision of modern experimental/laboratory atomic clocks have improved significantly to a level that renders a pulsar-only timescale obsolete over the averaging time of a few years [72]. Nevertheless, the long-term stability, the real-time accessibility, and the continuous availability of pulsar signals are advantageous for calibrating compact/portable atomic clocks at locations with no access to Global Positioning System. An example is a deep space exploration spacecraft.

Modern atomic clock such as NASA's Deep Space Atomic Clock (DSAC) has the frequency stability deviation of $\sim 10^{-15}$ at $\tau = 1\ day$ [73]. The frequency stability deviation of pulsar signals at the same averaging time is 3 to 4 orders higher. This is due to the radiometer noise and the white pulsar phase jitter [74]. A pulsar-only timescale would require decades of time averaging in order to achieve the equivalent stability of DSAC. Because

of this limitation, it is not feasible to develop a pulsar-only timescale that is useful at the short averaging time. However, it is challenging for compact atomic clocks to maintain high precision at the averaging time of years and decades. The Random Walk Frequency Noise (RWFN) eventually causes the clock frequency to drift away from the nominal value.

After fitting for the parameters of the pulsar timing model, the post-fit residuals of millisecond pulsars can achieve a fractional deviation of $\sim 10^{-15}$ at $\tau = 10\ yr$ [72, 75, 76]. The post-fit timing residuals consist of not only a white noise component but also an intrinsic pulsar spin noise with a fractional stochastic process. Given that the phase evolution of a millisecond pulsar is well captured by a second order model over multiple years and the fact that the magnitude of the frequency rate is on the order of 10^{-14} to $10^{-16}\ Hz/s$, there is a possibility that the diverging component in the pre-fit timing residuals is small relative to the clock noise at large timescale. Thus, this analysis focuses on the expected performance gain when using a pulsar signal to calibrate an atomic clock under the assumption that the pulsar timing model is representative of the pulsar signal evolution over the analysis period. The same analysis method is also applicable to the case when there is a diverging component in the pre-fit timing residuals. The main benefit of using millisecond pulsars to calibrate the atomic clocks is the suppression of the frequency drift induced by RWFN.

This paper presents an analysis procedure to quantify the performance of pulsar-aided compact atomic clocks in terms of the typical stability deviations used by the clock community. The analysis is presented from the perspective of state space system and filtering theory. It gives insights into the benefits and deficiencies of pulsar-aided atomic clocks.

The organization of this chapter is as follows. Section 5.2 discusses the clock model and the PSD of the clock noises. Section 5.3 describes the pulsar signal model and formulates a simplified but representative signal for analysis. This section also discusses the dominant noise sources and their PSD. Section 5.4 presents the filtered clock system. Section 5.5 shows a derivation of the relationship between Hadamard variance and the signal PSD. The results of the frequency stability analysis of the unfiltered and filtered systems are presented in Section 5.6.1 and Section 5.6.2 respectively. Following these sections are discussion and conclusions.

5.2 Clock Model

The time generating function of an atomic clock is modeled as

$$t_{clk}(t) := t - t_{clk,0} - \underbrace{\left[x(t) + a + bt + \frac{1}{2}ct^2\right]}_{t_c(t)}, \tag{5.1}$$

where

$$\begin{aligned} x(t) = \frac{\theta(t)}{\nu}, \quad a = \frac{1}{\nu}\left[\frac{1}{2}Dt_{clk,0}^2 - \delta\nu t_{clk,0} - \Phi_0\right] \\ b = \frac{1}{\nu}\left[\delta\nu - Dt_{clk,0}\right], \quad c = \frac{D}{\nu}. \end{aligned} \tag{5.2}$$

The variable, t, is the true time and $t_{clk,0}$ is the initialization time. The nominal frequency of the atomic clock is ν. The parameter Φ_0 is the initial phase of the oscillator at the start of the clock; $\delta\nu$ is frequency synchronization error; and D represents the aging of the oscillator [9]. These are unknown constants that need to be determined experimentally using a reference clock. Depending on the clock type, $\theta(t)$ can be white noise or fractional integration of white noise.

If the clock deviation, $t_c(t)$, is estimated, then the best estimate of the true time is $\hat{t}(t) = t_{clk}(t) + t_{clk,0} + \hat{t}_c(t)$, where the accuracy of $\hat{t}(t)$ is the error variance of $\hat{t}_c(t)$. The goal of this paper is to analyze the stability performance of the estimate of t_c, which is affected by the stochastic term $x(t)$. For a cesium clock, $\theta(t)$ is a combination of White Frequency Noise (WFN), $w_{\theta_1}(t)$, and white frequency rate noise, $w_{\theta_2}(t)$ [9]. The noise $\theta(t)$ is the output of the following linear stochastic differential equation,

$$\begin{aligned} \begin{bmatrix} \dot{\theta}_1 \\ \dot{\theta}_2 \end{bmatrix} &= \begin{bmatrix} 0 & 1 \\ 0 & 0 \end{bmatrix} \begin{bmatrix} \theta_1 \\ \theta_2 \end{bmatrix} + \begin{bmatrix} 1 & 0 \\ 0 & 1 \end{bmatrix} \begin{bmatrix} w_{\theta_1} \\ w_{\theta_2} \end{bmatrix} \\ \theta &= \theta_1. \end{aligned} \tag{5.3}$$

The time correlations of these noises are

$$\begin{aligned} E[w_{\theta_1}(t)w_{\theta_1}(\tau)] &= W_{\theta_1}\delta(t-\tau) \\ E[w_{\theta_2}(t)w_{\theta_2}(\tau)] &= W_{\theta_2}\delta(t-\tau). \end{aligned} \tag{5.4}$$

Since we are interested in estimating t_c using pulsar signal defined in Eq. (5.12), the filter model is obtained by differentiating $t_c(t)$ and taking into account Eq. (5.3). For cesium

atomic clock, $D = 0$; therefore, the state space system for t_c, b, and θ_2 is

$$\begin{bmatrix} \dot{t}_c \\ \dot{\theta}_2 \\ \dot{b} \end{bmatrix} = \begin{bmatrix} 0 & \frac{1}{\nu} & 1 \\ 0 & 0 & 0 \\ 0 & 0 & 0 \end{bmatrix} \begin{bmatrix} t_c \\ \theta_2 \\ b \end{bmatrix} + \begin{bmatrix} \frac{1}{\nu} & 0 \\ 0 & 1 \\ 0 & 0 \end{bmatrix} \begin{bmatrix} w_{\theta_1} \\ w_{\theta_2} \end{bmatrix}, \tag{5.5}$$

where θ_2 and b are not individually observable, so they are combined to form a dimensionless variable $\zeta = \theta_2/\nu + b$. The reduced system is

$$\begin{aligned} \underbrace{\begin{bmatrix} \dot{t}_c \\ \dot{\zeta} \end{bmatrix}}_{\dot{\boldsymbol{x}}_c} &= \underbrace{\begin{bmatrix} 0 & 1 \\ 0 & 0 \end{bmatrix}}_{A_c} \underbrace{\begin{bmatrix} t_c \\ \zeta \end{bmatrix}}_{\boldsymbol{x}_c} + \underbrace{\frac{1}{\nu} \begin{bmatrix} 1 & 0 \\ 0 & 1 \end{bmatrix}}_{B_c} \underbrace{\begin{bmatrix} w_{\theta_1} \\ w_{\theta_2} \end{bmatrix}}_{\boldsymbol{w}_c} \\ t_c &= \underbrace{\begin{bmatrix} 1 & 0 \end{bmatrix}}_{C_c} \boldsymbol{x}_c. \end{aligned} \tag{5.6}$$

The Power Spectral Density (PSD) of the white noises $w_{\theta_1}(t)$ and $w_{\theta_2}(t)$ are W_{θ_1} and W_{θ_2} respectively. Equation (5.6) is called the unfiltered clock noise model. Since the frequency stability depends on the stochastic part of the noise model, this analysis focuses on the output PSD of t_c. The transfer function of the clock system is

$$T_c(s) = \underbrace{C_c(sI - A_c)^{-1}B_c}_{G_c(s)} \boldsymbol{W}_c(s), \tag{5.7}$$

where s is the Laplace variable[1] and I is the identity matrix. The output PSD of Eq. (5.7) is

$$\begin{aligned} S_{t_c}(\omega) &= G_c(j\omega) W_\theta G_c(-j\omega)^T \\ &= \frac{W_1}{\omega^2} + \frac{W_2}{\omega^4}, \end{aligned} \tag{5.8}$$

where $W_\theta = diag\left([W_{\theta_1}, W_{\theta_2}]\right)$; $W_1 = W_{\theta_1}/\nu^2$; and $W_2 = W_{\theta_2}/\nu^2$. The independent variable ω is angular frequency.

[1] $X(s) = \mathcal{L}[x(t)]$, where $\mathcal{L}[\cdot]$ is the Laplace transform.

5.3 Pulsar Model

5.3.1 Signal Model

Like an atomic clock, a pulsar signal can also be modeled as a pseudo-periodic signal. The pulsar signal measured by an observer with a perfect clock in the Solar System is

$$y(t) = \lambda_b + \lambda_s s\left(\phi(t)\right) + v_{rad}(t), \tag{5.9}$$

where $s(\cdot)$ is the periodic signal model, and v_{rad} is the radiometer measurement noise, with a PSD of V_{rad}. The periodic signal model can be described by a sum of Gaussians or Fourier series. The phase of the signal is

$$\begin{aligned}\phi(t) = \phi_0 + \dot{\phi}[t - t_{p,0} - \Delta(t)] + \frac{1}{2}\ddot{\phi}[t - t_{p,0} - \Delta(t)]^2 \\ + \dot{\phi}n(t) + v_{jit}(t),\end{aligned} \tag{5.10}$$

where $t_{p,0}$ is the reference time of the pulsar timing model. The white phase jitter, $v_{jit}(t)$, has a PSD of V_{jit}. The pulsar timing noise is represented by $n(t)$. The pulsar timing noise is also known as the post-fit timing residual, which has long-term correlation. The background and source intensities of the pulsar signal are represented by λ_b and λ_s respectively. The time delay, $\Delta(t)$, can be decomposed into

$$\Delta(t) = \Delta_{\odot}(t) + \Delta_{IS}(t) + \Delta_B(t). \tag{5.11}$$

The Solar System, interstellar, and binary delays are represented by $\Delta_{\odot}(t)$, $\Delta_{IS}(t)$, and $\Delta_B(t)$ respectively [26]. Equation (5.11) is the general time transfer equation and it depends on the position of the observer and the Solar System ephemeris. Since this analysis is about clock calibration, all components of time transfer are considered as known values. The delays due to interstellar medium (dispersions, scintillation, pulse-broadening, and etc.) are assumed to be either correctable using multi-frequency measurements or captured by the post-fit timing residuals, $n(t)$.

Solving Eq. (5.1) for t and substituting the result into Eq. (5.10) gives

$$\begin{aligned}\phi(t) = \phi_0 &+ \dot{\phi}\left[t_{clk}(t) - t_0 + t_c(t) - \Delta(t)\right] \\ &+ \frac{1}{2}\ddot{\phi}\left[t_{clk}(t) - t_0 + t_c(t) - \Delta(t)\right]^2 \\ &+ \dot{\phi}n(t) + v_{jit}(t),\end{aligned} \tag{5.12}$$

where $t_0 = t_{p,0} - t_{clk,0}$. This equation describes the pulsar signal phase in terms of the readout of a real clock and the clock deviation at time t. Equation (5.12) assumes that the error in the clock, $t_c(t)$, does not have a significant effect on the slow varying components of the phase equation such as the observer position, the planetary ephemeris and the pulsar timing noise.

In an actual pulsar-aided atomic clock implementation, one would combine the clock noise and pulsar timing noise dynamics with Eq. (5.9) and Eq. (5.12) to form a nonlinear state-space system. Since this paper is about the frequency stability analysis and not about filter design, the goal of this section is to extract the essence of pulsar measurement equation (timing of the pulse) and formulate a simplified system (linear time invariant system) that is suitable for analysis.

There are several existing methods for tracking Eq. (5.12) [61, 31, 56]. These methods leverage the fast and slow components of the signal to simplify the signal model into a periodic signal with a constant phase offset. The periodicity comes from the fast varying component, which is the pulsar rotation. The constant phase offset comes from the sum of all the slow varying components: orbital dynamics, clock noise, pulsar timing noise and various time delays. As a result, the estimation uncertainty associated with tracking $\phi(t)$ is dominated by $v_{jit}(t)$ and $v_{rad}(t)$ in the short timescale.

In the astronomy community, the tracking of $\phi(t)$ is done by estimating the pulse Time-of-Arrivals (TOA) using epoch folding and cross-correlation method [61, 31]. A pulse TOA, t_{toa}, is defined as the detection time of the main pulse of a pulsar signal. Leveraging the different timescales in the signal simplifies Eq. (5.12) to

$$\phi(t) \approx \psi_i + f_{s,i}[t_{clk}(t) - t_i] + v_{jit}(t), \tag{5.13}$$

where $\psi_i = mod(\phi(t_i), 1)$ and $f_{s,i} = d\phi(t_i)/dt$. The frequency, $f_{s,i}$, is either a model predicted value from the derivative of Eq. (5.12) or an estimated value from Fast Fourier Transform of the raw data. The reference time, t_i, is typically the middle of the observation window, T_{obs}. Since the signal is periodic, ψ_i is the fractional phase of the signal, $y(t)$, at t_i. An estimate of ψ_i can be obtained by applying the cross-correlation method to Eq. (5.9) and Eq. (5.13) [31]. The estimate is denoted as $\bar{\psi}$. Once $\bar{\psi}$ is determined, the estimated pulse TOA can be calculated. Because the pulsar signal model is defined such that the phase corresponding to the main peak of the profile is an integer value, the estimated pulse TOA at the observatory is $\bar{t}_{toa,i} = t_i + \bar{\psi}_i/f_{s,i}$.

Assuming the uncertainties in $\bar{t}_{toa,i}$, $\bar{t}_c(\bar{t}_{toa,i})$, and $\bar{n}(\bar{t}_{toa,i})$ accumulate to a phase error less than $\pm 0.5\ cyc$, then the associated pulse number is $N_i := [\phi(\bar{t}_{toa,i})]_{int}$, where $[\cdot]$ denotes rounding to the nearest integer. Since the magnitude of $\ddot{\phi}$ is on the order of 10^{-14} to 10^{-16}, the stochastic behaviors of the signal is dominated by the linear term. Thus, $\ddot{\phi}$ it is neglected in this analysis. Solving Eq. (5.12) for the arrival time of the pulse N_i gives

$$t_{toa,i} = t_0 - t_c(t_i) + \Delta(t_i) - n(t_i) + \frac{N_i - \phi_0}{\dot{\phi}}. \tag{5.14}$$

Let the TOA estimation error be defined as $v(t_i) := t_{toa,i} - \bar{t}_{toa,i}$. Substituting Eq. (5.14) into the expression for $v(t_i)$ and solving for $\bar{t}_{toa,i}$ gives the TOA measurement equation

$$\bar{t}_{toa,i} = t_0 - t_c(t_i) + \Delta(t_i) - n(t_i) + \frac{N_i - \phi_0}{\dot{\phi}} - v(t_i). \tag{5.15}$$

For analysis purpose, Eq. (5.15) is further simplified by removing the deterministic terms and changing the signs in front of $t_c(t_i)$, $n(t_i)$, and $v(t_i)$ to be positive. Since the clock and pulsar timing noise models are given in continuous time, the measurement equation is also converted to continuous time to facilitate analysis. The measurement equation for the frequency stability analysis of pulsar-aided atomic clock is

$$z(t) := t_c(t) + n(t) + v(t). \tag{5.16}$$

Since the slow varying components are approximately constant over the observation duration, T_{obs}, the TOA estimation error $v(t)$ is dominated by white noises. The PSD of $v(t)$ is represented by V.

5.3.2 Noise Model

Because each pulsar and telescope pair has different V_{jit}, profile, frequency, and V_{rad}, the pulsar astronomy community instead provides a Root-Mean-Square (RMS) value and an epoch folding window length, T_{obs} to characterize the timing accuracy of an individual pulse TOA. The definition of the RMS value is $\sigma_{ave} := \sqrt{\text{var}[v(t_i)]}$. Since the formulation in this paper is expressed in continuous time, σ^2_{ave} has to be converted to PSD. Let the variance of the band-limited white noise, $v(t)$, be $\sigma^2 := V/\Delta t$, where Δt is the sample interval [44]. Since epoch folding is essentially time averaging, the averaged noise value can be represented by

$$v_{ave} = \frac{1}{N}\sum_{i=1}^{N} v(t_i), \tag{5.17}$$

where $N = T_{obs}/\Delta t$ is the number of measurement in the observation period. Applying the variance operator, var[·], on Eq. (5.17) gives $\sigma^2_{ave} = \sigma^2/N$. Using the definition of N and σ^2 gives

$$\sigma^2_{ave} = \frac{\sigma^2}{N} = \frac{V}{N\Delta t} = \frac{\Delta t}{T_{obs}}\frac{V}{\Delta t} = \frac{V}{T_{obs}}; \tag{5.18}$$

therefore, $V = \sigma^2_{ave} T_{obs}$.

The PSD of the pulsar timing noise, $n(t)$, obtained experimentally, has a form

$$S_n(\omega) = \frac{\omega_c^{2\alpha}}{(\omega_c^2 + \omega^2)^{\alpha}} W_r, \tag{5.19}$$

where W_r, α, and ω_c are positive fitting parameters . They represent the strength of the white noise, the integration order, and the corner frequency of a fractional Linear Time Invariant (LTI) system. The reason $S_n(\omega)$ is considered as a fractional PSD is because α is a real number. Equation (5.19) is the time correlated noise model used by the pulsar timing community to determine the pulsar timing model [42]. The parameters were obtained experimentally and iteratively during fitting of the pulsar frequency and frequency rate [53]. Since there is no theoretical result on the intrinsic pulsar stability, there is no guarantee that pulsar timing noise is truly fractional stationary. In order to address this issue, the following analysis considers two scenarios. The first scenario assumes that the pulsars are not intrinsically stable and the corner frequency in Eq. (5.19) is artificial. In this scenario,

the diverging behavior is modeled by fractional integration of white noise,

$$S_n(\omega) = \frac{\omega_c^{2\alpha}}{\omega^{2\alpha}} W_r. \tag{5.20}$$

The second scenario assumes that the fractional stationary noise model in Eq. (5.19) is a representative model of the timing noise over the analysis period.

The stable fractional transfer function that produces the PSD in Eq. (5.19) is

$$G_n(s) = \underbrace{\left(\frac{\omega_c}{s+\omega_c}\right)^{\beta}}_{G_{n,1}(s)} \underbrace{\left(\frac{\omega_c}{s+\omega_c}\right)^{\gamma}}_{G_{n,2}(s)}, \tag{5.21}$$

where $\alpha = \beta + \gamma$ and β is an integer. The output of the fractional system in frequency domain is

$$N(s) = G_n(s) W_n(s), \tag{5.22}$$

where $W_n(s)$ is the Laplace transform of $w_n(t)$ and the PSD of $w_n(t)$ is W_r. The first term of $G_n(s)$ is finite dimensional while the second is infinite dimensional. Approximating $G_n(s)$ using Charef method gives a finite dimensional LTI system that is representative for $\omega \in [0, \omega_{max}]$ [54]. Let the approximate transfer function be denoted by $\hat{G}_{n,2}(s)$, then $G_n(s) \approx G_{n,1}(s)\hat{G}_{n,2}(s) := \hat{G}_n(s)$.

The Charef method uses a set of stable poles and zeros to approximate the fractional transfer function $G_{n,2}(s)$ in Eq. (5.21). The advantage of this method is the matching of the steady state gain. Once $\hat{G}_{n,2}(s)$ is found, the state-space representation of the approximate timing noise model, $\hat{G}_n(s)$ can be obtained, which is denoted as

$$\begin{aligned} \dot{\boldsymbol{x}}_{n,app} &= \hat{A}_n \boldsymbol{x}_{n,app} + \hat{B}_n w_n \\ n_{app} &= \hat{C}_n \boldsymbol{x}_{n,app}. \end{aligned} \tag{5.23}$$

The approximate pulsar timing noise is denoted by $n_{app}(t)$; whereas, the true timing noise is $n(t)$.

5.4 Filtered Clock System

Combining the clock system in Eq. (5.6) with the approximate pulsar timing noise model in Eq. (5.23) gives

$$\begin{aligned}\underbrace{\begin{bmatrix}\dot{\boldsymbol{x}}_c\\ \dot{\boldsymbol{x}}_{n,app}\end{bmatrix}}_{\dot{\boldsymbol{x}}} &= \underbrace{\begin{bmatrix}A_c & 0\\ 0 & \hat{A}_n\end{bmatrix}}_{\tilde{A}}\underbrace{\begin{bmatrix}\boldsymbol{x}_c\\ \boldsymbol{x}_{n,app}\end{bmatrix}}_{\boldsymbol{x}} + \underbrace{\begin{bmatrix}B_c & 0\\ 0 & \hat{B}_n\end{bmatrix}}_{\tilde{B}}\begin{bmatrix}\boldsymbol{w}_c\\ w_n\end{bmatrix}\\ z_{app} &= \underbrace{\begin{bmatrix}C_c & \hat{C}_n\end{bmatrix}}_{\tilde{C}}\begin{bmatrix}\boldsymbol{x}_c\\ \boldsymbol{x}_{n,app}\end{bmatrix} + v.\end{aligned} \tag{5.24}$$

The measurement equation is constructed by replacing $n(t)$ in Eq. (5.16) with $n_{app}(t)$. This system is used for the design of the steady state Kalman filter, whose gain and error covariance are denoted by K and P respectively. The steady state Kalman filter is

$$\begin{aligned}\dot{\hat{\boldsymbol{x}}} &= \left[\tilde{A} - K\tilde{B}\right]\hat{\boldsymbol{x}} + Kz\\ \hat{t}_c &= \begin{bmatrix}C_c & 0\end{bmatrix}\hat{\boldsymbol{x}},\end{aligned} \tag{5.25}$$

whose frequency domain representation is

$$\hat{T}_c(s) = \underbrace{\begin{bmatrix}C_c & 0\end{bmatrix}\left(sI - \tilde{A} + K\tilde{C}\right)^{-1}K}_{H(s)}\,Z(s). \tag{5.26}$$

Because Eq. (5.21) cannot be expressed in state-space form, the filtered system has to be constructed using transfer functions. Taking the Laplace transform of Eq. (5.16) and substituting Eq. (5.7) and Eq. (5.22) into the resulting expression give

$$\begin{aligned}Z(s) &= T_c(s) + N(s) + V_m(s)\\ &= G_c(s)\boldsymbol{W}_c(s) + G_n(s)W_n(s) + V_m(s),\end{aligned} \tag{5.27}$$

where $V_m(s)$ is the TOA measurement noise. Subtracting Eq. (5.7) from Eq. (5.26) gives the clock estimation error, $e(t) = t_c(t) - \hat{t}_c(t)$, in frequency domain,

$$\begin{aligned}E(s) &= T_c(s) - \hat{T}_c(s)\\ &= \underbrace{\begin{bmatrix}(1 - H(s))\,G_c(s), & -H(s)G_n(s), & -H(s)\end{bmatrix}}_{H_{cl}(s)}\begin{bmatrix}\boldsymbol{W}_c(s)\\ W_n(s)\\ V_m(s)\end{bmatrix}.\end{aligned} \tag{5.28}$$

The PSD of $e(t)$ is

$$S_e(\omega) = H_{cl}(j\omega) W H_{cl}^T(-j\omega), \tag{5.29}$$

where $W = diag\left(\begin{bmatrix} W_{\theta_1} & W_{\theta_2} & W_r & V \end{bmatrix}\right)$. Substituting Eq. (5.29) into Eq. (5.43) and evaluate the integral numerically give the Hadamard variance of the clock estimation error $e(t)$. This filtered system includes the fractional pulsar timing noise, $G_n(s)$, the clock noise, $G_c(s)$, and the steady state Kalman filter, $H(s)$, designed using the Charef approximation, $\hat{G}_n(s)$.

5.5 Frequency Stability Analysis

5.5.1 Allan and Hadamard Variance

The Hadamard variance is a stability variance similar to the Allan variance [77, 78]. They were devised to obtain the PSD of the input noise of a non-stationary process, $x(t)$, from its output. Hadamard variance is used in this analysis instead of Allan variance or σ_z from [76] because of two reasons. First the PSD of the pulsar timing residuals can have slopes less than to -4 ($\alpha > 2$). Second the Hadamard variance has a transfer function interpretation that allows the stability variance to be computed directly using the PSD of the pulsar timing residuals. Such an interpretation is not available for σ_z. The formal definition of Allan and Hadamard variances respectively are

$$\sigma_y^2(\tau) = \frac{1}{2} E\left[(\bar{Y}(t+\tau) - \bar{Y}(t))^2\right] \tag{5.30}$$

and

$$\sigma_H^2(\tau) = \frac{1}{6} E\left[(\bar{Y}(t+2\tau) - 2\bar{Y}(t+\tau) + \bar{Y}(t))^2\right], \tag{5.31}$$

where

$$\bar{Y}(t) = \frac{1}{\tau} \int_t^{t+\tau} \dot{x}(\sigma)\, d\sigma = \frac{x(t+\tau) - x(t)}{\tau} \tag{5.32}$$

The signal $\bar{Y}(t)$ is interpreted as the averaged frequency from t to $t+\tau$. The units are (s/s). The Allan variance is the first difference of the averaged clock frequency, whereas the Hadamard variance is the second difference. One can interpret the Allan and the Hadamard

deviations as the average change in $\bar{Y}(t)$ between two measurement times that are τ seconds apart.

Substituting Eq. (5.32) into Eq. (5.31) gives

$$\begin{aligned} \sigma_H^2(\tau) &= E\left[q^2(t)\right] \\ q(t) &= \frac{1}{\sqrt{6}\tau}\left[x(t+3\tau) - 3x(t+2\tau) + 3x(t+\tau) - x(t)\right]. \end{aligned} \tag{5.33}$$

Taking the expectation of $q(t)$ in Eq. (5.33) gives 0 because all the initial conditions are 0, i.e., $E[q(t)] = 0$. Even though $x(t)$ is a non-stationary process, $q(t)$ remains stationary because of the differencing operation. The output, $q(t)$, can be obtained by feeding $x(t)$ into three differencing filters with identical impulse response of the form

$$h_\tau(t) = \delta(t+\tau) - \delta(t). \tag{5.34}$$

In other words,

$$q(t) = \frac{1}{\sqrt{6}\tau} h_\tau(t) * h_\tau(t) * h_\tau(t) * x(t), \tag{5.35}$$

where $*$ denotes convolution. The frequency domain representation of $q(t)$ is

$$Q(s) = \frac{1}{\sqrt{6}\tau} H_\tau(s) H_\tau(s) H_\tau(s) X(s), \tag{5.36}$$

where the transfer function is

$$H_\tau(s) = e^{\tau s} - 1. \tag{5.37}$$

From linear system theory, the output PSD, $S_y(\omega)$, of a single-input-single-output system, $H(s)$, with input PSD, $S_x(\omega)$, is

$$S_y(\omega) = \|H(j\omega)\|^2 S_x(\omega), \tag{5.38}$$

where $\|z\|$ is the magnitude of z [44]. For a multiple-input-single-output system, the output PSD is

$$S_y(\omega) = |H(j\omega) W_x H(-j\omega)^T|, \tag{5.39}$$

where $|\cdot|$ is absolute value. Thus, the PSD of $q(t)$ is

$$S_q(\omega) = \frac{1}{6\tau^2} \|H_\tau(j\omega)\|^6 S_x(\omega). \tag{5.40}$$

where $S_x(\omega)$ is the PSD of $x(t)$. The transfer function of the differencing filter evaluated along the ω axis is

$$\begin{aligned} H_\tau(j\omega) &= e^{j\tau\omega} - 1 \\ &= \cos(\tau\omega) + j\sin(\tau\omega) - 1. \end{aligned} \tag{5.41}$$

Substituting Eq. (5.41) into Eq. (5.40) gives

$$\begin{aligned} S_q(\omega) &= \frac{1}{6\tau^2}\left((\cos(\tau\omega)-1)^2 + \sin^2(\tau\omega)\right)^{\frac{6}{2}} S_x(\omega) \\ &= \frac{1}{6\tau^2}\left(2 - 2\cos(\tau\omega)\right)^3 S_x(\omega) \\ &= \frac{32}{3\tau^2}\sin^6\left(\frac{\tau\omega}{2}\right) S_x(\omega). \end{aligned} \tag{5.42}$$

The Hadamard variance, $\sigma_H^2(\tau)$, of $x(t)$ or equivalently the variance of $q(t)$ is obtained by integrating the output PSD, $S_q(\omega)$, with respect to the frequency, ω, from $-\infty$ to ∞,

$$\sigma_H^2(\tau) = \frac{1}{2\pi}\int_{-\infty}^{\infty} \frac{32}{3\tau^2}\sin^6\left(\frac{\tau\omega}{2}\right) S_x(\omega)d\omega. \tag{5.43}$$

The integral equation for Allan variance can be derived similarly, which is

$$\sigma_y^2(\tau) = \frac{1}{2\pi}\int_{-\infty}^{\infty} \frac{8}{\tau^2}\sin^4\left(\frac{\tau\omega}{2}\right) S_x(\omega)d\omega. \tag{5.44}$$

For certain special cases Eq. (5.43) and Eq. (5.44) have known closed form solutions.

5.5.1.1 Fractional Integration of White Noise

Fractional integration of white noise is modeled as

$$\overset{\alpha}{x}(t) = w(t), \tag{5.45}$$

where α is a real number and represents the integration order. The continuous time white noise, $w(t)$, has a correlation function of $E[w(t)w(\tau)] = W_\alpha\delta(t-\tau)$. An example of this type of process is t_c in Eq. (5.6). Taking the Laplace transform of Eq. (5.45) gives

$$X(s) = \frac{1}{s^\alpha}W(s). \tag{5.46}$$

Table 5.1: Relationship Between Stability Variances and Input PSD, W_α [9, 10, 11]

Name	**Abbrev.**	α	$\sigma_y^2(\tau)$	$\sigma_H^2(\tau)$
White Phase Noise	(WPN)	0	$\frac{6W_0}{\tau^2\Delta t}$	$\frac{10W_0}{3\tau^2\Delta t}$
Flicker Phase Noise	(FPN)	0.5	$\frac{\left[3\left(\gamma+\ln(\frac{\pi\tau}{\Delta t})\right)-\ln(2)\right]W_{0.5}}{\pi\tau^2}$	$\frac{\left[10\left(\gamma+\ln(\frac{\pi\tau}{\Delta t})\right)+\ln(3)-\ln(64)\right]W_{0.5}}{3\pi\tau^2}$
White Frequency Noise	(WFN)	1	$\frac{W_1}{\tau}$	$\frac{W_1}{\tau}$
Flicker Frequency Noise	(FFN)	1.5	$\frac{2\ln(2)W_{1.5}}{\pi}$	$\frac{\ln(\frac{256}{27})W_{1.5}}{2\pi}$
Random Walk Frequency Noise	(RWFN)	2	$\frac{\tau W_2}{3}$	$\frac{\tau W_2}{6}$
Flicker Walk Frequency Noise	(FWFN)	2.5		$\frac{2\tau^2\left(\frac{27\ln(3)}{16}-\ln(4)\right)W_{2.5}}{3\pi}$
Random Run Frequency Noise	(RRFN)	3		$\frac{11\tau^3W_3}{120}$
Euler's constant, $\gamma = 0.577216$. The bandwidth of the band-limited white noise $w(t)$ is $f_b = 1/(2\Delta t)$, where Δt is the sample interval of the measurement				

The units of $x(t)$ are typically given in seconds. Applying Eq. (5.38) gives the PSD of $x(t)$,

$$S_x(\omega) = \frac{W_\alpha}{|\omega^{2\alpha}|}. \tag{5.47}$$

It is well known that Eq. (5.43) and Eq. (5.44) have closed form solutions for Eq. (5.45) with certain values of α, and they are listed in Table 5.1. While there are no closed form solutions for general values of α, numerical integration shows the result is consistent in the sense that the slope of the resulting curve is in between that of the two neighboring cases in Table 5.1.

5.5.1.2 Stationary Process

Even though the Hadamard and Allan variances were devised for non-stationary processes, they are also applicable to stationary processes. If $S_x(\omega)$ is the PSD of a stationary process, then Eq. (5.43) and Eq. (5.44) converge as well because

$$\begin{aligned}
\frac{3\tau^2}{32}\sigma_H^2(\tau) &= \frac{1}{2\pi}\int_{-\infty}^{\infty}\sin^6\left(\frac{\tau\omega}{2}\right)S_x(\omega)d\omega \\
\frac{\tau^2}{8}\sigma_y^2(\tau) &= \frac{1}{2\pi}\int_{-\infty}^{\infty}\sin^4\left(\frac{\tau\omega}{2}\right)S_x(\omega)d\omega
\end{aligned} \tag{5.48}$$

are bounded from above by

$$P_\infty = \frac{1}{2\pi} \int_{-\infty}^{\infty} S_x(\omega) d\omega, \tag{5.49}$$

which is the steady state variance of the stationary process. Section 5.6 relies on this fact to evaluate the stability of the pulsar timing noise, and the filtered clock system.

Since a stationary process has a steady state variance, P_∞, the following derives a relationship between P_∞ and the long-term Hadamard variance, $\sigma^2_{H,\infty}(\tau)$. Equation (5.43) can be rewritten using trigonometric identity as

$$\begin{aligned}
\sigma_H^2(\tau) &= \frac{1}{2\pi} \int_{-\infty}^{\infty} \frac{32}{3\tau^2} \sin^6\left(\frac{\tau\omega}{2}\right) S_x(\omega) d\omega \\
&= \frac{1}{6\pi\tau^2} \int_{-\infty}^{\infty} \big[10 - 15\cos(\tau\omega) + 6\cos(2\tau\omega) - \cos(3\tau\omega)\big] S_x(\omega) d\omega \\
&= \frac{1}{3\pi\tau^2} \Big[10 \int_0^{\infty} S_x(\omega) d\omega + \int_0^{\infty} \big[-15\cos(\tau\omega) + 6\cos(2\tau\omega) - \cos(3\tau\omega)\big] S_x(\omega) d\omega \Big].
\end{aligned} \tag{5.50}$$

The first integral is independent of τ and is related to P_∞. The intent is to show that as τ approaches infinity the second integral approaches 0. The second integral can be decomposed into three integrals of the form

$$\begin{aligned}
I &= \lim_{\tau\to\infty} \int_0^{\infty} \cos(a\tau\omega) S_x(\omega) d\omega \\
&= \lim_{\tau\to\infty} \left[\frac{S_x(\omega)\sin(a\tau\omega)}{a\tau} \Big|_0^{\infty} - \int_0^{\infty} \frac{\sin(a\tau\omega)}{a\tau} S_x'(\omega) d\omega \right] \\
&= \lim_{\tau\to\infty} - \int_0^{\infty} \frac{\sin(a\tau\omega)}{a\tau} S_x'(\omega) d\omega.
\end{aligned} \tag{5.51}$$

In order to show Eq. (5.51) approaches 0, we bound the magnitude of the integral and show

the bound approaches to 0 as τ approaches infinity,

$$\begin{aligned}
&\left|\lim_{\tau\to\infty}\int_0^\infty \frac{\sin(a\tau\omega)}{a\tau}S'_x(\omega)d\omega\right| \\
&\leq \lim_{\tau\to\infty}\int_0^\infty \left|\frac{\sin(a\tau\omega)}{a\tau}S'_x(\omega)\right| d\omega \\
&\leq \lim_{\tau\to\infty}\frac{1}{a\tau}\int_0^\infty |\sin(a\tau\omega)|\,|S'_x(\omega)|\,d\omega \\
&\leq \lim_{\tau\to\infty}\frac{1}{a\tau}\int_0^\infty |S'_x(\omega)|\,d\omega \\
&\leq \lim_{\tau\to\infty}\frac{1}{a\tau}M,
\end{aligned} \tag{5.52}$$

where

$$\begin{aligned}
M &= \int_0^\infty |S'_x(\omega)|\,d\omega \\
&= \int_0^{\omega_b} |S'_x(\omega)|d\omega - \int_{\omega_b}^\infty S'_x(\omega)d\omega \\
&= \int_0^{\omega_b} |S'_x(\omega)|d\omega - \Big[\cancelto{0}{S_x(\infty)} - S_x(\omega_b)\Big]
\end{aligned} \tag{5.53}$$

In Eq. (5.53), the second line breaks the integration interval into two parts. The frequency, ω_b, is defined such that $S'_x(\omega)$ no longer changes sign when $\omega > \omega_b$. Assuming $S_x(\omega)$ is strictly proper, then $S'_x(\omega) < 0$ for $\omega > \omega_b$; hence, the negative sign is added in front of the second integral. This integral is finite because $\lim_{\omega\to\infty} S_x(\omega) = 0$. Inside the first interval, $S'_x(\omega)$ can be both positive and negative due to under-damped notch or resonance mode. If there is no under-damped modes, then $\omega_b = 0$. Because the anti-derivative of $S'_x(\omega)$ is the PSD itself, $S_x(\omega)$ is required to be $0 \leq S_x(\omega) < \infty$ for all $\omega \geq 0$. This is true for stationary system because it has no poles on the imaginary axis. Since the integration limits and the integrand of the first integral are finite and bounded, the first term in Eq. (5.53) is also finite.

Since both integrals in Eq. (5.53) are finite, $M < \infty$, which implies the bound on the magnitude of the integral in Eq. (5.52) approaches 0 as τ approaches infinity. Because the

magnitude cannot be negative, the integral itself has to be 0, i.e, $I = 0$. Therefore, the Hadamard variance in Eq. (5.50) reduces to

$$\begin{aligned}\sigma_H^2(\tau) &= \frac{10}{3\tau^2} P_\infty \\ &:= \sigma_{H,\infty}^2(\tau).\end{aligned} \tag{5.54}$$

This result applies to both the finite dimensional LTI system and the factional stationary system in Eq. (5.21). Equation (5.54) implies that minimizing the long-term Hadamard variance for stationary process is the same as minimizing the steady state variance. A practical application of Eq. (5.54) is obtaining the steady state variance of the system from the Hadamard deviation plot.

From the form of Eq. (5.54), one can see that it is similar to that of the WPN in Table 5.1, which is

$$\sigma_{H,\alpha=0}^2(\tau) = \frac{10}{3\tau^2} P_{\alpha=0}, \tag{5.55}$$

where $P_{\alpha=0} = W_0/\Delta t$ is the variance of the band-limited white noise. This means that the long-term Hadamard variance, $\sigma_{H,\infty}^2(\tau)$ for stationary process, is the same as that of WPN whose variance is equal to the steady state variance of the system. Their slopes on the Hadamard deviation plot are both -1. Intuitively, this relationship make sense because in steady state $x(t)$ is ergodic, which means time averaging is equal to the ensemble averaging.

For certain special cases of stationary processes, Eq. (5.54) can be shown to be true explicitly. If $x(t)$ in the frequency domain is

$$X(s) = \left(\frac{\omega_c}{s+\omega_c}\right)^\alpha W(s), \quad \omega_c > 0, \tag{5.56}$$

where $\alpha = 1, 2, 3$, then the closed form solution of Eq. (5.43) can be found using an integral table [79]. They are

$$\begin{aligned}
\sigma_{H,1}^2(\tau) &= \frac{W_r \omega_c}{6\tau^2}\left[10 - 15e^{-\omega_c\tau} + 6e^{-2\omega_c\tau} - e^{-3\omega_c\tau}\right] \\
\sigma_{H,2}^2(\tau) &= \frac{W_r \omega_c}{12\tau^2}\left[10 - 15\left(\omega_c\tau + 1\right)e^{-\omega_c\tau} + 6\left(2\omega_c\tau + 1\right)e^{-2\omega_c\tau} - \left(3\omega_c\tau + 1\right)e^{-3\omega_c\tau}\right] \\
\sigma_{H,3}^2(\tau) &= \frac{W_r \omega_c}{16\tau^2}\left[10 - 5\left(\omega_c^2\tau^2 + 3\omega_c\tau + 3\right)e^{-\omega_c\tau} + 2\left(4\omega_c^2\tau^2 + 6\omega_c\tau + 3\right)e^{-2\omega_c\tau}\right. \\
&\qquad \left. - \left(3\omega_c^2\tau^2 + 3\omega_c\tau + 1\right)e^{-3\omega_c\tau}\right]
\end{aligned} \tag{5.57}$$

respectively, where W_r is the PSD of the input noises. Since the exponentials, $e^{-\omega_c\tau}$, $e^{-2\omega_c\tau}$ and $e^{-3\omega_c\tau}$, all decay faster than $1/\tau^2$, the variances at large τ are

$$\begin{aligned}\sigma^2_{H,\infty,1}(\tau) &= \frac{5W_r\omega_c}{3\tau^2}\\ \sigma^2_{H,\infty,2}(\tau) &= \frac{5W_r\omega_c}{6\tau^2}\\ \sigma^2_{H,\infty,3}(\tau) &= \frac{5W_r\omega_c}{8\tau^2}.\end{aligned} \tag{5.58}$$

The steady state variance of Eq. (5.56) for $\alpha = 1, 2, 3$ can be obtained by solving the algebraic Lyapunov equation. They are

$$\begin{aligned}P_{\infty,1} &= \frac{W_r\omega_c}{2}\\ P_{\infty,2} &= \frac{W_r\omega_c}{4}\\ P_{\infty,3} &= \frac{3W_r\omega_c}{16}.\end{aligned} \tag{5.59}$$

Substituting Eq. (5.59) into Eq. (5.54) recovers Eq. (5.58).

5.6 Frequency Stability Analysis Result

5.6.1 Atomic Clocks and Pulsar Signals

The commercially available Cs 5071A cesium clock manufactured by Microsemi is chosen for the analysis [80]. Because long-term frequency stability data for this clock is not available, it was assumed that the noises of Cs 5071A is dominated by RWFN after $\tau = 1$ *month*. The strengths of WFN and RWFN for the clock are $W_1 = 2.60 \times 10^{-22}(s^2/s)$ and $W_2 = 1.00 \times 10^{-34}$ (s^2/s^3) respectively.

As mentioned in Section 5.3.2, this analysis considers two scenarios. The Hadamard deviations of the pulsar timing noise, $n(t)$, for scenario #1 are plotted in Fig. 5.1. They are obtained by substituting Eq. (5.20) for $S_x(\omega)$ in Eq. (5.43). This figure does not include the effects of phase and radiometer noises on the frequency stability. The curves in Fig. 5.1 represent fractional integration of white noise. The slopes of the curves are related to the value of α. Several pulsar timing noises have diverging frequency stability while others have decreasing trend. The following analysis only focuses on J0437+4715 and J1909-3744

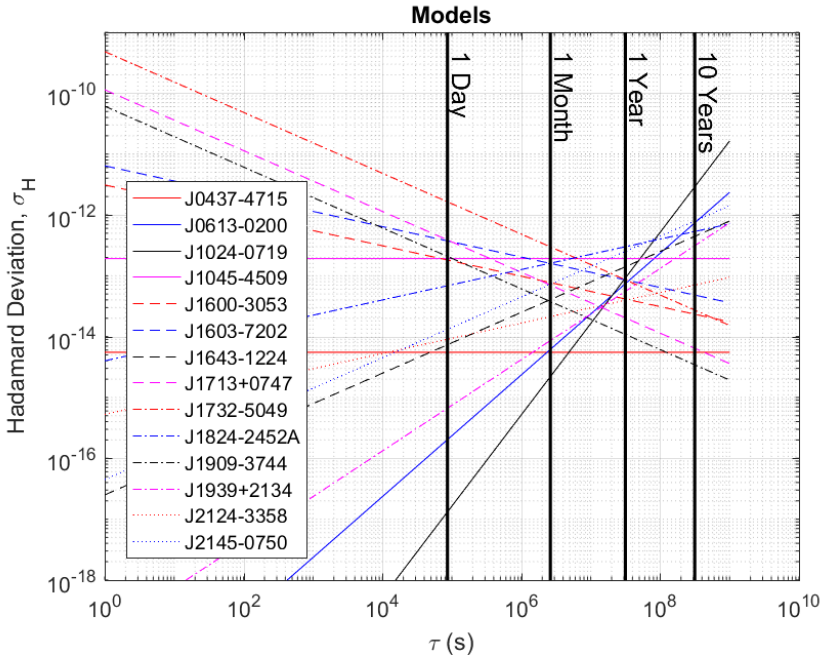

Figure 5.1: Hadamard deviation of the pulsar timing noise, $n(t)$ for scenario #1. The TOA uncertainty, $v(t)$, due to radiometer and phase jitter is not included.

because they have the least amount of timing noise and non-diverging frequency stability.

The Hadamard deviations of the pulsar timing noise for the second scenario are plotted in Fig. 5.2. Eq. (5.19) is used instead of Eq. (5.20). At small averaging time ($\tau < 1\ yr$), the slopes are the same as the previous scenario. They are governed by the order of α and the σ_H value at $\tau = 1$ is dictated by the strength of the white noise, W_r. In this scenario, the pulsar timing noises behave like fractional integration of white noise at short averaging time. At large averaging time ($\tau > 1\ yr$) all pulsars have a slope of -1, and this is a result of the model being stationary. The transition time from fractional integration of white noise to stationary process is dictated by the corner frequency, $\omega_c = 2\pi f_c$.

The model parameters for J0437+4715 are $\alpha = 1.5$, $f_c = 0.067\ yr^{-1}$, and $W_r = 1.14 \times 10^{-27}\ yr^3$. The model parameters for J1909-3744 are $\alpha = 1$, $f_c = 0.5\ yr^{-1}$, and $W_r = 1.2 \times 10^{-29}\ yr^3$. The fractional PSD of J0437+4715 for both scenarios are plotted in Fig. 5.3. The model $\hat{G}_n(s)$ is approximately equal to $G_n(s)$ over the frequency range of $\omega \in [0,\ 8 \times 10^{-7}\ rad/s]$, and this is the region where pulsar timing noise is dominant. Since the model

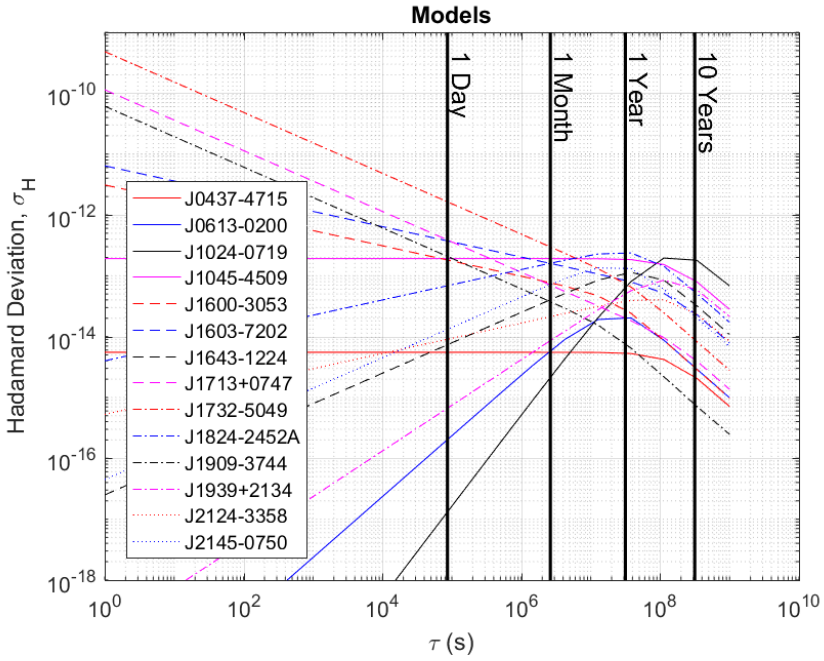

Figure 5.2: Hadamard deviation of the pulsar timing noise, $n(t)$ for scenario #2. The TOA uncertainty, $v(t)$, due to radiometer and phase jitter is not included.

parameter α of J1909-3744 is 1, the Charef approximation is not needed for this pulsar. The white noise curve corresponds to a RMS value of $\sigma_{ave} = 100\ ns$ after an averaging time of $T_{obs} = 30\ min$. This RMS value accounts for the TOA uncertainty due to radiometer noise and the phase jitter.

The Hadamard variance of the unfiltered clock $\sigma^2_{H,u}$, and the pulsar timing noise, $\sigma^2_{H,n}$, were obtained by substituting Eq. (5.8) and Eq. (5.19) for $S_x(\omega)$ in Eq. (5.43), respectively. The results are plotted in Fig. 5.4. The dominant noise of the clock for $\tau < 1\ yr$ and $\tau > 1\ yr$ are WFN and RWFN, respectively. The pulsar signal in the plot is obtained by subtracting $t_c(t)$ from Eq. (5.16),

$$\begin{aligned} p(t) &= y(t) - t_c(t) \\ &= n(t) + v(t). \end{aligned} \tag{5.60}$$

This signal represents the ideal pulsar signal without clock deviation. Since the pulsar timing noise, $n(t)$, and the white measurement noise, $v(t)$, are assumed to be independent, the Hadamard variance of the pulsar signal, $\sigma^2_{H,p}(\tau)$, is obtained by adding $\sigma^2_{H,n}(\tau)$ and

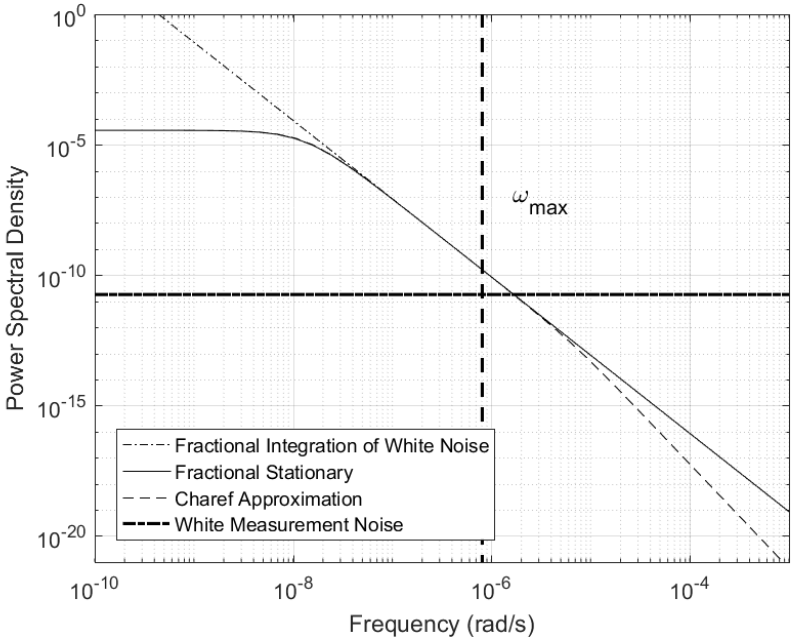

Figure 5.3: The timing noise PSD of J0437-4715 for both scenarios. The Charef model well approximates the fractional stationary noise model from 0 to 8×10^{-7} rad/s.

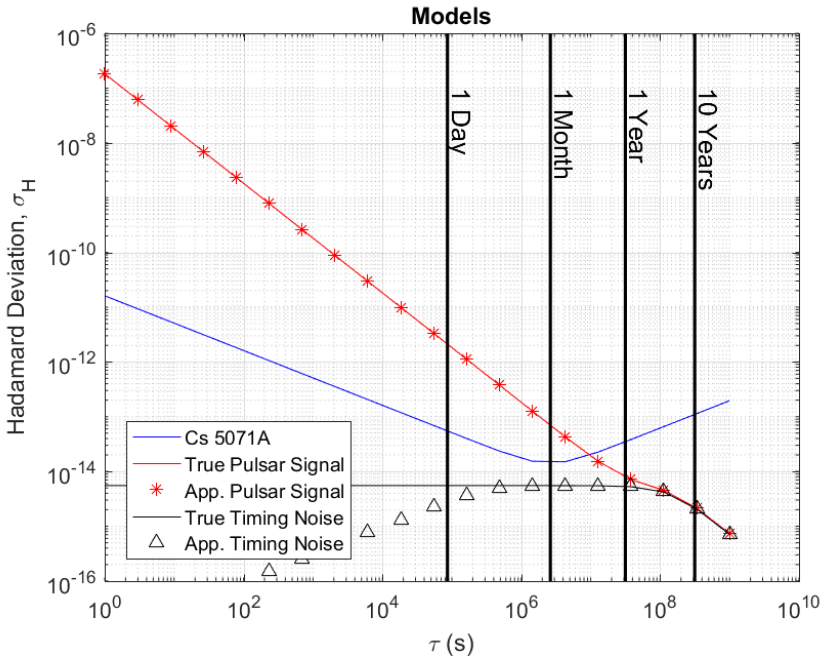

Figure 5.4: Hadamard deviation of Cs 5071A, J0437-4715 signal, J0437-4715 timing noise, and Charef approximation. The timing noise model in this figure is Eq. (5.19) rather than Eq. (5.20)

$\sigma^2_{H,v}(\tau)$ together,

$$\sigma^2_{H,p}(\tau) = \sigma^2_{H,n}(\tau) + \sigma^2_{H,v}(\tau), \tag{5.61}$$

where $\sigma^2_{H,v}(\tau)$ is computed using Eq. (5.55). When $\tau < 1\ yr$ the pulsar signal is dominated by the white measurement noise, $v(t)$, and when $\tau > 1\ yr$ the pulsar timing noise, $n(t)$, dominates. The relative position of the curves in Fig. 5.4 suggests one can use a Kalman filter to combine the short-term stability of the atomic clock and the long-term stability of the pulsar signal to realize a pulsar-aided atomic clock.

5.6.2 Pulsar-Aided Atomic Clocks

The performance of two clock and pulsar pairs are presented in this section. The first pair uses J0437-4715 as the calibration source. The second pair uses J1909-3744 to show the improvement of the filtered system when a more stable pulsar signal is used. For simplicity purposes, the RMS values of the white measurement noise, $v(t)$, in Eq. (5.16) for the two pairs are $\sigma_{ave} = 100\ ns$ after an averaging time of $T_{obs} = 30\ min$.

5.6.2.1 Scenario #1

In this scenario, the pulsar timing noise is integration of white noise which is indistinguishable from the clock deviation. This type of system is termed unobservable. Therefore, the Kalman filter is designed using only $\boldsymbol{x}_c$. The frequency stability of the filtered clock is expected to merge into that of the pulsar signal at large averaging time. The filtered system performance for the first pair is shown in Fig. 5.5. The Hadamard deviation of the filtered system is denoted as $\sigma_{H,f}$. The solid curve is the filtered clock and it is computed by substituting $S_e(\omega)$ for $S_x(\omega)$ in Eq. (5.43). The UTC curve is included in Fig. 5.5 as a reference point [81]. The improvements relative to the exponents of the pulsar-only timescale and the unfiltered clock are defined as

$$\begin{aligned} \epsilon_p &= \frac{\log(\sigma_{H,p}(\tau)) - \log(\sigma_{H,f}(\tau))}{\log(\sigma_{H,p}(\tau))} \times 100, \\ \epsilon_u &= \frac{\log(\sigma_{H,u}(\tau)) - \log(\sigma_{H,f}(\tau))}{\log(\sigma_{H,u}(\tau))} \times 100. \end{aligned} \tag{5.62}$$

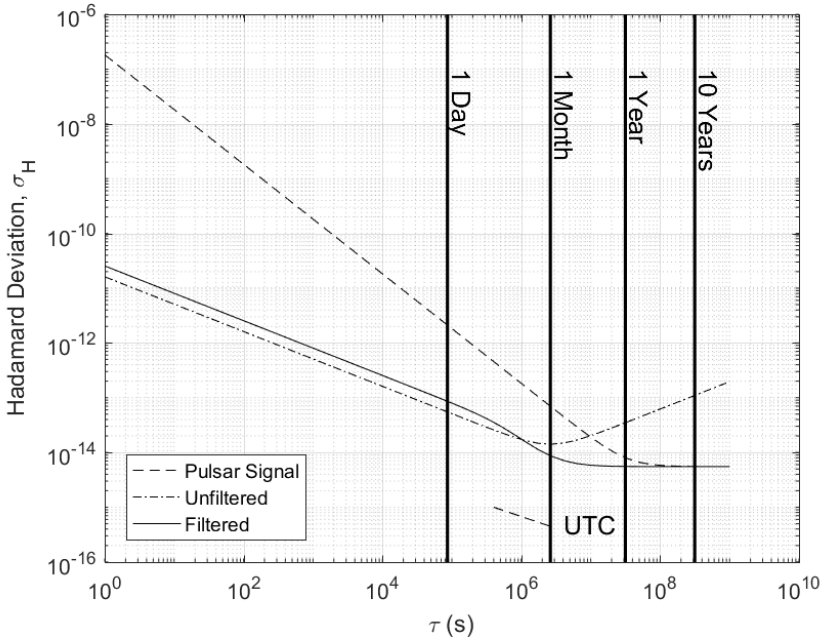

Figure 5.5: Filtered clock performance if the pulsar timing noise for J0437-4715 is fractional integration of white noise.

At small averaging time, there is a small gap between the filtered clock and the unfiltered clock. This small gap is caused by the filtering operation, the error system in Eq. (5.28) is not only forced by the clock noise but also the measurement noise and pulsar timing noise. As a result, $\sigma_{H,f}$ is slightly higher than $\sigma_{H,u}$, and this is the reason that pulsars are not useful at short averaging time. If the filtering operation is removed by setting $K = 0$, then $\sigma_{H,f} = \sigma_{H,u}$. At large averaging time, the filtered clock has improved frequency stability relative to the unfiltered clock because the α parameter for J0437-4715 is equal to 1.5. The performance improvement, ϵ_u, at $\tau = 1\ month$, $\tau = 1\ yr$ and $\tau = 10\ yr$ are 2%, 6%, and 10% respectively.

For the second pair, the frequency stability at $\tau = 1\ month$ is worse than the previous pair because the pulsar timing noise of J1909-3744 is stronger than J0437-4715 at $\tau = 1\ month$. However, the improvement in frequency stability relative to the unfiltered clock at large averaging time is more significant than the previous pair. Since the α parameter for J1909-3744 is 1, the frequency stability decreases following the trend of WFN. The performance

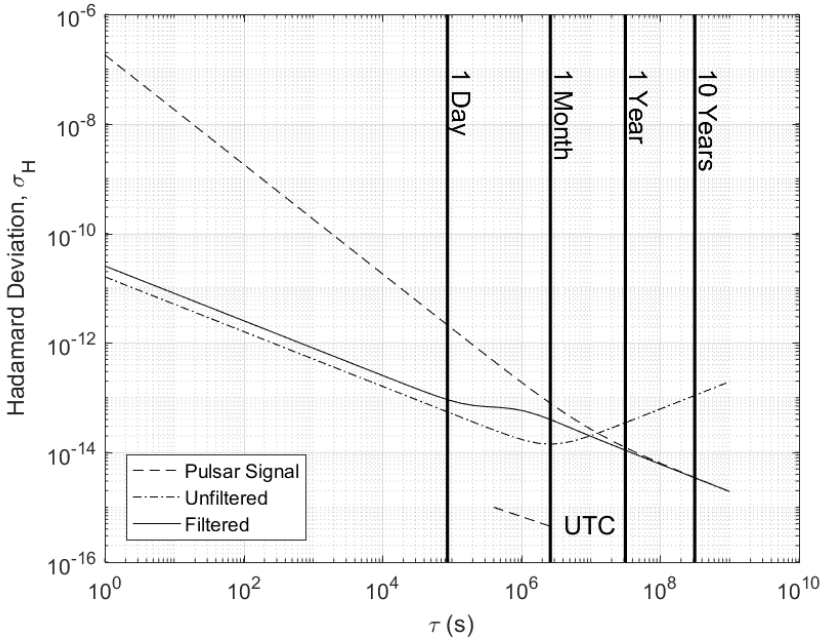

Figure 5.6: Filtered clock performance if the pulsar timing noise for J1909-3744 is fractional integration of white noise.

improvement ϵ_u at $\tau = 1\ month$, $\tau = 1\ yr$ and $\tau = 10\ yr$ are -3%, 4%, and 11% respectively. This example illustrates the importance of the pulsar selection.

5.6.2.2 Scenario #2

In this scenario, the pulsar timing noise is modeled as fractional stationary noise; therefore, one can design a Kalman filter that distinguishes the pulsar timing noise from clock deviation using the dynamics of the fractional stationary noise. In this scenario, the combined system in Eq. (5.24) is observable and controllable, so the error covariance of the filtered system has a steady state. Figure 5.7 shows the frequency stability of Cs 5071A with J0437-4715. The gap at small averaging time is slightly larger than the previous scenario because the Kalman gain is larger. The filtered system reaches the steady state condition at $\tau = 10\ yr$ as indicated by the -1 slope. The ϵ_u for the first pair are 1%, 6% and 13% at $\tau = 1\ month$, $\tau = 1\ yr$ and $\tau = 10\ yr$ respectively.

Figure 5.8 shows the Hadamard deviation of the filtered system for the second pair. The

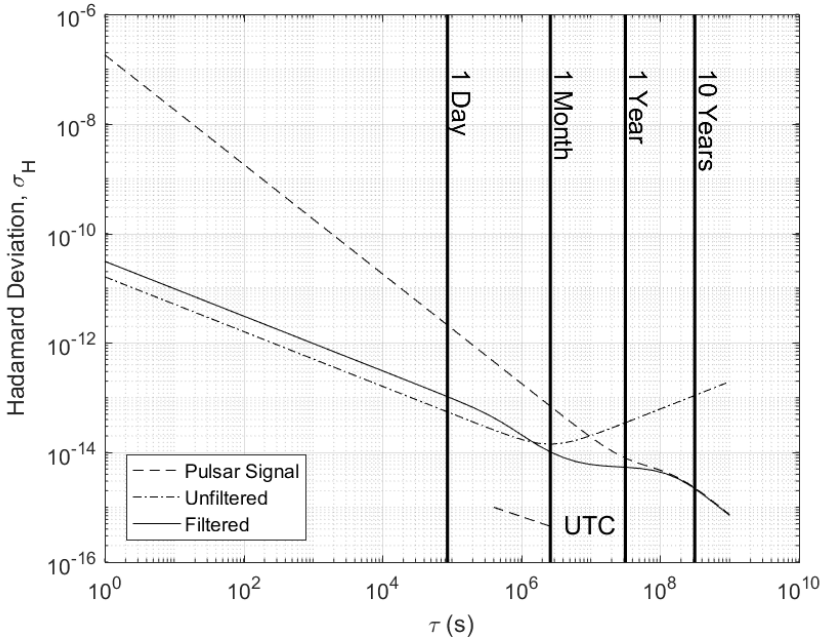

Figure 5.7: Filtered clock performance if the pulsar timing noise for J0437-4715 is fractional stationary noise.

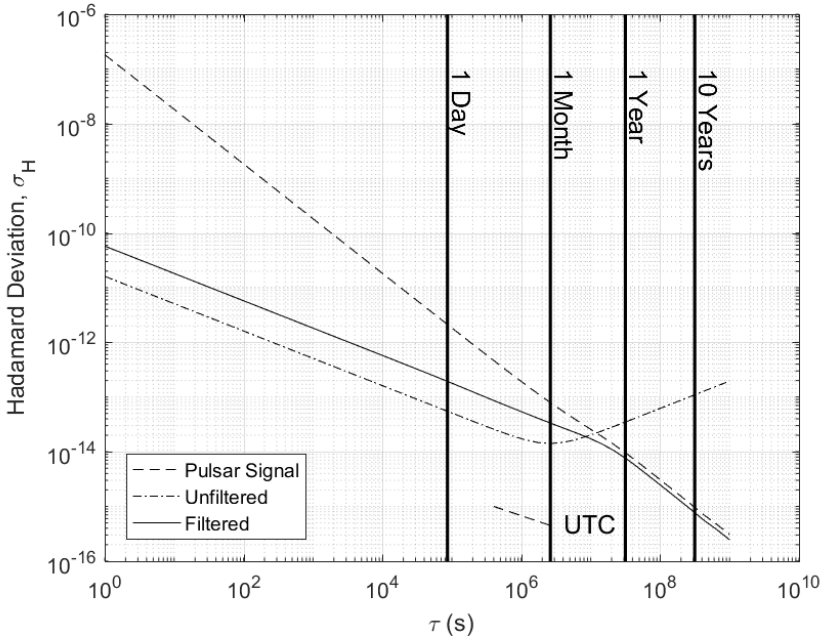

Figure 5.8: Filtered clock performance if the pulsar timing noise for J1909-3744 is fractional stationary noise.

Hadamard deviation at 10 yr is 8.1×10^{-16} and continues to decrease with a slope of -1. The filtered system begins to show improvements over the unfiltered clock at $\tau = 5$ $month$. Comparing to the unfiltered clock, the improvements are -3%, 5%, and 17% at $\tau = 1$ $month$, $\tau = 1$ yr and $\tau = 10$ yr respectively. The steady state filter 1σ bound is reduced from 393 ns to 136 ns by simply observing a different pulsar. This improvement is a result of the smaller W_r value of J1909-3744. Furthermore, the improvement, ϵ_p, is 0.6% during steady state.

The Kalman filter in this scenario is designed using an approximate model of the pulsar timing noise, $\hat{G}_n(s)$. As a result, the steady state condition from the algebraic Ricatti equation is not exact. However, this mismatch can be made arbitrarily small by increasing the order of $\hat{G}_n(s)$. The difference between the filter 1σ and the value obtained using Eq. (5.54) at the largest τ is $< 1\%$. As for the second pair, the steady state conditions are exact because the integration order, α, of J1909-3744 is an integer. The differences in both cases are $< 0.1\%$, which is likely a result of numerical integration. Since a Kalman filter is used, the steady state error covariance is not only dependent on the pulsar measurement noise covariance but also that of the process noise. In other words, a more precise atomic clock not only improves the short-term frequency stability but also lowers the error covariance of the time estimate at large averaging time.

5.7 Discussion

Since this model-based method does not require numerical integration of the stochastic processes to simulate individual measurements, it efficiently determines the expected frequency stability for a given pulsar and clock pair. The clock model used in the analysis consists of WFN and RWFN, but this method can also accommodate other noise model such as Flicker Frequency Noise (FFN) by adding one additional term in Eq. (5.8). While it is not possible to explicitly include FFN in the design of a Kalman filter, one can increase the PSD of WFN in the Kalman filter design to mitigate the effect of FFN. The overall performance of such a system can still be analyzed using the above method. The error system is still represented by Eq. (5.28). The differences are in the functional form of $G_c(s)$ and the

steady state gain of the Kalman filter, K.

The results from scenario #1 shows that it is possible to choose a pulsar signal with α less than 1.5 to improve the frequency stability of an unfiltered clock at large averaging time. The frequency stability, $\sigma_{H,f}$, at averaging time between $\tau = 1\ month$ and $\tau = 1\ yr$ can have different behaviors depending on the values of α and W_r. However, due to the lack of observability, the error covariance of the estimate $\hat{t}_c$ is expected to increase following the diverging behavior of the pulsar timing noise (fractional integration of white noise). The choice of pulsar only reduces the divergence rate.

In scenario #2, similar improvement in frequency stability can also be achieved. If the pulsar timing noise truly is fractional stationary, then the error covariance of the time estimate has a steady state that is dependent not only on the PSD of the pulsar timing noise but also that of the clock noise. However, it should be kept in mind that even though this system is observable and controllable, it does not necessarily mean that pulsar-aided atomic clock has infinite stability. The reason is that Eq. (5.19) obtained experimentally may deviate from reality at large averaging time due to un-modeled long-term effects, which can cause the estimation error covariance to diverge. Nevertheless, pulsar signals remain useful in enhancing the long-term frequency stability of an unfiltered clock in either scenario. Such capability is beneficial to deep space exploration probes because it reduces the need for frequent clock synchronization using Earth-based references.

The current approach for analyzing the long-term pulsar frequency stability is to perform model fitting using the pre-fit timing residuals before computing the frequency stability deviation [75, 76]. While it is reasonable to use all available data to construct a new and more refined pulsar timing model, it is also important to verify the accuracy of the existing pulsar timing model. Combining the existing pulsar timing model with a finite dimensional pulsar timing noise model such as the Charef model allows one to make TOA predictions into the future and obtain the pre-fit timing residuals to study the long-term frequency stability of the pulsar signal. If there is a diverging component in pre-fit residual, then it should be characterized and modeled. Once the statistics of the diverging component are obtained, they can be included in Eq. (5.28) to generate a more realistic frequency deviation plot. If

the pulsar timing model deviates from reality at a slow rate, then a segment of the filtered clock curve in Fig. 5.7, and Fig. 5.8 may be achievable. For example, if the frequency stability of the pre-fit residual over one year does not have a significant diverging component, then the pulsar timing signal can be used to suppress the clock RWFN for one year before the pulsar-aided system requires an update from an external reference.

CHAPTER 6

Relative Pulsar Positioning and Common Mode Rejection

6.1 Overview

This chapter investigates the potential of using differential phase measurement to estimate the position of observer #2 relative to observer #1 while rejecting common mode errors such as ephemeris bias, clock error, and pulsar timing noise in the pulsar waveform measurement. The approach to reject the common mode error is to manipulate the raw measurements in such a way that the common errors are cancelled algebraically. In order to determine the performance of such a mechanism, this chapter considered ground based pulsar measurements collected from radio observatory such as those of the Deep Space Network. Monte Carlo method is used to compare the differential phase mechanism with non-differential phase approach. The observer dynamics, pulsar model and the combined state space model are presented in Section 6.2, Section 6.3, and Section 6.4 respectively. The differential phase mechanism is shown in Section 6.5. Following this section are the numerical simulation in Section 6.6 and discussion in Section 6.7.

6.2 Observer Dynamics

Since this chapter investigates the use of differential phase measurement for ground-based observatory, the observer dynamics is related to the motion of Earth. The following gives a brief discussion of the kinematic model associated the motion of Earth relative to the Solar System Barycenter (SSB) [26, 62, 82]. Figure 6.1 shows the definition of the position vectors

used in this chapter. Let the position of the observatory in Geocentric Celestial Reference System (GCRS) be $\boldsymbol{r}_{s,i}$, where i indicates the i^{th} observatory. GCRS is an inertial reference system whose origin is located at the center of mass of Earth. Since the observatory is fixed to the ground, its position is usually provided in the International Terrestrial Reference System (ITRS) denoted as $\boldsymbol{s}_i$. Unlike GCRS, ITRS is an Earth fixed coordinate system. The transformation between ITRS and GCRS is

$$\boldsymbol{r}_{s,i}(t) = \underbrace{Q(t)R(t)W(t)}_{L(t)}\boldsymbol{s}_i. \tag{6.1}$$

The precession-nutation matrix Q represents the Celestial Intermediate Reference System (CIRS) with respect to the GCRS. This matrix accounts for the slow precession and nutation of Earth's rotational axis. The matrix R is the rotation of Earth. The matrix W models the changes of the ITRS relative to the Terrestrial Intermediate Reference System (TIRS) due to polar motion (motion of the crust). The sequence of frame transformation is

$$GCRS \Leftarrow CIRS \Leftarrow TIRS \Leftarrow ITRS. \tag{6.2}$$

If one models the above rotations using rigid body dynamics, then the velocity of the observatory relative to the GCRS frame is

$$\dot{\boldsymbol{r}}_{s,i}(t) = \underbrace{\Omega L(t)W(t)^{-1}Z_{\times}}_{J(t)}\boldsymbol{s}_i. \tag{6.3}$$

where Ω is the rotation rate of Earth; and

$$Z_{\times} = \begin{bmatrix} 0 & -1 & 0 \\ 1 & 0 & 0 \\ 0 & 0 & 0 \end{bmatrix}. \tag{6.4}$$

Let the position of Earth relative to the SSB be defined as

$$\boldsymbol{r}_{\oplus}(t) = \bar{\boldsymbol{r}}_{\oplus}(t) + \boldsymbol{b}_{ssb}, \tag{6.5}$$

where $\bar{\boldsymbol{r}}_{\oplus}$ is the ephemeris position of Earth and $\boldsymbol{b}_{ssb}$ is the ephemeris error. Because GCRS and Barycentric Celestial Reference System (BCRS) have the same orientation, the position of the observatory relative to the SSB in BCRS is

$$\boldsymbol{r}_i(t) = \boldsymbol{r}_{\oplus}(t) + \boldsymbol{r}_{s,i}(t). \tag{6.6}$$

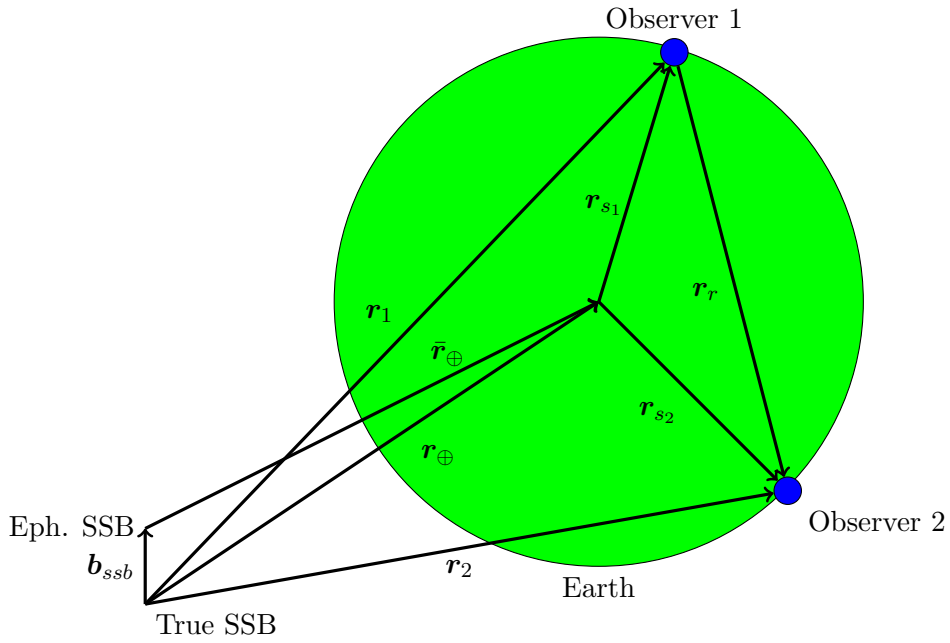

Figure 6.1: Coordinate system

Let the difference between the two observer position and velocity vectors be defined as

$$\begin{aligned}\boldsymbol{r}_r(t) &= \boldsymbol{r}_2(t) - \boldsymbol{r}_1(t) \\ &= \bar{\boldsymbol{r}}_\oplus(t) + \boldsymbol{b}_{ssb}(t) - \bar{\boldsymbol{r}}_\oplus - \boldsymbol{b}_{ssb}(t) + L(t)\left[\boldsymbol{s}_2 - \boldsymbol{s}_1\right] \\ &= L(t)\boldsymbol{s}_r.\end{aligned} \tag{6.7}$$

and

$$\begin{aligned}\dot{\boldsymbol{r}}_r(t) &= \dot{\boldsymbol{r}}_2(t) - \dot{\boldsymbol{r}}_1(t) \\ &= \dot{\bar{\boldsymbol{r}}}_\oplus(t) - \dot{\bar{\boldsymbol{r}}}_\oplus(t) + J(t)\left[\boldsymbol{s}_2 - \boldsymbol{s}_1\right] \\ &= J(t)\boldsymbol{s}_r\end{aligned} \tag{6.8}$$

Expressing the position and the velocity vector of observer #1 in terms of # 2 gives

$$\begin{aligned}\boldsymbol{r}_1(t) &= \bar{\boldsymbol{r}}_\oplus(t) + \boldsymbol{b}_{ssb} + L(t)\left[\boldsymbol{s}_2 - \boldsymbol{s}_r\right] \\ \dot{\boldsymbol{r}}_1(t) &= \dot{\bar{\boldsymbol{r}}}_\oplus(t) + J(t)\left[\boldsymbol{s}_2 - \boldsymbol{s}_r\right].\end{aligned} \tag{6.9}$$

6.3 Pulsar Model

Let the signal waveform of the radio pulsar at the SSB be modeled as

$$\lambda(t) = \lambda_b + \lambda_s s(\phi(t)), \tag{6.10}$$

where λ_b is the background rate and λ_s is the source rate. The function $s(\cdot)$ is periodic and describes the pulsar signal profile. The phase equation is

$$\phi(t) = \phi_0 + \dot{\phi}[t - t_0] + \frac{\ddot{\phi}}{2}[t - t_0]^2, \tag{6.11}$$

where ϕ_0, $\dot{\phi}$, $\ddot{\phi}$ and t_0 are all known values. The measurement equation at the observatory is

$$y(t) = \lambda_b + \lambda_s s(\phi_i(t)) + v(t), \tag{6.12}$$

where $v(t)$ is the measurement noise from the radiometer. See. Appendix A. In order to limit the scope of the study, only the geometric delay, $\boldsymbol{r}_i(t)$, clock error, $t_c(t)$, and pulsar timing noise, $n_\eta(t)$, are modeled. Therefore, the phase equation at the observatory is simply

$$\phi_i(t) = \phi_0 + \dot{\phi}\left[t + \frac{\boldsymbol{n}^T\boldsymbol{r}_i(t)}{c} - t_c(t) - t_0\right] + \frac{\ddot{\phi}}{2}\left[t + \frac{\boldsymbol{n}^T\boldsymbol{r}_i(t)}{c} - t_c(t) - t_0\right]^2 + n_\eta(t), \tag{6.13}$$

where $\boldsymbol{n}$ is the direction of the pulsar.

While millisecond pulsars have stable rotation dynamics, they are still corrupted by a small amount of fractional stationary noise whose PSD is

$$S_n(\omega) = \frac{W_\eta}{\left(1 + \left(\frac{\omega}{\omega_c}\right)^2\right)^\alpha}, \tag{6.14}$$

where W_r, α, and ω_c are positive fitting parameters [42]. They represent the strength of the white noise, the integration order, and the corner frequency of the fractional Linear Time Invariant (LTI) system. The parameters of Eq. (6.14) for various pulsars can be found in current literature [53]. The reason $S_n(\omega)$ is considered as a fractional PSD is because α is a real number. If $\alpha = 1.21$, then the slope of the high frequency roll-off in log-log plot is -2.42. This is different from the typical LTI system whose roll-off is an integer multiple of 2. The fractional PSD in Eq. (6.14) can be approximated by finite dimensional LTI system [54]. The approximated system is essentially a high order stable LTI system. Therefore, the pulsar timing noise in this study is modeled using a shaping filter with large correlation time,

$$\begin{aligned} \dot{\boldsymbol{\eta}}(t) &= F_\eta\boldsymbol{\eta}(t) + G_\eta w_\eta(t) \\ n_\eta(t) &= H_\eta\boldsymbol{\eta}(t) \end{aligned} \tag{6.15}$$

where F_η is a stable matrix.

6.4 Relative Positioning System

Combining the observer dynamics in Section 6.2 and the pulsar measurements in Section 6.3, the state space system for relative positioning problem is

$$\begin{bmatrix} \dot{\boldsymbol{s}}_1(t) \\ \dot{\boldsymbol{s}}_2(t) \\ \dot{\boldsymbol{b}}_{ssb}(t) \\ \dot{\boldsymbol{t}}_c(t) \\ \dot{\boldsymbol{\eta}}_p(t) \end{bmatrix} = \begin{bmatrix} 0 & 0 & 0 & 0 & 0 \\ 0 & 0 & 0 & 0 & 0 \\ 0 & 0 & 0 & 0 & 0 \\ 0 & 0 & 0 & F_c & 0 \\ 0 & 0 & 0 & 0 & F_{\eta,p} \end{bmatrix} \begin{bmatrix} \boldsymbol{s}_1(t) \\ \boldsymbol{s}_2(t) \\ \boldsymbol{b}_{ssb}(t) \\ \boldsymbol{t}_c(t) \\ \boldsymbol{\eta}_p(t) \end{bmatrix} + \begin{bmatrix} G_{s,1} & 0 & 0 & 0 & 0 \\ 0 & G_{s,2} & 0 & 0 & 0 \\ 0 & 0 & G_{ssb} & 0 & 0 \\ 0 & 0 & 0 & G_c & 0 \\ 0 & 0 & 0 & 0 & G_{\eta,p} \end{bmatrix} \begin{bmatrix} \boldsymbol{w}_{s,1} \\ \boldsymbol{w}_{s,2} \\ \boldsymbol{w}_{ssb} \\ \boldsymbol{w}_c \\ \boldsymbol{w}_{\eta,p} \end{bmatrix} \tag{6.16}$$

$$\begin{bmatrix} y_{1,p}(t) \\ y_{2,p}(t) \end{bmatrix} = \begin{bmatrix} h_p(\phi_{1,p}(t)) \\ h_p(\phi_{2,p}(t)) \end{bmatrix} + \begin{bmatrix} v_{1,p}(t) \\ v_{2,p}(t) \end{bmatrix}.$$

The index, p, is the pulsar index and the dimensions of $\boldsymbol{y}_1(t)$ and $\boldsymbol{y}_2(t)$ are N_p, where N_p is the number of observed pulsars. The phase equation in the measurement is

$$\begin{aligned} \boldsymbol{\phi}_{i,p}(t) &= \phi_{0,p} + \dot{\phi}_p \left[t - \boldsymbol{\Lambda}_{i,p}(t)\right] + \frac{\ddot{\phi}_p}{2} \left[t - \boldsymbol{\Lambda}_{i,p}(t)\right]^2 + H_5 \boldsymbol{\eta}_p(t) \\ \boldsymbol{\Lambda}_{i,p}(t) &= -\frac{\boldsymbol{n}_p^T \boldsymbol{r}_i(t)}{c} + H_4 \boldsymbol{t}_c(t) + t_0 \\ \boldsymbol{r}_i(t) &= \bar{\boldsymbol{r}}_\oplus(t) + \boldsymbol{b}_{ssb}(t) + L(t)\boldsymbol{s}_i \\ \dot{\boldsymbol{r}}_i(t) &= \dot{\bar{\boldsymbol{r}}}_\oplus(t) + J(t)\boldsymbol{s}_i, \end{aligned} \tag{6.17}$$

The Power Spectral Densities (PSD) of the white disturbance and measurement noises are

$$\begin{aligned} E[\boldsymbol{w}_{s,1}(t)\boldsymbol{w}_{s,1}(\tau)^T] &= W_{s,1}\delta(t-\tau), \\ E[\boldsymbol{w}_{s,2}(t)\boldsymbol{w}_{s,2}(\tau)^T] &= W_{s,2}\delta(t-\tau), \\ E[\boldsymbol{w}_{ssb}(t)\boldsymbol{w}_{ssb}(\tau)] &= W_{ssb}\delta(t-\tau), \\ E[\boldsymbol{w}_c(t)\boldsymbol{w}_4(\tau)] &= W_c\delta(t-\tau), \\ E[\boldsymbol{w}_{\eta,p}(t)\boldsymbol{w}_{\eta,p}(\tau)] &= W_{\eta,p}\delta(t-\tau), \\ E[v_{1,p}(t)v_{1,p}(\tau)] &= V_{1,p}\delta(t-\tau), \\ E[v_{2,p}(t)v_{2,p}(\tau)] &= V_{2,p}\delta(t-\tau). \end{aligned}$$

6.5 Estimation Algorithm

6.5.1 Differential Phase Mechanism

Because of the measurement nonlinearity, position information is embedded in the phase of $y_1(t)$ and $y_2(t)$. In order to difference the two phases, some form of nonlinear operation is needed to explicitly difference the phase. Since the pulsar signal can be modeled as a periodic signal at short-term (small $\ddot{\phi}$), this approximation is used in the following development. The notation in the following derivation only considers one pulsar. The periodic signal is obtained by linearizing the phase equation Eq. (6.17) about a time γ to obtain a linearized frequency and linearized phase offset. Thus, the phase evolution over an observation window, $T_{obs,i}$, is simplified to

$$\begin{aligned} \phi_1(t) &\approx \psi_1 + f_{s,1}(t-\gamma) \\ \phi_2(t) &\approx \psi_2 + f_{s,2}(t-\gamma), \end{aligned} \tag{6.18}$$

where

$$\begin{aligned} \psi_1(\gamma) &= \phi_1(\gamma) \\ &= \phi_0 + \dot{\phi}\left[\gamma - \Lambda_1(\gamma)\right] + \frac{\ddot{\phi}}{2}\left[\gamma - \Lambda_1(\gamma)\right]^2 + H_5\boldsymbol{\eta}(\gamma) \\ \psi_2(\gamma) &= \phi_2(\gamma) \\ &= \phi_0 + \dot{\phi}\left[\gamma - \Lambda_2(\gamma)\right] + \frac{\ddot{\phi}}{2}\left[\gamma - \Lambda_2(\gamma)\right]^2 + H_5\boldsymbol{\eta}(\gamma) \\ f_{s,1}(\gamma) &= \frac{d\phi_1(t)}{dt}\Big|_{t=\gamma} \\ &= \left[\dot{\phi} + \ddot{\phi}[\gamma - \Lambda_1(\gamma)]\right]\left[1 - \dot{\Lambda}_1(\gamma)\right] + \dot{\phi}H_5\dot{\boldsymbol{\eta}}(\gamma) \\ f_{s,2}(\gamma) &= \frac{d\phi_2(t)}{dt}\Big|_{t=\gamma} \\ &= \left[\dot{\phi} + \ddot{\phi}[\gamma - \Lambda_2(\gamma)]\right]\left[1 - \dot{\Lambda}_2(\gamma)\right] + \dot{\phi}H_5\dot{\boldsymbol{\eta}}(\gamma), \end{aligned} \tag{6.19}$$

and

$$\begin{aligned}
\Lambda_1(\gamma) &= -\frac{\boldsymbol{n}^T\left[\bar{\boldsymbol{r}}_{\oplus}(\gamma)+\boldsymbol{b}_{ssb}(\gamma)+L(\gamma)\left[\boldsymbol{s}_2-\boldsymbol{s}_r\right]\right]}{c}+H_4\boldsymbol{t}_c(\gamma)+t_0\\
\Lambda_2(\gamma) &= -\frac{\boldsymbol{n}^T\left[\bar{\boldsymbol{r}}_{\oplus}(\gamma)+\boldsymbol{b}_{ssb}(\gamma)+L(\gamma)\boldsymbol{s}_2\right]}{c}+H_4\boldsymbol{t}_c(\gamma)+t_0\\
\dot{\Lambda}_1(\gamma) &= -\frac{\boldsymbol{n}^T\left[\dot{\bar{\boldsymbol{r}}}_{\oplus}(\gamma)+J(\gamma)\left[\boldsymbol{s}_2-\boldsymbol{s}_r\right]\right]}{c}+H_4\dot{\boldsymbol{t}}_c(\gamma)\\
\dot{\Lambda}_2(\gamma) &= -\frac{\boldsymbol{n}^T\left[\dot{\bar{\boldsymbol{r}}}_{\oplus}(\gamma)+J(\gamma)\boldsymbol{s}_2\right]}{c}+H_4\dot{\boldsymbol{t}}_c(\gamma).
\end{aligned} \tag{6.20}$$

The observation window, $T_{obs,i}$ is an integer multiple of $1/f_{s,i}$, i.e.

$$N_{c,i} = T_{obs,i} f_{s,i}, \tag{6.21}$$

where $N_{c,i}$ is an integer number. This condition is needed in order to utilize the orthogonality property of $\sin(\cdot)$ and $\cos(\cdot)$. This requirement creates a problem in implementing the differential phase method directly to $y_i(t)$. A solution to this problem is to process the epoch folded profile, $y_{i,ave}(\theta_l)$ instead. The output of epoch folding automatically satisfies Eq. (6.21). However, epoch folding cannot bypass the need for an estimate of the signal frequency, $f_{s,i}$. See Section 6.5.3. Instead of presenting the differential phase mechanism using epoch folded profiles, we first apply the mechanism to $y_i(t)$ and assume Eq. (6.21) is satisfied.

For the rest of the development, the argument γ is dropped for notation simplicity. Since a periodic signal can be approximated by Fourier series, the orthogonality property is used to obtained a differential phase measurement. The waveform measurement over each observation is approximated as

$$y_i(t) = \lambda_b + \lambda_s\left[\frac{a_0}{2}+\sum_{j=1}^{N} a_j\cos(j2\pi(f_{s,i}(t-\gamma)+\psi_i)) + b_j\sin(j2\pi(f_{s,i}(t-\gamma)+\psi_i))\right] + v_i. \tag{6.22}$$

Manipulating Eq. (6.22) using the following trigonometric identities,

$$\begin{aligned}
\sin(\alpha\pm\beta) &= \sin(\alpha)\cos(\beta)\pm\sin(\alpha)\cos(\beta)\\
\cos(\alpha\pm\beta) &= \cos(\alpha)\cos(\beta)\mp\sin(\alpha)\sin(\beta)
\end{aligned}$$

gives

$$
\begin{aligned}
y_i(t) &= \lambda_b + \lambda_s \Bigg[\frac{a_0}{2} + \sum_{j=1}^{N} a_j \big[\cos(j2\pi f_{s,i}(t-\gamma)) \cos(j2\pi\psi_i) \\
&\qquad\qquad - \sin(j2\pi f_{s,i}(t-\gamma)) \sin(j2\pi\psi_i) \big] \\
&\qquad + b_j \big[\sin(j2\pi f_s(t-\gamma)) \cos(j2\pi\psi_i) \\
&\qquad\qquad + \cos(j2\pi f_s(t-\gamma)) \sin(j2\pi\psi_i) \big] \Bigg] + v_i \\
&= \lambda_b + \lambda_s \Bigg[\frac{a_0}{2} + \sum_{j=1}^{N} \cos(j2\pi f_{s,i}(t-\gamma)) \left[a_j \cos(j2\pi\psi_i) + b_j \sin(j2\pi\psi_i) \right] \\
&\qquad\qquad + \sin(j2\pi f_{s,i}(t-\gamma)) \left[b_j \cos(j2\pi\psi_i) - a_j \sin(j2\pi\psi_i) \right] \Bigg] + v_i \\
&= A_0 + \sum_{j=1}^{N} A_{ij} \cos(j2\pi f_{s,i}(t-\gamma)) + B_{ij} \sin(j2\pi f_{s,i}(t-\gamma)) + v_i \\
&:= h(t,\psi_i) + v_i \quad i = 1,2
\end{aligned}
\tag{6.23}
$$

where

$$
\begin{aligned}
A_0 &= \lambda_b + \lambda_s \frac{a_0}{2} \\
A_{ij} &= \lambda_s \left(a_j \cos(j2\pi\psi_i) + b_j \sin(j2\pi\psi_i) \right) \\
B_{ij} &= \lambda_s \left(b_j \cos(j2\pi\psi_i) - a_j \sin(j2\pi\psi_i) \right).
\end{aligned}
\tag{6.24}
$$

The proposed differential phase scheme is illustrated in Fig. 6.2. Multiplying Eq. (6.23) by components of the Fourier Series gives

$$
\begin{aligned}
y_{s,ij} &= \int_0^{T_{obs,i}} h(t,\psi_i) \sin(j2\pi f_{s,i}(t-\gamma)) dt + \int_0^{T_{obs,i}} v_i(t) \sin(j2\pi f_{s,i}(t-\gamma)) dt \\
&= \underbrace{\frac{T_{obs,i}}{2} B_{ij}}_{h_{s,ij}} + v_{s,ij}
\end{aligned}
\tag{6.25}
$$

and

$$
\begin{aligned}
y_{c,ij} &= \int_0^{T_{obs,i}} h(t,\psi_i) \cos(j2\pi f_{s,i}(t-\gamma)) dt + \int_0^{T_{obs,i}} v_i(t) \cos(j2\pi f_{s,i}(t-\gamma)) dt \\
&= \underbrace{\frac{T_{obs,i}}{2} A_{ij}}_{h_{c,ij}} + v_{c,ij}.
\end{aligned}
\tag{6.26}
$$

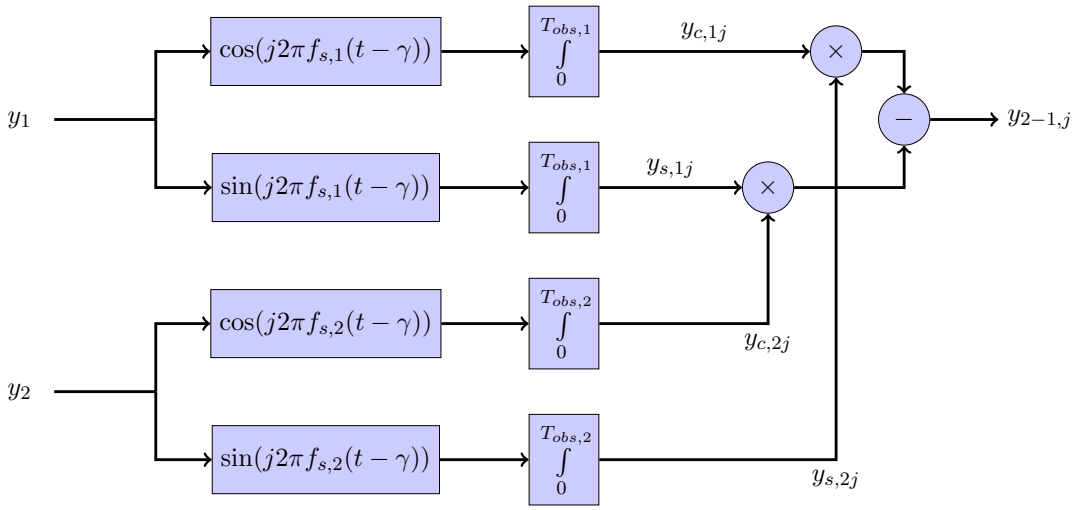

Figure 6.2: Block diagram

The noise $v_{s,ij}$ is zero mean,

$$E[v_{s,ij}] = E\left[\int_0^{T_{obs,i}} v_i(t)\sin(j2\pi f_{s,i}(t-\gamma))dt\right] = 0, \tag{6.27}$$

and has a variance of

$$\begin{aligned}
\text{var}[v_{s,ij}] &= E[v_{s,ij}^2] - \cancel{E[v_{s,ij}]^2}^{0} \\
&= E\left[\int_0^{T_{obs,i}} v_i(t)\sin(j2\pi f_{s,i}(t-\gamma))dt \int_0^{T_{obs,i}} v_i(\tau)\sin(j2\pi f_{s,i}(\tau-\gamma))d\tau\right] \\
&= \int_0^{T_{obs,i}}\int_0^{T_{obs,i}} E\left[v_i(t)v_i(\tau)\right]\sin(j2\pi f_{s,i}(t-\gamma))\sin(j2\pi f_{s,i}(\tau-\gamma))dtd\tau \\
&= \int_0^{T_{obs,i}}\int_0^{T_{obs,i}} V\delta(t-\tau)\sin(j2\pi f_{s,i}(t-\gamma))\sin(j2\pi f_{s,i}(\tau-\gamma))dtd\tau \\
&= \int_0^{T_{obs,i}} V\sin^2(j2\pi f_{s,i}(t-\gamma))dt \\
&= V\frac{T_{obs}}{2}
\end{aligned} \tag{6.28}$$

Similarly the mean and variance of $v_{c,ij}$ are

$$E[v_{c,ij}] = 0, \quad \text{and} \quad \text{var}[v_{c,ij}] = V\frac{T_{obs}}{2}. \tag{6.29}$$

The noises $v_{c,ij}$ and $v_{s,ij}$ are uncorrelated for every i^{th} and j^{th} indices. The i^{th} index represents different observers and the j^{th} index represents the Fourier series term.

$$\begin{aligned}
E[v_{s,ij}v_{s,ik}] &= E\left[\int_0^{T_{obs,i}} v_i(t)\sin(j2\pi f_{s,i}(t-\gamma))dt \int_0^{T_{obs,i}} v_i(\tau)\sin(k2\pi f_{s,i}(\tau-\gamma))d\tau\right] \\
&= \int_0^{T_{obs,i}} V\sin(j2\pi f_{s,i}(t-\gamma))\sin(k2\pi f_{s,i}(t-\gamma))dt \\
&= 0 \\
E[v_{s,ij}v_{c,ij}] &= E\left[\int_0^{T_{obs,i}} v_i(t)\sin(j2\pi f_{s,i}(t-\gamma))dt \int_0^{T_{obs,i}} v_i(\tau)\cos(j2\pi f_{s,i}(\tau-\gamma))d\tau\right] \\
&= \int_0^{T_{obs,i}} V\sin(j2\pi f_{s,i}(t-\gamma))\cos(j2\pi f_{s,i}(t-\gamma))dt \\
&= 0 \\
E[v_{c,ij}v_{c,ik}] &= 0
\end{aligned} \tag{6.30}$$

The differential phase measurement, $y_{2-1,j}$, is obtained by combining $y_{s,ij}$ and $y_{c,ij}$ together as follows

$$\begin{aligned}
y_{2-1,j} &= y_{s,1j}y_{c,2j} - y_{s,2j}y_{c,1j} \\
&= (h_{s,1j}+v_{s,1j})(h_{c,2j}+v_{c,2j}) - (h_{s,2j}+v_{s,2j})(h_{c,1j}+v_{c,1j}) \\
&= \underbrace{h_{s,1j}h_{c,2j} - h_{s,2j}h_{c,1j}}_{\text{Signal}} \\
&\quad + \underbrace{h_{s,1j}v_{c,2j} + h_{c,2j}v_{s,1j} + v_{s,1j}v_{c,2j} - (h_{s,2j}v_{c,1j} + h_{c,1j}v_{s,2j} + v_{s,2j}v_{c,1j})}_{Noise} \\
&:= \breve{h}_j(\psi_2 - \psi_1) + v_{2-1,j}
\end{aligned} \tag{6.31}$$

6.5.1.1 Signal Term

Substituting the Eq. (6.25) and Eq. (6.26) into Eq. (6.31) gives the differential phase signal

$$\begin{aligned}
\breve{h}_j(\psi_2-\psi_1) &= h_{s,1j}h_{c,2j} - h_{s,2j}h_{c,1j} \\
&= \frac{\lambda_s^2 T_{obs,1}T_{obs,2}}{4}\big[\,(b_jC_{1j}-a_jS_{1j})\,(a_jC_{2j}+b_jS_{2j}) \\
&\qquad\qquad -(b_jC_{2j}-a_jS_{2j})\,(a_jC_{1j}+b_jS_{1j})\,\big] \\
&= \frac{\lambda_s^2 T_{obs,1}T_{obs,2}}{4}\Big[-a_j^2S_{1j}C_{2j}+\cancel{a_jb_jC_{1j}C_{2j}}-\cancel{a_jb_jS_{1j}S_{2j}}+b_j^2C_{1j}S_{2j} \\
&\qquad\qquad a_j^2S_{2j}C_{1j}-\cancel{b_ja_jC_{2j}C_{1j}}+\cancel{a_jb_jS_{2j}S_{1j}}-b_j^2C_{2j}S_{1j}\Big] \\
&= \frac{\lambda_s^2 T_{obs,1}T_{obs,2}}{4}\left[a_j^2\left(S_{2j}C_{1j}-S_{1j}C_{2j}\right)+b_j^2\left(C_{1j}S_{2j}-C_{2j}S_{1j}\right)\right] \\
&= \frac{\lambda_s^2 T_{obs,1}T_{obs,2}}{4}\left[\left(a_j^2+b_j^2\right)\left(S_{2j}C_{1j}-S_{1j}C_{2j}\right)\right] \\
&= \frac{\lambda_s^2 T_{obs,1}T_{obs,2}}{4}\left(a_j^2+b_j^2\right)\sin(j2\pi(\psi_2-\psi_1))
\end{aligned} \tag{6.32}$$

where $S_{ij}=\sin(j2\pi\psi_i)$ and $C_{ij}=\cos(j2\pi\psi_i)$. Note the above operation reduces a batch of measurement collected over $T_{obs,i}$ into N number of measurement, where N is the order of the Fourier series approximation of the signal profile. Taking into account Eq. (6.19) gives

$$\begin{aligned}
\psi_2(\gamma)-\psi_1(\gamma) &= \phi_2(\gamma)-\phi_1(\gamma) \\
&= \left[\dot{\phi}+\frac{\ddot{\phi}}{2}\left(2\gamma-(\Lambda_1(\gamma)+\Lambda_2(\gamma))\right)\right]\left[\Lambda_1(\gamma)-\Lambda_2(\gamma)\right],
\end{aligned} \tag{6.33}$$

where

$$\begin{aligned}
\Lambda_1(\gamma)-\Lambda_2(\gamma) &= \left[-\frac{\boldsymbol{n}^T\boldsymbol{r}_1(\gamma)}{c}+H_4\boldsymbol{t}_c(\gamma)\right]-\left[-\frac{\boldsymbol{n}^T\boldsymbol{r}_2(\gamma)}{c}+H_4\boldsymbol{t}_c(\gamma)\right] \\
&= \frac{\boldsymbol{n}^T\left[\boldsymbol{r}_2(\gamma)-\boldsymbol{r}_1(\gamma)\right]}{c} \\
&= \frac{\boldsymbol{n}^TL(\gamma)\boldsymbol{s}_r}{c}
\end{aligned} \tag{6.34}$$

and

$$\begin{aligned}\Lambda_1(\gamma)+\Lambda_2(\gamma) &= \left[-\frac{\boldsymbol{n}^T\boldsymbol{r}_1(\gamma)}{c}+H_4\boldsymbol{t}_c(\gamma)\right]+\left[-\frac{\boldsymbol{n}^T\boldsymbol{r}_2(\gamma)}{c}+H_4\boldsymbol{t}_c(\gamma)\right]\\ &= -\frac{\boldsymbol{n}^T\left[\boldsymbol{r}_1(\gamma)+\boldsymbol{r}_2(\gamma)\right]}{c}+2H_4\boldsymbol{t}_c(\gamma)\\ &= -\frac{\boldsymbol{n}^T\left[2\bar{\boldsymbol{r}}_{\oplus}(\gamma)+2\boldsymbol{b}_{ssb}+L(\gamma)\left[\boldsymbol{s}_1+\boldsymbol{s}_2\right]\right]}{c}+2H_4\boldsymbol{t}_c(\gamma)\\ &= -\frac{\boldsymbol{n}^T\left[2\bar{\boldsymbol{r}}_{\oplus}(\gamma)+2\boldsymbol{b}_{ssb}+L(\gamma)\left[2\boldsymbol{s}_2-\boldsymbol{s}_r\right]\right]}{c}+2H_4\boldsymbol{t}_c(\gamma).\end{aligned} \tag{6.35}$$

Because the magnitude of $\ddot{\phi}$ is on the order of 10^{-14} and 10^{-16}, the component $\ddot{\phi}\left(\Lambda_1(\gamma)+\Lambda_2(\gamma)\right)$ is much smaller than $\dot{\phi}$ and is negligible.

6.5.1.2 Noise Term

From Eq. (6.31), the noise term is

$$v_{2-1,j} = h_{s,1j}v_{c,2j}+h_{c,2j}v_{s,1j}+v_{s,1j}v_{c,2j}-(h_{s,2j}v_{c,1j}+h_{c,1j}v_{s,2j}+v_{s,2j}v_{c,1j}). \tag{6.36}$$

The mean of $v_{2-1,j}$ is

$$\begin{aligned}E[v_{2-1,j}] &= E[h_{s,1j}v_{c,2j}+h_{c,2j}v_{s,1j}+v_{s,1j}v_{c,2j}-(h_{s,2j}v_{c,1j}+h_{c,1j}v_{s,2j}+v_{s,2j}v_{c,1j})]\\ &= E[[h_{s,1j}]E[v_{c,2j}]+E[[h_{c,2j}]E[v_{s,1j}]+E[v_{s,1j}]E[v_{c,2j}]\\ &\quad -(E[[h_{s,2j}]E[v_{c,1j}]+E[h_{c,1j}]E[v_{s,2j}]+E[v_{s,2j}]E[v_{c,1j}])\\ &= 0.\end{aligned} \tag{6.37}$$

From Eq. (6.30), one can see the noise, $v_{2-1,j}$, is composed of terms that are uncorrelated with each other, so all covariance are zero. Thus, its variance reduces to

$$
\begin{aligned}
\operatorname{var}[v_{2-1,j}] &= \operatorname{var}[h_{s,1j}v_{c,2j} + h_{c,2j}v_{s,1j} + v_{s,1j}v_{c,2j} - (h_{s,2j}v_{c,1j} + h_{c,1j}v_{s,2j} + v_{s,2j}v_{c,1j})] \\
&= \operatorname{var}[h_{s,1j}v_{c,2j}] + \operatorname{var}[h_{s,2j}v_{c,1j}] + \operatorname{var}[h_{c,2j}v_{s,1j}] + \operatorname{var}[h_{c,1j}v_{s,2j}] \\
&+ \operatorname{var}[v_{s,1j}v_{c,2j}] + \operatorname{var}[v_{s,2j}v_{c,1j}] \\
&= \operatorname{var}[h_{s,1j}]\operatorname{var}[v_{c,2j}] + E[h_{s,1j}]^2\operatorname{var}[v_{c,2j}] + \cancel{E[v_{c,2j}]^2}\operatorname{var}[h_{s,1j}] \\
&+ \operatorname{var}[h_{s,2j}]\operatorname{var}[v_{c,1j}] + E[h_{s,2j}]^2\operatorname{var}[v_{c,1j}] + \cancel{E[v_{c,1j}]^2}\operatorname{var}[h_{s,2j}] \\
&+ \operatorname{var}[h_{c,2j}]\operatorname{var}[v_{s,1j}] + E[h_{c,2j}]^2\operatorname{var}[v_{s,1j}] + \cancel{E[v_{s,1j}]^2}\operatorname{var}[h_{c,2j}] \\
&+ \operatorname{var}[h_{c,1j}]\operatorname{var}[v_{s,2j}] + E[h_{c,1j}]^2\operatorname{var}[v_{s,2j}] + \cancel{E[v_{s,2j}]^2}\operatorname{var}[h_{c,1j}] \\
&+ \operatorname{var}[v_{s,1j}]\operatorname{var}[v_{c,2j}] + \cancel{E[v_{s,1j}]^2}\operatorname{var}[v_{c,2j}] + \cancel{E[v_{c,2j}]^2}\operatorname{var}[v_{s,1j}] \\
&+ \operatorname{var}[v_{s,2j}]\operatorname{var}[v_{c,1j}] + \cancel{E[v_{s,2j}]^2}\operatorname{var}[v_{c,1j}] + \cancel{E[v_{c,1j}]^2}\operatorname{var}[v_{s,2j}] \\
&= (\operatorname{var}[h_{s,1j}] + E[h_{s,1j}]^2)\operatorname{var}[v_{c,2j}] \\
&+ (\operatorname{var}[h_{s,2j}] + E[h_{s,2j}]^2)\operatorname{var}[v_{c,1j}] \\
&+ (\operatorname{var}[h_{c,2j}] + E[h_{c,2j}]^2)\operatorname{var}[v_{s,1j}] \\
&+ (\operatorname{var}[h_{c,1j}] + E[h_{c,1j}]^2)\operatorname{var}[v_{s,2j}] \\
&+ \operatorname{var}[v_{s,1j}]\operatorname{var}[v_{c,2j}] + \operatorname{var}[v_{s,2j}]\operatorname{var}[v_{c,1j}] \\
&= E[h_{s,1j}^2]\operatorname{var}[v_{c,2j}] + E[h_{s,2j}^2]\operatorname{var}[v_{c,1j}] + E[h_{c,2j}^2]\operatorname{var}[v_{s,1j}] + E[h_{c,1j}^2]\operatorname{var}[v_{s,2j}] \\
&+ \operatorname{var}[v_{s,1j}]\operatorname{var}[v_{c,2j}] + \operatorname{var}[v_{s,2j}]\operatorname{var}[v_{c,1j}] \\
&= \left(E[h_{s,1j}^2] + E[h_{c,1j}^2]\right)\frac{V_2T_{obs,2}}{2} + \left(E[h_{s,2j}^2] + E[h_{c,2j}^2]\right)\frac{V_1T_{obs,1}}{2} + \frac{V_1V_2T_{obs,1}T_{obs,2}}{2} \\
&= \frac{\lambda_s^2T_{obs,1}^2}{4}E\left[(-a_jS_{1j} + b_jC_{1j})^2 + (a_jC_{1j} + b_jS_{1j})^2\right]\frac{V_2T_{obs,2}}{2} \\
&+ \frac{\lambda_s^2T_{obs,2}^2}{4}E\left[(-a_jS_{2j} + b_jC_{2j})^2 + (a_jC_{2j} + b_jS_{2j})^2\right]\frac{V_1T_{obs,1}}{2} + \frac{V_1V_2T_{obs,1}T_{obs,2}}{2} \\
&= \frac{\lambda_s^2V_2T_{obs,1}^2T_{obs,2}}{8}(a_j^2 + b_j^2) + \frac{\lambda_s^2V_1T_{obs,2}^2T_{obs,1}}{8}(a_j^2 + b_j^2) + \frac{V_1V_2T_{obs,1}T_{obs,2}}{2} \\
&= \frac{T_{obs,1}T_{obs,2}}{2}\left[\frac{\lambda_s^2(a_j^2 + b_j^2)}{4}(V_2T_{obs,1} + V_1T_{obs,2}) + V_1V_2\right] \\
&:= \Sigma_{2-1,j}.
\end{aligned}
\tag{6.38}
$$

If $V_i = \sigma_i^2 \Delta t = V = \sigma^2 \Delta t$ and $f_{s,i} = f_s$ for all i, then

$$\Sigma_{2-1,j} = \frac{T_{obs}^2 V}{2} \left[\frac{\lambda_s^2 T_{obs}(a_j^2 + b_j^2)}{2} + V \right]. \tag{6.39}$$

6.5.2 Covariance Analysis

This section discusses the phase estimation accuracy of $\psi_{2-1} := \psi_2 - \psi_1$ using $y_i(t)$ in Eq. (6.22) and y_{2-1} in Eq. (6.31) . Let the continuous time signal $y_i(t)$ be sampled by a computer with a sample interval of Δt. The phase ψ_i is assumed to be an unknown constant over the observation interval, $T_{obs,i}$. The discrete time measurement is

$$y_{i,k} = \underbrace{\lambda_b + \lambda_s \left[\frac{a_0}{2} + \sum_{j=1}^{N} a_j \cos(j2\pi(f_{s,i}(t_k - \gamma) + \psi_i)) + b_j \sin(j2\pi(f_{s,i}(t_k - \gamma) + \psi_i)) \right]}_{h(f_{s.i}(t_k - \gamma) + \psi_i)} + v_i, \tag{6.40}$$

where the variance of v_i is σ_i^2. The total number of measurement is $n_i = T_{obs,i}/\Delta t$. Taking the partial derivative of $y_{i,k}$ with respect to ψ_i gives

$$H_{i,k} = 2\lambda_s \pi \sum_{j=1}^{N} j b_j \cos(j2\pi(f_{s,i}(t_k - \gamma) + \psi_i)) - j a_j \sin(j2\pi(f_{s,i}(t_k - \gamma) + \psi_i)). \tag{6.41}$$

Assembling the measurements into a vector and the partial derivatives into a matrix gives

$$\boldsymbol{y} = \begin{bmatrix} \boldsymbol{y}_1 \\ \boldsymbol{y}_2 \end{bmatrix} = \begin{bmatrix} y_{1,1} \\ \vdots \\ y_{1,n_1} \\ y_{2,1} \\ \vdots \\ y_{2,n_2} \end{bmatrix}, \qquad H = \begin{bmatrix} H_{1,1} & 0 \\ \vdots & \vdots \\ H_{1,n_1} & 0 \\ 0 & H_{2,1} \\ \vdots & \vdots \\ 0 & H_{2,n_2} \end{bmatrix} \tag{6.42}$$

The measurement noise covariance matrix is

$$\Sigma = \begin{bmatrix} \Sigma_1 & 0 \\ 0 & \Sigma_2 \end{bmatrix} = \begin{bmatrix} \sigma_1^2 I_{n_1 \times n_1} & 0 \\ 0 & \sigma_2^2 I_{n_2 \times n_2} \end{bmatrix}, \tag{6.43}$$

where $V_i = \Sigma_i \Delta t$. The error covariance of ψ_{2-1} is

$$\begin{aligned} P_{2-1} &= CPC^T \\ &= C(H^T\Sigma^{-1}H)^{-1}C^T \\ &= C \begin{bmatrix} \sum_{k=1}^{n_1} H_{1,k}^T \Sigma_{1,k}^{-1} H_{1,k} & 0 \\ 0 & \sum_{k=1}^{n_2} H_{2,k}^T \Sigma_{2,k}^{-1} H_{2,k} \end{bmatrix}^{-1} C^T \\ &= \frac{1}{\sum_{k=1}^{n_1} H_{1,k}^T \Sigma_{1,k}^{-1} H_{1,k}} + \frac{1}{\sum_{k=1}^{n_2} H_{2,k}^T \Sigma_{2,k}^{-1} H_{2,k}}, \end{aligned} \tag{6.44}$$

where $C = \begin{bmatrix} 1 & -1 \end{bmatrix}$ and P is the error covariance of $\begin{bmatrix} \psi_1 & \psi_2 \end{bmatrix}^T$. Substituting Eq. (6.41) into the denominator of Eq. (6.44) gives

$$\begin{aligned} H_i^T \Sigma_i^{-1} H_i &= \sum_{k=1}^{n_i} H_{i,k}^T \Sigma_{i,k}^{-1} H_{i,k}, \quad i = 1, 2 \\ &= \frac{1}{\sigma_i^2} \sum_{k=1}^{n_i} \Bigg[2\lambda_s \pi \sum_{j=1}^{N} j b_j \cos(j2\pi(f_{s,i}(t_k - \gamma) + \bar{\psi}_i)) \\ &\qquad - j a_j \sin(j2\pi(f_{s,i}(t_k - \gamma) + \bar{\psi}_i)) \Bigg]^2 \\ &= \frac{\lambda_s^2 4\pi^2}{\sigma_i^2 \Delta t} \sum_{k=1}^{n_i} \Bigg[\sum_{j=1}^{N} j b_j \cos(j2\pi(f_{s,i}(t_k - \gamma) + \bar{\psi}_i)) \\ &\qquad - j a_j \sin(j2\pi(f_{s,i}(t_k - \gamma) + \bar{\psi}_i)) \Bigg]^2 \Delta t \\ &= \frac{\lambda_s^2 4\pi^2}{V_i} \int_0^{T_{obs,i}} \Bigg[\sum_{j=1}^{N} j b_j \cos(j2\pi(f_{s,i}(t_k - \gamma) + \bar{\psi}_i)) \\ &\qquad - j a_j \sin(j2\pi(f_{s,i}(t_k - \gamma) + \bar{\psi}_i)) \Bigg]^2 dt \\ &= \frac{\lambda_s^2 4\pi^2}{V_i} \left[\frac{T_{obs,i}}{2} \sum_{j=1}^{N} j^2 [a_j^2 + b_j^2] \right] \\ &= \frac{\lambda_s^2 2\pi^2 T_{obs,i}}{V_i} \sum_{j=1}^{N} j^2 \left(a_j^2 + b_j^2 \right) \end{aligned} \tag{6.45}$$

where V_i is the PSD of $v_i(t)$. The phase prediction, $\bar{\psi}_i$ and $f_{s,i}\gamma$ are integrated out because $T_{obs,i}$ is an integer multiple of $1/f_{s,i}$. Setting $V_1 = V_2 = V$, $f_{s,1} = f_{s,2} = f_s$ and substituting

Eq. (6.45) back into Eq. (6.44) gives

$$P_{2-1} = \frac{2V}{\lambda_s^2 2\pi^2 T_{obs} \sum_{j=1}^{N} j^2 \left(a_j^2 + b_j^2\right)}. \tag{6.46}$$

Linearizing Eq. (6.32) gives

$$\breve{H}_j = \frac{j\pi\lambda_s^2 T_{obs}^2}{2}(a_j^2 + b_j^2)\cos(j2\pi(\psi_2 - \psi_1)) \tag{6.47}$$

The error variance of estimating ψ_{2-1} from Eq. (6.31) using an EKF is

$$\begin{aligned}
\breve{P}_{2-1} &= \frac{1}{\sum_{j=1}^{N} \breve{H}_j^T \Sigma_{2-1,j}^{-1} \breve{H}_j} \\
&= \frac{1}{\sum_{j=1}^{N} \frac{2j^2\pi^2\lambda_s^4 T_{obs}^4 (a_j^2+b_j^2)^2 \cos^2(j2\pi\psi_{2-1})}{4T_{obs}^2 V\left(\frac{\lambda_s^2}{2} T_{obs}(a_j^2+b_j^2)+V\right)}} \\
&= \frac{2V}{\pi^2\lambda_s^4 T_{obs}^2 \sum_{j=1}^{N} \frac{j^2(a_j^2+b_j^2)^2 \cos^2(j2\pi\psi_{2-1})}{\frac{\lambda_s^2}{2} T_{obs}(a_j^2+b_j^2)+V}}.
\end{aligned} \tag{6.48}$$

In order to compare the performance of the two approaches, we consider the ratio of the two error variances. If R is greater than 1, then the differential approach is more effective than the regular approach.

$$\begin{aligned}
R &= \frac{P_{2-1}}{\breve{P}_{2-1}} \\
&= \frac{2V}{\lambda_s^2 2\pi^2 T_{obs} \sum_{j=1}^{N} j^2 \left(a_j^2 + b_j^2\right)} \frac{\pi^2\lambda_s^4 T_{obs}^2 \sum_{j=1}^{N} \frac{j^2(a_j^2+b_j^2)^2 \cos^2(j2\pi\psi_{2-1})}{\frac{\lambda_s^2}{2} T_{obs}(a_j^2+b_j^2)+V}}{2V} \\
&= \frac{\lambda_s^2 T_{obs}}{2\sum_{j=1}^{N} j^2(a_j^2 + b_j^2)} \sum_{j=1}^{N} \frac{j^2(a_j^2 + b_j^2)^2 \cos^2(j2\pi\psi_{2-1})}{\frac{\lambda_s^2}{2} T_{obs}(a_j^2 + b_j^2) + V} \\
&= \frac{\lambda_s^2 T_{obs}}{\sum_{j=1}^{N} j^2(a_j^2 + b_j^2)} \sum_{j=1}^{N} \frac{j^2(a_j^2 + b_j^2)^2 \cos^2(j2\pi\psi_{2-1})}{\lambda_s^2 T_{obs}(a_j^2 + b_j^2) + 2V}.
\end{aligned} \tag{6.49}$$

The performance ratio, R, of five different pulsars are plotted in Fig. 6.4 for values of ψ_{2-1} between 0 and 1. The designations of the pulsars are $J0437-4715$, $J1643-1224$, $J1713+$

0747, $J1939+2134$, and $J2145-0750$. Their pulse profiles, $s(\cdot)$, at 1.4 GHz frequency band are plotted in Fig. 6.3 and the signal intensities, λ_s, are 149 mJy, 4.8 mJy, 10.2 mJy, 13.2 mJy, and 8.9 mJy respectively. The observation time was set to $T_{obs} = 30$ min and the PSD of the measurement noise, V, was held constant for all pulsars. The value of V was computed using the radiometer equation in Appendix A. These plots indicate the performance is ratio is independent of the signal strength, but it is dependent on the signal profile. Furthermore, when ψ_{2-1} is equal to a half or a full cycle, $R \approx 1$, which means the accuracy of the differential phase estimate using Eq. (6.31) is approximately equal to that of differencing the estimates of ψ_2 and ψ_2 obtained using Eq. (6.22). In general, ψ_{2-1} is dependent on the relative position between the two observers, so it is not equal to an integer multiple of 0.5. The desire to keep ψ_{2-1} as close to 0 as possible is another motivation for using the epoch folded profiles $y_{i,ave}(\theta)$ rather than $y_i(t)$ in computing the differential phase measurement.

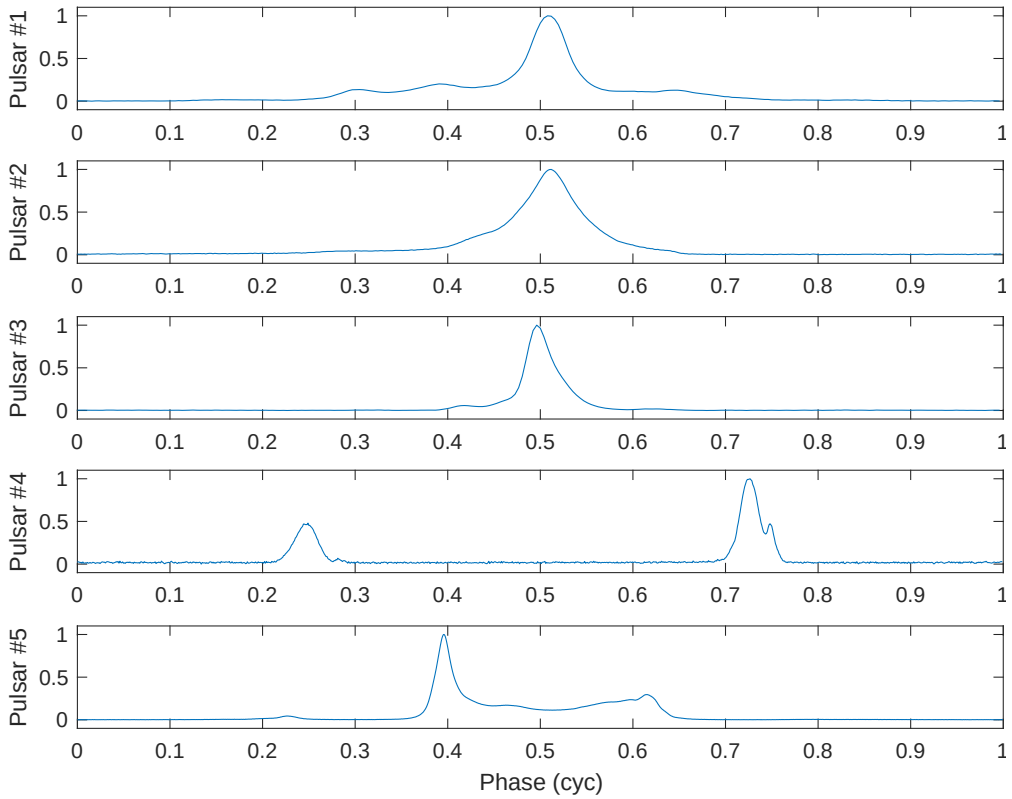

Figure 6.3: Pulsar profiles

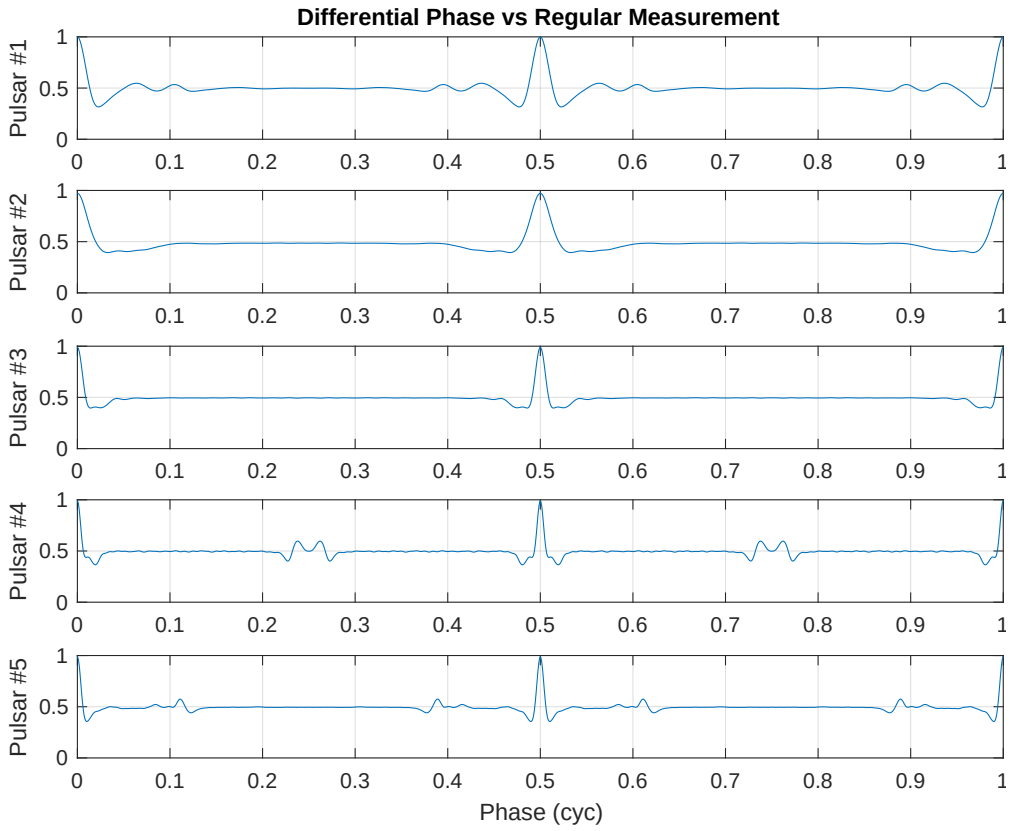

Figure 6.4: Performance ratio

6.5.3 Differential Phase of Epoch Folded Profiles

Let the following signals be the epoch folded profiles of $y_i(t)$,

$$\begin{aligned} y_{1,ave}(\theta_l) &= h(\theta_l + \psi_1 - \bar{\psi}_1) + v_{1,ave}(\theta_l) \\ y_{2,ave}(\theta_l) &= h(\theta_l + \psi_2 - \bar{\psi}_2) + v_{2,ave}(\theta_l), \end{aligned} \tag{6.50}$$

The two signals span exactly one period and the periods are $P_i = 1/f_{s,i}$ where $i = 1, 2$. The phases ψ_1 and ψ_2 and frequencies $f_{s,1}$ and $f_{s,2}$ are defined in Eq. (6.19). The phase estimates $\bar{\psi}_1$ and $\bar{\psi}_2$ correspond to the filter estimate used to perform folding. The signal frequencies $f_{s,i}$ are assumed known. If $\bar{\psi}_i = \psi_i$, then the epoch folding process is perfect. This implies that the phases associated with $y_{1,ave}(\theta_l)$ and $y_{2,ave}(\theta_l)$ are 0. As a result $\psi_{2-1} = 0$ and the differential phase mechanism is as effective as differencing the individual phase estimates as indicated by Fig. 6.4.

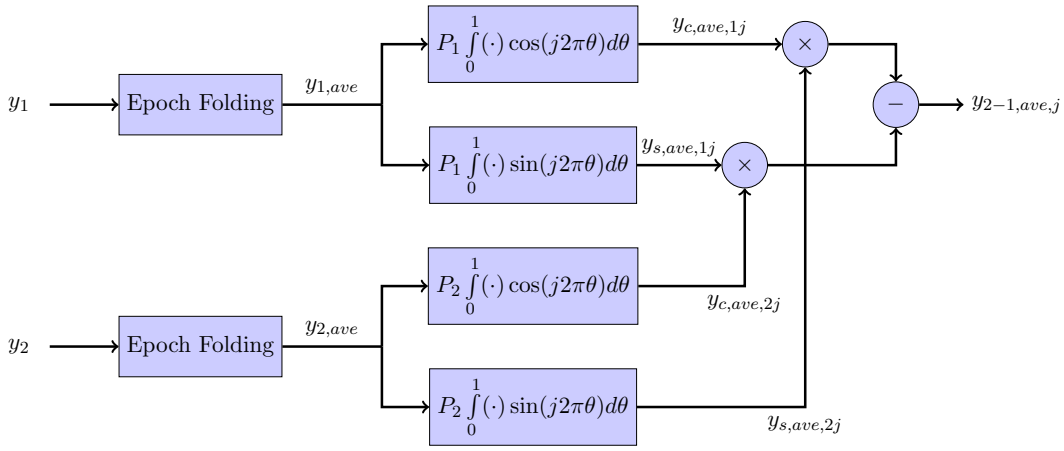

Figure 6.5: Differential phase measurement of epoch folded profiles

The bin width is $\Delta\theta = 1/N_b$ and the bins are

$$\theta_l = \theta_{l-1} + \Delta\theta, \quad l = 2...N_b \tag{6.51}$$

where $\theta_1 = \Delta\theta/2$. The number of bin used in the sorting is N_b. The folded noise is zero mean, $E[v_{i,ave}(\theta_l)] = 0$ because $E[v_i(t)] = 0$. The variances of the two folded noises, $v_{i,ave}(\theta_l)$, are

$$\sigma^2_{i,ave} = \frac{\sigma_i^2}{N_{c,i}} = \frac{\sigma_1^2 P_i}{T_{obs,i}} = \frac{V_i P_i}{\Delta t_i T_{obs,i}} = \frac{V_i N_b}{T_{obs,i}}, \tag{6.52}$$

where $N_{c,i} = T_{obs,i} f_{s,i}$ is the number of pulsar cycles within the observation duration $T_{obs,i}$ and $P_i/N_b = P_i\Delta\theta = \Delta t_i$. The PSD of the unfolded noise is V_i and the PSD of the folded noise is

$$V_{i,ave} = \frac{V_i}{N_{c,i}} = \frac{V_i P_i}{T_{obs,i}} = \sigma^2_{i,ave}\Delta t_i. \tag{6.53}$$

The overall scheme is summarized in Fig. 6.5.

Multiplying Eq. (6.50) by the components of the Fourier series and integrate over one

period gives

$$
\begin{aligned}
y_{s,ave,ij} &= P_i \Delta\theta \left[\sum_{l=1}^{N_b} h(\theta_l + \psi_i - \bar{\psi}_i) \sin(j2\pi\theta_l) + v_{i,ave}(\theta_l) \sin(j2\pi\theta_l) \right] \\
&= \Delta t_i \left[\sum_{l=1}^{N_b} h(\theta_l + \psi_i - \bar{\psi}_i) \sin(j2\pi\theta_l) + v_{i,ave}(\theta_l) \sin(j2\pi\theta_l) \right] \\
&= \Delta t_i \left[\sum_{l=1}^{N_b} h(f_{s,i} t_l + \psi_i - \bar{\psi}_i) \sin(j2\pi f_{s,i} t_l) + v_{i,ave}(t_l) \sin(j2\pi f_{s,i} t_l) \right] \\
&= \int_0^{P_i} h(f_{s,i} t + \psi_i - \bar{\psi}_i) \sin(j2\pi f_{s,i} t) dt + \int_0^{P_i} v_{i,ave}(t) \sin(j2\pi f_{s,i} t) dt \\
&= \underbrace{\frac{P_i}{2} B_{ij}}_{h_{s,ij}} + v_{s,ave,ij} \\
y_{c,ave,ij} &= P_i \Delta\theta \left[\sum_{l=1}^{N_b} h(\theta_l + \psi_i - \bar{\psi}_i) \cos(j2\pi\theta_l) + v_{i,ave}(\theta_l) \cos(j2\pi\theta_l) \right] \\
&= \int_0^{P_i} h(f_{s,i} t + \psi_i) \cos(j2\pi f_{s,i} t) dt + \int_0^{P_i} v_{i,ave}(t) \cos(j2\pi f_{s,i} t) dt \\
&= \underbrace{\frac{P_i}{2} A_{ij}}_{h_{c,ij}} + v_{c,ave,ij}.
\end{aligned}
\tag{6.54}
$$

This operation removes the signal frequency. The noise $v_{s,ave,ij}$ is zero mean,

$$
E[v_{s,ave,ij}] = E\left[P_i \Delta\theta \sum_{l=1}^{N_b} v_{i,ave}(\theta_l) \sin(j2\pi\theta_l) \right] = 0, \tag{6.55}
$$

and has a variance of

$$
\begin{aligned}
\mathrm{var}[v_{s,ave,ij}] &= E[v_{s,ave,ij}^2] - \cancelto{0}{E[v_{s,ave,ij}]^2} \\
&= E\left[\left(P_i\Delta\theta\sum_{l=1}^{N_b} v_{i,ave}(\theta_l)\sin(j2\pi\theta_l)\right)\left(P_i\Delta\theta\sum_{l=1}^{N_b} v_{i,ave}(\theta_l)\sin(j2\pi\theta_l)\right)\right] \\
&= \frac{P_i^2}{N_b^2}E\left[\sum_{l=1}^{N_b}\sum_{k=1}^{N_b} v_{i,ave}(\theta_l)v_{i,ave}(\theta_k)\sin(j2\pi\theta_l)\sin(j2\pi\theta_k)\right] \\
&= \Delta t_i^2\sum_{l=1}^{N_b}\sum_{k=1}^{N_b} E\left[v_{i,ave}(\theta_l)v_{i,ave}(\theta_k)\right]\sin(j2\pi\theta_l)\sin(j2\pi\theta_k) \\
&= \Delta t_i^2\sum_{l=1}^{N_b}\sum_{k=1}^{N_b} \sigma_{i,ave}^2\delta_{lk}\sin(j2\pi\theta_l)\sin(j2\pi\theta_k), \quad \delta_{lk} = \begin{cases} 1, & l = k \\ 0, & l \neq k \end{cases} \\
&= \Delta t_i^2\sum_{l=1}^{N_b} \sigma_{i,ave}^2\sin^2(j2\pi\theta_l) \\
&= \Delta t_i\sigma_{i,ave}^2\int_0^{P_i}\sin^2(j2\pi f_{s,i}t)dt \\
&= V_{i,ave}\frac{P_i}{2}.
\end{aligned}
\tag{6.56}
$$

Similarly the mean and the variance of $v_{c,ave,ij}$ are

$$
E[v_{c,ave,ij}] = 0, \quad \text{and} \quad \mathrm{var}[v_{c,ave,ij}] = V_{i,ave}\frac{P_i}{2}. \tag{6.57}
$$

Applying the differential phase method to Eq. (6.50) gives

$$
\begin{aligned}
y_{2-1,ave,j} &= y_{s,ave,1j}y_{c,ave,2j} - y_{s,ave,2j}y_{c,ave,1j} \\
&= (h_{s,1j} + v_{s,ave,1j})(h_{c,2j} + v_{c,ave,2j}) - (h_{s,2j} + v_{s,ave,2j})(h_{c,1j} + v_{c,ave,1j}) \\
&= h_{s,1j}h_{c,2j} - h_{s,2j}h_{c,1j} + v_{2-1,ave,j} \\
&= \frac{\lambda_s^2 P_1 P_2}{4}\left(a_j^2 + b_j^2\right)\sin\Big(j2\pi(\underbrace{\left[\psi_2 - \bar{\psi}_2\right] - \left[\psi_1 - \bar{\psi}_1\right]}_{\tilde{\psi}_{2-1}})\Big) + v_{2-1,ave,j},
\end{aligned}
\tag{6.58}
$$

where

$$
\begin{aligned}
v_{2-1,ave,j} = {} & h_{s,1j}v_{c,ave,2j} + h_{c,2j}v_{s,ave,1j} + v_{s,ave,1j}v_{c,ave,2j} \\
& - (h_{s,2j}v_{c,ave,1j} + h_{c,1j}v_{s,ave,2j} + v_{s,ave,2j}v_{c,ave,1j}).
\end{aligned}
\tag{6.59}
$$

If $\bar{\psi}_2 = \psi_2$ and $\bar{\psi}_1 = \psi_1$, then $\tilde{\psi}_{2-1} = 0$, which means the differential phase mechanism is as effective as processing $y_1(t)$ and $y_2(t)$ using non-differential phase approach. See Section 6.5.2. Note this condition is achieved when the phase prediction in the epoch folding process is perfect. The mean of $v_{2-1,ave,j}$ is

$$\begin{aligned} E[v_{2-1,ave,j}] &= E\Big[h_{s,1j}v_{c,ave,2j} + h_{c,2j}v_{s,ave,1j} + v_{s,ave,1j}v_{c,ave,2j} \\ &\qquad - (h_{s,2j}v_{c,ave,1j} + h_{c,1j}v_{s,ave,2j} + v_{s,ave,2j}v_{c,ave,1j})\Big] \\ &= 0. \end{aligned} \tag{6.60}$$

Following the derivation in Eq. (6.38), the variance of $v_{2-1,ave,j}$ is

$$\begin{aligned} \mathrm{var}[v_{2-1,ave,j}] &= \left(E[h_{s,1j}^2] + E[h_{c,1j}^2]\right)\frac{V_{2,ave}P_2}{2} + \left(E[h_{s,2j}^2] + E[h_{c,2j}^2]\right)\frac{V_{1,ave}P_1}{2} \\ &\quad + \frac{V_{1,ave}V_{2,ave}P_1P_2}{2} \\ &= \frac{\lambda_s^2 V_{2,ave}P_1^2P_2}{8}(a_j^2 + b_j^2) + \frac{\lambda_s^2 V_{1,ave}P_2^2P_1}{8}(a_j^2 + b_j^2) + \frac{V_{1,ave}V_{2,ave}P_1P_2}{2} \\ &= \frac{\lambda_s^2 P_1P_2(a_j^2 + b_j^2)}{8}(V_{2,ave}P_1 + V_{1,ave}P_2) + \frac{V_{1,ave}V_{2,ave}P_1P_2}{2} \\ &= \frac{P_1^2P_2^2}{2}\left[\frac{\lambda_s^2(a_j^2 + b_j^2)}{4}\left(\frac{V_2}{T_{obs,2}} + \frac{V_1}{T_{obs,1}}\right) + \frac{V_1V_2}{T_{obs,1}T_{obs,2}}\right]. \end{aligned} \tag{6.61}$$

The same performance ratio, R, shown in Eq. (6.49) can also be derived using Eq. (6.58) and Eq. (6.61). The signal periods, P_i, will be canceled in the derivation which means the performance ratio is independent of the signal frequency. It dependents on T_{obs}, ψ_{2-1} and the waveform of the signal. From Eq. (6.58), it is clear that the magnitude of the differential phase measurement does not increase relative to the observation time, T_{obs}. This is different from that of Eq. (6.32). However, the variance of $v_{2-1,ave,j}$ does decrease with increasing T_{obs}.

6.5.3.1 Auxiliary Measurement

In order to obtain the epoch folded profiles in Eq. (6.50), it is necessary to process one of the non-differential phase measurements in the filter to estimate the signal frequency, $f_{s,i}$. We chose to process $y_2(t)$ and leverage the same differential phase mechanism in Fig. 6.5 to obtain a measurement of ψ_2. This approach replaces the measurement $y_{1,ave}(\theta_l)$ in Eq. (6.54)

with the signal template, $y_{\bar{2},ave}(\theta_l) = h(\theta_l)$. The intermediate measurements are

$$y_{s,ave,\bar{2},j} = \underbrace{\frac{\lambda_s P_2}{2} b_j}_{h_{s,\bar{2}j}} \quad , \text{ and } \quad y_{c,ave,\bar{2},j} = \underbrace{\frac{\lambda_s P_2}{2} a_j}_{h_{c,\bar{2}j}} . \tag{6.62}$$

As a result,

$$\begin{aligned}
y_{2-\bar{2},ave,j} &= y_{s,ave,\bar{2}j} y_{c,ave,2j} - y_{s,ave,2j} y_{c,ave,\bar{2}j} \\
&= h_{s,\bar{2}j}(h_{c,2j} + v_{c,ave,2j}) - (h_{s,2j} + v_{s,ave,2j}) h_{c,\bar{2}j} \\
&= h_{s,\bar{2}j} h_{c,2j} - h_{s,2j} h_{c,\bar{2}j} + v_{2-\bar{2},ave,j} \\
&= \frac{\lambda_s P_2}{2} \left(b_j h_{c,2j} - a_j h_{s,2j}\right) + v_{2-\bar{2},ave,j} \\
&= \frac{\lambda_s P_2^2}{4} \left(b_j A_{2j} - a_j B_{2j}\right) + v_{2-\bar{2},ave,j} \\
&= \frac{\lambda_s^2 P_2^2}{4} \Big[b_j \Big(\cancel{a_j \cos(j2\pi \left(\psi_2 - \bar{\psi}_2\right))} + b_j \sin\left(j2\pi \left(\psi_2 - \bar{\psi}_2\right)\right) \Big) \\
&\qquad - a_j \Big(\cancel{b_j \cos(j2\pi \left(\psi_2 - \bar{\psi}_2\right))} - a_j \sin(j2\pi \left(\psi_2 - \bar{\psi}_2\right)) \Big) \Big] + v_{2-\bar{2},ave,j} \\
&= \frac{\lambda_s^2 P_2^2}{4} \left(a_j^2 + b_j^2\right) \sin\left(j2\pi \left(\psi_2 - \bar{\psi}_2\right)\right) + v_{2-\bar{2},ave,j},
\end{aligned} \tag{6.63}$$

where

$$\begin{aligned}
v_{2-\bar{2},ave,j} &= h_{s,\bar{2}j} v_{c,ave,2j} - h_{c,\bar{2}j} v_{s,ave,2j} \\
&= \frac{\lambda_s P_2}{2} \left(-a_j v_{c,ave,2j} + b_j v_{s,ave,2j}\right).
\end{aligned} \tag{6.64}$$

The noise variance is

$$\begin{aligned}
\mathrm{var}[v_{2-\bar{2},ave,j}] &= \frac{\lambda_s^2 P_2^2}{4} E\left[a_j^2 v_{c,ave,2j}^2 - 2a_j b_j \cancel{v_{c,ave,2j} v_{s,ave,2j}} + b_j^2 v_{s,ave,2j}^2\right] \\
&= \frac{V_{2,ave} \lambda_s^2 P_2^3}{8} \left(a_j^2 + b_j^2\right) \\
&= \frac{V_2 \lambda_s^2 P_2^4}{8 T_{obs,2}} \left(a_j^2 + b_j^2\right).
\end{aligned} \tag{6.65}$$

The correlation between $v_{2-\bar{2},ave,j}$ and $v_{2-1,ave,j}$ is

$$\begin{aligned}
E[v_{2-\bar{2},ave,j}v_{2-1,ave,j}] &= E\Bigg[\left(h_{s,\bar{2}j}v_{c,ave,2j} - h_{c,\bar{2}j}v_{s,ave,2j}\right) \\
&\qquad \Big[\left(h_{s,1j}v_{c,ave,2j} + h_{c,2j}\cancel{v_{s,ave,1j}} + \cancel{v_{s,ave,1j}v_{c,ave,2j}}\right) \\
&\qquad - \left(h_{s,2j}\cancel{v_{c,ave,1j}} + h_{c,1j}v_{s,ave,2j} + \cancel{v_{s,ave,2j}v_{c,ave,1j}}\right)\Big]\Bigg] \\
&= E\left[\left(h_{s,\bar{2}j}v_{c,ave,2j} - h_{c,\bar{2}j}v_{s,ave,2j}\right)\left(h_{s,1j}v_{c,ave,2j} - h_{c,1j}v_{s,ave,2j}\right)\right] \\
&= E\left[h_{s,\bar{2}j}h_{s,1j}v_{c,ave,2j}^2 - 2h_{s,\bar{2}j}h_{s,1j}\cancel{v_{c,ave,2j}v_{s,ave,2j}} + h_{s,\bar{2}j}h_{s,1j}v_{s,ave,2j}^2\right] \\
&= E\left[h_{s,\bar{2}j}h_{s,1j}v_{c,ave,2j}^2 + h_{s,\bar{2}j}h_{s,1j}v_{s,ave,2j}^2\right] \\
&= \frac{V_{2,ave}P_2}{2}E\left[h_{s,\bar{2}j}h_{s,1j} + h_{s,\bar{2}j}h_{s,1j}\right] \\
&= \frac{V_{2,ave}\lambda_s^2P_2^2P_1}{8}E\Big[a_j\left(a_j\cos\left(j2\pi(\psi_1-\bar{\psi}_1)\right) + b_j\sin\left(j2\pi(\psi_1-\bar{\psi}_1)\right)\right) \\
&\qquad + b_j\left(b_j\cos\left(j2\pi(\psi_1-\bar{\psi}_1)\right) - a_j\sin\left(j2\pi(\psi_1-\bar{\psi}_1)\right)\right)\Big].
\end{aligned} \tag{6.66}$$

If $\psi_1 \approx \bar{\psi}_1$, then

$$\begin{aligned}
E[v_{2-\bar{2},ave,j}v_{2-1,ave,j}] &\approx \frac{V_{2,ave}\lambda_s^2P_2^2P_1}{8}\left(a_j^2+b_j^2\right) \\
&\approx \frac{V_2\lambda_s^2P_2^3P_1}{8T_{obs,2}}\left(a_j^2+b_j^2\right).
\end{aligned} \tag{6.67}$$

Because $E[v_{c,ave,ij}v_{c,ave,ik}] = 0$ and $E[v_{s,ave,ij}v_{s,ave,ik}] = 0$ for $k \neq j$, $E[v_{2-\bar{2},ave,j}v_{2-1,ave,k}] = 0$ for $k \neq j$.

6.6 Numerical Simulation

6.6.1 Simulation Setup

In order to determine the performance of the differential phase mechanism, the performance of the non-differential phase system (system #1) is compared with that of the differential phase system (system #2). The state space model of system #1 is the same as

Eq. (6.16), which is

$$\begin{bmatrix} \dot{\boldsymbol{s}}_1(t) \\ \dot{\boldsymbol{s}}_2(t) \\ \dot{\boldsymbol{b}}_{ssb}(t) \\ \dot{\boldsymbol{t}}_c(t) \\ \dot{\boldsymbol{\eta}}_p(t) \end{bmatrix} = \begin{bmatrix} 0 & 0 & 0 & 0 & 0 \\ 0 & 0 & 0 & 0 & 0 \\ 0 & 0 & 0 & 0 & 0 \\ 0 & 0 & 0 & F_c & 0 \\ 0 & 0 & 0 & 0 & F_{\eta,p} \end{bmatrix} \underbrace{\begin{bmatrix} \boldsymbol{s}_1(t) \\ \boldsymbol{s}_2(t) \\ \boldsymbol{b}_{ssb}(t) \\ \boldsymbol{t}_c(t) \\ \boldsymbol{\eta}_p(t) \end{bmatrix}}_{\boldsymbol{x}_{sys1}(t)} + \begin{bmatrix} G_{s,1} & 0 & 0 & 0 & 0 \\ 0 & G_{s,2} & 0 & 0 & 0 \\ 0 & 0 & G_{ssb} & 0 & 0 \\ 0 & 0 & 0 & G_c & 0 \\ 0 & 0 & 0 & 0 & G_{\eta,p} \end{bmatrix} \begin{bmatrix} \boldsymbol{w}_{s,1}(t) \\ \boldsymbol{w}_{s,2}(t) \\ \boldsymbol{w}_{ssb}(t) \\ \boldsymbol{w}_c(t) \\ \boldsymbol{w}_{\eta,p}(t) \end{bmatrix}$$

$$\begin{bmatrix} \boldsymbol{y}_{1,ave,p}(t) \\ \boldsymbol{y}_{2,ave,p}(t) \end{bmatrix} = \begin{bmatrix} \boldsymbol{h}_p(\phi_{1,p}(t)) \\ \boldsymbol{h}_p(\phi_{2,p}(t)) \end{bmatrix} + \underbrace{\begin{bmatrix} \boldsymbol{v}_{1,ave,p}(t) \\ \boldsymbol{v}_{2,ave,p}(t) \end{bmatrix}}_{\boldsymbol{v}_{sys1,ave,p}(t)}. \tag{6.68}$$

The state space model for system # 2 is

$$\begin{bmatrix} \dot{\boldsymbol{s}}_r(t) \\ \dot{\boldsymbol{s}}_2(t) \\ \dot{\boldsymbol{b}}_{ssb}(t) \\ \dot{\boldsymbol{t}}_c(t) \\ \dot{\boldsymbol{\eta}}_p(t) \end{bmatrix} = \begin{bmatrix} 0 & 0 & 0 & 0 & 0 \\ 0 & 0 & 0 & 0 & 0 \\ 0 & 0 & 0 & 0 & 0 \\ 0 & 0 & 0 & F_c & 0 \\ 0 & 0 & 0 & 0 & F_{\eta,p} \end{bmatrix} \underbrace{\begin{bmatrix} \boldsymbol{s}_r(t) \\ \boldsymbol{s}_2(t) \\ \boldsymbol{b}_{ssb}(t) \\ \boldsymbol{t}_c(t) \\ \boldsymbol{\eta}_p(t) \end{bmatrix}}_{\boldsymbol{x}_{sys2}(t)} + \begin{bmatrix} -G_{s,1} & G_{s,2} & 0 & 0 & 0 \\ 0 & G_{s,2} & 0 & 0 & 0 \\ 0 & 0 & G_{ssb} & 0 & 0 \\ 0 & 0 & 0 & G_c & 0 \\ 0 & 0 & 0 & 0 & G_{\eta,p} \end{bmatrix} \begin{bmatrix} \boldsymbol{w}_{s,1}(t) \\ \boldsymbol{w}_{s,2}(t) \\ \boldsymbol{w}_{ssb}(t) \\ \boldsymbol{w}_c(t) \\ \boldsymbol{w}_{\eta,p}(t) \end{bmatrix}$$

$$\begin{bmatrix} \boldsymbol{y}_{2-\bar{2},ave,p}(t) \\ \boldsymbol{y}_{2-1,ave,p}(t) \end{bmatrix} = \begin{bmatrix} \breve{\boldsymbol{h}}_{2-\bar{2},p}(\psi_{2,p}(t)) \\ \breve{\boldsymbol{h}}_{2-1,p}(\psi_{2,p}(t) - \psi_{1,p}(t)) \end{bmatrix} + \underbrace{\begin{bmatrix} \boldsymbol{v}_{2-\bar{2},ave,p}(t) \\ \boldsymbol{v}_{2-1,ave,p}(t) \end{bmatrix}}_{\boldsymbol{v}_{sys2,ave,p}(t)}. \tag{6.69}$$

The relative position estimate $\hat{\boldsymbol{s}}_r$ can be obtained by multiplying the state estimate of system #1 with $C = \begin{bmatrix} -I & I & 0 & 0 & 0 \end{bmatrix}$. Thus, the mean and covariance are

$$\hat{\boldsymbol{s}}_{r,sys1}(t) = C\hat{\boldsymbol{x}}_{sys1}(t), \quad \text{and} \quad P_{\boldsymbol{s}_r,sys1}(t) = CP_{sys1}(t)C^T, \tag{6.70}$$

where $P_{sys1}(t)$ is the error covariance of the EKF. In short, system #1 estimates the position of the observatories without using the differential phase measurements and system #2 uses one differential phase measurement, $\boldsymbol{y}_{2-1,ave,p}(t)$, and one non-differential phase measurement, $\boldsymbol{y}_{2-\bar{2},ave,p}(t)$. Both systems are processed by an Extended Kalman Filter (EKF) with

Table 6.1: Antenna System

Parameters	Units	Value
G	K/Jy	1
n_p		1
Δf	MHz	500
T_{sys}	K	30

epoch folding [44, 56].

The PSD of the measurement noise, $V_{i,p}$ for all pulsars are chosen to be the same, $V_{i,1} = V_{i,2} = V_i$ and V_i is obtained using Eq. (A.17). The parameters of the radiometer equation are listed in Table 6.1. From Eq. (6.52), the measurement noise covariance of system #1 is

$$\begin{aligned}\Sigma_{sys1,p} &= E\left[\boldsymbol{v}_{sys1,ave,p}(t)\boldsymbol{v}^T_{sys1,ave,p}(t)\right] \\ &= \begin{bmatrix} \frac{V_1 N_{b,p}}{T_{obs,1}} I_{N_{b,p}\times N_{b,p}} & 0 \\ 0 & \frac{V_2 N_{b,p}}{T_{obs,2}} I_{N_{b,p}\times N_{b,p}} \end{bmatrix}.\end{aligned} \tag{6.71}$$

The measurement noise covariance of system #2 is obtained from Eq. (6.64), Eq. (6.65), and Eq. (6.67),

$$\begin{aligned}\Sigma_{sys2,p} &= E\left[\boldsymbol{v}_{sys2,ave,p}(t)\boldsymbol{v}^T_{sys2,ave,p}(t)\right] \\ &= \begin{bmatrix} [\Sigma_{sys2,p}]_{11} & [\Sigma_{sys2,p}]_{12} \\ [\Sigma_{sys2,p}]_{12} & [\Sigma_{sys2,p}]_{22} \end{bmatrix},\end{aligned} \tag{6.72}$$

where

$$\begin{aligned}[\Sigma_{sys2,p}]_{11} &= \mathrm{diag}\left(\frac{V_2\lambda^2_{s,p}P^4_{2,p}}{8T_{obs,2}}\left(a^2_{j,p}+b^2_{j,p}\right)\right) \\ [\Sigma_{sys2,p}]_{12} &= \mathrm{diag}\left(\frac{V_2\lambda^2_{s,p}P^3_{2,p}P_{1,p}}{8T_{obs,2}}\left(a^2_{j,p}+b^2_{j,p}\right)\right) \\ [\Sigma_{sys2,p}]_{22} &= \mathrm{diag}\left(\frac{P^2_{1,p}P^2_{2,p}}{2}\left[\frac{\lambda^2_{s,p}(a^2_{j,p}+b^2_{j,p})}{4}\left(\frac{V_2}{T_{obs,2}}+\frac{V_1}{T_{obs,1}}\right)+\frac{V_1V_2}{T_{obs,1}T_{obs,2}}\right]\right)\end{aligned} \tag{6.73}$$

for $j = 1 \ldots N$.

The pulsar parameters used in the simulation are listed in Table 6.2. The pulsar timing noise model from Eq. (B) are approximated using Charef method. See Appendix B. The

Table 6.2: Pulsar Parameters [7]

Pulsar	$\lambda_b\ (Jy)$	$\lambda_s\ (mJy)$	$\dot{\phi}\ (Hz)$	RA (°)	DEC (°)
J0437-4715	30	149	173.7	69.32	-47.25
J1643-1224	30	4.8	216.4	250.91	-12.42
J1713+0747	30	10.2	218.8	258.46	7.79
J1939+2134	30	13.2	641.9	294.91	21.58
J2145-0750	30	8.9	62.3	326.46	-7.84

initial error covariance matrix is

$$P(0) = \text{diag}([P_{s,1}(0), P_{s,2}(0), P_{ssb}(0), P_c(0), P_{\eta,p}(0)]), \tag{6.74}$$

where

$$\begin{aligned} P_{s,1}(0) &= \text{diag}([10^2, 10^2, 10^2])\ km^2 \\ P_{s,2}(0) &= \text{diag}([10^2, 10^2, 10^2])\ km^2 \\ P_{ssb}(0) &= \text{diag}([0.1^2, 0.1^2, 0.1^2])\ km^2 \\ P_c(0) &= \text{diag}([10^{-8}\ s^2, 10^{-18}\ (s/s)^2]) \\ P_{\eta,p}(0) &= \text{diag}([10^{-12}\ s^2, 10^{-24}\ (s/s)^2, 10^{-36}\ (s/s^2)^2, \ldots]) \end{aligned} \tag{6.75}$$

The initial state vector for the simulation are realized randomly with the above variance around the mean value. The mean observatory positions in ITRS are

$$\begin{aligned} \bar{\boldsymbol{s}}_1 &= [-2200.61, 7458.10, -7131.09]\ km \\ \bar{\boldsymbol{s}}_2 &= [-4554.23, 2816.76, -3454.04]\ km \end{aligned} \tag{6.76}$$

The mean values for the rest of the states are 0. The PSD of $\boldsymbol{w}_c(t)$ is $W_c = \text{diag}[(1.60 \times 10^{-21}\ s^2/s, 10^{-32}\ s^2/s^3)]$. The PSD of $\boldsymbol{w}_{s,i}(t)$ is $W_{s,i} = 10^{-6}\ km^2/s$ for $i = 1, 2$. The PSD of $\boldsymbol{w}_{ssb}(t)$ is $W_{ssb} = 0$.

A 40-trial Monte Carlo Analysis was used to compare the 2 formulations. In the simulation, each system observes 5 radio pulsars for $T_{obs,i} = 10\ minutes$ and the time interval between observations is 4.8 $hours$. A total of 15 observations were simulated. The sampling interval of the waveform is 100 μs and each observation generates one epoch folded profile $y_{i,ave}(\theta_l)$.

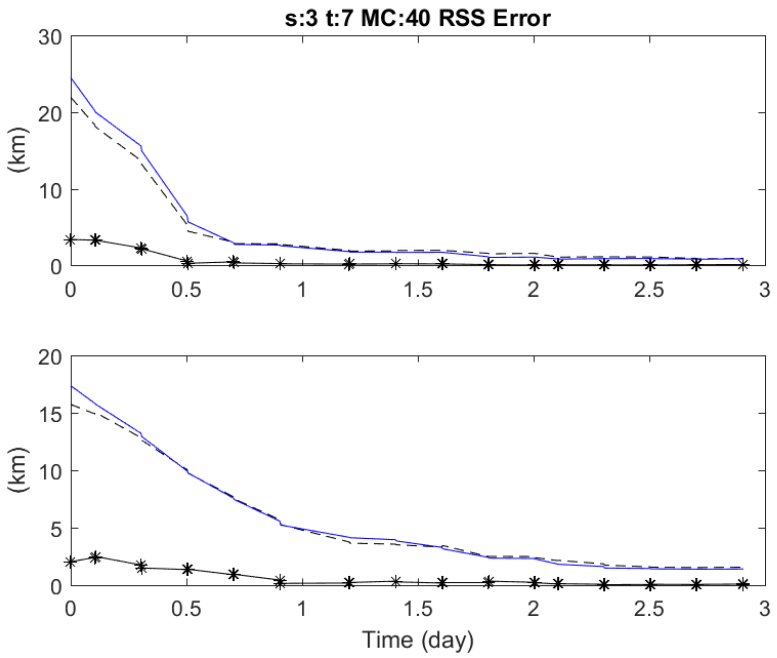

Figure 6.6: RSS position errors of $\boldsymbol{s}_r$ and $\boldsymbol{s}_2$ for system 1. The black dashed lines are the ensemble RSS bounds and the blue lines are the filter RSS bounds. The black stars are the ensemble errors

6.6.2 Simulation Result

The simulation results are plotted in Fig. 6.6 and Fig. 6.7. For both systems, the initial RSS bounds for the relative position, $\boldsymbol{s}_r$, is 24.5 km, and the initial RSS bound for observatory #2 position, $\boldsymbol{s}_2$, is 17.3 km. After processing 15 pulsar observations, the two RSS bounds for both the non-differential phase and differential phase systems reduce to 0.9 km and 1.4 km respectively. The ensemble bounds marked by black dashed lines match the filter bounds marked by blue. The ensemble errors are closed to zero for both systems. This is an indication that the programming and the derivation presented in this chapter are correct. The surprising result is that there is virtually no difference between the differential and non-differential systems. The fact that the common errors are eliminated in one of the measurement equation does not seem to improve the overall performance of the system.

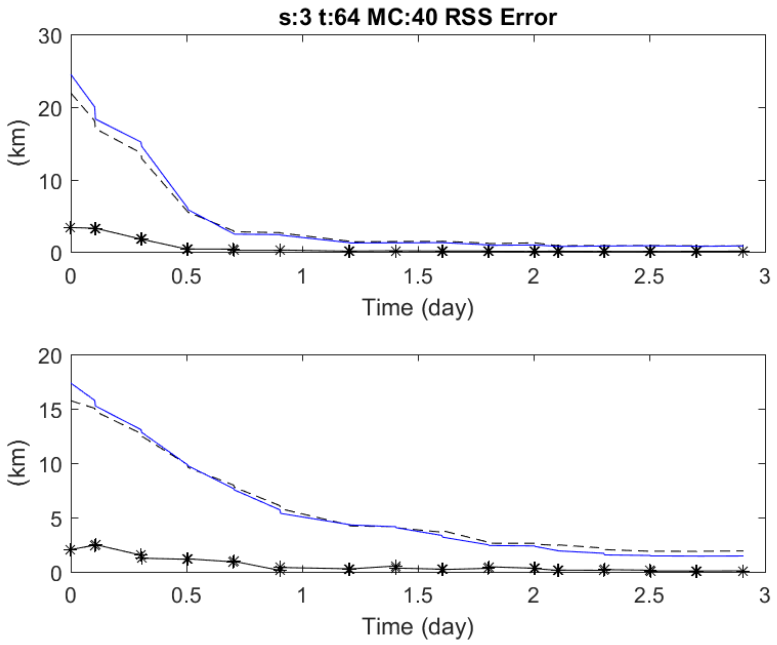

Figure 6.7: RSS position errors of $\boldsymbol{s}_r$ and $\boldsymbol{s}_2$ for system 2. The black dashed lines are the ensemble RSS bounds and the blue lines are the filter RSS bounds. The black stars are the ensemble errors

6.7 Discussion

After a closer examination of the system in Eq. (6.69), it reveals a fundamental limitation that prevents one to obtain a system that is truly capable of rejecting common mode errors. While $\boldsymbol{y}_{2-1,ave,p}(t)$ can tolerate common mode errors, $\boldsymbol{y}_{2-\bar{2},ave,p}(t)$ cannot, and the reason for processing $\boldsymbol{y}_{2-\bar{2},ave,p}(t)$ is to obtain a frequency estimate of $f_{s,2}(t)$ for epoch folding. Since this frequency is related to the absolute position of observatory #2 and the common mode errors, they have to be included in the state vector of system #2. Therefore, it is not possible to decouple the absolute and relative system using the above formulation. This is likely to be the reason that both systems have the same performance because the common mode errors are not explicitly eliminated. Perhaps, the approach presented in this chapter is merely a coordinate transformation.

While it is possible to replace the filter predicted $f_{s,2}(t)$ with an online estimate, it is unclear which method could be used to efficiently obtain such an estimate with sufficient accuracy. The goal of online estimation is to estimate $f_{s,2}(t)$ in the presence of unknown phase offset, $\psi_2(t)$, without explicitly tracking the unknown phase. The first method that comes into mind is the Fast Fourier Transform of $y_i(t)$. It can be used to obtain a frequency estimate with a resolution of $1/T_{obs,i}$. However, the trade of this approach is that the observation time $T_{obs,i}$ has to be long enough to achieve the required resolution, but short enough such that constant frequency approximation is reasonable. Further investigation is required to determine the feasibility of this approach. The ability to estimate $f_{s,2}(t)$ accurately would allow one to decoupled the relative system from the absolute system and realize a relative navigation that rejects common mode errors.

The differential phase mechanism can also be used to estimate the absolute phase as shown by the auxiliary measurement, $\boldsymbol{y}_{2-\bar{2},ave,p}(t)$. It is worth comparing the performance of using the mechanism in Section 6.5.3 for absolute phase tracking with the epoch folding method presented in [56]. Since the differential phase mechanism breaks the highly nonlinear profiles into sine and cosine functions, it eliminates an issue associated with linearization of the measurement equation. Namely, the derivative of the measurement function, $h(\cdot)$ with

respective to the phase is essentially zero when evaluated at phase region corresponding to zero signal intensity. Therefore, if the non-zero measurement residuals lie in the region with zero signal intensity, then the update from an EKF with epoch folding is essentially zero. In other words, the filter is unable to correct errors in the filter prediction using pulsar measurements if the initial error is larger then the pulse width

On the other hand, if the differential phase mechanism is used to extract the first harmonic associated with the pulsar profile, then one can utilize the properties of sine function to relax the initial uncertainty to ± 0.5 *cyc*. From Eq. (6.63), the first harmonic measurement is

$$y_{2-\bar{2},ave,1} = \frac{\lambda_s^2 P_2^2}{4}\left(a_1^2 + b_1^2\right)\sin\left(2\pi\left(\psi_2 - \bar{\psi}_2\right)\right) + v_{2-\bar{2},ave,1}. \tag{6.77}$$

The key is the sine function. Since the filter prediction of ψ_2 is $\bar{\psi}_2$, the EKF predicted measurement is always 0. This means the residual is $r \propto \sin(e_2)$, where $e_2 := \psi_2 - \bar{\psi}_2$. Furthermore, the derivative of Eq. (6.77) with respect to ψ_2 evaluated at $\bar{\psi}_2$, is a positive value. This means the EKF gain, K, is always positive. Recall, the EKF update equation is $\hat{\psi}_2 = \bar{\psi}_2 + Kr$. From the definition of e_2, if $e_2 > 0$, then $\bar{\psi}_2 < \psi_2$. Thus, if the error, e_2, is between 0 and π, then the product of the residual and the gain, Kr, generates a positive correction value that drives e_2 to 0, i.e., $\bar{\psi}_2 \to \psi_2$. If e_2 is between $-\pi$ and 0, the correction value is always negative which also drives e_2 to 0. The rest of the harmonics do not have this property due to multiple cycles in the interval of $-\pi$ and π. Based on this simple intuition, the first harmonic measurement is a suitable measurement for filter initialization. Once the filter 1σ bound on ψ_2 is below a pre-defined threshold, then all harmonics can be used to achieve the optimal condition in Eq. (6.49).

CHAPTER 7

Conclusions

On the topic of autonomous spacecraft navigation using pulsar signals, one can draw the following conclusions from the analysis and simulation results. Given a minimum of 4 representative pulsar timing models and an initial position uncertainty within ± 0.5 *cyc* of the fastest pulsars in the observation schedule, it is definitely possible to coherently process either radio or X-ray pulsar measurements to estimate the spacecraft states in the presence of time-correlated measurement noise. This research used Extended Kalman Filter with epoch folding to process X-ray pulsar measurements. Numerical simulations showed an RSS position bound of 7 km can be achieved after 20 hours of continuous simultaneous pulsar observation or 4 days of sequential observation (50 minute observation once every hour). When sequential observation is used in the presence of significant process noise, it is important to allow for sufficient observation time in order to keep the estimation error below ± 0.5 *cyc*.

The question of whether pulsar signals can be used to determine the position of an observer on Earth is studied in the second topic. Through the use of experimental pulsar timing data, it was shown in this dissertation that the idea of using pulsar signals for positioning is feasible over short timescale. Straight forward enhancements can be applied to the current implementation to extend the concept as long as the pulsar timing models remain valid. This first implementation shows the root-sum-squared positioning accuracy on Earth using five isolated millisecond radio pulsars is about 1 km. The accuracy is expected to improve to ~ 250 m if the bias in the pulsar timing model can be calibrated out using more data. Furthermore, the uncertainty bound associated with the white radiometer noise would also decrease if more pulsar time-of-arrival measurements are processed.

Regarding the use of pulsar signals for atomic clock calibration, one can draw the following conclusions from the frequency stability analysis result. Since there is no theoretical result that guarantees pulsar signals are long-term stable, this study considered two scenarios. The first scenario is more conservative and models the pulsar timing noise as fractional integration of white noise, while the second scenario models the pulsar timing noise as fractional stationary noise. In the first scenario, if one chooses a pulsar with integration order, α, less than 1.5, then it prevents the frequency stability of the filtered clock system from diverging at large averaging time. However, because of the lack of observability, the time estimation error remains divergent. The choice of α only reduces the rate of time divergence. On the other hand, if the pulsar timing noise can be modeled by a fractional stationary process, then a Kalman filter can be designed to separate the clock noise from the pulsar timing noise. In this scenario, the estimation error covariance has a steady state as long as the noise model is representative of the reality. Both scenarios show that pulsar-aided clock is beneficial to deep space exploration probes because it reduces the need for frequent clock synchronization using Earth-based references.

The last topic in this research focuses on the use of differential phase measurement to reject common mode errors embedded in the pulsar measurement equation. While it is relatively easy to manipulate the pulsar measurement equation to algebraically cancel common mode errors in the phase equation when the signal frequencies measured at the two observers are known and equal. In reality the signal frequencies are usually unknown and different due to the motion of the observers. This study utilized epoch folding method to compensate for the difference in signal frequencies. However, this approach requires the filter to estimate the signal frequency by tracking the pulsar signal using the pulsar timing models and observer dynamics. As a result of this formulation, it is necessary to account for all common mode errors; otherwise, the estimated signal phase is corrupted by a phase bias. Such a bias can lead to filter divergence due to linearization error. In other words, the approach presented in the last chapter does not truly reject common model errors. The difficulty that one has to overcome is to estimate signal frequency without explicitly relating the pulsar signal phase to the observer states. Further investigation is required.

Future research topics in pulsar based navigation include (1) further investigation into differential phase measurement, (2) filter initialization via integer ambiguity resolution, and (3) optimization of pulsar observation sequence for a given observer trajectory. On the implementation and verification of pulsar based navigation, it would be informative to test the algorithm presented in Chapter 4 with more experimental data to investigate the limitations of this approach in the areas of positioning accuracy, long term feasibility, and practicality. On the pulsar timing aspect, further research into the intrinsic pulsar stability is necessary to realize a pulsar based navigation and timing system in real life. Therefore, continuing pulsar timing experiments and fundamental pulsar research carried out at national laboratories and observatories are of utmost importance.

APPENDIX A

Radiometer Equation

The following is the derivation of the radiometer equation [18]. The radiometer equation is used to calculate the measurement noise variance, σ_v^2. The fundamental quantity used in radio astronomy observation is the one sided spectral flux density, S, which describes the rate at which energy (i.e. power) is received from the source via electromagnetic radiation, per unit area and per unit bandwidth. Even though $Jansky$ is the unit used to quantify the radiation strength of the source, the inner working of the antenna and receiver system use units of power instead. The antenna and receiver system are modeled using a simple circuit consists of two wires (antenna) and a resistor (receiver). As electromagnetic energy hits the wires (antenna), it induces voltage variations across the resister.

For a given antenna and receiver system, the quantity at the output terminal after the source signal has been amplified, band-passed, down-converted and low-passed is given in the units of $Volts$ or more accurately a voltage scaled by a resistance, i.e. $Volts/\sqrt{Ohms} = \sqrt{Watts}$. Let's define this quantity as x_i for the i^{th} channel. Typically, an antenna has two channels: one detects the electric field and the other detects the magnetic field of the signal. The relationship between x_i and spectral flux density is through power. The power received by the antenna from a source per unit bandwidth per channel is

$$P_i = \frac{SA_e}{2}, \tag{A.1}$$

where the effective antenna area is $A_e = \eta A$. The units of S are Ws/m^2 or Jy ($1\ Jy = 10^{-26}\ Ws/m^2$). The physical antenna area is A and the antenna efficiency is η. P can be interpreted as the 2-sided PSD of the source. The definition of the bandwidth, Δf is

$$\Delta f = \frac{1}{2\Delta\tau}, \tag{A.2}$$

where $\Delta\tau$ is the sampling rate of the radiometer. P_i represents the strength of the signal detected by the antenna, which consists of the source signal and unwanted noises.

Unfortunately, the spectral flux density of a pulsar is significantly smaller than the contribution from the environment and the antenna/receiver system. Thus, the radiometer equation describes the strength of the measurement noise, which is independent of the source strength. In other words, x_i, is a noise signal. The convention used by the radio astronomy community to describe the noise strength is given in terms of the temperature of the aforementioned resistor rather than the spectral flux density. The thermal noise of the i^{th} resister can be modeled as zero mean Gaussian white noise, whose PSD is

$$P_i = k_B T, \tag{A.3}$$

where $k_B = 1.38064852 \times 10^{-23}\ (m^2 Kg)/(s^2 K)$ is the Boltzman constant. Setting Eq. (A.3) equal to Eq. (A.1) and solving for S give

$$S = \frac{2k_B T}{A_e} = \frac{T}{G}, \tag{A.4}$$

where G is defined as the antenna gain and has units of Jy/K. This equation establishes the relationship between spectral flux density, S, and temperature, T. The system spectral flux density, S_{sys}, can be obtained by summing the temperature of the individual noise source. Thus,

$$S_{sys} = \frac{T_{sys}}{G}. \tag{A.5}$$

The variance of x_i can be found by dividing Eq. (A.3) by $\Delta\tau$. Substituting the relationship in Eq. (A.3) gives

$$\begin{aligned} \sigma_x^2 &= \frac{P_i}{\Delta\tau} \\ &= 2k_B T_{sys} \Delta f. \end{aligned} \tag{A.6}$$

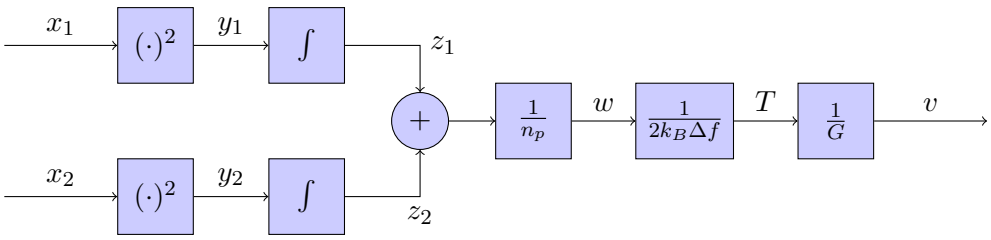

Figure A.1: Square detector and integrator

The next step is to convert the signal from voltage to power using the square detector. This nonlinear transformation converts the Gaussian density function to

$$f_{Y_i}(y_i) = \frac{1}{\sqrt{2\pi y_i}\sigma_x} exp\left(\frac{-y_i}{2\sigma_x^2}\right), \tag{A.7}$$

where $y_i > 0$. The mean and variance of y_i is

$$E[y_i] = \sigma_x^2, \text{ and } var[y_i] = 2\sigma_x^4. \tag{A.8}$$

The integrator in Figure A.1 transforms y_i to z_i through averaging. Thus z_i is a Gaussian random variable via the Central Limit theorem. The integration or averaging time is t_{int},

$$z_i = \frac{1}{t_{int}} \int_{t_0}^{t_0+t_{int}} y_i(t)dt = \frac{1}{N}\sum_{j=1}^{N} y_i(t_j), \tag{A.9}$$

where $N = \frac{t_{int}}{\Delta\tau}$ is the number of receiver samples over t_{int}. The integration time,t_{int}, is also the measurement sampling time, Δt, of the Kalman filter. N is typically a large number because of the fast sampling rate of the radiometer. The mean and variance of z_i are

$$E[z_i] = \sigma_x^2 \text{ and } var[z_i] = \frac{2\Delta\tau\sigma_x^4}{t_{int}}, \text{ where } i = 1, ..., n_p. \tag{A.10}$$

Averaging signals from both polarization gives

$$w = \frac{1}{n_p}\sum_{i=1}^{n_p} z_i, \tag{A.11}$$

and the variance is

$$\begin{aligned} var[w] &= \frac{2\Delta\tau\sigma_x^4}{t_{int}n_p} \\ &= \frac{4k_B^2T_{sys}^2\Delta f}{t_{int}n_p}. \end{aligned} \tag{A.12}$$

Taking the square root of Eq. (A.12) gives

$$\begin{aligned} \sigma_w &= \frac{2k_B T_{sys}\sqrt{\Delta f}}{\sqrt{t_{int} n_p}} \\ \frac{\sigma_w}{2k_B \Delta f} &= \frac{T_{sys}}{\sqrt{t_{int} n_p \Delta f}} \end{aligned} \tag{A.13}$$

Because the unit on the left hand side is temperature, the above expression can be rewritten as

$$\sigma_T := \frac{T_{sys}}{\sqrt{t_{int} n_p \Delta f}}. \tag{A.14}$$

This is the well-known radiometer equation. Substituting the above into Eq. (A.5) gives an equivalent equation in spectral flux density units that describes the standard deviation of the fluctuation of the spectral flux density noise,

$$\sigma_v = \frac{T_{sys}}{G\sqrt{t_{int} n_p \Delta f}}. \tag{A.15}$$

Squaring Eq. (A.15) gives the noise variance for the unfolded pulsar signal,

$$\sigma_v^2 = \frac{T_{sys}^2}{G^2 t_{int} n_p \Delta f}. \tag{A.16}$$

Expressing Eq. (A.15) in PSD form gives

$$V = \frac{T_{sys}^2}{G^2 n_p \Delta f}. \tag{A.17}$$

Since pulsar signals are much weaker than the environment and the hardware noises, epoch folding is required to obtain a visually observable pulse. The mean of the radiometer noise is

$$E[v] = \frac{T_{sys}}{G}. \tag{A.18}$$

APPENDIX B

Charef Approximation

There are various methods for approximating the fractional LTI system. This section gives a the formulas of the Charef method for determining the locations of stable poles and zeros to approximate the fractional transfer function $G_{n,2}(s)$ in Eq. (5.21) [54]. The advantage of this method is simplicity, and the matching of the steady state gain. The finite dimensional approximation of the fractional system is

$$\hat{G}_{n,2}(s) = \frac{\prod_{i=0}^{N_{pole}-1} \left(1 + \frac{s}{z_i}\right)}{\prod_{i=0}^{N_{pole}} \left(1 + \frac{s}{p_i}\right)}, \tag{B.1}$$

where $-z_i$ and $-p_i$ are the zeros and poles and they are given by the following formulas. They are

$$\begin{aligned} p_0 &= \omega_c 10^{\frac{\delta}{20\gamma}} \\ z_0 &= p_0 10^{\frac{\delta}{10(1-\gamma)}} \\ p_i &= (ab)^i p_0, \quad i = 1, 2, \ldots N_{pole} \\ z_i &= (ab)^i a p_0, \quad i = 1, 2, \ldots N_{pole}, \end{aligned} \tag{B.2}$$

where $a = 10^{\frac{\delta}{10(1-\gamma)}}$ and $b = 10^{\frac{\delta}{10\gamma}}$. The number of poles, N_{pole}, is given by

$$N_{pole} = \left\lceil \frac{\log\left(\frac{\omega_{max}}{p_0}\right)}{\log(ab)} \right\rceil + 1, \tag{B.3}$$

where $\lceil \cdot \rceil$ is the ceiling operator, and

$$\delta = \left| \|G(s)\| - \|\hat{G}(s)\| \right| \tag{B.4}$$

is the maximum allowable deviation in the gain of the approximate transfer function for $\omega \in [0, \omega_{max}]$ expressed in dB.

REFERENCES

[1] NASA/JPL. Home page - deep space network.

[2] Luke Winternitz, Keith C Gendreau, Monther A Hasouneh, Jason W Mitchell, Wai H Fong, Wing-Tsz Lee, Fotis Gavriil, and Zaven Arzoumanian. The role of x-rays in future space navigation and communication. Technical report, NASA, 2013.

[3] F D'Alessandro, AA Deshpande, and PM McCulloch. Power spectrum analysis of the timing noise in 18 southern pulsars. *Journal of Astrophysics and Astronomy*, 18(1):5–14, 1997.

[4] David A Moffett and Timothy H Hankins. Multifrequency radio observations of the crab pulsar. *arXiv preprint astro-ph/9604163*, 1996.

[5] Marc D Rayman and Robert A Mase. The second year of dawn mission operations: Mars gravity assist and onward to vest. *Acta Astronautica*, 67(3-4):483–488, 2010.

[6] RN Manchester, GB Hobbs, A Teoh, and M_ Hobbs. The australia telescope national facility pulsar catalogue. *The Astronomical Journal*, 129(4):1993, 2005.

[7] ATNF pulsar catelog. [Online Database], May 2013.

[8] Luke MB Winternitz, Munther A Hassouneh, Jason W Mitchell, Jennifer E Valdez, Samuel R Price, Sean R Semper, H Yu Wayne, Paul S Ray, Kent S Wood, Zaven Arzoumanian, et al. X-ray pulsar navigation algorithms and testbed for sextant. In *2015 IEEE Aerospace Conference*, pages 1–14. IEEE, 2015.

[9] Stefano Bregni. *Synchronization of digital telecommunications networks*, volume 27. Wiley New York, 2002. 203-279.

[10] Cristina Zucca and Patricia Tavella. The clock model and its relationship with the allan and related variances. *IEEE transactions on ultrasonics, ferroelectrics, and frequency control*, 52(2):289–296, 2005.

[11] Alaa Makdissi, François Vernotte, and Emeric Clercq. Stability variances: a filter approach. *Ultrasonics, Ferroelectrics, and Frequency Control, IEEE Transactions on*, 57(5):1011–1028, 2010.

[12] Olaf Frohn. What's up in the solar system diagram, 2018.

[13] Francesco Padovani. Timeline of solar system exploration. 2014.

[14] Leslie J Deutsch, Robert A Preston, and Barry J Geldzahler. Future plans for NASA's deep space network. Technical report, NASA, 2008.

[15] Catherine L Thornton and James S Border. *Radiometric tracking techniques for deep-space navigation*. John Wiley and Sons, Inc., 2003. 3-58.

[16] Caltech Jet Propulsion Laboratory and Dave Doody. Basics of space flight: Spacecraft navigation.

[17] Tim Pham and Alina Bedrossian. Deep space network services catalog.

[18] Duncan Ross Lorimer and Michael Kramer. *Handbook of pulsar astronomy*, volume 4. Cambridge University Press, 2005.

[19] D. C. Backer, Shrinivas R Kulkarni, Carl Heiles, MM Davis, and WM Goss. A millisecond pulsar. *Nature*, 300(5893):615–618, 1982.

[20] LA Rawley, JH Taylor, MM Davis, and DW Allan. Millisecond pulsar psr 1937+ 21- a highly stable clock. *Science*, 238(6):761–765, 1987.

[21] Jr. Taylor, J.H. Millisecond pulsars: nature's most stable clocks. *Proceedings of the IEEE*, 79(7):1054–1062, Jul 1991.

[22] Gérard Petit and P Tavella. Pulsars and time scales. *Astronomy and Astrophysics*, 308:290–298, 1996.

[23] AG Lyne. Pulsars as clocks. 1996.

[24] G Hobbs, W Coles, RN Manchester, MJ Keith, RM Shannon, D Chen, M Bailes, NDR Bhat, S Burke-Spolaor, D Champion, et al. Development of a pulsar-based time-scale. *Monthly Notices of the Royal Astronomical Society*, 427(4):2780–2787, 2012.

[25] RN Manchester, L Guo, G Hobbs, and WA Coles. Pulsars: Celestial clocks. In *The Science of Time 2016*, pages 253–265. Springer, 2017.

[26] RT Edwards, GB Hobbs, and RN Manchester. TEMPO2, a new pulsar timing package–II. the timing model and precision estimates. *Monthly Notices of the Royal Astronomical Society*, 372(4):1549–1574, 2006.

[27] G Hobbs, A Lyne, and M Kramer. Pulsar timing noise. *Chinese Journal of Astronomy and Astrophysics*, 6(S2):169, 2006.

[28] Andrew Lyne and Francis Graham-Smith. *Pulsar astronomy*. Cambridge University Press, 2012.

[29] GS Downs. Interplanetary navigation using pulsating radio sources. Technical report, NASA, NASA-CR-140398, 1974.

[30] Suneel I Sheikh and Darryll J Pines. Recursive estimation of spacecraft position using x-ray pulsar time of arrival measurements. In *ION 61st Annual Meeting*, pages 464–475, 2005.

[31] Amir Abbas Emadzadeh and Jason Lee Speyer. *Navigation in Space by X-ray Pulsars*. Springer, 2011. 13-85.

[32] A Robert Golshan and Suneel I Sheikh. On pulse phase estimation and tracking of variable celestial x-ray sources. In *Proceedings of the 63rd Annual Meeting of the Institute of Navigation*, pages 413–422, 2001.

[33] SpaceOps Conferences. *Methods of Pulse Phase Tracking for X-ray Pulsar Based Spacecraft Navigation using Low Flux Pulsars*, number AIAA 2014-1858, 2014.

[34] Luke MB Winternitz, Jason W Mitchell, Munther A Hassouneh, Jennifer E Valdez, Samuel R Price, Sean R Semper, H Yu Wayne, Paul S Ray, Kent S Wood, Zaven Arzoumanian, et al. Sextant x-ray pulsar navigation demonstration: Flight system and test results. In *Aerospace Conference, 2016 IEEE*, pages 1–11. IEEE, 2016.

[35] Howard Curtis. *Orbital mechanics for engineering students*. Butterworth-Heinemann, 2013.

[36] NASA JPL planetary and lunar ephemerides. [Online Database], 2015.

[37] Suneel I Sheikh, Darryll J Pines, Paul S Ray, Kent S Wood, Michael N Lovellette, and Michael T Wolff. Spacecraft navigation using x-ray pulsars. *Journal of Guidance, Control, and Dynamics*, 29(1):49–63, 2006.

[38] Rachel J Dewey and James M Cordes. The scaling of radio pulsar timing noise with spin parameters. In *Timing Neutron Stars*, pages 119–124. Springer, 1989.

[39] JM Cordes and DJ Helfand. Pulsar timing. iii-timing noise of 50 pulsars. *The Astrophysical Journal*, 239:640–650, 1980.

[40] James M Cordes. The detectability of planetary companions to radio pulsars. In *Planets around pulsars*, volume 36, pages 43–60, 1993.

[41] Delphine Perrodin, Fredrick Jenet, Andrea Lommen, Lee Finn, Paul Demorest, Robert Ferdman, Marjorie Gonzalez, David Nice, Scott Ransom, and Ingrid Stairs. Timing noise analysis of nanograv pulsars. *arXiv preprint arXiv:1311.3693*, 2013.

[42] W Coles, G Hobbs, DJ Champion, RN Manchester, and JPW Verbiest. Pulsar timing analysis in the presence of correlated noise. *Monthly Notices of the Royal Astronomical Society*, 418(1):561–570, 2011.

[43] Hu Sheng, YangQuan Chen, and TianShuang Qiu. *Fractional processes and fractional-order signal processing: techniques and applications*. Springer Science & Business Media, 2011. 49-76.

[44] Jason L Speyer and Walter H Chung. *Stochastic processes, estimation, and control*, volume 17. Siam, 2008. 153-192, 241-255.

[45] Richard B Langley et al. Dilution of precision. *GPS world*, 10(5):52–59, 1999.

[46] Bob Schutz, Byron Tapley, and George H Born. *Statistical orbit determination*. Academic Press, 2004. 194-210.

[47] DE Gustafson and JL Speyer. Linear minimum variance filters applied to carrier tracking. *Automatic Control, IEEE Transactions on*, 21(1):65–73, 1976.

[48] Orville J Oaks, Thomas B McCaskill, Marie M Largay, Wilson G Reid, and James A Buisson. Performance of GPS on-orbit NAVSTAR frequency standards and monitor station time references. Technical report, DTIC Document, 1998.

[49] James R Wright. GPS composite clock analysis. *International Journal of Navigation and Observation*, 2008, 2008.

[50] NASA. Dawn at vesta. Press Kit, July 2011.

[51] Clarence R Gates. *A simplified model of midcourse maneuver execution errors*. Jet Propulsion Laboratory, California Institute of Technology, 1963.

[52] Alan W Irwin and Toshio Fukushima. A numerical time ephemeris of the earth. *Astronomy and Astrophysics*, 348:642–652, 1999.

[53] DJ Reardon, G Hobbs, W Coles, Y Levin, MJ Keith, M Bailes, NDR Bhat, S Burke-Spolaor, S Dai, M Kerr, et al. Timing analysis for 20 millisecond pulsars in the parkes pulsar timing array. *Monthly Notices of the Royal Astronomical Society*, 455(2):1751–1769, 2015.

[54] A Charef, HH Sun, YY Tsao, and B Onaral. Fractal system as represented by singularity function. *IEEE Transactions on Automatic Control*, 37(9):1465–1470, 1992.

[55] G Prigozhin, K Gendreau, R Foster, G Ricker, J Villasenor, J Doty, S Kenyon, Z Arzoumanian, R Redus, and A Huber. Characterization of the silicon drift detector for nicer instrument. In *SPIE Astronomical Telescopes+ Instrumentation*, pages 845318–845318. International Society for Optics and Photonics, 2012.

[56] Po-Ting Chen, Jason L Speyer, David S Bayard, and Walid A Majid. Autonomous navigation using x-ray pulsars and multirate processing. *Journal of Guidance, Control, and Dynamics*, 40(Special Issue on The Kalman Filter and Its Aerospace Applications (2017)):2237–2249, 2017.

[57] Jodrell Bank Observatory. The european pulsar network data archive. [Online Database], 2016.

[58] J Kocz, W Majid, L White, L Snedeker, and M Franco. Pulsar timing at the deep space network. *Journal of Astronomical Instrumentation*, 5(04):1641013, 2016.

[59] XP Deng, G Hobbs, XP You, MT Li, MJ Keith, RM Shannon, W Coles, RN Manchester, JH Zheng, XZ Yu, et al. Interplanetary spacecraft navigation using pulsars. *Advances in Space Research*, 52(9):1602–1621, 2013.

[60] GB Hobbs, RT Edwards, and RN Manchester. TEMPO2, a new pulsar-timing package–i. an overview. *Monthly Notices of the Royal Astronomical Society*, 369(2):655–672, 2006.

[61] Joseph H Taylor. Pulsar timing and relativistic gravity. *Philosophical Transactions of the Royal Society of London A: Mathematical, Physical and Engineering Sciences*, 341(1660):117–134, 1992.

[62] Dennis D McCarthy and Gerard Petit. Iers conventions (2003). Technical report, DTIC Document, 2004.

[63] Simon J Julier and Jeffrey K Uhlmann. A new extension of the kalman filter to nonlinear systems. In *Int. symp. aerospace/defense sensing, simul. and controls*, volume 3. Orlando, FL, 1997.

[64] Eric Wan, Ronell Van Der Merwe, et al. The unscented kalman filter for nonlinear estimation. In *Adaptive Systems for Signal Processing, Communications, and Control Symposium 2000. AS-SPCC. The IEEE 2000*, pages 153–158. IEEE, 2000.

[65] Commonwealth Scientific and Industrial Research Organization (CSIRO). CSIRO Data Access Portal. [Online Database], July 2017.

[66] Matthew Bailes. Precision timing at the parkes 64-m radio telescope. In *Radio Pulsars*, volume 302, page 57, 2003.

[67] Willem van Straten, Paul Demorest, and Stefan Osłowski. Pulsar data analysis with psrchive. *arXiv preprint arXiv:1205.6276*, 2012.

[68] AW Hotan, W Van Straten, and RN Manchester. Psrchive and psrfits: an open approach to radio pulsar data storage and analysis. *Publications of the Astronomical Society of Australia*, 21(3):302–309, 2004.

[69] S Dai, G Hobbs, RN Manchester, M Kerr, RM Shannon, W van Straten, A Mata, M Bailes, NDR Bhat, S Burke-Spolaor, et al. A study of multifrequency polarization pulse profiles of millisecond pulsars. *Monthly Notices of the Royal Astronomical Society*, 449(3):3223–3262, 2015.

[70] G Desvignes, RN Caballero, L Lentati, JPW Verbiest, DJ Champion, BW Stappers, GH Janssen, P Lazarus, S Osłowski, S Babak, et al. High-precision timing of 42 millisecond pulsars with the european pulsar timing array. *Monthly Notices of the Royal Astronomical Society*, 458(3):3341–3380, 2016.

[71] W van Straten and M Bailes. Dspsr: digital signal processing software for pulsar astronomy. *Publications of the Astronomical Society of Australia*, 28(1):1–14, 2011.

[72] John G Hartnett and Andre N Luiten. Colloquium: Comparison of astrophysical and terrestrial frequency standards. *Reviews of Modern Physics*, 83(1):1, 2011.

[73] Robert L Tjoelker, John D Prestage, Eric A Burt, Pin Chen, Yong J Chong, Sang K Chung, William Diener, Todd Ely, Daphna G Enzer, Hadi Mojaradi, et al. Mercury ion clock for a nasa technology demonstration mission. *IEEE transactions on ultrasonics, ferroelectrics, and frequency control*, 63(7):1034–1043, 2016.

[74] JM Cordes and RM Shannon. A measurement model for precision pulsar timing. *arXiv preprint arXiv:1010.3785*, 2010.

[75] JPW Verbiest, M Bailes, WA Coles, GB Hobbs, W Van Straten, DJ Champion, FA Jenet, RN Manchester, NDR Bhat, JM Sarkissian, et al. Timing stability of millisecond pulsars and prospects for gravitational-wave detection. *Monthly Notices of the Royal Astronomical Society*, 400(2):951–968, 2009.

[76] Demetrios Nicholas Matsakis, Joseph Hooton Taylor, and T Marshall Eubanks. A statistic for describing pulsar and clock stabilities. *Astronomy and Astrophysics*, 326:924–928, 1997.

[77] Richard A Baugh. Frequency modulation analysis with the hadamard variance. In *25th Annual Symposium on Frequency Control. 1971*, pages 222–225. IEEE, 1971.

[78] David W Allan et al. Time and frequency(time-domain) characterization, estimation, and prediction of precision clocks and oscillators. *IEEE transactions on ultrasonics, ferroelectrics, and frequency control*, 34(6):647–654, 1987.

[79] David Scherfgen. Integral calculator. [Online Calculator].

[80] Microsemi Corporate Headquarters, One Enterprise, Aliso Viejo, CA 92656 USA. *5071A Primary Frequency Standard Datasheet*, 2017.

[81] Thomas E Parker. Three-corner hat analysis of the stability of utc and various utc (k) s. In *Proc. 2013 Precise Time and Time Interval Systems and Applications Meeting (ION PTTI)*, pages 296–73, 2013.

[82] Gérard Petit and Brian Luzum. Iers conventions (2010). Technical report, DTIC Document, 2010.